



Vrije Universiteit Brussel

Faculty of Engineering
Department of Mechanical Engineering

**Design of a Below-Knee Prosthesis Powered by
Electric Drives**

by
Tehrani Arman
Vermeire Maxime

Master's thesis submitted in partial fulfilment of the requirements for
the degree of Electro-Mechanical engineer
(Burgerlijk Werktuigkundig-Elektrotechnisch ingenieur)

Academic year: 2007-2008

Promoter: Prof. dr. ir. Dirk Lefeber

Acknowledgements

As this thesis nears completion, we feel that it is more than appropriate to take a moment to acknowledge and thank those who have made this last year at the VUB more than enjoyable.

We have known each other for almost five years now, and it is with great joy and a bit of nostalgia that we look back upon this period. We have worked on many projects together and helped each other a lot during exam preparations. When we found out we could work on this challenging assignment together, we were very delighted. Having shared lots of emotions, especially during this year, we developed a friendship for life.

Therefore, the first persons we want to thank for participating to this thesis are each other. We worked very hard and although teamwork is not always easy, we made it work.

But all egocentricity aside, we specially want to thank our promoter Dirk Lefeber and PhD candidate Rino Versluys, who always found time to guide and assist us when needed. This thesis would not have been possible without their endless support.

We also want to thank our close friends Ebrahim and Mohamed who provided us with fresh insights and practical ideas. And last but not least, special thanks go to our families and all the persons, who took the time to read or got involved in any way with this thesis.

Brussels,
May 2008

Maxime Vermeire
Arman Tehrani

Abstract

Most of today's existing prostheses are purely passive devices. They have fixed stiffness properties independent of the walking conditions. This leads to a higher metabolic energy cost than seen in normals. It is seen that an ingenious combination of the passive elements results in a slight enhancement of the amputee's ankle behaviour throughout stride in comparison to the first generation sockets. Until now, however, none of the available passive prostheses is yet able to achieve more than approximately 70% of the required ankle power during stride.

There is a clear need in the market for active below-knee prostheses in order to improve amputee ambulation. The objective of this Master thesis is the development of a below-knee prosthesis powered by electric drives. The main hurdle that hinders such a development is respecting the size and weight of a healthy below-knee limb, but still providing a sufficiently large instantaneous power and torque output to propel an amputee forward.

This thesis starts with a conceptual modelisation of an active below-knee prosthesis using lightweight passive elements, based on the MACCEPA concept (*Mechanically Adjustable Compliance and Controllable Equilibrium Position Actuator*). The main objective of this part is to develop a model, which meets the requirements to mimic a sound ankle behaviour for slow, normal and fast cadence. Therefore, some modifications were introduced to the classical MACCEPA concept. It is seen that these modifications lead to a more energy efficient model with improved theoretical properties. In order to determine the optimal model parameters, simulations were performed based on the ankle data published by Winter et al..

Further on, a light-weighted, energy efficient driving system is developed, by combining a MAXON RE-40 DC-motor with a ball screw mechanism.

The control aspects of this system, which is considered as a Finite State Machine, are discussed using Boolean expressions based on the Huffman's method. In this part, the required sensors for a real time control are determined.

Further on, the various system parts are designed based on a procedure that takes weight, size and static/dynamic stress analysis into account.

Finally, dynamic simulations were performed in order to confirm the results obtained from the modelisation stage.

The findings can be summarized as follows:

- A *compact* powered below-knee prosthesis that imitates the natural ankle behaviour throughout the *entire* stance phase, in contrast with the precedent prostheses, which only mimic specific parts of the behaviour.
- The prosthesis is capable of providing 100% of the Push-Off power required in stance.
- A driving system with a remarkable total efficiency of 77%.
- An energy consumption of 22,19 J/step for normal cadence with a possible autonomy of 8 hours (for a 75 kg subject).
- An overall weight of 2,85 kg, excluding the batteries.

Compte rendu

La majorité des prothèses utilisées ce jour sont des systèmes purement passifs. Elles ont de qualités de raideur invariable indépendamment de la condition de marche. Ceci mène à une consommation d'énergie métabolique plus élevée que celle vue dans la norme. Il est clair qu'une combinaison ingénieuse des éléments passifs améliore déjà le mouvement de la cheville en comparaison avec les prothèses de la première génération. Néanmoins, actuellement, aucune des prothèses passives atteint plus d'environ 70 % de la puissance requise dans cheville lors de la marche.

Il y a donc clairement une demande importante et de débouché pour des prothèses transtibial active afin d'améliorer l'ambulation des amputés. L'objectif de cette thèse de Master est le développement d'une prothèse transtibial activée par un actuateur électrique. Le problème principal dans le développement d'une telle prothèse est qu'il faut respecter la forme et le poids d'une jambe transtibial normale et en même temps générer assez d'énergie lors de la phase de *Heel-Off*.

Cette thèse commence par une modélisation conceptuelle d'une prothèse transtibial utilisant des éléments légers passifs, basée sur le concept MACCEPA (*Mechanically Adjustable Compliance and Controllable Equilibrium Position Actuator*). Le but actuel est un modèle qui satisfait aux exigences du comportement de la cheville pour une cadence, lente, normale et rapide. A cet effet certaines modifications ont été apportées au concept classique de MACCEPA. Ces modifications ont conduit à un modèle plus efficace en énergie et à une amélioration de la performance théorique. Afin de déterminer le modèle optimal, les paramètres de simulation ont été basés sur les données de cheville publiées par Winter.

Suite à cela, un système de propulsion léger et efficace a été développé en combinant un moteur MAXON RE-40 DC avec un mécanisme de joint à boulet. L'aspect de contrôle de ce système, considéré comme une « Finite State Machine », utilise des expressions Boolean, basées sur la méthode d'*Huffman*. Les sensors requis pour un contrôle en temps réel ont été déterminés.

De plus, les différentes pièces du système ont été constituées et finalisées selon une procédure

en tenant compte du poids, des dimensions et de l'analyse statique/dynamique de tension. Au stade final, des simulations *dynamiques* ont été exécutées afin de confirmer les résultats obtenus au stade de modélisation.

Les résultats peuvent être résumés comme suit :

- Une prothèse transtibial *compacte* qui imite le comportement d'une cheville naturelle *dans toutes ses phases*, contrairement aux prothèses antérieures qui étaient limitées à quelques phases spécifiques.
- 100% de la capacité de propulsion nécessaire pendant la phase de *Push-Off*.
- Un système de propulsion avec une efficacité totale de 77 %.
- Une consommation d'énergie de 22,19 J/marche pour une cadence normale avec une autonomie possible de 8 heures (pour une personne de 75 kg).
- Un poids total de 2,85 kg, hors batteries.

Samenvatting

De meerderheid van de bestaande onderbeenprothesen zijn zuiver passieve systemen. Ze hebben vaste stijfheidseigenschappen onafhankelijk van het stappatroon. Dit leidt tot een hogere metabolisch energie verbruik in vergelijking met dat van een gezonde persoon. Het blijkt dat men met een ingenieuze combinatie van de passieve elementen het enkelgedrag van een patiënt tijdens de wandelcyclus in beperkte mate kunnen verbeteren in vergelijking met de eerste generatie prothesen. Zelfs met de meest geavanceerde passieve prothesen, slaagt men er niet in om meer dan ongeveer 70% van het vereiste enkel vermogen tijdens de wandelcyclus genereren.

Er bestaat er een duidelijke noodzaak in de markt voor actieve onderbeenprothese die het gangpatroon van een patient moeten verbeteren. Het doel van deze thesis is het ontwikkelen van een onderbeenprothese bekrachtigd met elektrische actuatoren. De grootste uitdaging bestaat erin om het gewicht en de afmetingen van een onderbeen niet te overschrijden en er toch voor te zorgen dat de patient voorzien wordt van voldoende vermogen en koppel om zich vooruit te stuwten.

Deze thesis begint met een conceptuele modelisatie van actieve onderprothese gebruik makende van lichte, passieve elementen, die gebaseerd is op het MACCEPA concept (*Mechanically Adjustable Compliance and Controllable Equilibrium Position Actuator*). Het doel is om een model te ontwikkelen die voldoet aan de vereisten van een gezonde enkel voor traag, normaal en snel wandelen. Om die doelstelling te realiseren, zijn enige modificaties aangebracht aan het klassieke MACCEPA concept. Het blijkt dat deze modificaties tot een energie-efficiënter model zullen leiden met een verbetering van de theoretische performantie. Om de modelparameters te optimaliseren zijn simulaties uitgevoerd gebaseerd op de enkeldata gepubliceerd door Winter et al..

Verder is een lichte, energie-efficiënte actuator systeem ontwikkeld door een MAXON RE-40 DC-motor met een kogelspindel-mechanisme te combineren.

De controle aspecten van dit systeem, dat als een *Finite State Machine* beschouwd wordt, zijn besproken gebruik makende van Booleaanse uitdrukkingen gebaseerd op de methode van *Huffman*. In dit deel worden de vereiste sensoren voor een *real-time* controle bepaald.

Verder zijn de verschillende onderdelen van het systeem ontworpen volgens een procedure rekening houdend met het gewicht, de afmetingen en een statische/dynamische analyse.

Ten laatste zijn er dynamische simulaties uitgevoerd die de resultaten bekomen tijdens de modelistatie moeten bevestigen.

De resultaten kunnen als volgt opgesomd worden:

- Een *compacte* actieve onderbeenprothese die het gedrag van een gezonde onderbeen nabootst gedurende de volledige steunfase van de wandelcyclus.
- De prothese heeft de mogelijkheid om 100% van het *Push-Off* vermogen nodig tijdens de steunfase te genereren.
- Een actuator systeem met een totale efficiëntie van 77%.
- Een energieverbruik van 22,19J/stap voor normaal wandelen met een mogelijke autonomie van 8 uren (voor een patient van 75 kg).
- Een totaal gewicht van 2,85 kg, exclusief de batterijen.

Abbreviations

PBP: Powered Below-knee Prosthesis

DF: Dorsi-Flexion

PF: Plantar-Flexion

CP: Controlled Plantar-flexion

CD: Controlled Dorsi-flexion

PP: Powered Plantar-flexion

FSM: Finite State Machine

MCP: Maximum CP ankle angle

MPP: Maximum PP ankle angle

AM: Angle added by the Motor

BLDC: Brushless DC-motors

C-Spring: Compliant Spring

S-Spring: Stiff Spring

C-Lever arm: Lever arm connected to the C-Spring

S-Lever arm: Lever arm connected to the S-Spring

MACCEPA: Mechanically Adjustable Compliance and Controllable Equilibrium Position
Actuator

DF-Locked: Dorsi-Flexion motion Locked

Table of Contents

Table of Contents	1
Chapter 1 Biomechanics	12
1.1. Gait Analysis	12
1.2. Phases of Gait	14
1.3. Ankle Mobility	17
1.4. Characterisation of the Ankle Function for Normal Cadence	18
1.4.1. Ankle Motion	18
1.4.2. Ankle Torque.....	19
1.4.3. Ankle Angular Velocity and Ankle Power	22
Chapter 2 Below-Knee Prosthesis	24
2.1. Prior Work.....	24
2.2. Future Perspectives	30
Chapter 3 Design of a Below Knee Prosthesis Powered by Electric Drives	31
3.1. System Characterization.....	31
3.1.1. Modelisation.....	31
3.1.1.1. Introduction	31
3.1.1.2. Final Model	31
3.1.1.3. Mathematical Expressions.....	33
3.1.1.4. Physical Model.....	34
3.1.1.5. Conclusion.....	45
3.1.2. Simulations.....	46
3.1.2.1. Design Parameters.....	48
3.1.2.2. Conclusion.....	57
3.2. Driving System.....	60
3.2.1. Motor.....	60
3.2.2. Transmission	66
3.2.2.1. Gears	66
3.2.2.2. Ball Screw	71
3.2.2.3. Belt	79

3.2.3.	Final Driving System	82
3.2.4.	Driving System for Compliance Adjustability (MACCEPA).....	84
3.2.5.	Unlocking Mechanism for Ratchet and Pawl.....	85
3.2.6.	Power Supply	87
3.3.	Control Aspects	92
3.3.1.	Finite State Machine.....	92
3.3.2.	Huffman’s Method	96
3.3.3.	Conclusion.....	98
3.4.	Design and Assembly of the parts	100
3.4.1.	Procedure.....	100
3.4.2.	Part Design	102
3.4.3.	Total Assembly	138
3.4.4.	Conclusion.....	141
3.5.	Dynamic Simulations	142
3.5.1.	Introduction	142
3.5.2.	Dynamic Simulation Using the ‘Imposed Motion’-Approach.....	142
3.5.3.	Dynamic Simulation Using the ‘Imposed Torque’-Approach.....	145
Chapter 4	General Conclusions	149
References	151
Appendices	153

Chapter 1

Biomechanics

1.1. Gait Analysis [1],[2]

Although walking seems obvious to everybody, a human walking pattern is more complex as one might think. It is a series of interaction between two multi-segmented lower limbs and the total body mass. In this chapter, the human walking pattern or gait cycle will be elaborated with the emphasis on the function of the ankle. In order to build a powered below-knee prosthesis (PBP) that will help recreating a sound gait cycle, the natural human ankle behaviour has to be analyzed in detail.

The gait cycle can be described with two basic methods:

1. Cycle divisions
2. Stride and step

Cycle divisions

The gait cycle can be divided in a number of periods depending on the ground contact. First, the gait cycle can be divided in a stance period, which is the period where the foot has ground contact and a swing period, which is the period where the foot has no ground contact at all. During this latter period, the foot returns to its original starting position.

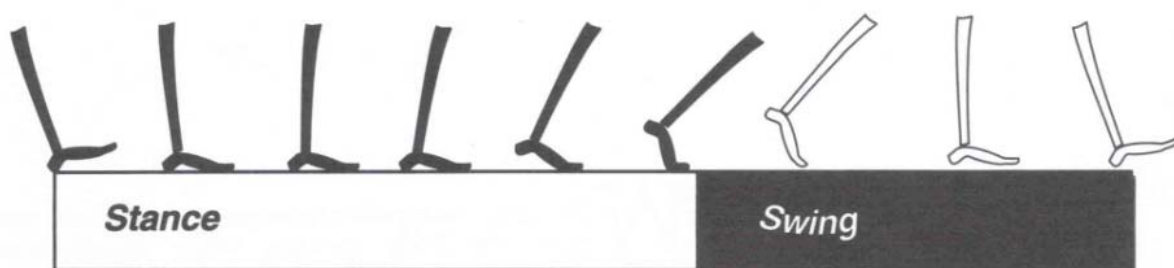


Fig. 1: Divisions of the gait cycle. The white bar represents the duration of the stance period and the black bar represents the duration of the swing period

Stride and step

The second method to describe the gait cycle is explained by introducing the term *stride*. A step is the distance travelled between the initial contacts of each foot. A stride is the distance travelled between the initial contact of one foot and the next initial contact of that same foot. Therefore, the duration of a stride is the interval between two sequential initial floor contacts by the same limb. As one can see in Fig. 1, the bigger part of the gait cycle is the stance period, which is approximately 60% of the total gait cycle. The swing period is about 40% of the gait cycle. Notice that these periods dependent on the walking velocity. Winter[2] measures the velocity through stride length and cadence with Eqtn.1.

$$\text{Velocity} = (\text{stride length} \times \text{cadence}) / 120 \quad (\text{m/s}) \quad \text{Eqtn. 1}$$

The stride length is the distance travelled between successive stance periods (in meter) and the cadence is the number of steps performed per minute. In a summary of 53 trials, average cadence and stride lengths were measured for fast, normal and slow adult walkers. Table 1 shows the results of these measurements. [2]

Table 1: calculation of velocity and gait cycle times from the measurements performed by Winter et al.

	Cadence (steps/min)	Stride length (m)	Stride velocity (m/s)	Stride time (s)	Stance time (s)	Swing time (s)
Slow walkers	86,8	1,38	1,00	1,38	0,83	0,55
Natural walkers	105,3	1,51	1,33	1,14	0,68	0,46
Fast walkers	123,1	1,64	1,68	0,97	0,58	0,39

For these cadences, stance and swing time are calculated from the stride time assuming that stance time is approximately 60% of the stride time. This is of reasonable accuracy as all the researchers involved in this experiment reported a stance period varying from 58% to 61% of the stride period. As cadence and velocity increase, both stance and swing times decrease. The stance and swing time will give insight to how fast the system of the designed PBP will have to react. As it is seen further on, this time interval is crucial for the design of the necessary electric drives.

1.2. Phases of Gait [1]

After introducing different terms to describe the gait cycle, the stance and swing period are divided into 3 tasks, comprising 8 phases. Fig. 2 illustrates these tasks and phases.

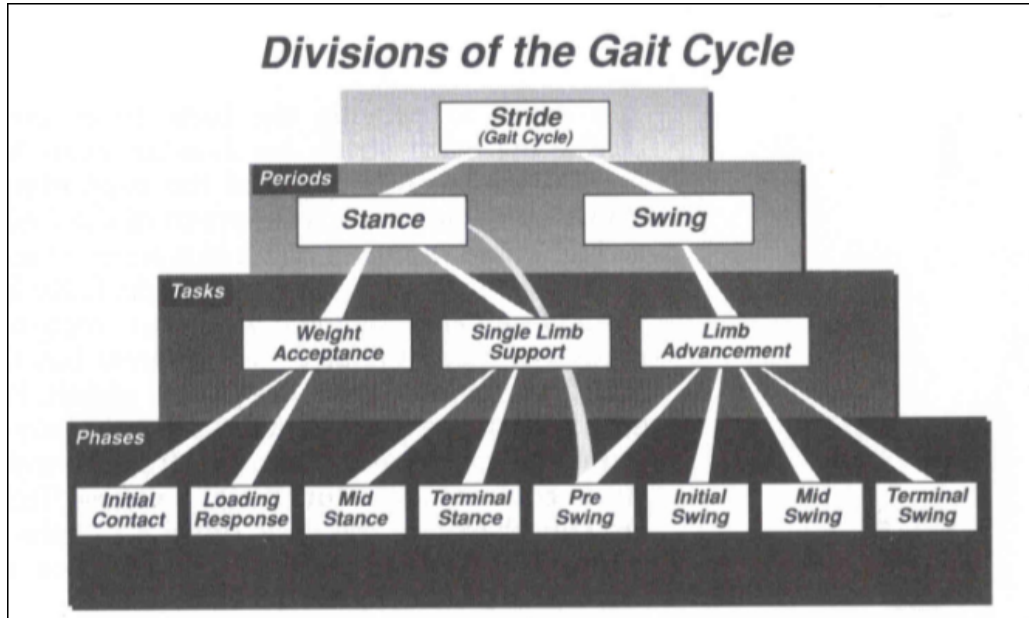


Fig. 2: Divisions of the gait cycle

Task A: Weight Acceptance

This task consists of 2 phases: the *Initial Contact* and the *Loading Response*. This task is a very important and challenging one, considering the fact that the whole bodyweight has to be transferred and balanced from one limb to the other, which just finished a swing phase.

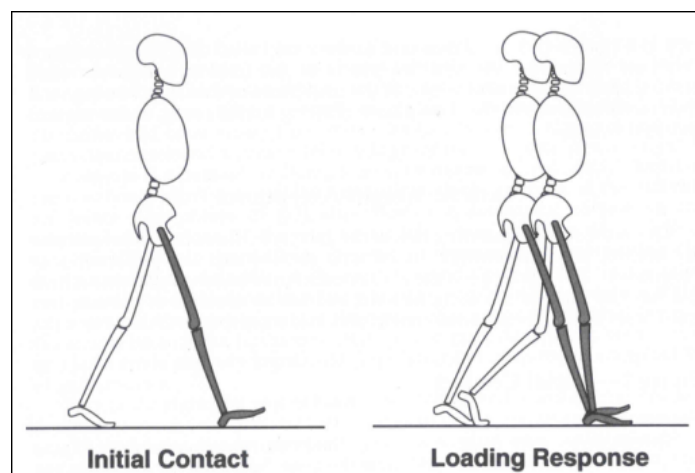


Fig. 3: Phase 1: the Initial Contact (left) and Phase 2: the Loading response (right). The main objective of this period is the shock absorption, initial limb stability and the preservation of progression.

Phase 1: Initial Contact

This interval extends from 0 to 2% of the gait cycle. It consists of a heel impact and the limb preparing itself for a rolling motion over the heel.

Phase 2: Loading Response

This interval extends from 0 to 10% of the gait cycle. In this phase the heel has the function of a rocker and the whole body weight is transferred to the other limb. This phase ends when the other foot is lifted from the ground (Toe-Off).

Task B: Single Limb Support

The Single Limb Support task consists of, as the name implies, supporting the whole body on a single limb, while the other limb is in swing phase and repositioning itself for initial contact. The stability is of great importance during this period, as only one foot rests on the ground.

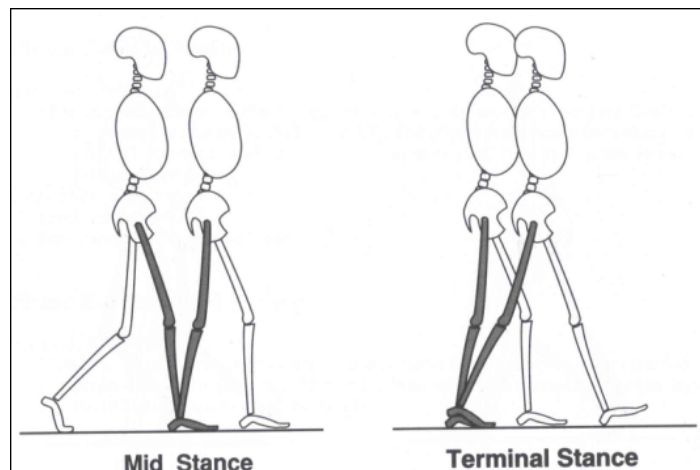


Fig. 4: Phase 3: Mid-Stance (left), Phase 4: Terminal Stance (right). The main objective of this period is the transfer of the full body weight to a single limb and to maintain body stability.

Phase 3: Mid-Stance

The *Mid-Stance* phase extends from 10 to 30% of the gait cycle. In this phase the foot remains flat on the floor and the ankle has the function of a rocker. The main objective during this period is the progression over the supporting foot and the stability of the body.

Phase 4: Terminal Stance

The *Terminal Stance* phase interval extends from 30 to 50% of the gait cycle. It begins with the rising of the heel and ends with the initial contact of the other foot. In the *Terminal Stance* phase the forefoot has the rocker function. The end of this phase is the completion of the *Single Limb support*.

Task C: Limb Advancement

The objective of this task is the progression of body motion and preparing the position of the balancing foot in order to achieve a proper Heel-Strike in the following cycle. It comprises 4 phases: *Pre-Swing*, *Initial Swing*, *Mid Swing* and *Terminal Swing*.

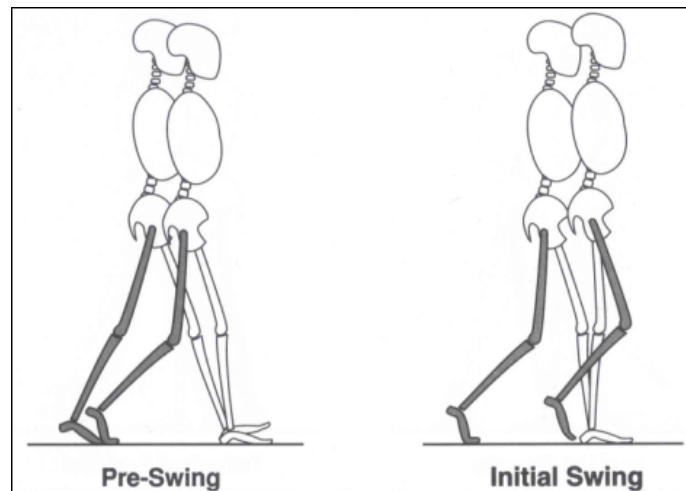


Fig. 5: Phase 5: Pre-Swing (left), Phase 6: Initial Swing (right). This period is the swing phase and its main objective is to maintain movement by advancing the limb and positioning it for the following initial contact (completion of the gait cycle)

Phase 5: Pre-Swing

The Pre-Swing can be interpreted as the transition period between stance and swing and extends from 50 to 60% of the gait cycle. It is the end of the stance period and the main objective is the complete transfer of bodyweight to the supporting limb in order to start the swing phase.

Phase 6: Initial Swing

This interval extends from 60 to 73% of the gait cycle and is approximately one third of the swing period. It initiates at the complete lifting of the foot (Toe-Off) and culminates when the swinging foot is opposite to the supporting foot.

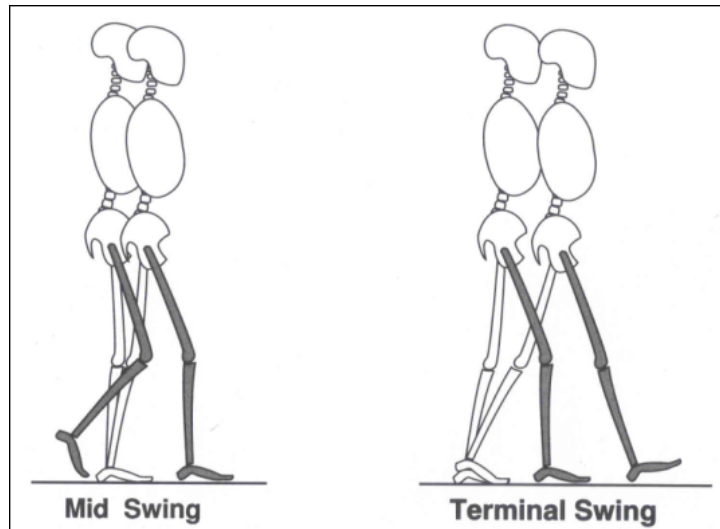


Fig. 6: Phase 7: Mid Swing (left) and Phase 8: Terminal Swing (right). This period is the swing phase and its main objective is to maintain movement by advancing the limb and positioning it for the following initial contact (completion of the gait cycle)

Phase 7: Mid Swing

The *Mid Swing* interval extends from 73 to 87% of the gait cycle. It starts when the swinging foot is opposite to the supporting foot and ends when the angle between the foot and the lower-limb is 90°.

Phase 8: Terminal Swing

This interval extends from 87 to 100% of the gait cycle. It is the last phase of the cycle and its objective is the completion of the leg advancement and the preparation of the limb for the following initial contact.

1.3. Ankle Mobility [3]

The ankle has mobility in three planes: the sagittal plane, a vertical plane that divides the body into right and left parts, the coronal (or frontal) plane, a vertical plane that divides the body into anterior and posterior parts and the transverse plane, a horizontal plane that divides the body in an upper and lower part as illustrated in Fig. 7. In this thesis only the ankle characteristics in the sagittal plane will be discussed. The designed PBP will only have motion ability in this plane in order to avoid too great complexity. As 93% of the work done

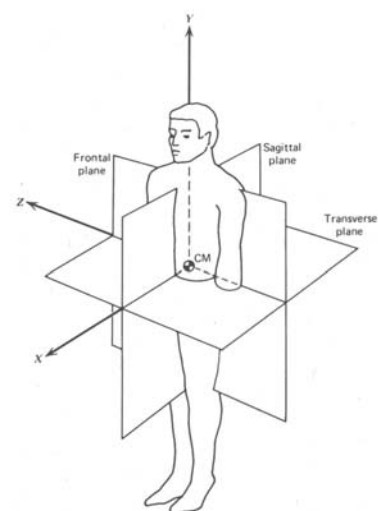


Fig. 7: Mobility planes of human body

at the ankle is done in the sagittal plane, it seems reasonable to assume that a model based only on sagittal movement would capture the most important features of ankle function during stance [4]. It is important to know the progression of angle between the foot and the lower limb during the gait cycle. More important is to understand how these angles are achieved or in other words, to examine the ankle torque during the gait cycle.

1.4. Characterisation of the Ankle Function for Normal Cadence [1],[2],[4],[5]

The various curves of the ankle characterization used in this thesis are collected from Winter et al.. For this research, data of 60 normal subjects (mainly university students, aged 19-32) were recorded.

1.4.1. Ankle Motion

The sagittal plane motion consists of *dorsi-flexion* (DF), where the foot rotates towards the tibia, and *plantar-flexion* (PF), where the foot rotates away from the tibia. Fig. 8 shows the normal ankle angle range during a normal stride.

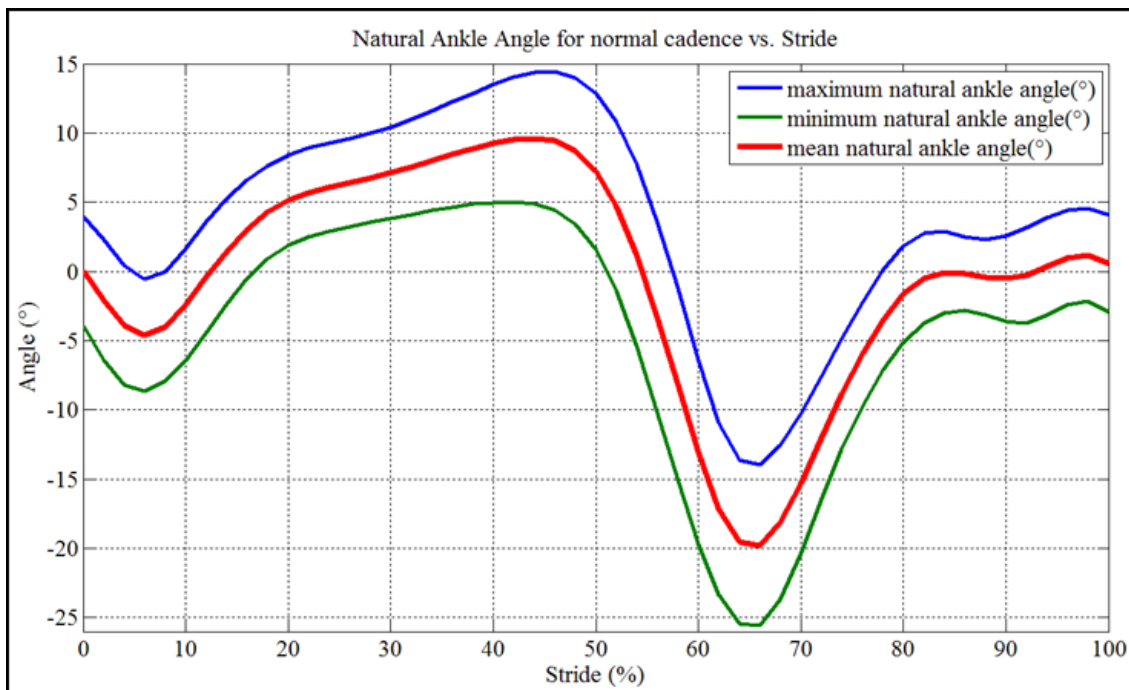


Fig. 8: Ankle motion of normal stride: the angle between the tibia and a vertical axis perpendicular to the foot is measured. (Overall mean, STD=1). Notice that the angle on the abscissa is the angle between the tibia and a vertical axis perpendicular to the foot, which means that when the angle between the foot and the tibia is 90° (stand up straight) the measured angle is 0°. Positive angles represent DF and negative angles represent PF.

At Heel-Strike (initial contact) the ankle angle is approximately 0° . The ankle then plantar-flexes to minus $4-5^\circ$ until the end of the *Loading Response Phase* (Foot-Flat). At the beginning of the *Mid-Stance phase* the ankle alters direction and starts to dorsi-flex to $9-10^\circ$ until the end of the *Single Limb Support* period. The ankle then reinitiates PF to minus $19-20^\circ$, which occurs at Toe-Off (complete lifting of the foot). The Toe-Off initiates the final DF action until 0° at *Mid Swing Phase* and the angle remains approximately at 0° during the rest of the swing period.

1.4.2. Ankle Torque

Body Weight Vector

In order control stability and progression of movement during stride, muscles have to compensate the moment imposed by the body load. This load can be interpreted as a vector of which the direction and magnitude is continuously changing during stride. The amplitude and the alignment of the body weight vectors determine the required torque in the ankle, which will further be referred to as the ankle torque.

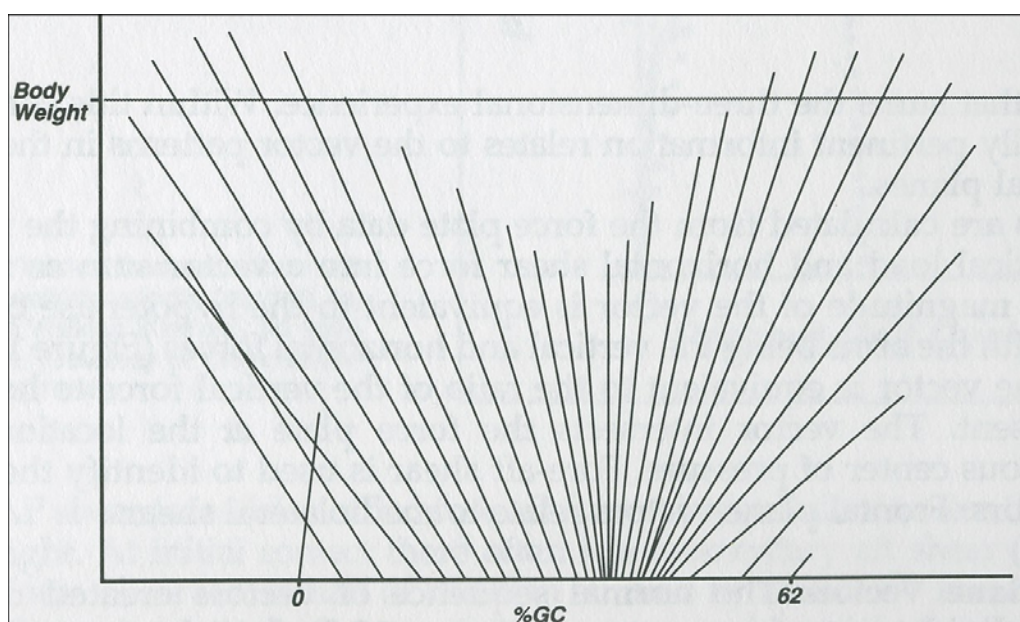


Fig. 9: Body Weight Vector: the body load can be interpreted as a vector of which the alignment and magnitude change throughout stride.

At initial Heel-Contact the body weight vector is centred in the heel, which is behind the ankle joint and will therefore generate a PF torque. This torque achieves a maximum value at the beginning of the *Loading Response* phase. The normalized ankle torque as a function of the stride is displayed in Fig. 10.

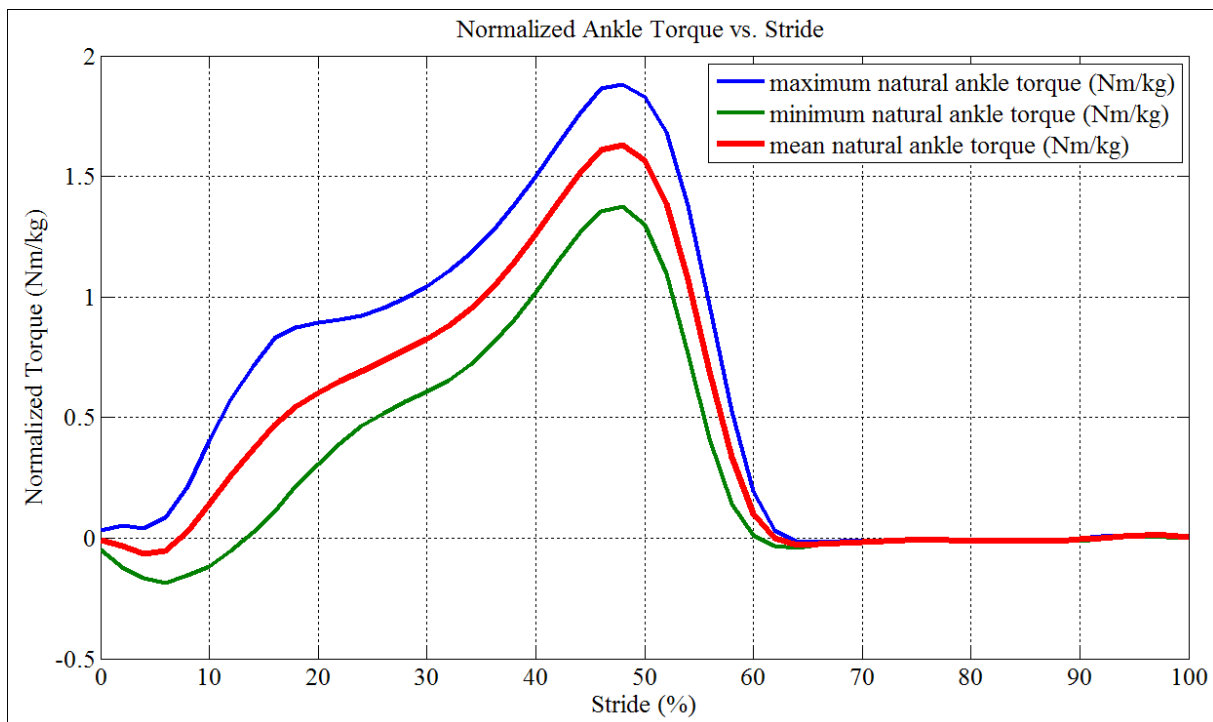


Fig. 10: normalized ankle torque in Nm/kg as a function of the stride (%). (Overall mean, STD=1). [2]

As the limb advances, so does the Body Weight Vector. The ankle is in DF and the PF torque gradually diminishes to zero torque. This occurs when the Body weight vector intersects the ankle joint at midpoint of the *Loading Response* phase. Beyond this point, the Body Weight Vector is passed the ankle joint and a DF torque is created and is increasing until just before the opposite foot strikes the floor (end of *Terminal Stance* phase). Notice that slope of the curve increases in the beginning of the *Terminal Stance* phase (approximately 30% of gait cycle) as the Heel-Off starts.

Ankle Torque as a function of the Ankle Angle

The ankle torque as a function of the ankle angle is plotted in Fig. 11.

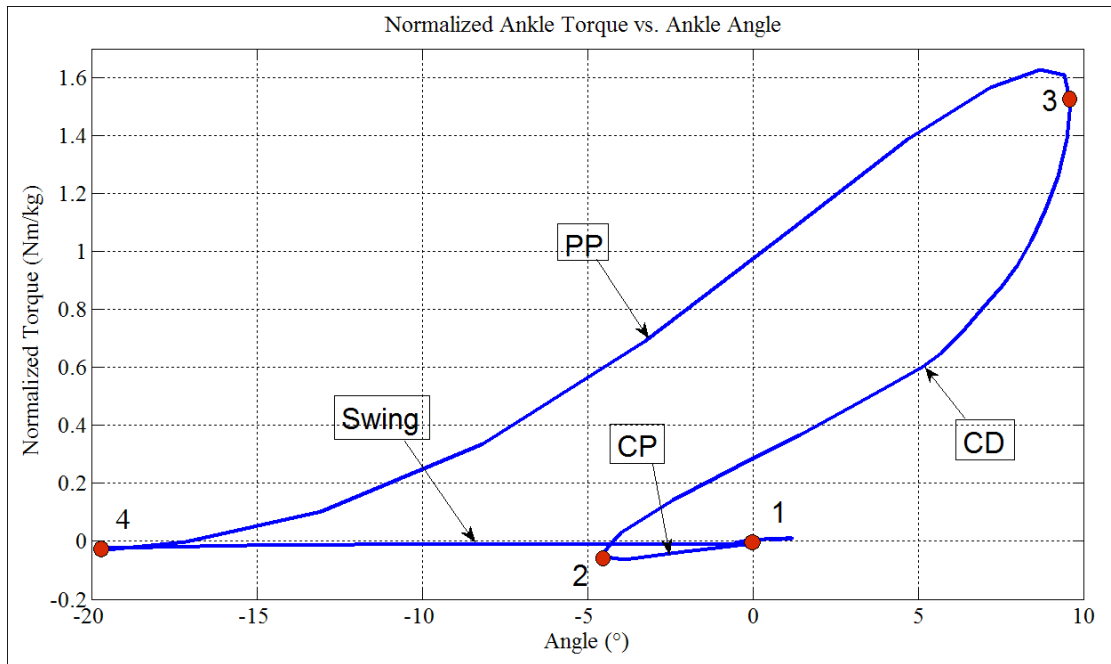


Fig. 11: Normalized Ankle Torque as a function of the Ankle Angle for normal cadence. The curve is divided in 4 parts: (1-2) controlled plantar-flexion, (2-3) controlled dorsi-flexion, (3-4) powered plantar-flexion, (4-1) swing period [2]

The three parts during stance will be analyzed and a curve fitting will be performed on each part.

The torque course can be divided in four major parts (1-2), (2-3), (3-4) and (4,1). The stance period comprises the first 3 parts and the last part is the swing period.

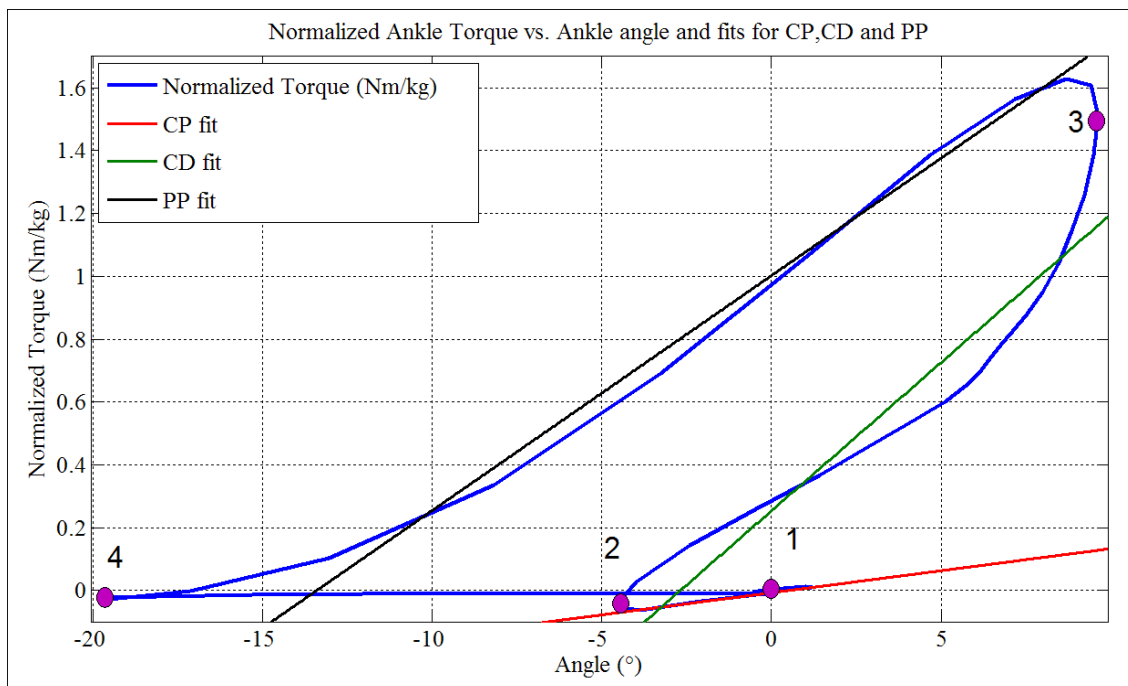


Fig. 12: Ankle Torque vs Ankle angle. The blue line represents the ankle torque, the red, green and black lines are the fits of CP, CD and PP, respectively.

Part (1-2) is called the *Controlled Plantar-Flexion (CP)*. This begins at Heel-Strike, which occurs at an ankle angle of 0° and ends at Foot-Flat (end of *Loading Response* phase), where the ankle angle is approximately minus 4° . As one can see in Fig. 12 this section of the torque curve can be assumed as linear. This can be assumed as the R^2 value of the CP-fit is 0,992.

Part (2-3) is the *Controlled Dorsi-Flexion (CD)*, which ends at approximately 9° (end of the *Terminal Stance* phase). In an attempt to approach the section by a linear curve (Fig. 12), the R^2 value of the CD-fit is 0,878. As this is not sufficient, a non-linear fit should be used to approach this part of the curve.

Part (3-4) is called the *Powered Plantar-Flexion (PP)* and ends approximately at minus 17° (end of *Pre-Swing* phase). This section can be approached by a linear curve as illustrated in Fig. 12. The R^2 value of the PP-fit is 0,991.

1.4.3. Ankle Angular Velocity and Ankle Power

The ankle angle velocity is necessary for calculating the ankle power, as this is done so by multiplying the ankle torque by the ankle angular velocity. The ankle power is also shown in Fig. 13. In order to comment on these two curves, it is interesting to add the ankle torque and the ankle angle and comparing all 4 curves simultaneously.

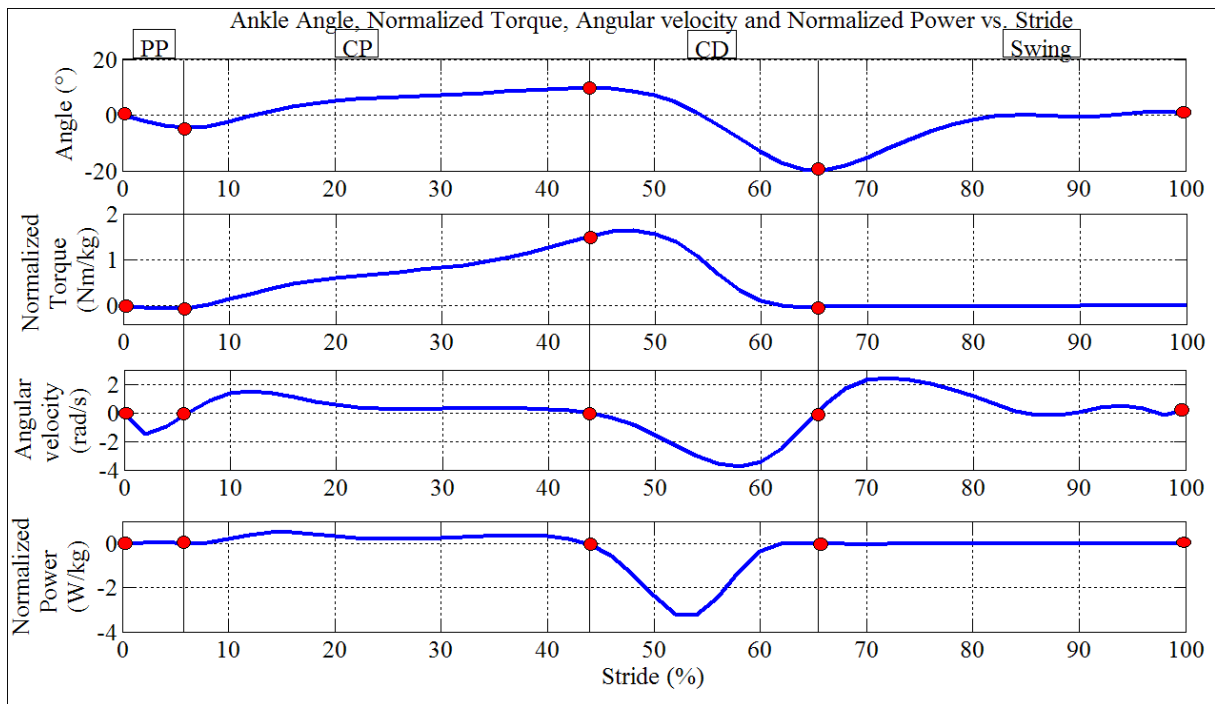


Fig. 13: Ankle Angle (°), Normalized Ankle Torque (Nm/kg), Ankle Angular Velocity (rad/s), Normalized Ankle Power (W/kg) vs. Stride (%)

The ankle angular velocity is zero when the ankle angle reaches a minimum or maximum value, which is when the rotation alters direction. Also notice that the ankle angular velocity is much higher in the first half of the swing phase than in the second half. The foot has to be quickly raised in the beginning of the period, as ground impact has to be avoided during swing period. The greatest power is required during PP as the body has to be raised during the *Terminal Stance* phase and the effect of that body weight is accentuated by the acceleration of the downward fall. The characterization of the ankle function for slow and fast cadence can be found in Appendix A.

Chapter 2

Below-Knee Prosthesis

2.1. Prior Work

Although the notion of importance of PBP's has been obvious since the late 1990's, not many attempts are made in order to provide such a device. The more recent research is mostly carried out in the direction of passive prostheses. Thus, there is a clear need in the market for PBP's in order to improve amputee ambulation.

The focus of this chapter is mainly on the previous projects done to develop *below-knee* prostheses and excludes the innumerable amount of work done to design and develop *above-knee* prostheses including an -active or passive- ankle joint. Some examples of the precedent advanced passive below-knee prostheses are shown in Fig. 14.

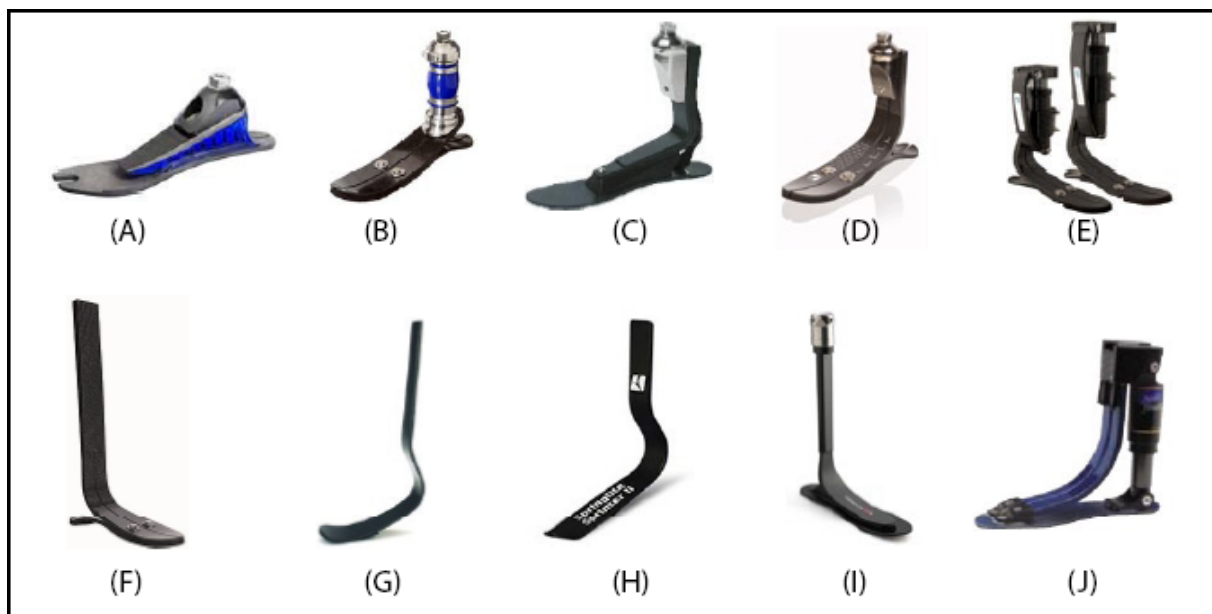


Fig. 14: Some examples of the precedent advanced passive below-knee prostheses: (A) Flex-Foot Axia (B) LP-Ceterus (C) Talux Foot (D) VariFlex (E) Re-Flex VSP (F) ModularIII (G) Flex-Sprint (H) Sprinter (I) Advantage DP (J) Pathfinder [22]

This paragraph describes some of the countless examples of recent works that we found interesting to mention.

C-Walk [8]:

C-Walk is a good example of a totally passive commercialized prosthetic foot. This prosthesis is only equipped with passive components, combined in an ingenious manner, which leads to an energy-efficient walking pattern in comparison with other passive prosthetic feet.



Fig. 15: C-Walk construction

As shown in Fig. 15, in the C-Walk® the C-shaped spring (1) and base spring (2) are dynamically coupled with a control ring (3). During each phase of gait, the energy efficiency of this combination ensures a physiological and harmonious roll-over. Fig. 16 shows the ankle moment (Nm) as a function of % of stance phase for a sound leg and a prosthetic leg.

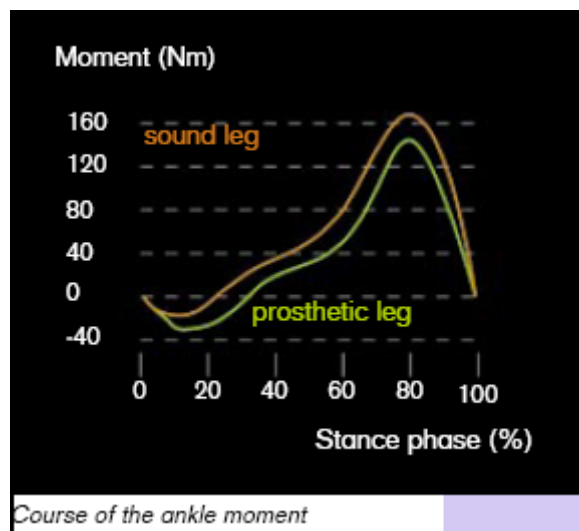


Fig. 16: Course of Ankle Torque (Nm) as a function of % of Stance for a sound leg and a prosthesis leg (C-Walk [8])

It is seen in Fig. 16 that the course of moments generated by the C-Walk corresponds with the course of a natural ankle. However, the moments generated in PF phase are slightly higher than a natural ankle in order to be able to store enough energy and to provide a higher ankle moment in the next phase in order to initiate a Heel-Off. Hence, the generated moment in the DF is still less than a natural ankle as a result of using only passive components.

Intelligent prosthetic ankle joint by MR brake (Osaka University) [7]:

This study consists in the development of a prosthetic ankle joint controlled by specially designed linear MR (Magneto-Rheological) brake. The rheology of MR fluid is controllable and depends on the intensity of an applied magnetic field. The main purpose of using MR brake is to function as a dorsiflexor. There are two prototypes developed in this study. So far, this concept is purely academic and is not commercialized yet.

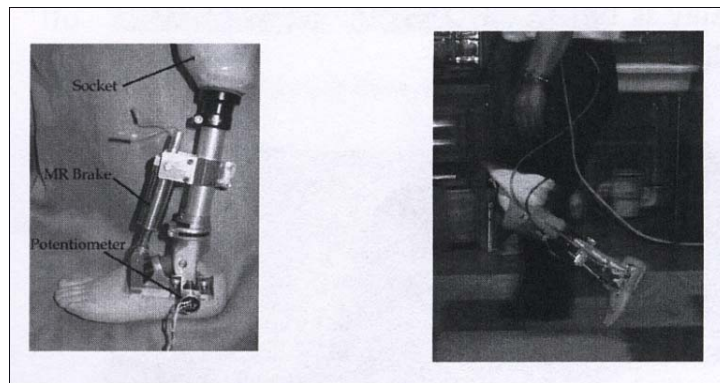


Fig. 17: Prototype of Intelligent prosthetic ankle joint by MR brake

Below-knee prosthesis powered by Pleated Pneumatic Artificial Muscles [6]:

This project -PhD thesis on the mechanical department of VUB (Vrije Universiteit Brussel) by R. Versluys- consists in a mechatronical development of a PBP using pleated pneumatic artificial muscles in order to generate ankle power, see Fig. 18. The amount of ankle power and the prosthetic ankle stiffness are adjustable during walking, by regulating the air-pressure in the artificial muscles. An advantageous property of this prosthesis is the fact that the ankle motion is no longer restricted to sagittal motion. The main hinder of this type of prostheses is the limited autonomy. This type of prostheses is applicable in rehabilitation processes.



Fig. 18: Powered Below-knee Prosthesis, using pleated pneumatic artificial muscles in order to generate ankle power (VUB). [22]

Powered ankle-foot prosthesis [9],[10]

Hugh Herr and his biomechatronics research group at the MIT Media Lab have developed the first PBP. The main purpose of this prosthesis, unlike the fully passive prosthetic ankles, is mimicking the action of a biological ankle, and providing amputees with a natural gait. There are some plans in order to commercialize this product.

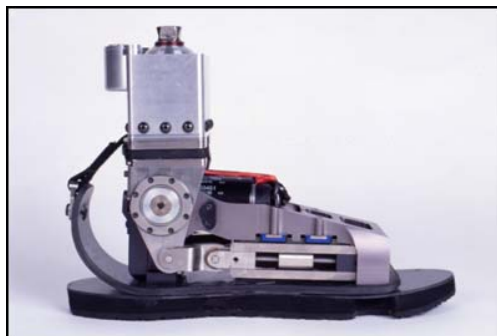


Fig. 19: Powered Ankle-Foot prosthesis by Hugh Herr and his Biomechatronics research group at the MIT Media Lab

As illustrated in Fig. 20, there are five main mechanical elements in the system: a high power output DC-motor, a transmission, a series spring, a unidirectional parallel spring, and a carbon composite leaf spring prosthetic foot. The first three components are combined to form a force-controllable actuator, called Series-Elastic Actuator (SEA). The SEA provides force control by controlling the extent to which the series spring is compressed.

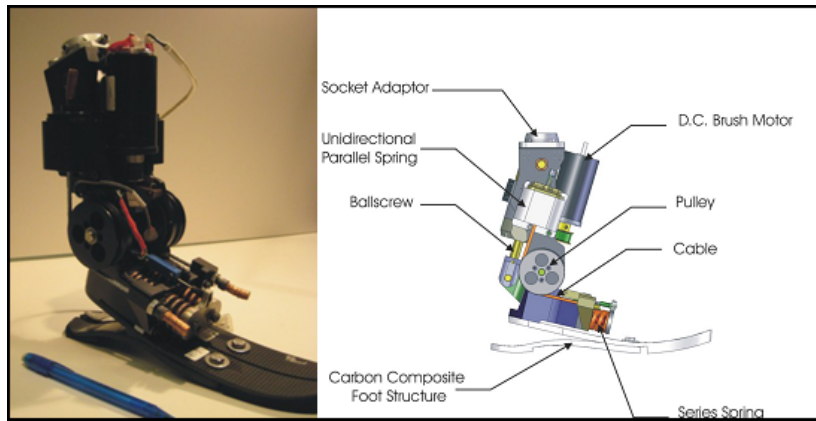


Fig. 20: a) Left: Physical prototype of the Ankle-Foot prosthesis, b) Right: Cad design of the Ankle-Foot prosthesis

In this study it is assumed that the normal human ankle behaviour has a "quasi-static stiffness" during the stance phase. The stiffness is defined as the slope of the measured ankle torque-angle curve during stance. Therefore, mimicking this quasi-static stiffness curve is considered as the main goal for the stance phase control.

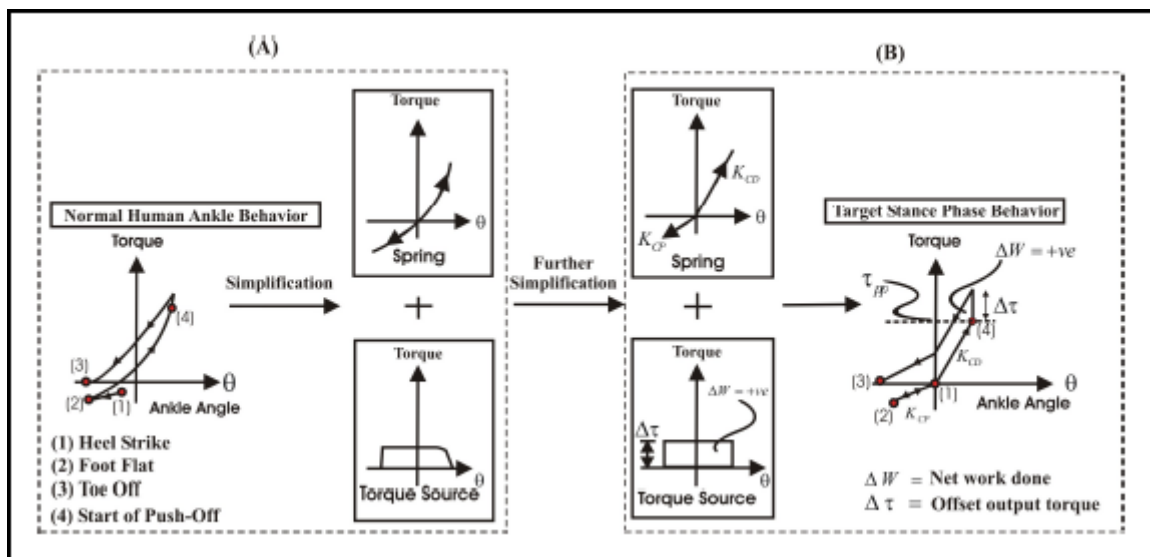


Fig. 21: Decomposition of the normal human ankle behaviour (quasi-static stiffness curve) into a spring component and a torque source. The stiffness of the spring component equals K_{cp} between (1)-(2) and K_{cd} between (1)-(4). The torque source is applied on the ankle joint between (4)-(3) as a constant value.

As shown in Fig. 21 the normal human ankle behaviour is decomposed into spring component and a torque source. The stiffness of the spring component is linearized and varies with the sign of the ankle angle; it equals K_{cp} between (1)-(2) and K_{cd} between (1)-(4). The torque source is applied as a constant offset between (4)-(3). It is seen in Fig. 21 that the course of the theoretical ankle torque is strongly simplified comparing to the natural human ankle behaviour.

THE SPARKy (SPRING ANKLE WITH REGENERATIVE KINETICS) PROJECT [11]:

The main objective of the SPARKy Project is the development of a smart and energy-storing PBP based on lightweight, energy-storing elastic elements in order to minimize energy requirement while providing the amputee enhanced ankle motion and “Push-Off” power. SPARKy is a multi-phased project led by Arizona State University Human Machine Integration Lab.

As shown in Fig. 22, a parallel two springs Robotic Tendon is attached to the leg and a Keel via a lever. The RE40 motor is coupled with the robotic tendon through a lead screw mechanism. It can be shown that this configuration will generate a dynamic moment about the ankle joint.

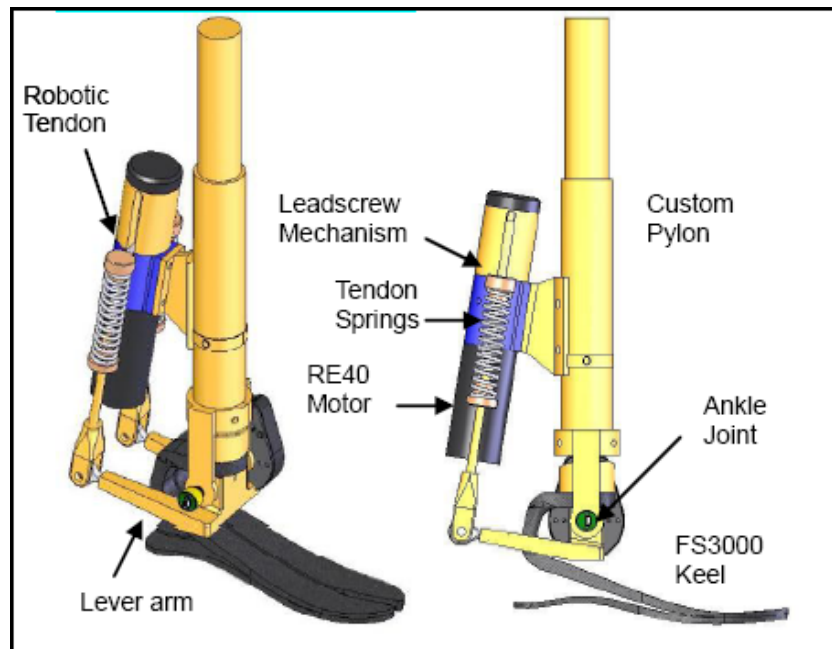


Fig. 22: Isometric and side views of SPARKy in solidworks [11].

The ankle joint is designed in such a way that it could get locked and released during certain phases of gait. It is seen that locking the ankle joint and isolating the Robotic Tendon during certain phases of gait would increase the energy storage potential in the keel and Robotic Tendon system. This lock is achieved using a spring-loaded pin that uses the patient’s body weight to compress and lock the ankle joint after Heel-Strike. A solenoid is used in order to unlock the pin.

The stiffness of the springs is determined through an optimization procedure in order to reduce the motor power peak required.

In Fig. 23 is the SPARKy's total motion (in green) compared to a natural ankle motion (in red). It is seen that all of the required PF during stance phase is provided, however, the DF required in the stance phase is not completely provided.

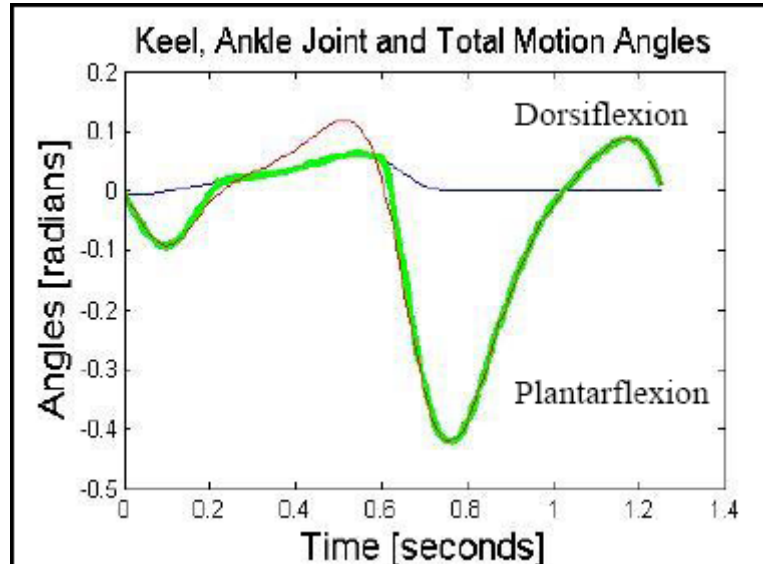


Fig. 23: The red line is the natural ankle joint angle. The blue line is the keel deflection angle. The green line represents the motion of SPARKy as a function of ankle joint motion and keel deflection. (From simulations) [11]

2.2. Future Perspectives

The major requirements towards design and developing a PBP can be summarized as follows:

- Respecting the weight and dimensions of a natural ankle
- High energy efficiency
- Real time control aspect
- Mimicking the natural ankle behaviour as accurate as possible
- Behaviour adjustable to the person's body weight and the cadence speed

As discussed in *Prior Works*, there is some effort done in order to develop such PBP. It is seen that each effort is based on some target requirements, not all of them. As an example, the PBP developed by Herr and his biomechatronics research group at the MIT Media Lab, mimics a simplified ankle behaviour instead of the natural ankle behaviour during stance. On the other hand the developed PBP is really compact and respects the weight and dimension limits very well. The SPARKy targets the energy efficiency and achieves an autonomy of 8 hours per day. The size aspect however, is less respected. We believe that the challenge is to develop a PBP which meets all the above mentioned requirements simultaneously.

Chapter 3

Design of a Below Knee Prosthesis

Powered by Electric Drives

3.1. System Characterization

3.1.1. Modelisation

3.1.1.1. Introduction

The main objective of this chapter is the conceptual modelisation of a PBP based on lightweight passive elements in order to mimic the natural human ankle behaviour during walking. The goal is to find a non-complex system with a great autonomy while providing the amputee improved ambulation. A great obstacle that had to be overcome, was respecting the physical properties (weight and size) of a natural below-knee limb.

In order to design such a PBP, both active and passive components are required. We assumed linear torsion, extension, compression springs, or a combination of them as passive, and DC-motors as active elements. The first step was to investigate how these components should be positioned on the PBP. The passive components can be placed on the foot and the active components on the tibia or vice versa.

In this part of the design phase, many models were generated using different combinations of components. A trade-off has been made between the different models, leading to a final model based on the MACCEPA (*the mechanically adjustable compliance and controllable equilibrium position actuator*) [14] concept.

3.1.1.2. Final Model

In the final model, the passive components are placed on the leg and the active component on the foot. Fig. 24a shows the schematics of this design, without the active components. As shown in Fig. 24, a linear extension spring is attached to the Lever arm through a cable.

Remark that the applied pulley leads to a more compact system in comparison with the other models.

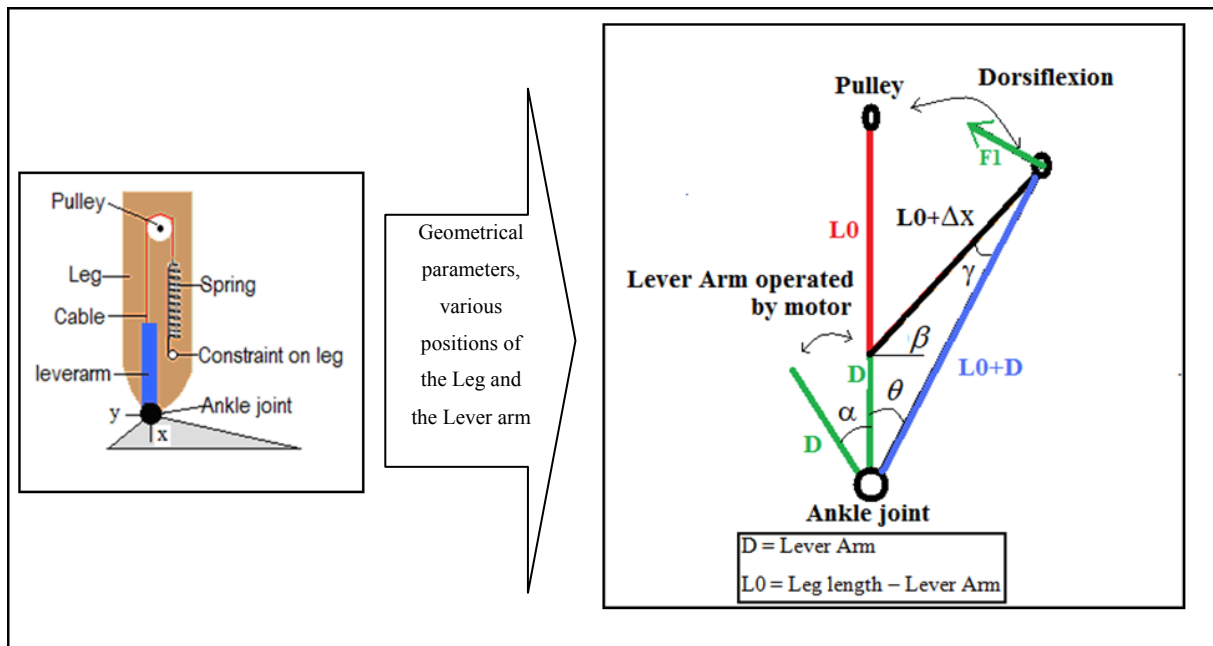


Fig. 24: a) Left: Schematics of the final design, b) Right: Geometrical characterization of the final design

With, see Fig. 24:

θ = The angle between the leg and the x-axis (Positive if the Leg is in DF)

α = The angle between the Lever arm and the x-axis (Positive if the Lever arm is in PF)

γ = The angle between the cable and the leg

All the angles mentioned above are zero in the position shown in Fig. 24a. Notice that the schematics in Fig. 24a shows the home position or the equilibrium position of the PBP and the ankle torque is 0 Nm in this position.

The Lever arm on the ankle joint is connected to the foot through a motor in combination with a transmission. Therefore, the Lever arm cannot rotate (α°) unless operated by the motor.

Fig. 25 shows the natural human ankle angle θ as a function of the % stride for normal cadence.

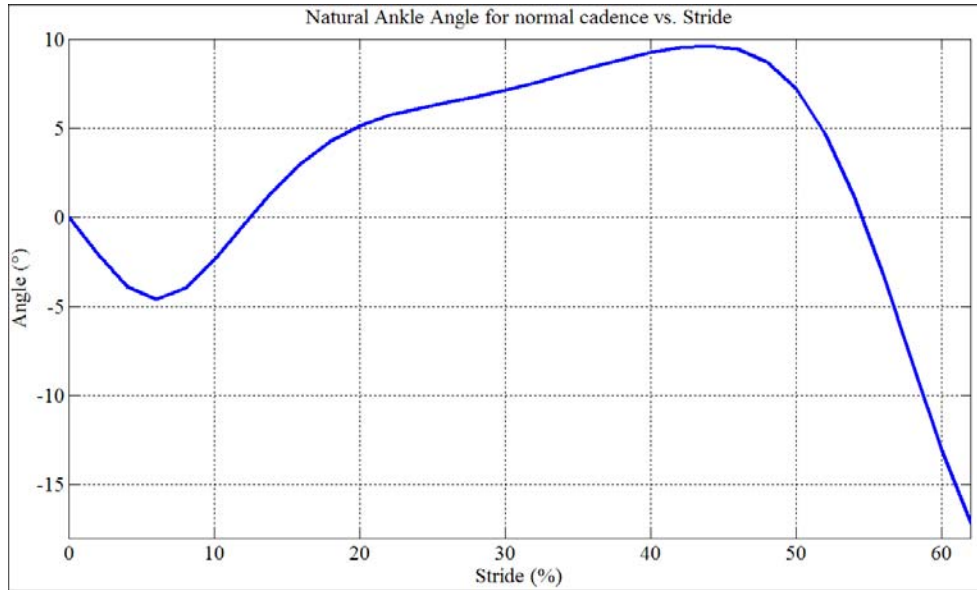


Fig. 25: Natural human Ankle Angle vs. Stride: Winter, normal cadence

Assume that a $\Delta\theta^\circ$ is imposed on the Leg (e.g. during the stance phase). It can be shown that the cable will extend the spring for Δx mm, assuming that the Lever arm's angle (α) remains unchanged unless operated by the motor. This spring extension will generate a pre-determined torque in the ankle joint depending on the spring extension Δx .

In this design a DC-motor is placed on the foot to operate the Lever arm. The pre-tension of the spring is adjustable by an extra DC-motor placed on the leg (see *Compliance adjusting Driving System of MACCEPA*).

3.1.1.3. Mathematical Expressions

The following formulas are derived by the triangle formed by the cable, the leg and the Lever arm shown in the Fig. 24b.

Applying the sine rule in this triangle gives:

$$\frac{L0 + \Delta x}{\sin \theta} = \frac{D}{\sin \gamma} \tag{Eqtn. 2}$$

Using the cosine rule gives:

$$L0 + \Delta x = \sqrt{D^2 + (L0 + D)^2 - 2 \cdot D \cdot (L0 + D) \cdot \cos(\theta)} \tag{Eqtn. 3}$$

After isolating γ and Δx :

$$\gamma = \arcsin\left(\frac{D \cdot \sin\theta}{L0 + \Delta x}\right) \quad \text{Eqtn. 4}$$

$$\Delta x = \sqrt{D^2 + (L0 + D)^2 - 2 \cdot D \cdot (L0 + D) \cdot \cos(\theta)} - L0 \quad \text{Eqtn. 5}$$

Furthermore, F_{cable} is calculated which equals to the spring force. This gives the following relation:

$$F_{cable} = K \cdot (\Delta x + pre-tension) \quad \text{Eqtn. 6}$$

In order to determine the ankle torque one should introduce $F1$, see Fig. 24b.

$$F1 = F_{cable} \cdot \sin \gamma \quad \text{Eqtn. 7}$$

And the torque in the ankle is

$$ankle_torque = F1 \cdot (L0 + D) \quad \text{Eqtn. 8}$$

Notice that the Lever arm angle α imposed by the motor will be taken into account by replacing θ by $(\theta + \alpha)$ in Eqtn. 2, Eqtn. 3, Eqtn. 4 and Eqtn. 5. In conclusion, the *ankle_torque* is rewritten as a function of its variables:

$$ankle_torque = function (K, pre-tension, L0, D, \theta, \alpha)$$

3.1.1.4. Physical Model

Further on in this study, it is assumed that the ankle stiffness is the slope of the torque-angle curve during stance. Fig. 26 shows the torque-angle characteristic of a natural ankle during normal walking (Winter et al.). It is seen in Fig. 26 that the ankle stiffness varies during the stride. The prosthesis should act less stiff during CP phase, from Heel-Strike till Foot-Flat, than the CD phase, from Foot-Flat till Heel-Off.

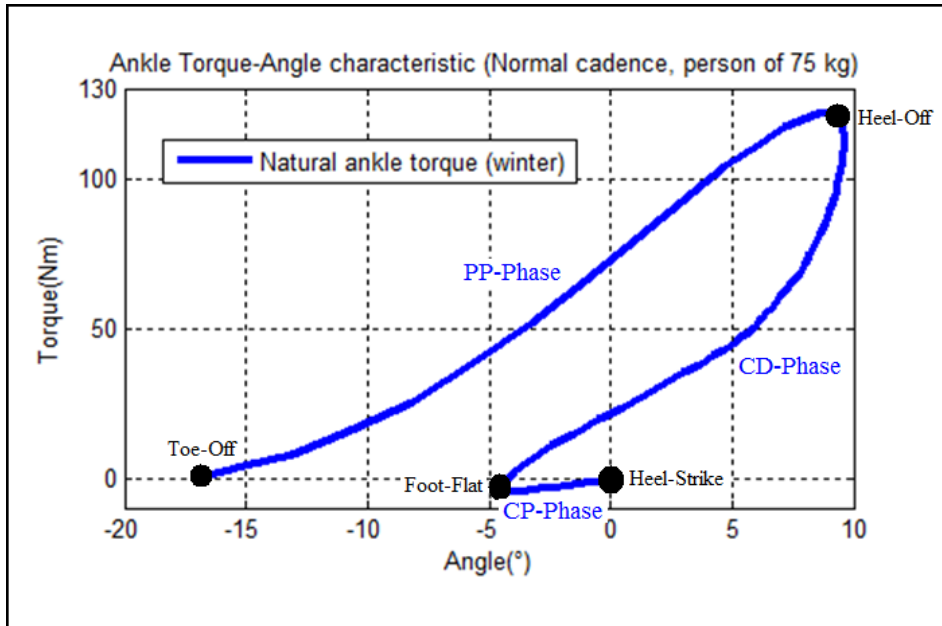


Fig. 26: Torque-Angle characteristic of a natural ankle (Winter): Normal cadence, a person of 75 kg.

Fig. 27 shows the evolution of the ankle angle and stiffness during the various phases. As mentioned earlier (*Biomechanics*), the ankle stiffness is constant during the CP phase. It can consequently be represented by a linear spring with stiffness K_{cp} . The torque in the ankle joint introduced by the spring should act linear as a function of the ankle angle (e.g. a torsion spring), as required in the CP phase shown in Fig. 26. The ankle stiffness behaves non-linear during the CD phase. Therefore, it should be represented by a variable spring with stiffness K_{cd} . In order to achieve Heel-Off, an additional amount of power should be added to the PBP through the torque source T_{pp} (active component of the system) at an appropriate time.[12]

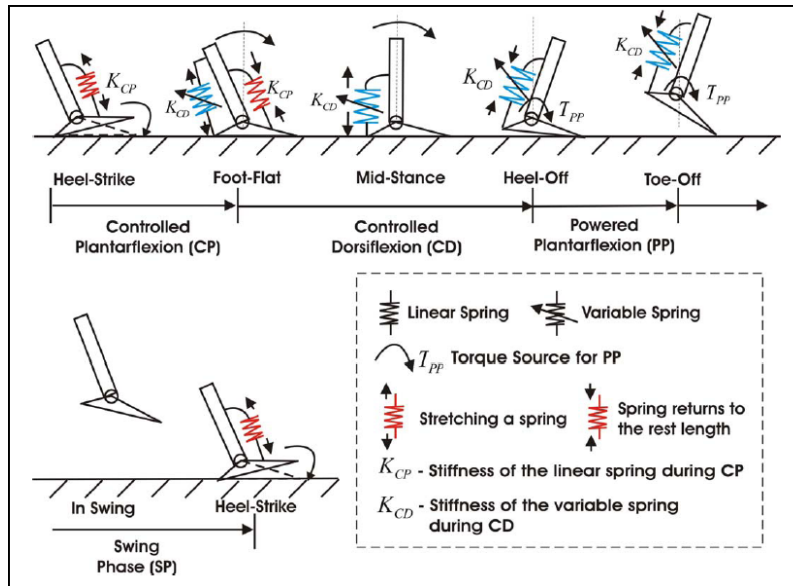


Fig. 27: The evolution of Ankle Angle and stiffness during various phases (Data originating from [12]).

Notice that the torque-angle characteristic of the system shown in Fig. 24 is perfectly symmetric independent of the sign of the imposed angle. This behaviour corresponds with the characteristic of a classical MACCEPA. Fig. 28 shows the theoretical performance of the system using the classical MACCEPA. Notice that the approached curve is not completely accurate. E.g., it is too stiff during the CP phase.

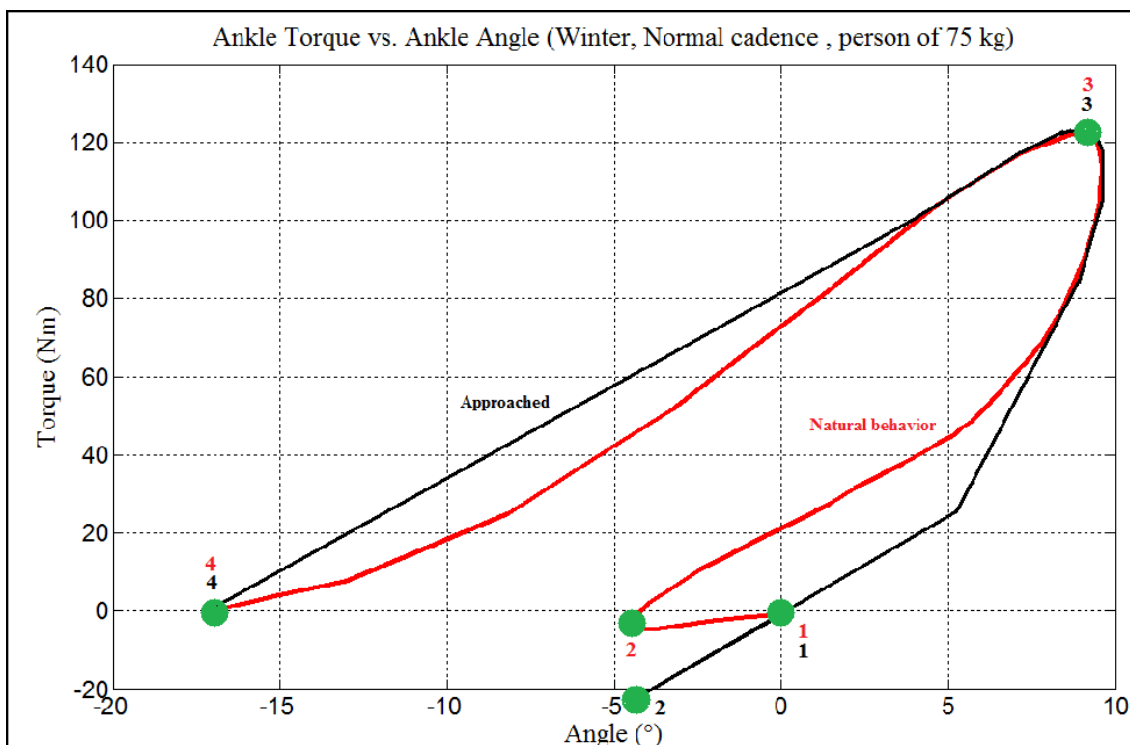


Fig. 28: Ankle Torque vs. Ankle Angle approached by using a classical MACCEPA (1: Heel-Contact, 2: Foot-Flat, 3: Heel-Off, 4: Toe-Off) (from simulations)

A first step towards better accuracy is obtaining a torque-angle characteristic, which has the stiffness of a natural ankle in the CP phase. Namely, K_{cp} for negative angles and this stiffness increases for positive angles conform the stiffness in the CD phase namely, K_{cd} . In other words, the stiffness of the actuator should vary during stance.

Evolution of ankle stiffness throughout stance in practice

Active compensation

The most obvious method to achieve a stiffness variation is an active compensation using the already existing active component. In other words, it is tried to approach the curve actively in the CP phase. Energy efficiency however, is a major design criteria and one should better opt for a passive implementation.

Passive compensation by adjusting the passive component

The stiffness variation is implemented by replacing the linear spring with a combination of linear springs in series. Regarding the fact that the CD phase as well as the CP phase should be approached, the use of two springs is required in this application. Notice that one spring is stiffer (S-Spring; Stiff-Spring) than the other one (C-Spring; Compliant-Spring). Remark that the maximum extension of the C-Spring is restricted by an internal wire with a length corresponding with the maximum extension of the C-Spring. In a first stage, the C-Spring will extend and after reaching the limit, the S-Spring will extend which leads to a stiffer actuator. As discussed previously, using a classical MACCEPA with only one spring will result in a characteristic, which is too stiff in the CP phase; see 1-2 in Fig. 28. Using this methodology will reduce this CP phase error. The main disadvantage of this method is the greater error during the CD phase in comparison with the curve shown in Fig. 28.

Passive compensation by adjusting the Lever arm (final design)

In order to realise a passive stiffness variation between the CP and CD phase, one should compensate the symmetrical characteristics of MACCEPA by introducing some modifications to the concept. The core of this method is using two Lever arms (identical height) on the joint connected to two linear springs with different stiffness, instead of one Lever arm and one spring. The Lever arm connected to the stiff spring is referred to as the S-Lever arm, the one connected to the compliant spring as the C-Lever arm.

C-Lever arm behaves similarly to a classical Lever arm, in other words it remains in its initial position unless operated with the motor. Therefore, its characteristic is fully symmetrical. Fig. 29 is obtained by using only C-Lever arm with linear spring K_{cp} . In this case, the stiffness of the actuator is acceptable for angles less than 0° (CP phase). However, the actuator is too compliant for angles greater than 0° , comparing to the natural ankle characteristic Fig. 26.

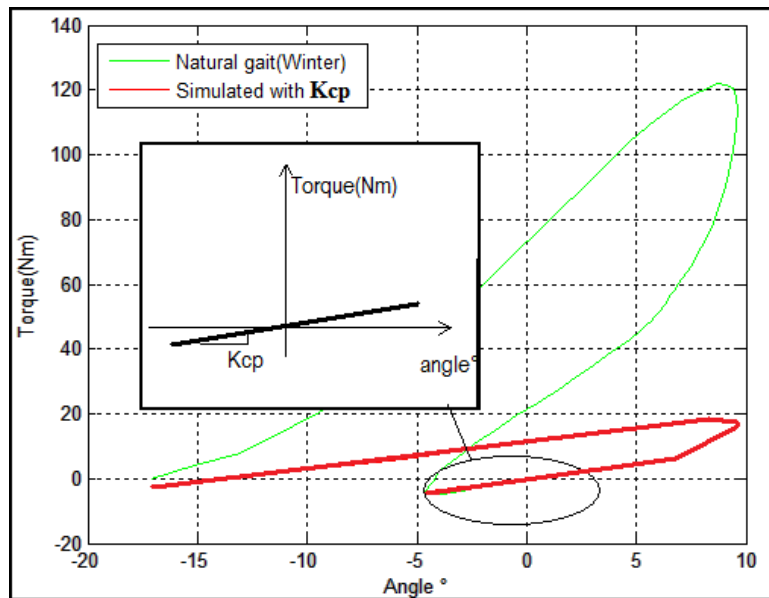


Fig. 29: Ankle Torque vs. Ankle Angle using only C-Lever arm with linear spring with stiffness K_{cp} (from simulations)

The S-Lever arm differs from the C-Lever arm. The S-Lever arm has an asymmetrical behaviour, depending on the sign of ankle angle. The S-Lever arm is attached to the ankle joint in such a way that it follows the leg for negative angles. Therefore, the linear spring connected to this Lever arm (K_{cd}) remains un-extended for negative angles and the actuator remains in equilibrium. In other words, this spring has no influence on the system in the CP phase. For positive ankle angles however, the S-Lever arm will not follow the leg and the spring K_{cd} will extend, resulting in a stiffer actuator. This is caused by a mechanical constraint like a pin. This pin-constraint can be positioned on the foot or on the C-Lever arm. In this case, the C-Lever arm is connected to the DC-motor on the foot. Notice that in order to provide enough Push-Off power in PP phase, both C-Lever arm and the S-Lever arm are operated by the motor. Therefore, the pin-constraint will be placed on the C-Lever arm. For angles greater than 0° , the S-Lever arm will meet the pin connected to the C-Lever arm, will stop following the leg and spring K_{cd} will begin to extend.

Fig. 30 is obtained by using only the S-Lever arm with linear spring K_{cd} . The actuator has zero stiffness for negative angles.

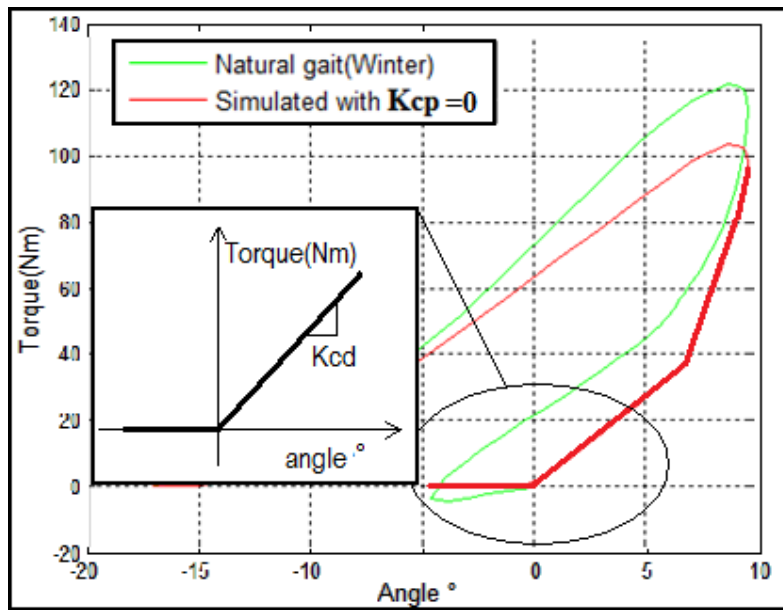


Fig. 30: Ankle Torque vs. Ankle Angle using only S-Lever arm with linear spring with stiffness K_{cd} (from simulations)

The combination of the two Lever arms will lead to a more acceptable theoretical performance curve as shown in Fig. 32. The motion of these components from Heel-Strike until Toe-Off is shown in Fig. 31. Notice that the numbering used in Fig. 31 corresponds with Fig. 32 and the springs and cables are not shown.

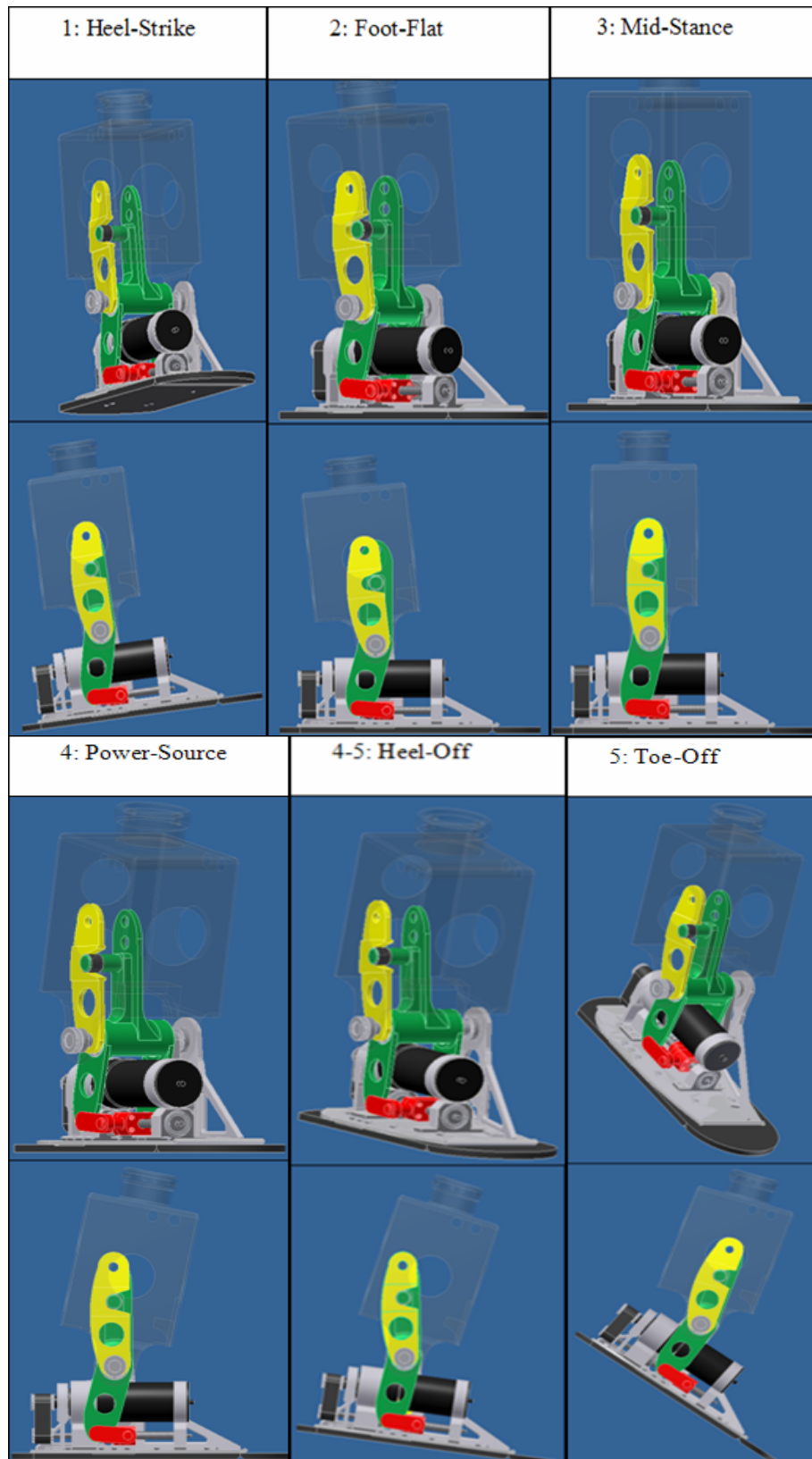


Fig. 31: The evolution of the PBP's parts motion during stance (above: isometric view, below: side view).
 Notice that the springs have a predetermined pre-tension. In order to avoid confusion, additional extension due to the Lever arms deviation will be referred to as extension. 1) Heel-Strike: No extension of C- and S-Spring, 2) Foot-Flat: No extension of S-Spring, slight extension of C-Spring, 3) Mid-Stance: No extension of C- and S-Spring, 4) Power-Source: Motor starts operating the C-Lever arm. S-Lever is operated through Pin, 4-5) Heel-Off: Maximum extension of C- and S-Spring 5) Toe-Off: Maximum deviation of C- and S-Lever arm, no extension of the S- and C-Springs

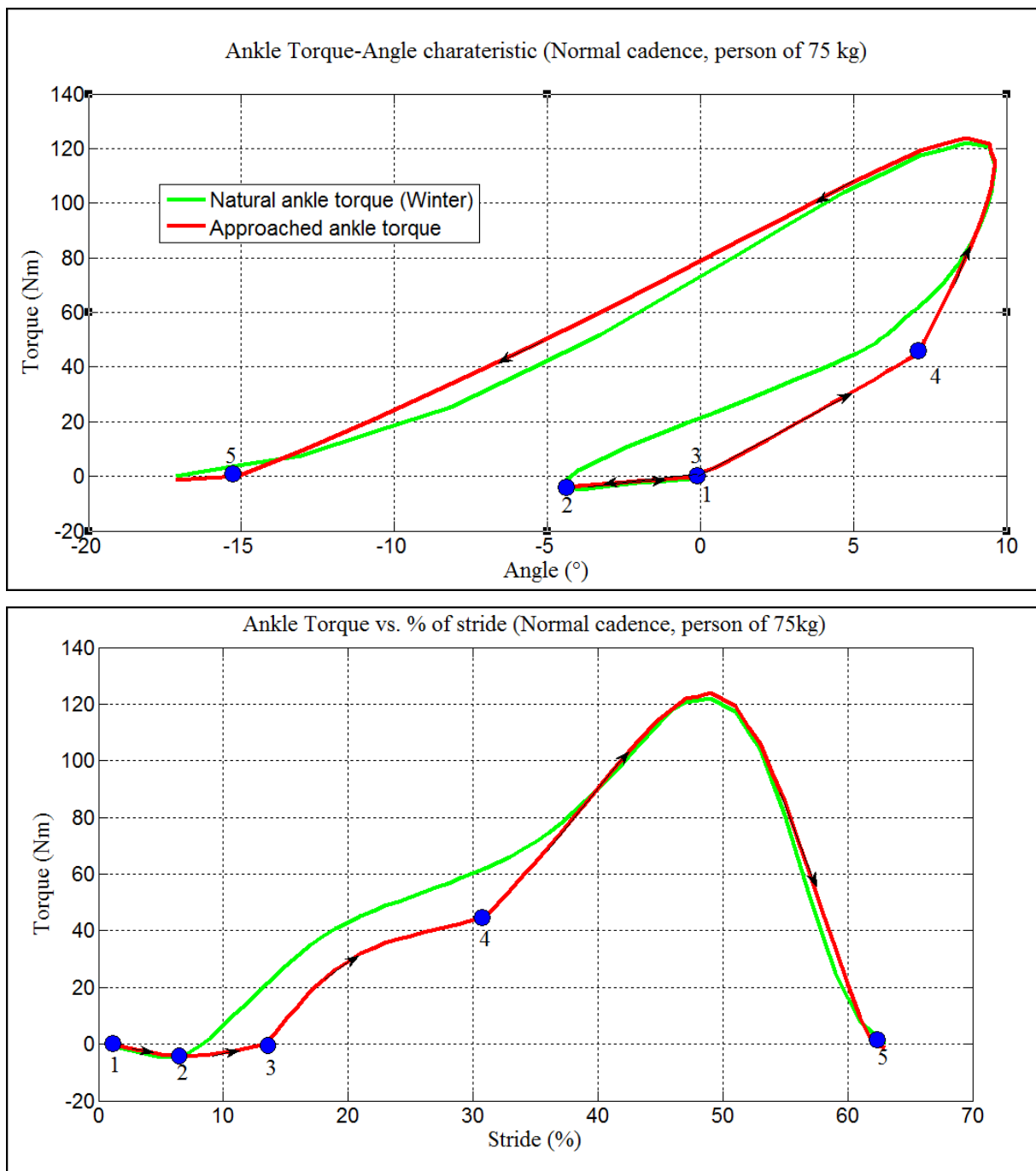


Fig. 32: Ankle characteristic by incorporating both C- and S-Lever arm, with 1: Heel-Strike, 2: Foot-Flat, 3:Mid-Stance, 4: Power-Source, 5: Toe-Off (from simulations), a) Above : Ankle Torque vs. Ankle Angle, b) Below: Ankle Torque vs. % of stride

It is seen in Fig. 32b that the dorsi-flexor torque starting at Heel-Contact continues much longer into stance comparing to the natural behaviour. This results in a great error in the CD phase, see Fig. 32a. Notice that in CD phase the theoretical ankle torque equals 0 Nm at 0°, the natural ankle torque however, is approximately 18 Nm (for person weighting 75kg).

Remark that this theoretical ankle behaviour during stance is similar to the one found by Herr et al. [10].

The next step to get a characteristic closer to the natural characteristic is to eliminate this error. There are different methodologies possible.

Active compensation by operating the C-Lever arm

The C-Lever arm is operated with the DC-motor during CP phase. In other words, the equilibrium position is actively shifted to the left (angles less than 0° , in a perfect case about 4.4° for normal cadence). Major disadvantage of this approach is the energy inefficiency. Control aspect is the other hinder for this approach, since the operation should be realised in a small period.

Passive compensation by introducing a *locking mechanism*

This method is a completely passive one and therefore energy efficient. It consists in defining a locking mechanism for the S-Lever arm. As mentioned previously, the S-Lever arm will rotate mutually with the leg for negative angles. This means that the S-Spring will not extend for negative angles, independent of the PF or DF of the leg.

It can be shown that introducing a locking mechanism will enhance the PBP theoretical performance. This mechanism should prohibit the motion of the S-Lever arm after reaching the Foot-Flat (at the end of CP phase). Therefore, the S-Lever arm will be prevented to rotate as soon as the maximum PF angle is reached so that the stiff spring (K_{cd}) will begin to extend from that point on. It is illustrated in Fig. 34a, that the actuator gets stiffer immediately after passing the Foot-Flat phase.

This locking mechanism can be realised practically by using a ratchet and pawl connected to the S-Lever arm through the ankle shaft. The ratchet allows effective motion only in one direction, in this case the PF. Therefore, the S-Lever arm is the only part that is locked by this mechanism in DF (*DF-locked*).

The challenge of using ratchets is unlocking them after each stance cycle, as the Lever arms should return to their home positions during swing phase. The working principle of unlocking this mechanism will be explained in detail in *Unlocking mechanism for ratchet and pawl*. The motion of the Lever arms with the *locking mechanism* during stance phase is illustrated in Fig. 33.



Fig. 33: The evolution of the PBP's parts motion during stance (including the locking mechanism) (above: isometric view, below: side view). 1) Heel-Strike: No extension of C- and S-Spring with *DF-locked* S-Lever arm 2) Foot-Flat: No extension of S-Spring, slight extension of C-Spring with *DF-locked* S-Lever arm, 2-3) Mid-Stance: No extension of C-Spring, slight extension of S-Spring with *DF-locked* S-Lever arm, 3) Power-Source: Motor starts operating the C-Lever arm with *DF-locked* S-Lever arm, 4) Pin-Contact: The *DF-locked* S-Lever arm is operated through the pin on the C-Lever arm 4-5) Heel-Off: Maximum extension of C- and S-Spring with *DF-locked* S-Lever arm 5) Toe-Off: Maximum deviation of C- and S-Lever arm, no extension of the S- and C-Springs with an unlocked S-Lever arm

Fig. 34 shows the simulated ankle torque vs. ankle angle when a ratchet is used and the S-Lever arm is *DF-locked* at a proper time, namely at the end of the CP phase. Notice that in order to achieve a characteristic as shown in Fig. 34, the active component should operate at a proper time as well; see *Driving system*. It can be shown that applying a locking mechanism will enhance the energy efficiency as well. This statement is based on the fact that a greater part of the curve is approached passively by using a locking mechanism. One can see that the active part of Fig. 32 (the one without locking mechanism) starts earlier than the one of Fig. 34. Comparing to the above-mentioned simulations, this last simulation is the most acceptable one, based on the method of least squares.

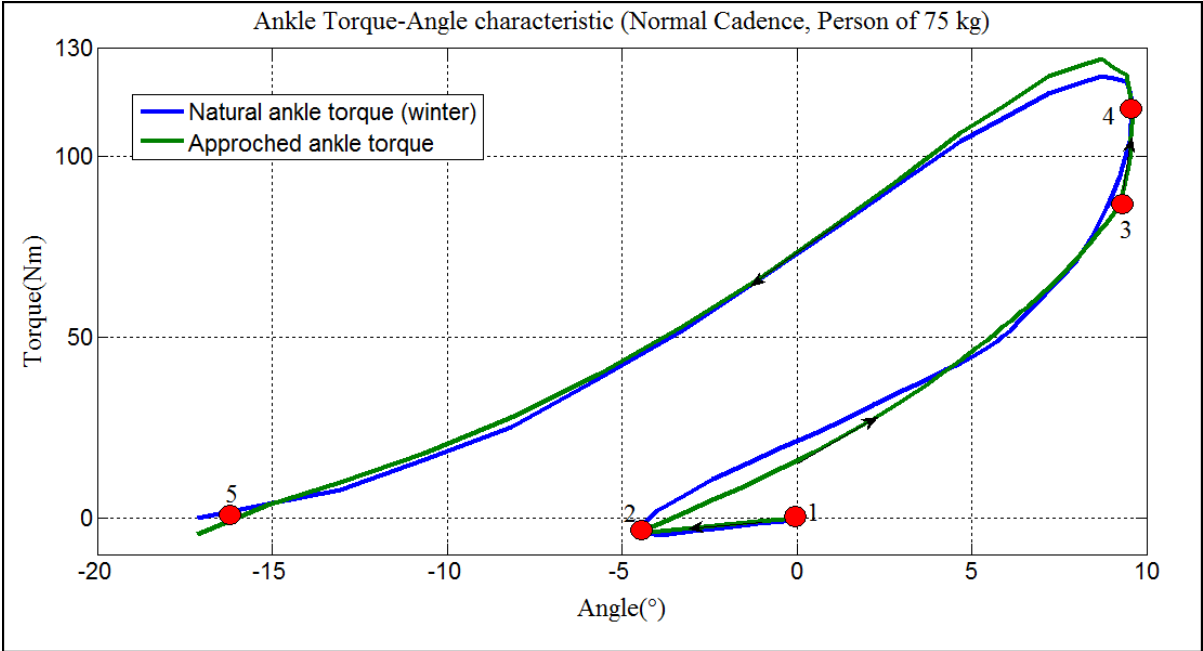


Fig. 34: a) Ankle Torque vs. Ankle Angle by incorporating a locking mechanism, with 1: Heel-Strike, 2: Foot-Flat, 3:Power-Source, 4: Pin-Contact and 5:Toe-Off (from simulations).

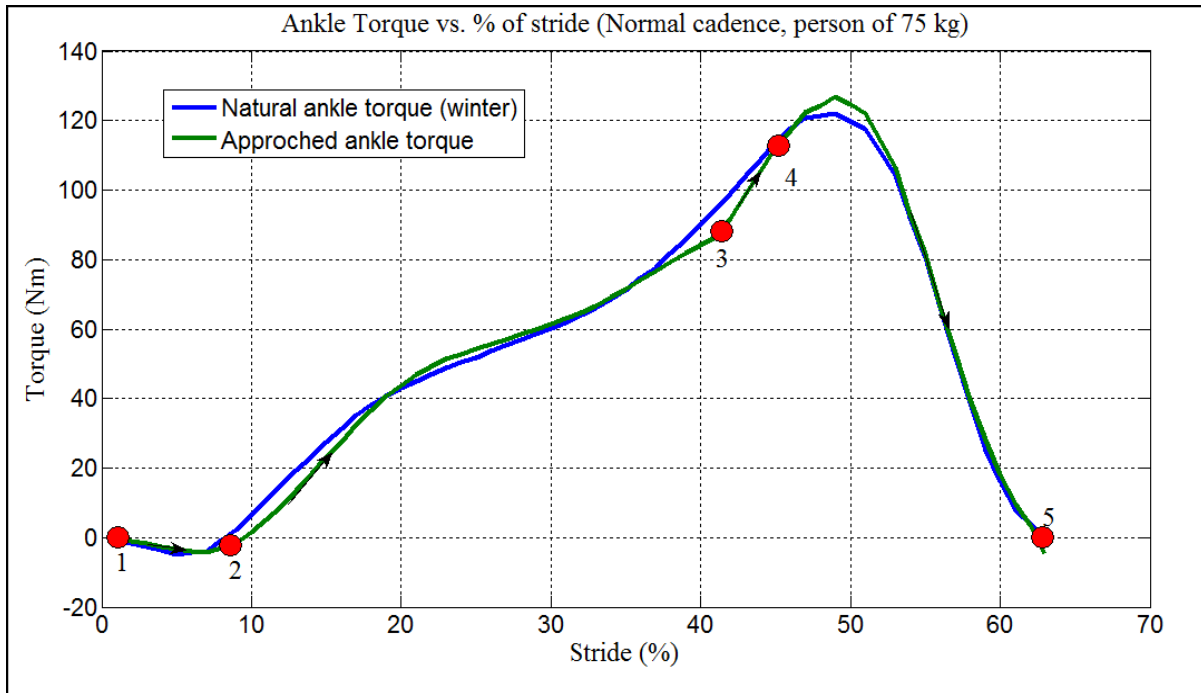


Fig. 34: b) Ankle Torque vs. % of stride by incorporating a locking mechanism, with 1: Heel-Strike, 2: Foot-Flat, 3: Power-Source, 4: Pin-Contact and 5: Toe-Off (from simulations).

3.1.1.5. Conclusion

A good approach of the natural ankle behaviour during walking is achieved by using the following components, as shown in Fig. 35 .

- S-Lever arm connected to a stiff linear extension spring positioned on the leg.
- C-Lever arm connected to a compliant linear extension spring positioned on the leg.
- A ratchet and pawl mechanism connected to the S-Lever arm.
- DC-motor on the foot connected to the C-Lever arm.
- A pin placed on the C-Lever arm to operate the S-Lever arm with the same DC-motor

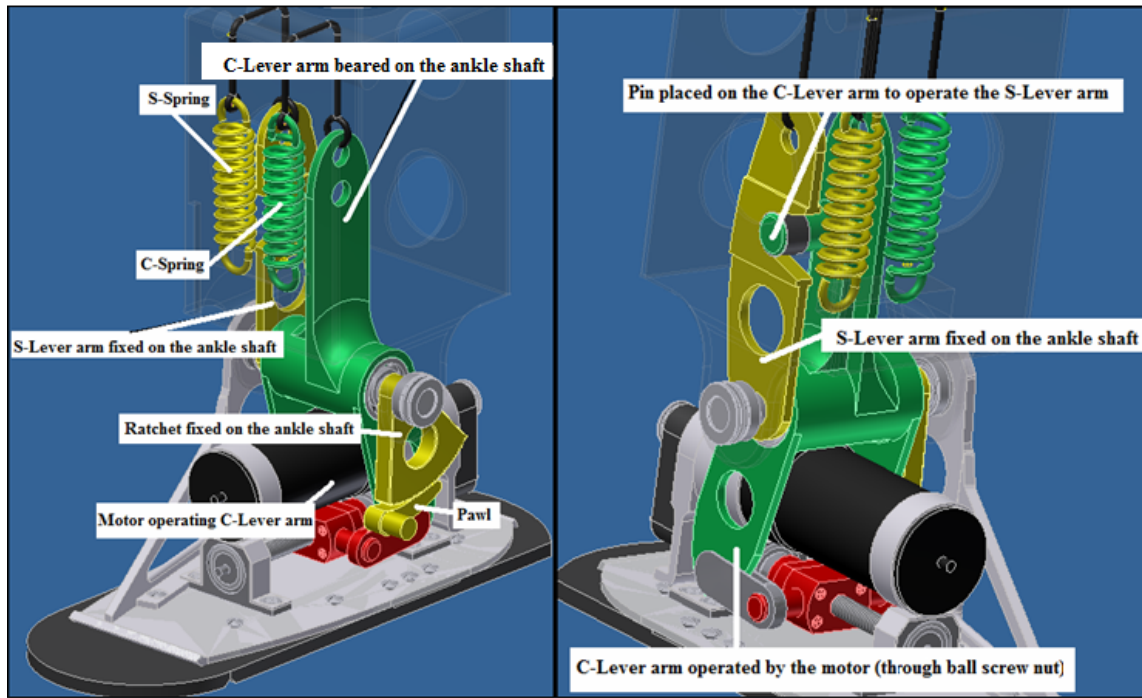


Fig. 35: Components of the final model

3.1.2. Simulations

The main goal of the simulations is to determine the different design parameters in order to achieve a theoretical performance that corresponds with the behaviour of a natural ankle, during walking. Natural ankle joint angle and torque data used in the simulations, as the reference, are from the data generated by inverse dynamics of motion capture and force plate test data published by Winter in [2] for slow, normal and fast cadence, as shown in Fig. 36. In this chapter, the design parameters are adjusted in order to achieve an acceptable approach of these reference characteristics.

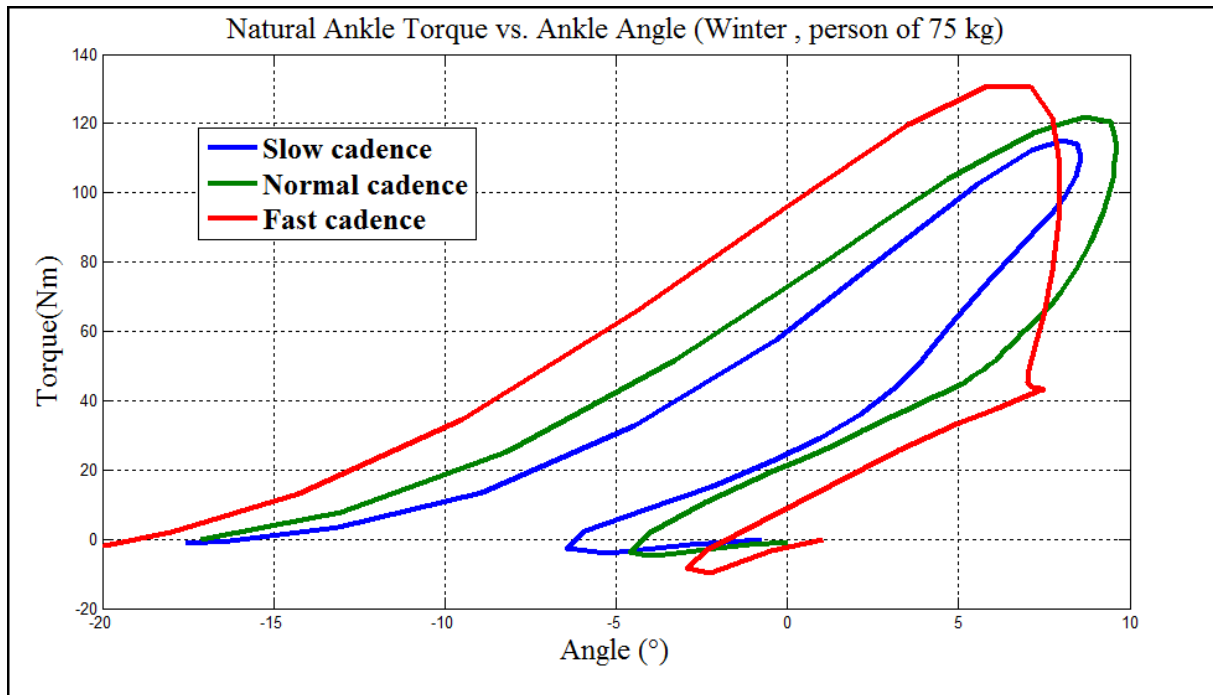


Fig. 36: Natural Ankle Torque vs. Ankle Angle for slow, normal and fast cadence for a person of 75 kg (Winter [2])

The simulations are based on the method of least squares. In this method it is assumed that the best-fit curve is the curve that has the minimal sum of the squared deviations (*least square error*) from a given set of data. Fig. 37 shows the used simulation's flow chart in order to determine the various design parameters. The simulations are performed in MATLAB [13]. The corresponding MATLAB sheets can be found in Appendix B.

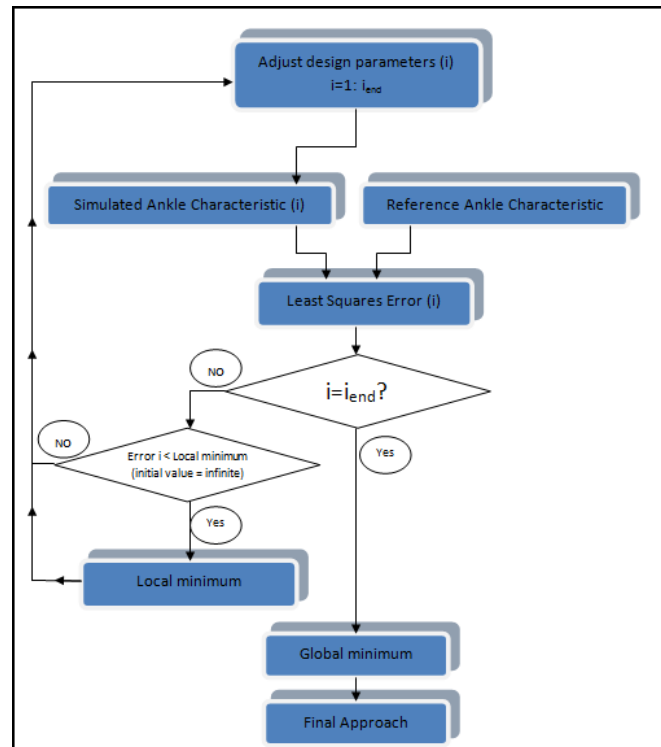


Fig. 37: Used simulation's flowchart in order to determine the various design parameters, design parameter (i) is adjusted with $i=1: i_{end}$, i_{end} depends on the physical and geometrical limits of the design. The global minimum equals the local minimum when $i=i_{end}$.

3.1.2.1. Design Parameters

Design parameters of a system determine the behaviour of that system. The required system behaviour can be achieved by choosing these parameters properly. There are two kinds of design parameters:

Fixed parameters, which depend on the material choice, geometrical design and etc. These parameters are fixed and cannot change once the system is made and is ready to function. An example of these *fixed parameters* is the spring stiffness.

Variable parameters can be adjusted, e.g. the pre-tension of the springs. The challenge is to choose the *fixed parameters* in such a way that the slow, normal and fast cadence could be approached as close as possible by only adjusting the *variable parameters*.

The design parameters are the following:

1. Power-Source timing
2. The duration of Power-Source
3. [Lever arm length (mm) /Leg Length (mm)] ratio
4. Stiffness of the S-Spring (N/m)

5. Stiffness of the C-Spring (N/m)
6. Pre-tension of the S-Spring (mm)
7. Pre-tension of the C-Spring (mm)

Power Source

Two parameters are distinguished in this section.

- Power-Source timing: % of stride at which the motor should start working.
- The duration of Power-Source: % of stride in which the motor should keep working once Power-Source timing is achieved.

Remark that these Power-Source parameters are *variable* and can be adjusted for each cadence separately. Fig. 38 shows Power-Source parameters by red circles on the ankle torque vs. ankle angle curve during normal walking. The simulation results are as follows:

- Power-Source timing: 39 % of stride
- The duration of Power-Source: 23 % of stride

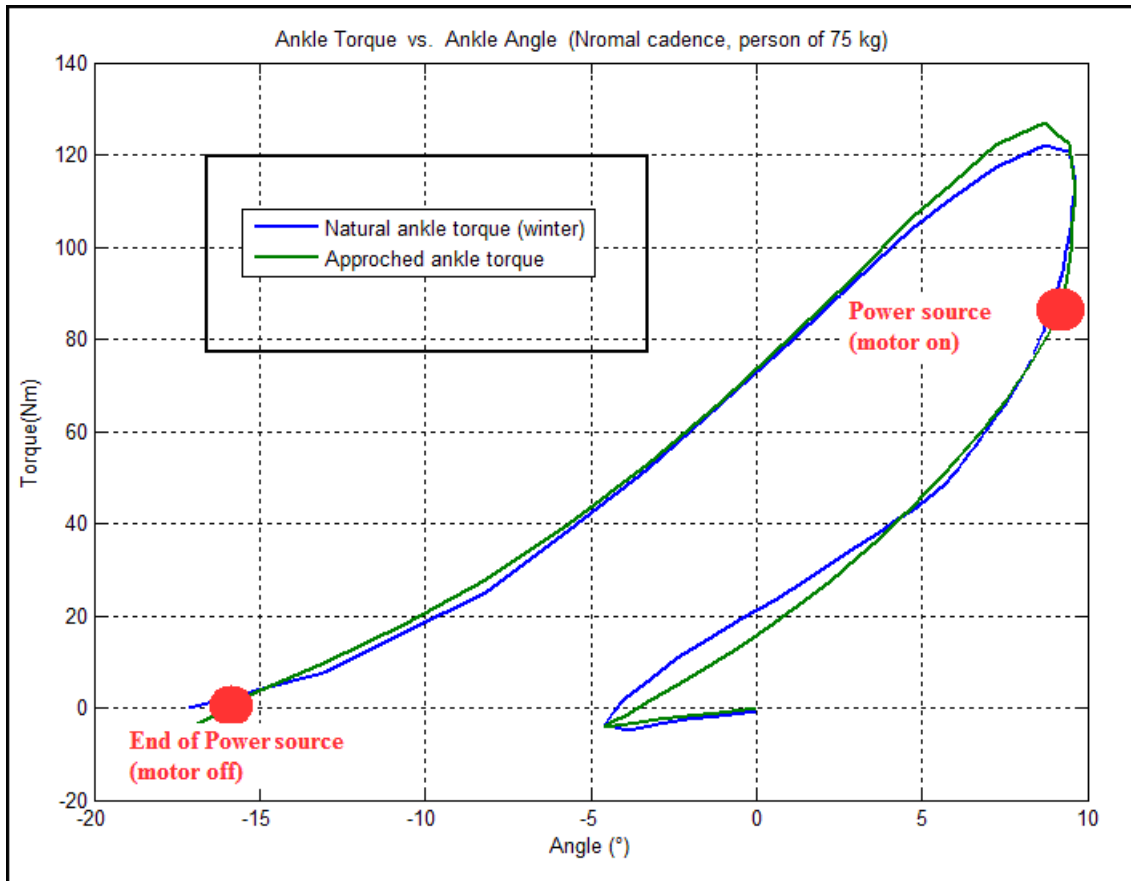


Fig. 38: Power-Source timing on Ankle Torque vs. Ankle Angle characteristic for normal cadence

Fig. 39 shows Power-Source parameters by red circles on the ankle torque vs. ankle angle curve during fast walking. The simulation results are as follows:

- Power-Source timing: 31 % of stride
- The duration of Power-Source: 31 % of stride

Comparing to normal cadence the motor should start working earlier.

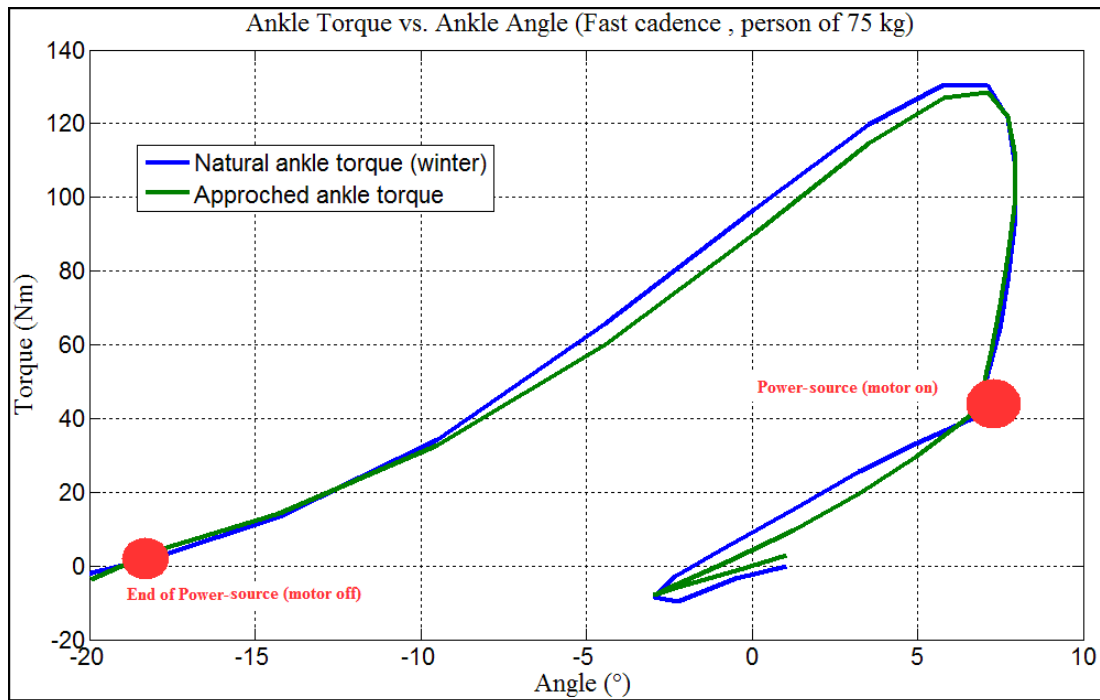


Fig. 39: Power-Source timing on Ankle Torque vs. Ankle Angle characteristic for fast cadence

Fig. 40 shows Power-Source parameters by red circles on the ankle torque vs. ankle angle curve during slow walking. The simulation results are as follows:

- Power-Source timing: 38 % of stride
- The duration of Power-Source: 24 % of stride

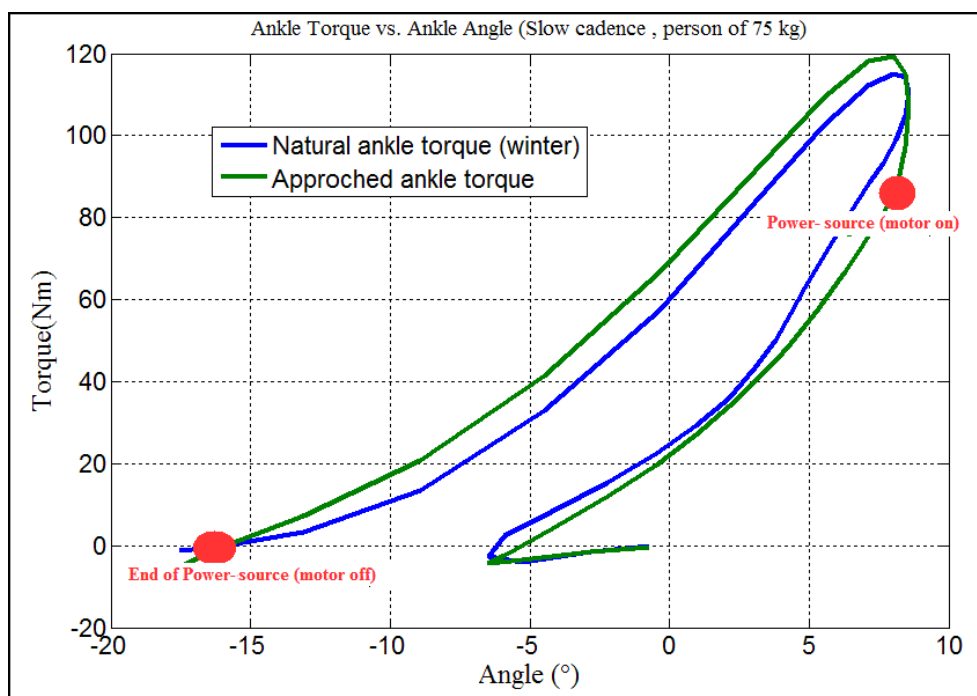


Fig. 40: Power-Source timing on Ankle Torque vs. Ankle Angle characteristic for slow cadence

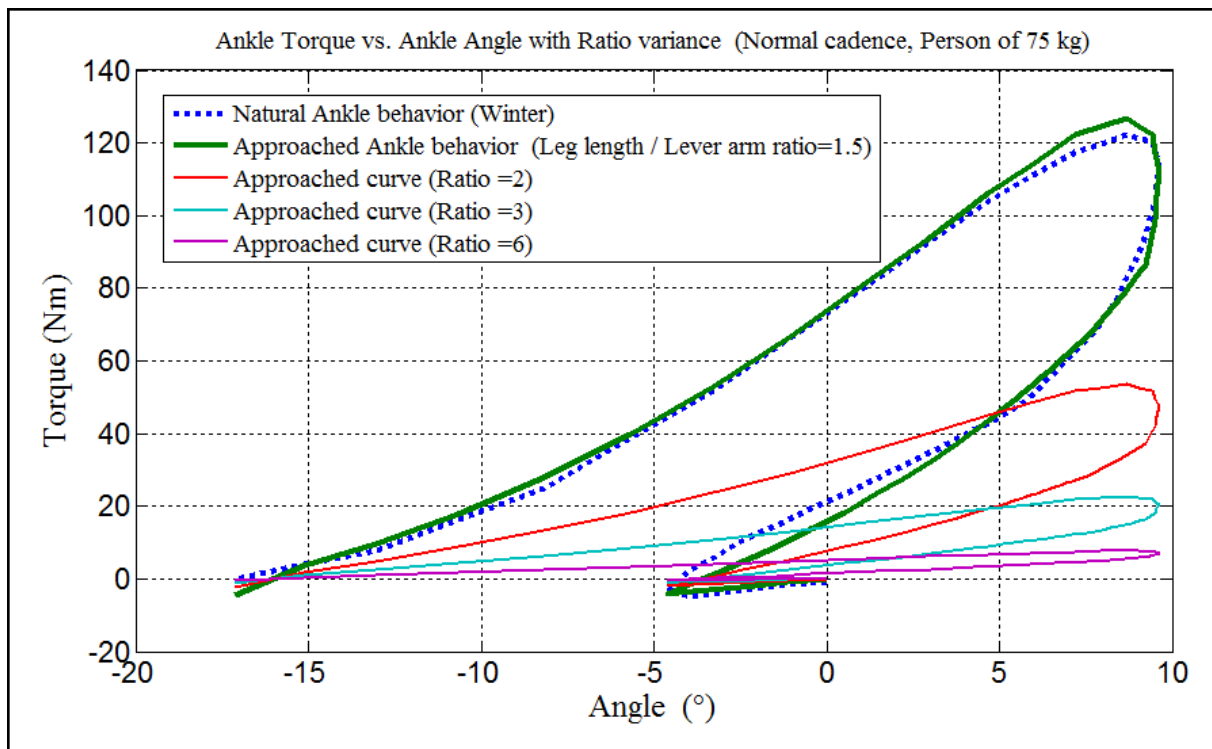


Fig. 42: Ankle Torque as a function of the Ankle Angle for different values of the Leg length / Lever arm ratio.

This ratio determines the non-linearity of the torque-angle behaviour and the magnitude of the torque for small angles. It can be shown that this ratio has no influence on the torque for high angles close to 60° [14]. Regarding the fact that these higher angles will not be reached in this application, the ankle torque is strongly dependent on this ratio.

It can be shown that a ratio of 5 is appropriate in order to achieve a quasi linear behaviour for angles between 0° and 60° [14]. For angles less than 10° however, a ratio of 1,5 is appropriate for such quasi linear behaviour.

It is seen in Fig. 42 that the best approach for normal cadence is achieved with Leg length / Lever arm ratio of 1,5.

C-Spring stiffness (Compliant spring)

Fig. 43 shows the ankle torque as a function of the ankle angle for different values of the C-Spring stiffness (KC). Notice that the C-Spring stiffness has a linear influence on the torque-angle characteristic. Due to the mechanical design, the variance of KC influences the slope of the ankle torque-angle curve (ankle stiffness) in all the different phases. Notice that KC is the only parameter on which the ankle stiffness in CP phase depends. Therefore, the theoretical ankle stiffness in the CP phase is the most important element, for the choice of the C-Spring stiffness.

It is seen in Fig. 43 that a KC of 20 kN/m leads to the most acceptable approach.

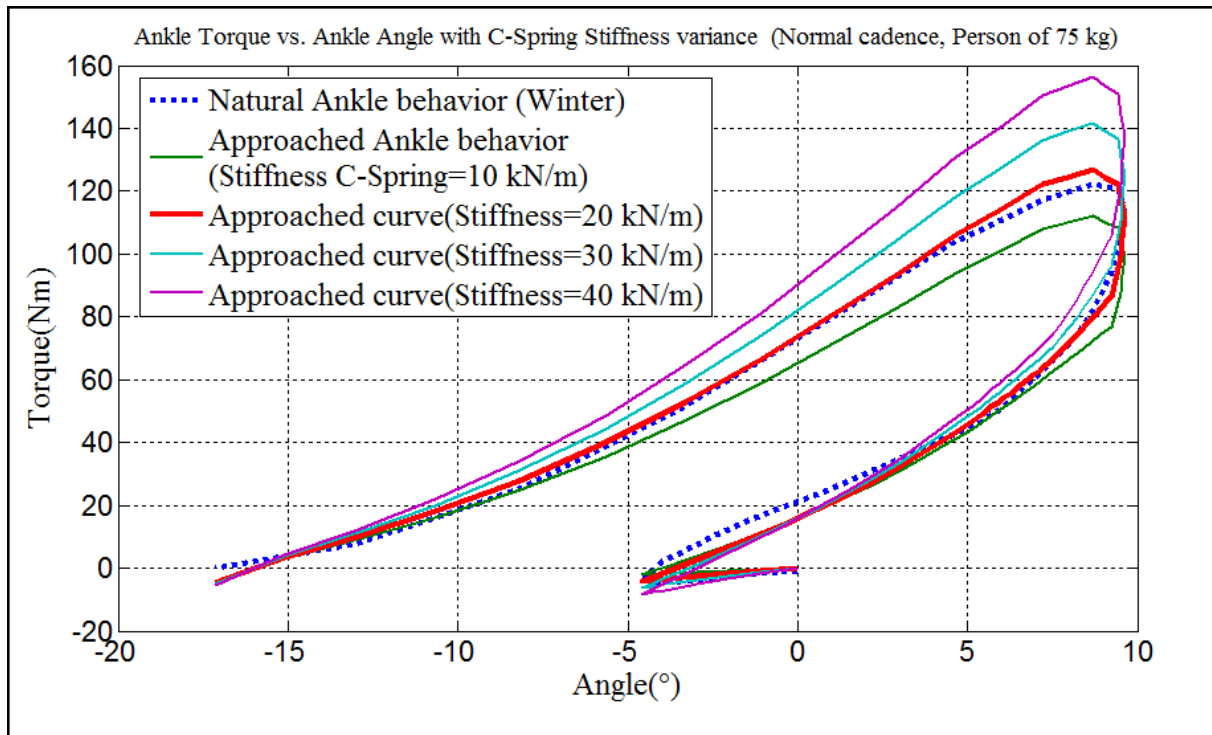


Fig. 43: Ankle Torque as a function of the Ankle Angle for different values of the C-Spring stiffness

S-Spring stiffness (Stiff spring)

Fig. 44 shows the ankle torque as a function of the ankle angle for different values of the S-Spring stiffness (KS). Due to the mechanical design, the variance of KS has no influence on the stiffness in the CP phase. Therefore, the choice of the S-Spring stiffness depends on the theoretical ankle stiffness in the CD and PP phase. It is seen in Fig. 44 that a KS of 60 KN/m leads to an acceptable theoretical performance.

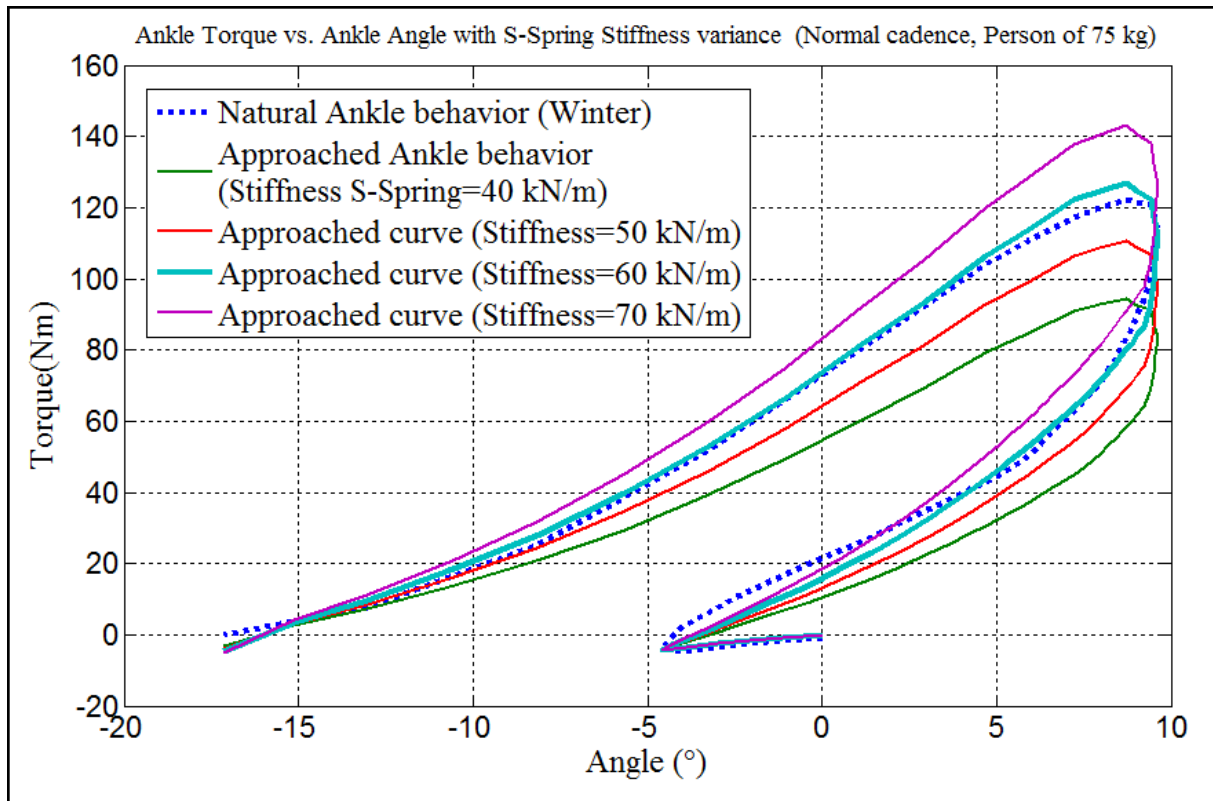


Fig. 44: Ankle Torque as a function of the Ankle Angle for different values of the S-Spring stiffness

Pre-tension of the springs

The pre-tension of the springs can be considered as *variable* parameters, since the MACCEPA concept is applied. In other words the pre-tension could be adjusted during walking depending on the cadence speed. Fig. 45 shows ankle torque as a function of the ankle angle for different values of the C-Spring pre-tension. Remark that the pre-tension has a quasi linear influence on the torque-angle characteristic. Fig. 46 shows ankle torque as a function of the ankle angle for different values of the S-Spring pre-tension. Based in Fig. 45 and Fig. 46, the normal cadence ankle torque-angle characteristic can be approached by C-Spring pre-tension of 8 mm and S-Spring pre-tension of 10 mm.

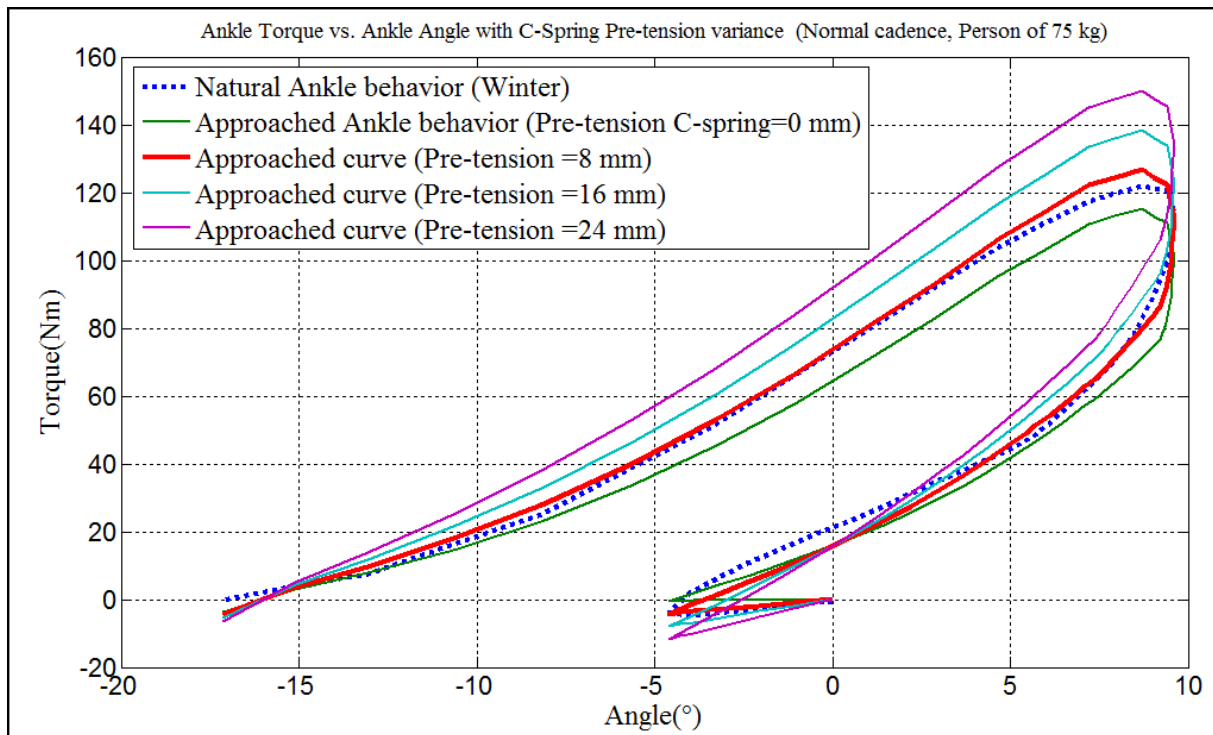


Fig. 45: Ankle Torque as a function of the Ankle Angle for different values of the C-Spring pre-tension

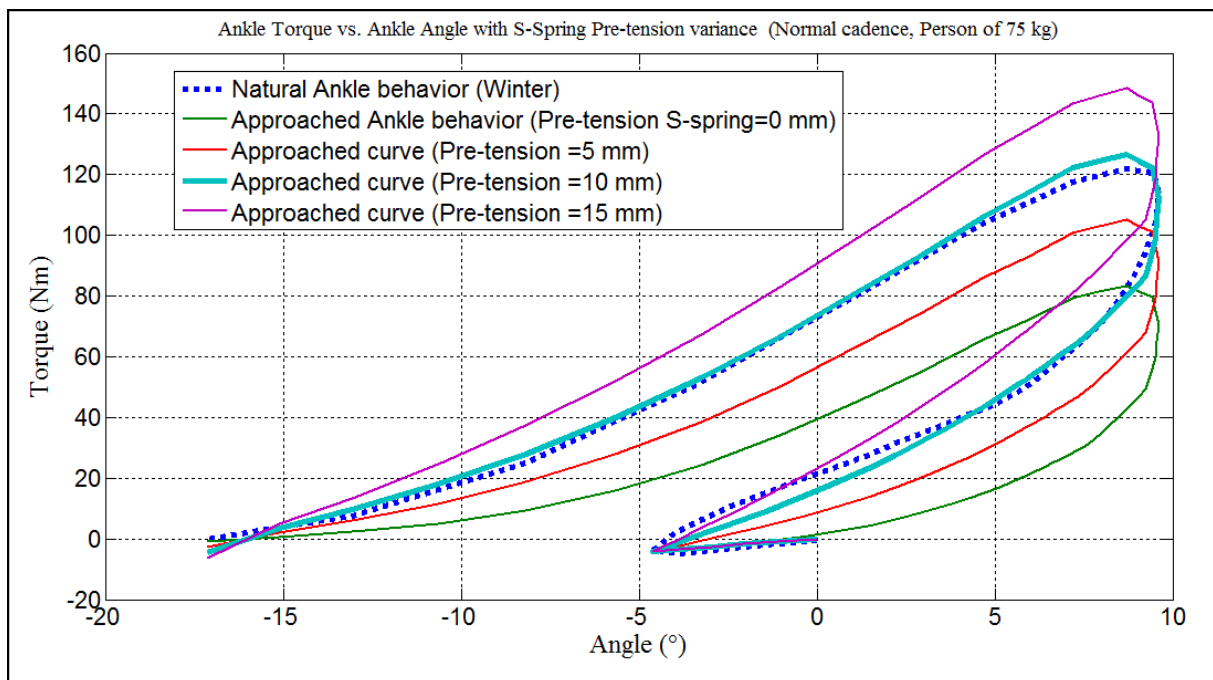


Fig. 46: Ankle Torque as a function of the Ankle Angle for different values of the S-Spring pre-tension

It is shown that the fast cadence can be approached by applying the following pre-tensions: C-Spring pre-tension 25 mm and S-Spring pre-tension 4 mm.

The slow cadence is approached as well by: C-Spring pre-tension 5 mm and S-Spring pre-tension 9 mm.

3.1.2.2. Conclusion

Based on the performed simulations, the ankle torque-angle characteristic with the least error applying the method of the Least squares can be achieved by using the *fixed parameters* as follows:

- Lever arm length = 100 mm
- Leg length = 150 mm
- S-Spring stiffness = 60 kN/m
- C-Spring stiffness = 20 kN/m

Fig. 47, Fig. 48 and Fig. 49 show the ankle torque as a function of the ankle angle for fast, normal and slow cadence, respectively, accompanied by the design parameters. Remark that the *variable parameters* should get adjusted separately for each cadence speed.

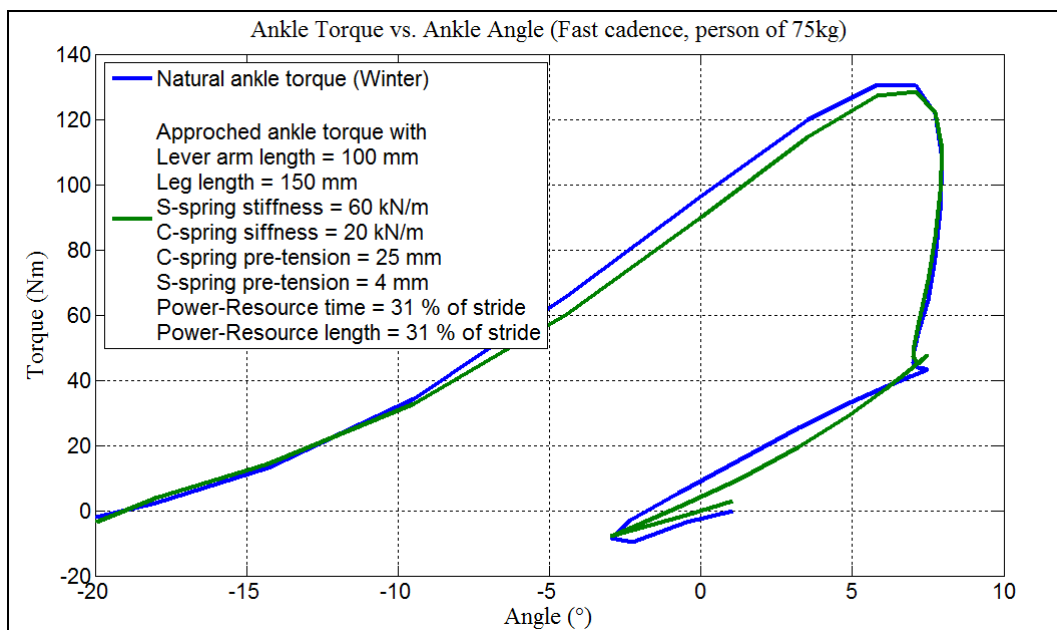


Fig. 47: Ankle Torque as a function of the Ankle Angle for fast cadence (design parameters)

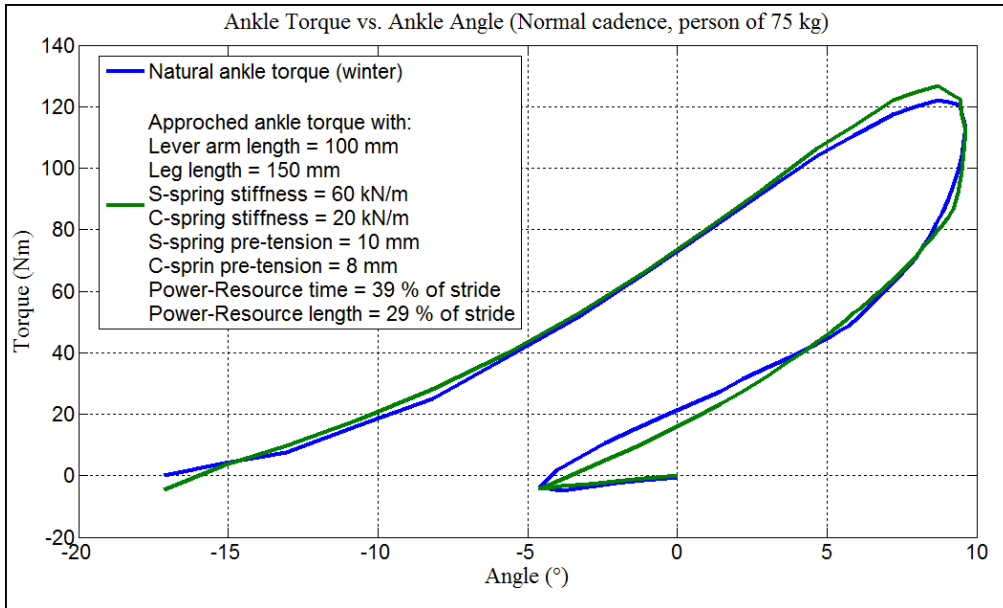


Fig. 48: Ankle Torque as a function of the Ankle Angle for normal cadence (design parameters)

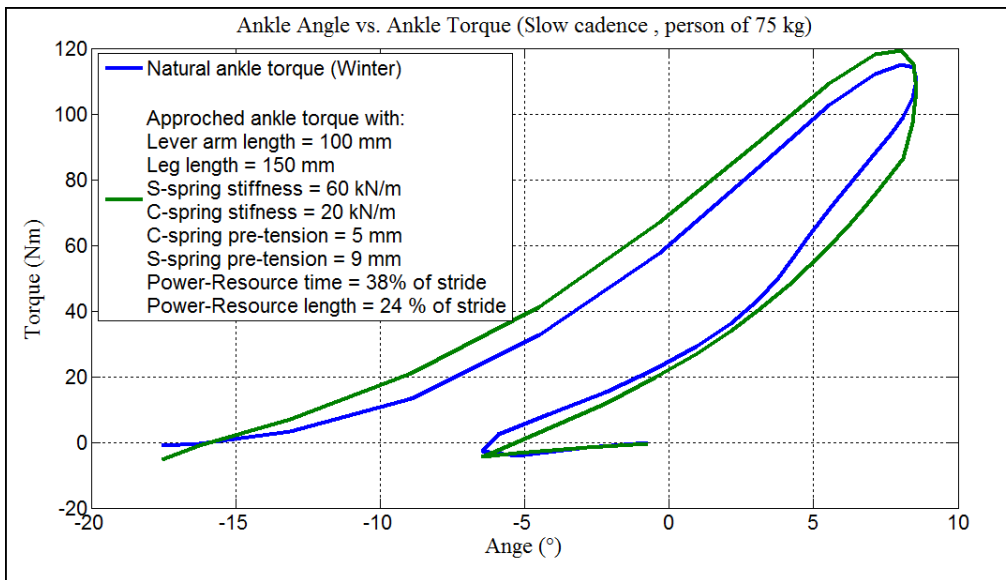


Fig. 49 : Ankle Torque as a function of the Ankle Angle for slow cadence (design parameters)

Fig. 50, Fig. 51 and Fig. 52 show the ankle torque as a function of the % of stride respectively for fast, normal and slow cadence accompanied by the design parameters.

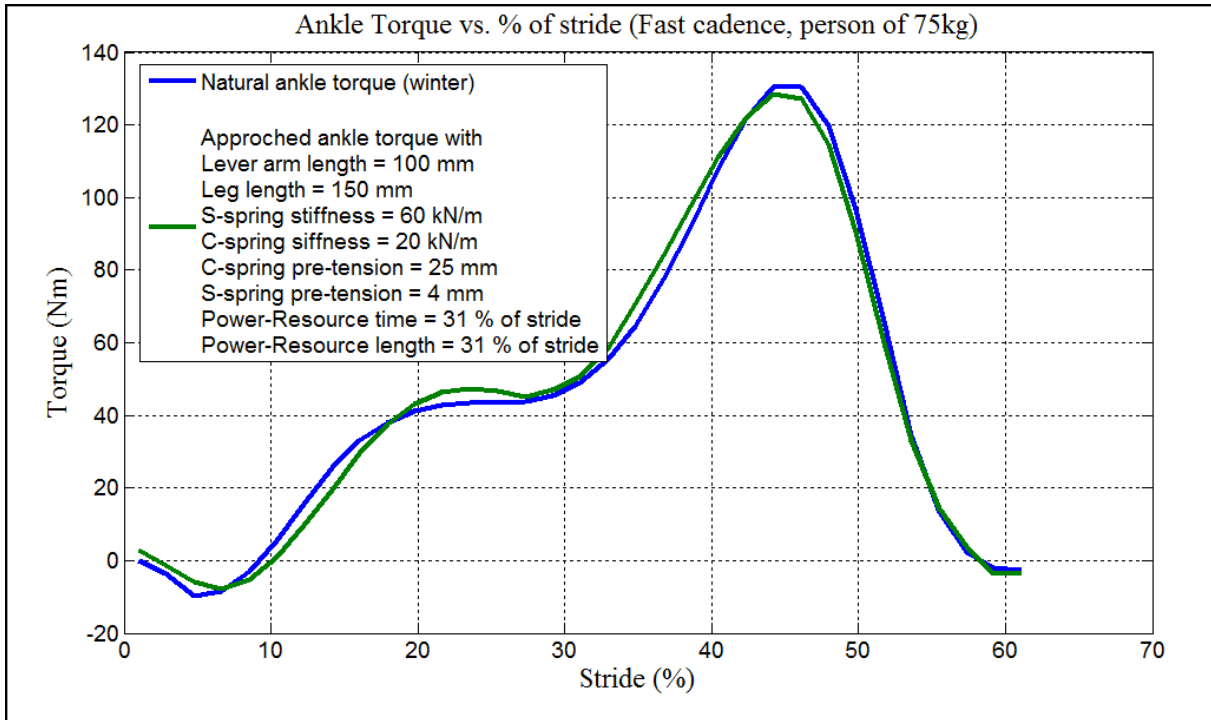


Fig. 50: Ankle Torque as a function of the % of Stride for fast cadence (design parameters)

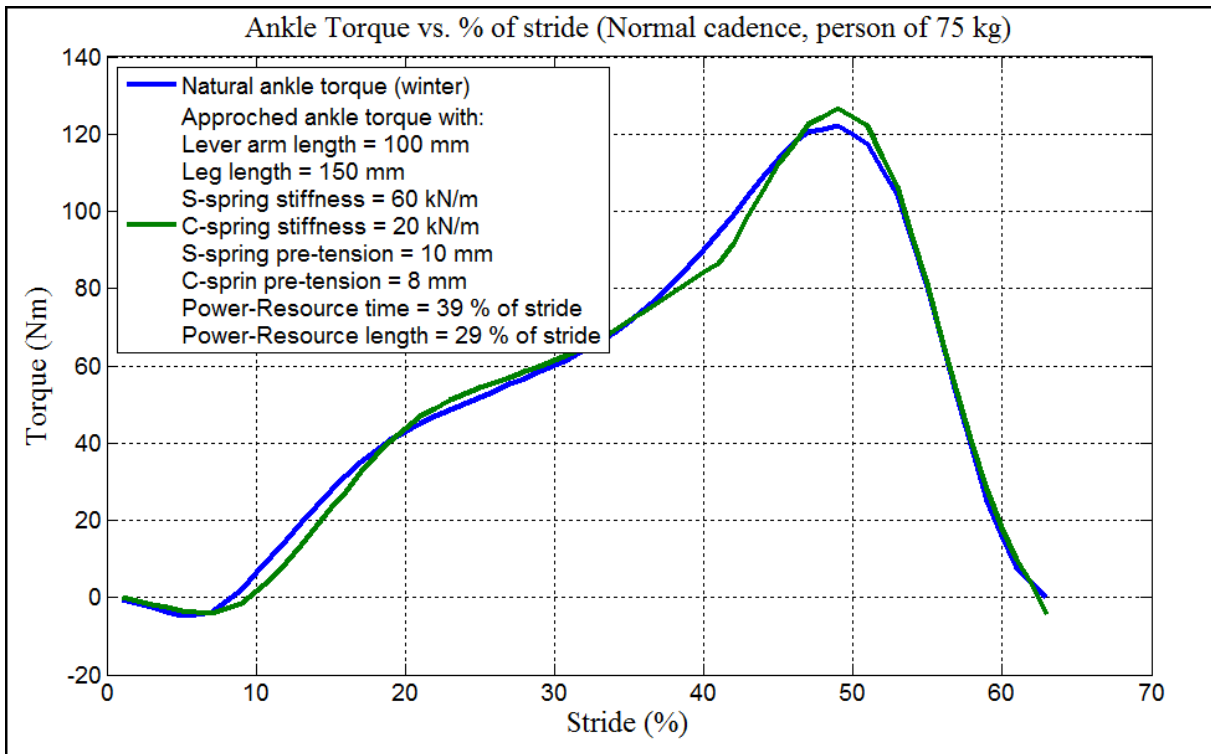


Fig. 51: Ankle Torque as a function of the % of Stride for normal cadence (design parameters)

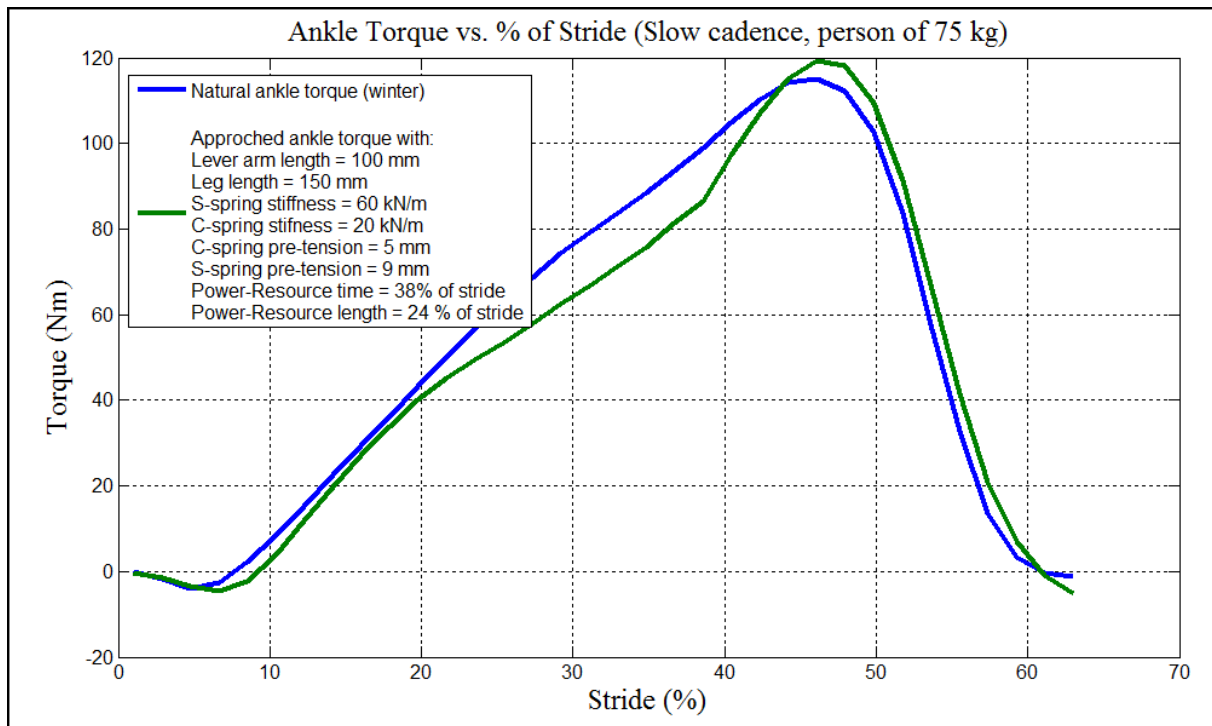


Fig. 52: Ankle Torque as a function of the % of Stride for slow cadence (design parameters)

3.2. Driving System

3.2.1. Motor

The active component of the PBP must provide the required power on the ankle joint to achieve an acceptable approach of the natural ankle behaviour. In this chapter, the selection of the motor and its transmission (driving system) is discussed. The main challenge was to design a driving system, which is highly energy efficient, has a low weight and remains within the size limits of a normal foot.

Motor Characteristics

A first task towards the design of the motor consists in evaluating the theoretical performance characteristics of the PBP when equipped with only passive elements. Based on these characteristics, the minimum required power of the active component was determined. The combination of these two components (active and passive) has to provide an acceptable PBP behaviour.

The simulations below were performed for a person weighting 75 kg. Fig. 53a shows the comparison of the theoretical torque capability of the PBP with the torque requirement during normal walking, when the PBP is equipped with only passive elements.

It is seen that using only passive elements will lead to an acceptable PBP characteristic between approximately 0% - 40% of the stride. The approached ankle torque after 35 % of the stride is lower than required torque during normal walking.

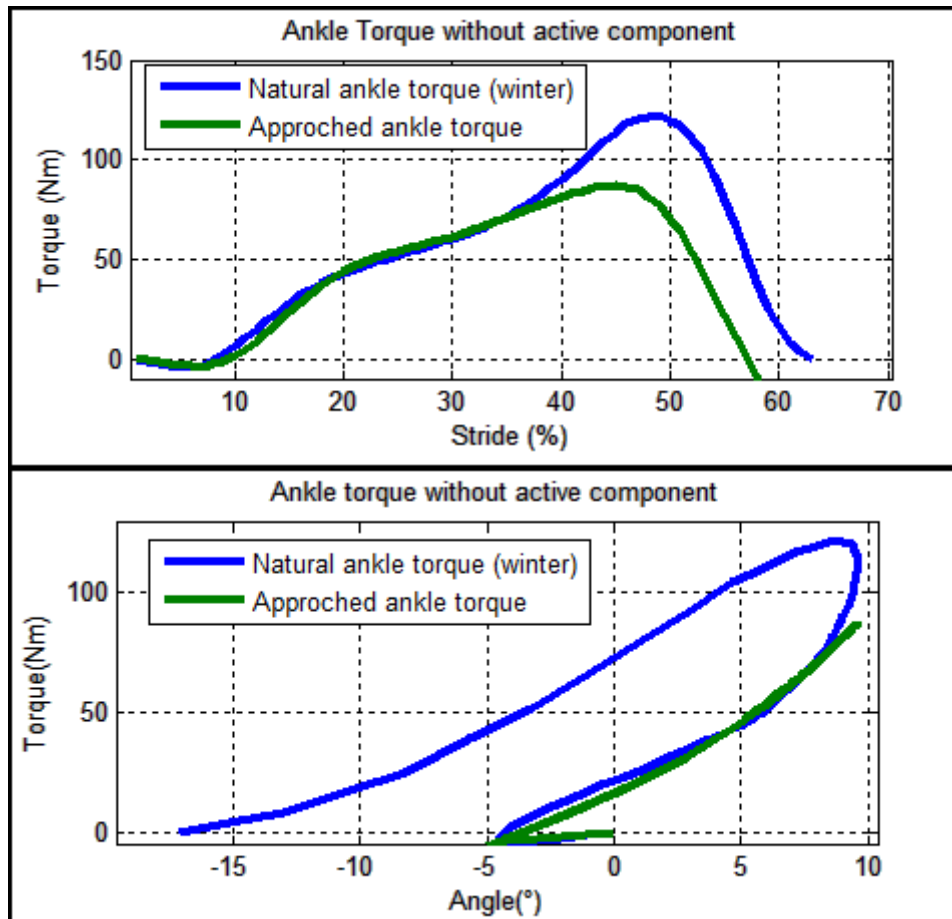


Fig. 53: Behaviour of the PBP when it is equipped with only passive elements a) Above: Ankle Torque (Nm) vs. Stride (%), b) Below: Ankle Torque (Nm) vs. Ankle Angle (°)

Fig. 53b shows a comparison of the torque required during normal walking with the theoretical ankle torque as a function of ankle angle, when the PBP is equipped with only passive elements.

It is seen in Fig. 53b that the approach is acceptable during both CP phase (0° till -5°) and CD phase (between -5° and 10°). Once the maximum DF angle is reached, the spring will return to its initial position. Consequently, the required torque peak during normal walking will not be reached. Regarding the fact that the curve follows his original course, no net work is done. Notice that the net work is proportional to the surface of the loop. In practice, this results in the lack of power in order to initiate a Heel-Off. One can conclude that the motor must apply torque to the PBP at approximately 35% of stride.

Fig. 54a shows the comparison of the theoretical torque capability of the PBP with the torque required during normal walking when a combination of active and passive components are used, as a function of % of stride. It is seen that by providing power by the motor on the PBP at approximately 35% of stride during normal cadence, an acceptable theoretical approach is obtained.

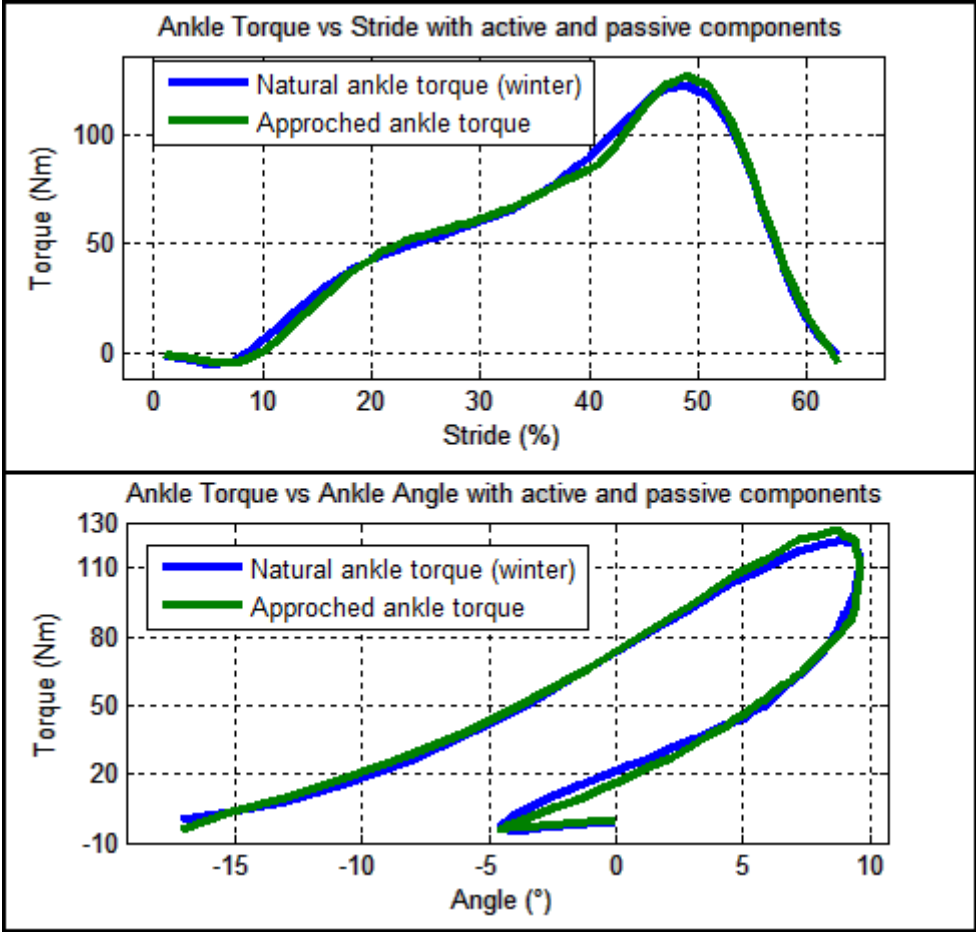


Fig. 54: Behaviour of the PBP when, it is equipped with passive and active elements. A) Above: Ankle Torque (Nm) vs. Stride (%), b) Below: Ankle Torque (Nm) vs. Ankle Angle (°)

Fig. 54b shows a comparison of the torque required during normal walking with the theoretical ankle torque as a function of ankle angle, when the PBP is equipped with a combination of active and passive elements.

The motor and transmission requirements are determined based on the above mentioned simulation results. Therefore, the power that the motor should provide on the ankle joint has to be simulated.

Fig. 55 shows the required torque (Nm) and the power (W) on the ankle joint versus % of stride, that the motor in combination with the transmission should provide. This characteristic can be divided in two main parts. The first part is the stance phase and covers 0% to 62% of the stride cycle. The motor must provide enough power in this part in order to mimic the natural ankle torque characteristic properly. The second part is the swing phase. During swing, the ankle angle position must be controlled in order to reset the foot to its initial position for the next Heel-Strike.

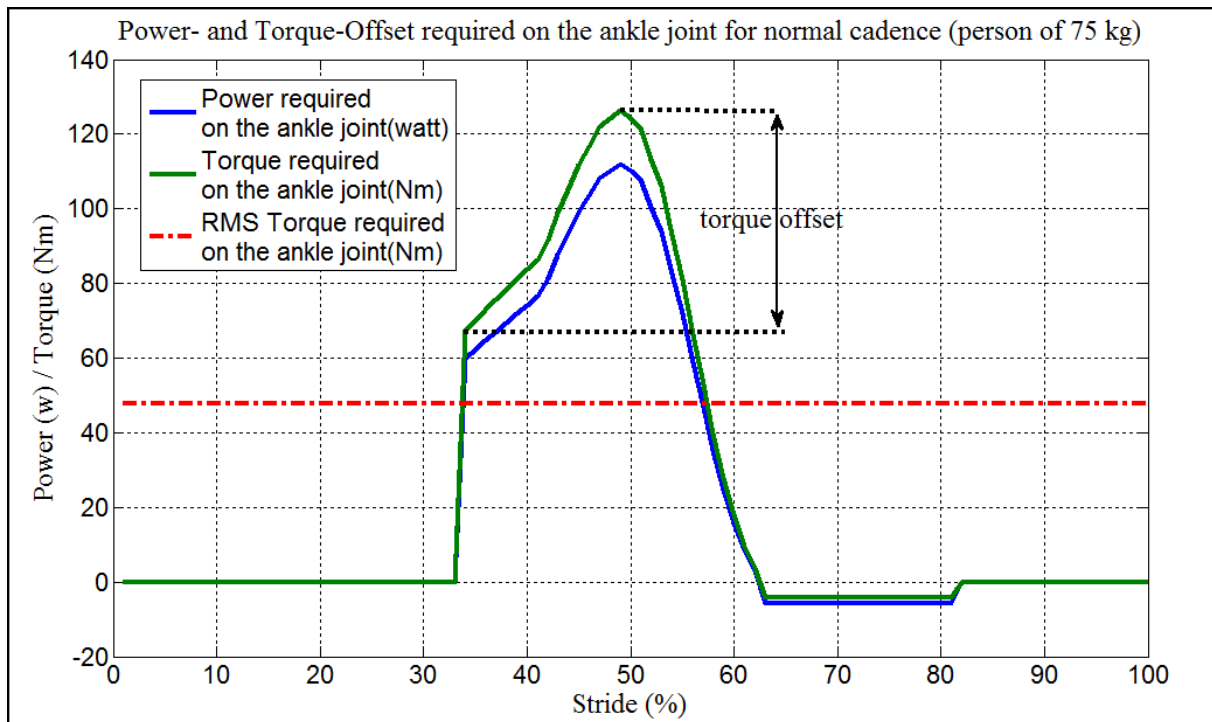


Fig. 55: Required Power (watt) and Torque (Nm) on the ankle joint for normal cadence vs. % of Stride

It is seen in Fig. 55 that the required motor torque varies between 35% - 62% of the gait cycle. This course is characterized using two variables: Root Mean Square (RMS) value of the motor torque and a peak motor torque.

The motor torque equals 0 Nm between 0% - 35 % since the motor should not operate and the PBP acts fully passive in that period. The motor initiates working at 35% of stride and reaches a peak value at approximately 49%. In the swing, the motor torque is constant between 62 % - 82 % and equals 0 Nm between 82% - 100 % of stride. As discussed in *Biomechanics*, the PBP should return to his home position at approximately 50% of the swing phase.

The motor specifications are determined based on the following assumption:

- The motor must be capable of providing the RMS torque required on the ankle joint as shown in Fig. 55, without exceeding the motor curve in the continuous operation region (nominal), see Fig. 56.
- The motor must be capable of providing the peak torque required on the ankle joint shown in Fig. 55, without exceeding the motor curve in the short-term operation region, see Fig. 56.

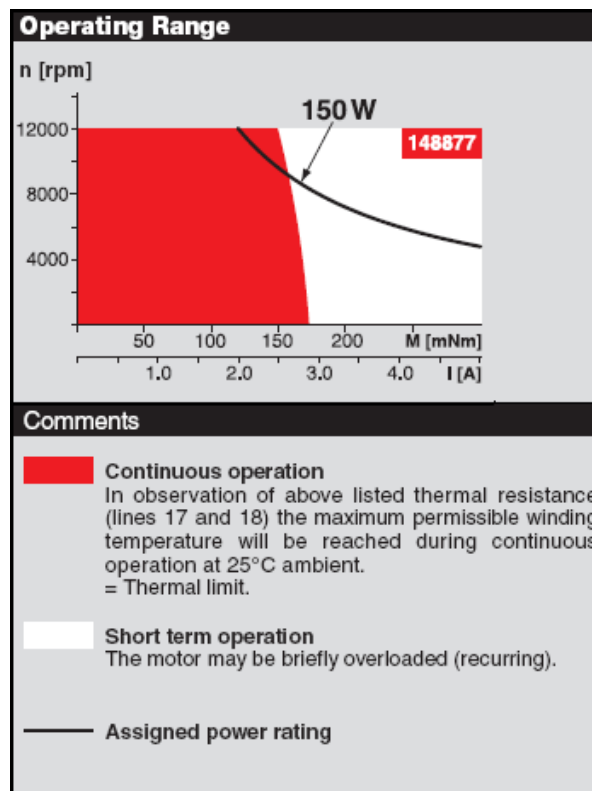


Fig. 56: Motor operation range (MAXON RE-40)

Notice that the speed of the motor is taken constant while working. This choice has been made in the simulations in order to make the system easier to control. A constant speed of motor results in a linear course of angle α° (angle of C-Lever arm) as shown in Fig. 57.

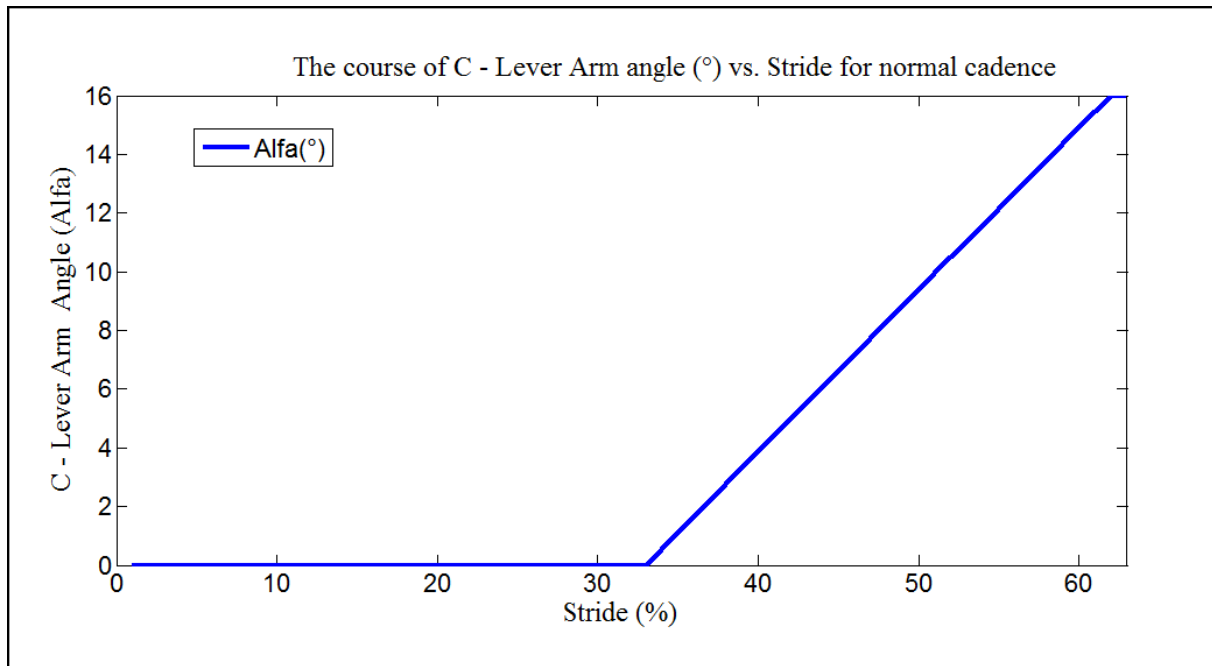


Fig. 57: C-Lever arm angle (°) vs. % of Stride required for normal cadence

Concerning the selection of the electric motor, two categories are commonly used: classical brushed DC-motors and brushless DC-motors (BLDC).

BLDC-motors offer several advantages compared to brushed DC-motors, such as: higher efficiency and reliability, reduced noise, longer lifetime (no brush erosion), elimination of ionizing sparks from the commutator, and overall reduction of electromagnetic interference (EMI). The maximum power that can be generated by a BLDC-motor is exceptionally high, limited almost exclusively by heat. BLDC's main disadvantage is the higher cost, resulting from the following aspects. First, BLDC-motors require complex electronic speed controllers to work. Brushed DC-motors can be regulated by a variable resistor, which is inefficient but also satisfactory for cost-sensitive applications. Second, BLDC-motors are considered to have a higher efficiency compared to brushed DC-motors, mostly due to the absence of friction of brushes. The enhanced efficiency is greatest in the no-load and low-load region of the motor's performance curve. Under high mechanical loads, BLDC-motors and high-quality brushed motors are comparable in efficiency.

In this application the motor should operate mainly at the high-load region of the motor characteristic curve, thus the efficiency advantage of the BLDC is negligible.

Regarding the fact that the control aspects of a fully integrated PBP are of great importance, it is desirable to choose a system, which is easier to control. Due to the negligible efficiency difference and the difficulty of controlling a BLDC-motor, we opted for a brushed DC-motor.

Motor Data

The selected motor is a Maxon DC-motor RE 40 150W, see Appendix C. Table 2 shows the motor data.

Table 2: Maxon motor RE40 (150 watt) data

Motor data Maxon RE40 (150 watt)	
Nominal voltage (V)	24
No load speed (rpm)	7580
No load current (mA)	137
Nominal speed (rpm)	6930
Nominal torque (max. continuous torque) (mNm)	170
Nominal current (max. continuous current) (A)	5,77
Stall torque (mNm)	2280
Starting current (A)	75,7
Max. efficiency (%)	91

3.2.2. Transmission

Due to the high torque - low speed character of this application it is obvious that a great reduction is needed. Based on the simulation results, the motor must provide a peak torque of 126 Nm (RMS torque of 50 Nm). The maximum rotation speed of the C-Lever arm is 11 rpm, which is related to fast cadence. Comparing these values to the motor data -nominal torque of 170 mNm and a nominal speed of 6930 rpm- explains the need of a large reduction. The challenge is designing a transmission system with high energy-efficiency, low weight within the size limits of a normal foot.

3.2.2.1. Gears [15]

Various kinds of gears can be used in order to provide the required reduction. Examples are bevel, helical and worm gears.



Fig. 58: a) Left: Bevel gear b) Middle: Helical gear c) Right: Worm gear (hpcgears catalog)

Helical gears

Helical gears offer some benefits relative to the other gears. They offer an increased contact ratio due to the axial tooth overlap, this results into having a greater load carrying capacity comparing to gears of similar size. Due to the above-mentioned benefits, they have a smooth working characteristic.

Worm gears

The advantage of the worm gears is the self-locking ability. Notice that there is some confusion about this self-locking ability, as not all the worm gears offer such ability. Theoretically, a worm gear will not back drive if the friction angle is greater than the worm lead angle. However, the actual surface finish and lubrication may reduce this significantly. More important, vibration may cause motion at the point of mesh with further reduction in the friction angle. A worm gear set with self-locking ability will have a very low efficiency due to high friction.

Regarding the low reduction offered by such a set, worm gears must be used in combination with a gearbox on the motor. The next formulas will be used in order to design the worm and wheel set.

The worm gears reduction ratio can be calculated by:

$$Ratio = \frac{Number - of - teeth - in - wheel}{Number - of - teeth - in - worm}$$

The efficiency depends on the lead angle and coefficient of friction and can be calculated by:

$$Efficiency = \frac{TAN(\theta)}{TAN(\theta + \gamma)}$$

With:

θ = Lead Angle

f = Coefficient of friction.

$$\theta = TAN^{-1}(f)$$

Notice that coefficient of friction depends on the rubbing speed of the teeth.

Table 3 shows two possible worm gear set for this application. These worm gears are chosen based on dimensions, strength, and the reduction ratio.

Table 3: Worm gear calculations

HPC worm gears: 2,5 MOD			
No. of teeth on wheel	15	No. of teeth on wheel	15
No. of starts on worm	2	No. of starts on worm	1
Ratio	7,5	Ratio	15
Diameter Wheel (mm)	37,5	Diameter Wheel (mm)	37,5
Diameter Worm (mm)	35	Diameter Worm (mm)	35
Lead angle (°)	9,28	Lead angle (°)	4,46
Speed (rpm)	50	Speed (rpm)	100
Rubbing speed (ft/min)	18,277	Rubbing speed (ft/min)	36,184
Coefficient of friction	0,073	Coefficient of friction	0,070
Theta (°)	4,175	Theta (°)	4,004
Efficiency	0,683	Efficiency	0,524

Notice that none of the above-mentioned worm gears offers a self-locking ability.

Motor and gearbox with worm gear (ratio 7,5):

The applied motor is a Maxon DC-motor RE 40 (150 Watt); see Table 2. The used worm gear has an efficiency of 68,3 % and a reduction ratio of 7,5 , see Table 3. One could determine the gearbox required using the data above and knowing that the required RMS motor torque is 50 Nm and the required peak motor torque equals 120 Nm.

In this case, the gearbox should have a reduction of 80. The chosen gearbox is the Maxon planetary gear-head (GP 42 C, see Appendix D) with reduction 81 and an efficiency of 72%.

Notice the required motor speed after reduction is 8,5 rpm for normal cadence and 11 rpm for fast cadence. The achieved speed after reduction equals 11,5 rpm. Thus, this configuration can offer enough power in order to have an acceptable approach of normal and fast cadence.

Table 4 shows the gear head design calculations.

Table 4: Gearbox transmission calculations with worm gear ratio 7,5

Nom. motor torque(mNm)	170
Nom. motor speed (rpm)	6930
RMS ankle torque required(Nm)	50
Peak ankle torque required(Nm)	120
Worm gear reduction	7,5
RMS Torque required on the worm(Nm)	9,761
Peak Torque required on the worm(Nm)	23,426
Efficiency worm gear	0,683
Extra reduction required	79,746
Available Maxon planetary gear-head GP 42 C	81
Efficiency gear head	0,72
Total reduction	607,5
Total transmission efficiency	0,492
Speed after reduction (rpm)	11,407

Motor and gearbox with worm gear (ratio 15):

The applied motor is the same as above. The used worm gear has an efficiency of 52,4% and a reduction ratio of 15, see Table 3. The required gearbox is determined as above. In this case, the gearbox should have a reduction of 52. The chosen gearbox is the Maxon planetary gear-head (GP 42 C, see Appendix D) with reduction 53 and an efficiency of 72%.

Based on the required motor speed after reduction as above, this configuration would not offer enough power for fast cadence. Table 5 shows the gear head design calculations.

Table 5: Gearbox transmission calculations with worm gear ratio 15

Nom. motor torque(mNm)	170
Nom. motor speed (rpm)	6930
RMS ankle torque required(Nm)	50
Peak ankle torque required(Nm)	120
Worm gear reduction	15
RMS Torque required on the worm(Nm)	6,373
Peak Torque required on the worm(Nm)	15,296
Efficiency worm gear	0,523
Extra reduction required	52,071
Available Maxon planetary gear-head GP 42 C	53
Efficiency gear head	0,72
Total reduction	795
Total transmission efficiency	0,377
Speed after reduction(rpm)	8,717

Conclusion:

The application of gear sets combined with a well-chosen motor gear-head could lead to achieving the torque–speed requirements. However, there are some disadvantages. The gears should bear the high ankle torque peak, which leads to excessive weight of the compatible gear sets. Thus, the weight of such design is unfavourable. The next hinder is the low efficiency of such design due to friction. The maximum achievable transmission efficiency with this approach is around 50%. This will result in energy inefficiency and should be avoided.

Another disadvantage of using the gears mentioned above is the following. Due to size and weight limits of this application and the large reduction needed, these gears cannot be applied solitary. Thus, an extra gearbox with a large reduction on the motor will be inevitable. Such gearbox - high torque with a large reduction- should have a large number of stages. This results in extra weight and lower efficiency.

3.2.2.2. Ball Screw

Up to this point, the Lever arms were directly driven by a gear (worm, helical or bevel). A completely different driving mechanism, comprising a ball screw will be explained in the following chapter. Before explaining the implementation of the ball screw into the design, the characteristics of the ball screw itself will briefly be overviewed.

Ball Screw Characteristics

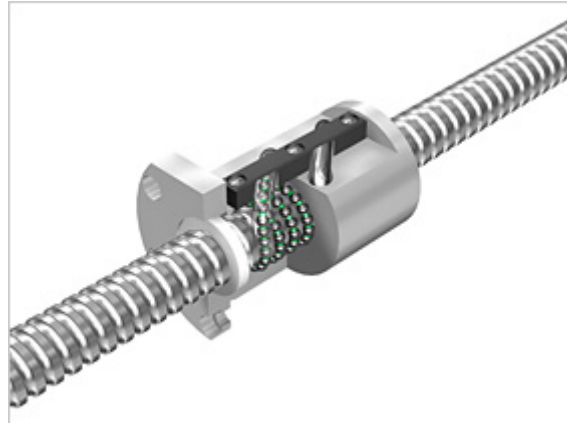


Fig. 59: Example of a ballscrew. Notice the tiny balls positioned between the nut and the screw. This will lead to a much higher efficiency than a conventional feed screw. This is a precision caged ball screw from THK. [16]

The ball screw is a device that converts a rotational motion into a translational motion or vice versa. It has the same mechanism as a conventional feed screw, but instead of screwing a nut directly on the screw axis, there are tiny balls making a rolling motion between the screw axis and the nut in order to achieve high efficiencies. The ball assembly acts as the nut while the threaded shaft is the screw axis. In comparison with a conventional sliding screw, a ball screw only needs drive torque of one-third or less, making it most suitable for saving drive motor power. This is very important in this application.

Following formulas are important in order to calculate the efficiency and the driving torque required to gain thrust:

$$\tan(\beta) = \frac{Ph}{\pi \cdot d} \qquad \text{Eqtn. 9}$$

β (°) being the lead angle of the screw axis, d (mm) is the ball centre-to-centre diameter and Ph (mm) is the feed screw lead. Using the calculated lead angle one can determine the efficiency of the ball screw with Fig. 60.

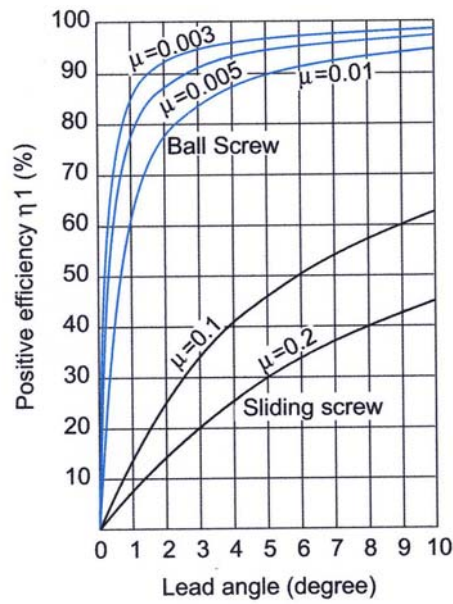


Fig. 60: Ball screw and conventional sliding screw positive efficiencies (%) vs. Lead Angles (°) for different frictional resistance μ .

Notice that the efficiency for ball screws is significantly higher than that for conventional sliding screws and that the higher the lead angle, the higher the efficiency. Also notice that this efficiency is dependant on the frictional resistance μ . Typical ball screw efficiencies with lead angles starting from 2,5° are 80-97%. An efficiency of 90% will be used in the calculations. Positive efficiency is used to characterise the efficiency for the rotation-translation conversion. Negative efficiency is used to characterise the efficiency for the translation-rotation conversion. As only the first application will be used within the design, positive efficiency will further be referred to as efficiency. The required torque can be calculated as follows (Appendix E):

$$T = \frac{F \cdot Ph}{2 \cdot \pi \cdot \eta} \quad \text{Eqtn. 10}$$

F (N) is the thrust required to rotate the Lever arm. η is the efficiency determined from the lead angle Ph (mm).

The relation between the angular velocity of the screw N (rpm) and the translation speed of the nut V (m/s) is set as follows:

$$N = \frac{V \cdot 1000 \cdot 60}{Ph} \quad \text{Eqtn. 11}$$

Implementation of the ball screw

The main advantage of using a ball screw as part of the driving mechanism is that a great reduction with high efficiency can be realized. This permits a smaller transmission on the motor, which allows a more compact and less heavy design. The issue that occurs by implementing only gear heads is the limited reduction, low efficiency, and high weight.

The nut, which performs a translational motion along the screw, has to be connected with the C-Lever arm in such a way that it allows the rotational motion of this Lever arm. For this reason, the nut and the C-Lever arm cannot have a rigid connection. Fig. 61 shows the ball screw assembly (ball screw, nut, and motor) and the Lever arms that have to be driven.

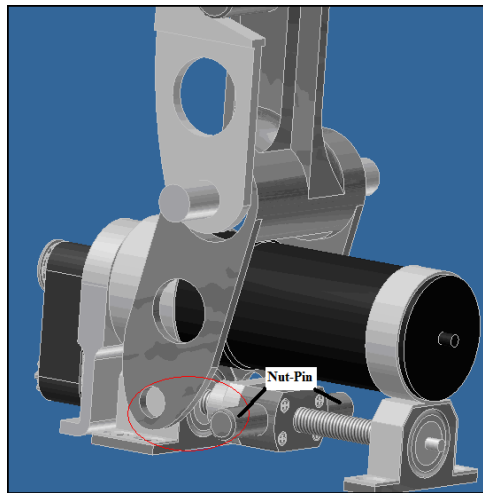


Fig. 61: Ball screw assembly and Lever arms without connection

Notice that the nut and C-Lever arm are not connected. Also notice the part connected to the nut has a pin sticking out on each side (Nut-Pin). These pins will have to drive the Lever arm. Two different mechanisms are developed in order to operate the Lever arm through the nut.

Mechanism 1: Involute groove

As illustrated in Fig. 62, the nut drives the Lever arm by simply pulling it towards the back of the motor. In this mechanism, a circle-involute shaped groove has been cut out in the Lever arm.

This way, the ball screw feels no radial load. Avoiding radial forces on the ball screw is crucial, as these forces may not exceed 10% of the allowable static load.

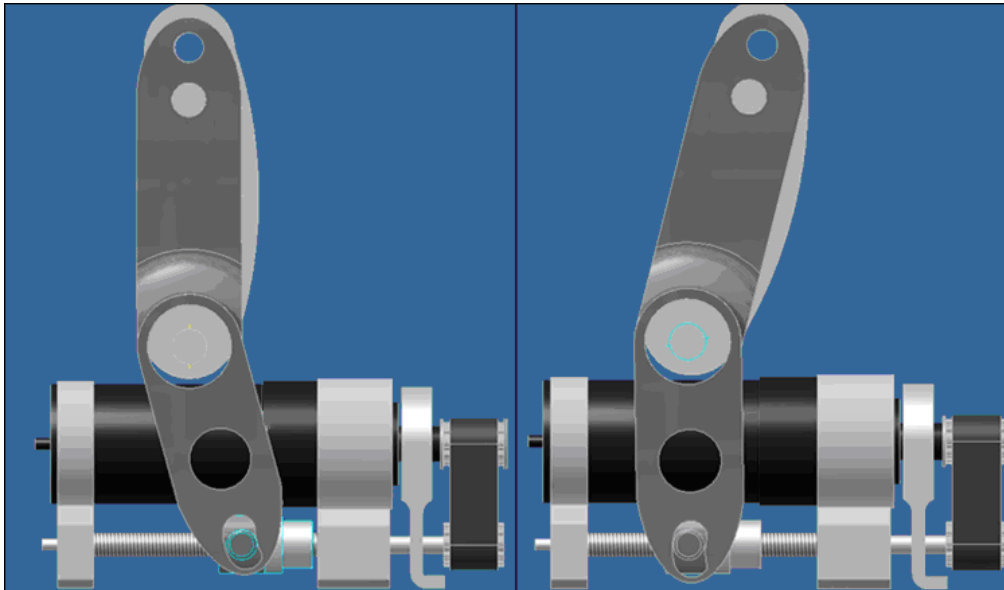


Fig. 62: Driving mechanism of the developed PBP. The C-Lever arm is driven by the nut. Due to the involute groove, the ball screw feels no radial force.

This mechanism however, causes some friction and has to be well designed in order to avoid that the pin of the nut gets jammed into the groove. Based on this issue, another mechanism has been developed.

Mechanism 2: Crankshaft

In this design, a crankshaft mechanism will be used to convert the translational motion of the nut into the rotational motion of the C-Lever arm.

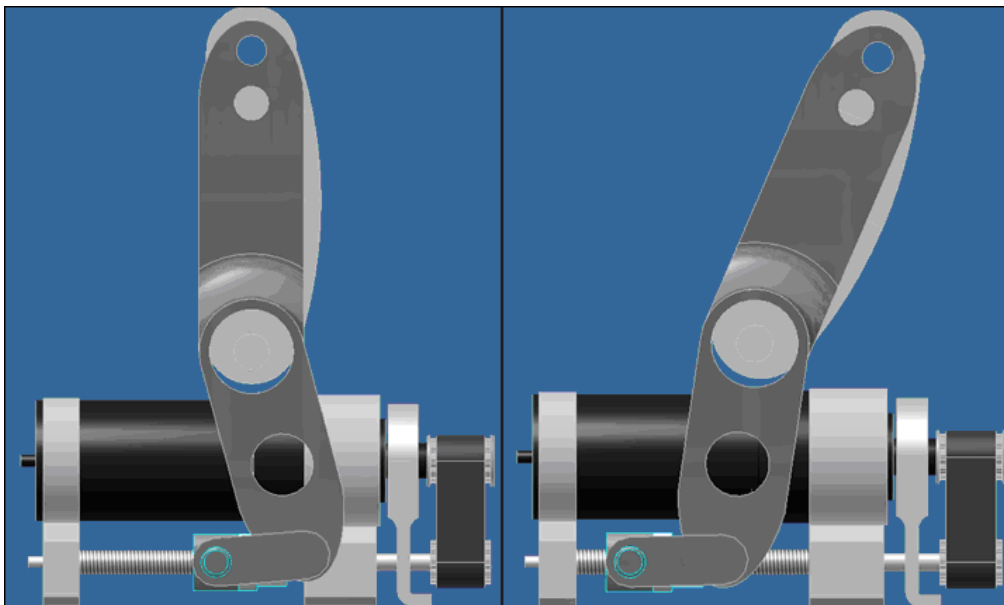


Fig. 63: Driving mechanism of the developed PBP :Crankshaft mechanism incorporated in the driving mechanism

Although this mechanism minimizes the friction problem, another problem arises; the radial forces are no longer eliminated. The model was parameterized in order to calculate the radial force acting on the ball screw.

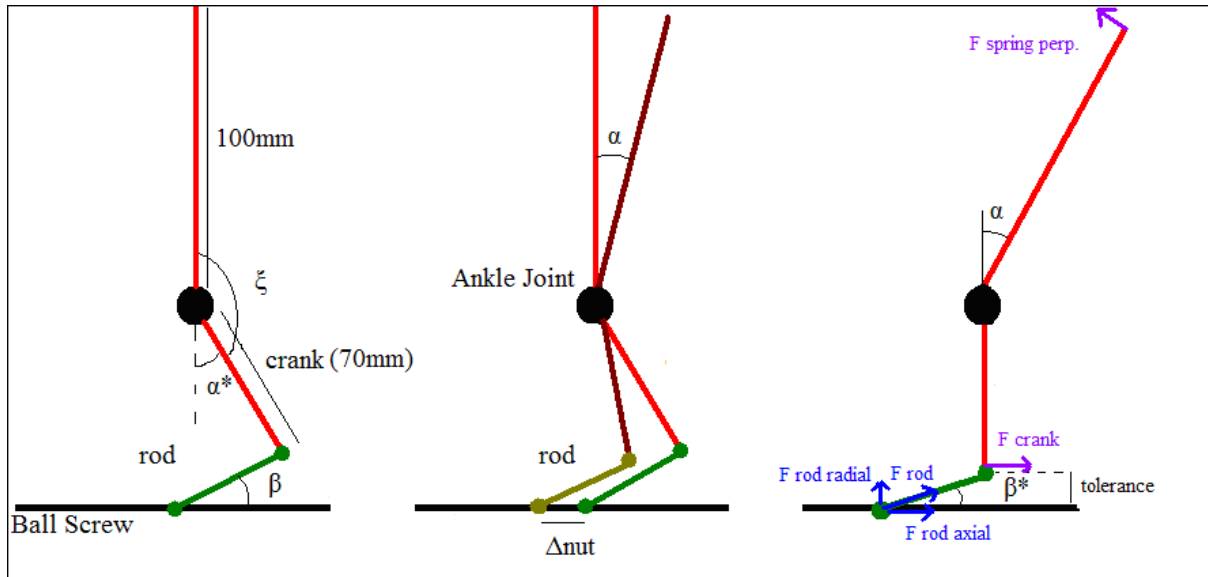


Fig. 64: parameters of the crankshaft mechanism. By optimising the parameters, the radial forces can be minimized

The fixed parameters are the crank length (70mm), ξ , the rod length and the tolerance. β^* is the angle between the rod and the Ball screw when α^* is zero. Fig. 64 characterizes the geometry of the mechanism.

$$\alpha^* = 180 - \xi - \alpha \quad \text{Eqtn. 12}$$

$$\beta^* = \text{tg} \sin\left(\frac{\text{tolerance}}{\text{rod}}\right)$$

$$\text{crank} \cdot \cos(\alpha^*) + \text{rod} \cdot \sin(\beta) = \text{crank} + \text{tolerance}$$

$$\text{crank} \cdot \sin(\alpha^*) + \text{rod} \cdot \cos(\beta) = \text{rod} \cdot \cos(\beta^*) + \Delta \text{nut}$$

The forces acting on the nut, hence on the ball screw are due to the force in the crank. The forces are determined with

$$F \text{ spring perp.} = \text{the force acting on both springs perpendicular to the Lever arm} \quad \text{Eqtn. 13}$$

$$F_{crank} = F_{springperp} \cdot \left(\frac{100}{70} \right)$$

$$F_{rod} = \frac{F_{crank}}{\cos(\alpha^* + \beta)}$$

$$F_{rod_radial} = F_{rod} \cdot \sin(\beta)$$

$$F_{rod_axial} = F_{rod} \cdot \cos(\beta)$$

Notice that in order to minimize the radial force, the tolerance, hence β^* , should be set to zero. In order to set a proper value for ξ , one has to determine the position of the crank, on which the highest forces appear and make sure that β is zero at that instant. This way the highest radial force will be reduced. From simulations, it is seen that with a rod length of 30 mm, a tolerance of 0 mm and ξ of 15° the radial forces do not exceed the 10% threshold. Fig. 65 shows the profile of the radial force (in % of the static load, which is explained in the ball screw calculations), β ($^\circ$), α ($^\circ$) and translation nut (mm) as a function of the stride (%) for normal cadence.

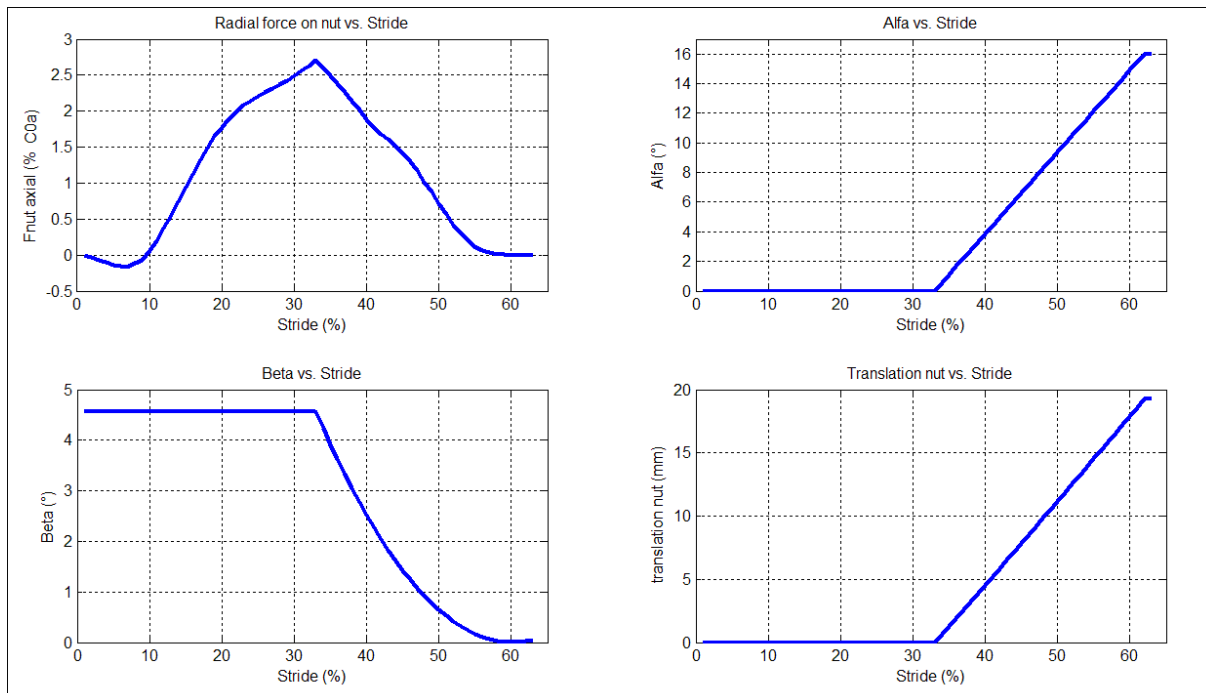


Fig. 65: Radial Force (% of the static load), α ($^\circ$), β ($^\circ$) and translation nut (mm) as a function of Alfa ($^\circ$)

Finally, Fig. 66 determines the relation between α (angle of the C-Lever arm with a vertical perpendicular to the foot cfr. *modélisation*) and translation nut. This is very important for control aspects.

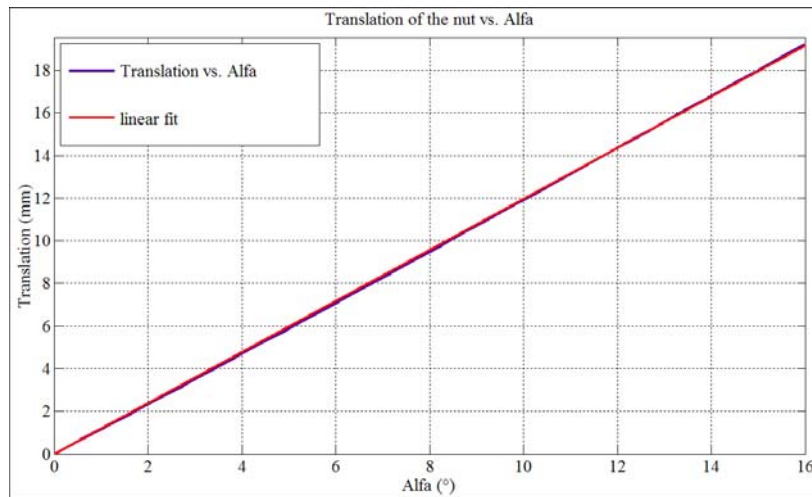


Fig. 66: Translation of the nut (mm) vs. α (°) (above), Residual vs. α (°) (below)

As Fig. 66 shows, the curve can be approached by a linear fit (R^2 -value = 0,999) and the slope is 1,2 mm/°. Notice that this approximate linearity is due to relatively small α and β .

Ball screw calculations

A great variety of ball screws are available on the market. Some of the various parameters are screw diameter, screw length, ball diameter, precision, screw end etc. In order to verify whether a particular ball screw is suitable for this application, two conditions have to be fulfilled.

First, it is imperative that the ball screw can carry the loads imposed on the nut.

Secondly, one must make sure that the required torque and the required rotational speed of the C-Lever arm is achieved.

Loads

For the following calculations, a ball screw with *Miniature Single Nut with Flange FEM-E-B* from Bosch Rexroth AG has been chosen [Appendix E]. Table 6 shows the characteristics of the ball screw and the system.

Table 6: Ball screw and system characteristics

ball screw characteristics		
Ph:	2,5	mm
Ca (dynamic)	2,2	kN
C0a (static)	2,8	kN
efficiency ballscrew	90	%
Torque_RMS	0,34	Nm
Torque_Peak	0,87	Nm
Required translationspeed nut	80,4	mm/s
Required rotation speed ballscrew	1929	rpm
Required average rotation speed ball screw	550,2	rpm
Reduction balscrew	172,8	
safetyfacor (fs)	1,42	
system characteristics		
T_ankle RMS	50	Nm
T_ankle max	130	Nm
Motor_Arm	70,00	mm
Lever_Arm	100	mm
Fm_RMS	760	N
Fm_Peak	1976	N
Required speed leverarm	11,17	rpm

Ca and C0a are the dynamic and static load ratings of the ball screw, respectively. The dynamic load rating is defined as the load rate at which the ball screw can perform 1 million revolutions. The static load rating is a maximum load that may not be exceeded. As can be seen in Table 6, the maximum load is never exceeded (safety factor = C0a/ Fm_Peak = 1,42). Notice that these loads are axial loads. The maximum radial load that a ball screw can carry is 10% of the static load. The radial loads are shown in Fig. 65 and never exceed 10% of C0a.

Torque and angular velocity

The Torque RMS and Peak values are calculated using Eqtn.10 with Fm_RMS and Fm_peak, respectively. These loads are the RMS and peak values of the forces imposed by the springs.

The required translational speed of the nut (mm/s) is calculated with Eqtn. 14.

$$v_{nut} = \omega_{Leverarm} * slope_ \Delta nut_ \alpha * \frac{360}{60} \quad \text{Eqtn. 14}$$

With $\omega_{\text{Lever arm}}$ = required angular velocity (rpm) of the C-Lever arm and slope $\Delta_{\text{nut}} \alpha$ is 1,2 (mm/°) as already discussed above.

It is seen in Table 6 that both conditions (loads and Torque/speed) are fulfilled.

With these results, the Service Life of the ball screw can be calculated.

$$L = \left(\frac{C0a}{F_{\text{RMS}}} \right)^3 * 10^6 \text{ (rev)} \quad \text{Eqtn. 15}$$

$$Lh = \left(\frac{L}{n_{\text{average}} * 60} \right) \text{ (h)}$$

L is the number of revolutions that can be made in a service life and n_{average} is the average rotation speed of the ball screw. This results in a service life Lh of 700 h.

The incorporation of a ball screw in the driving mechanism seems an adequate choice based on the following advantages:

- Low weight
- High reduction
- High speed

3.2.2.3. Belt

The main motivation of using a belt transmission is to achieve a compact design. A belt transmission will be applied to avoid an unnecessary length of the motor-gearhead placed along the ball screw set. This results in a more optimal use of the available space in the PBP. Timing belts have an efficiency of approximately 95%. Therefore, the loss of such transmission will not have a major effect on the system. Another favourable characteristic of timing belts is the ‘no-slip’ property, when the pulleys and the belt are installed properly.

Belt calculations[17]:

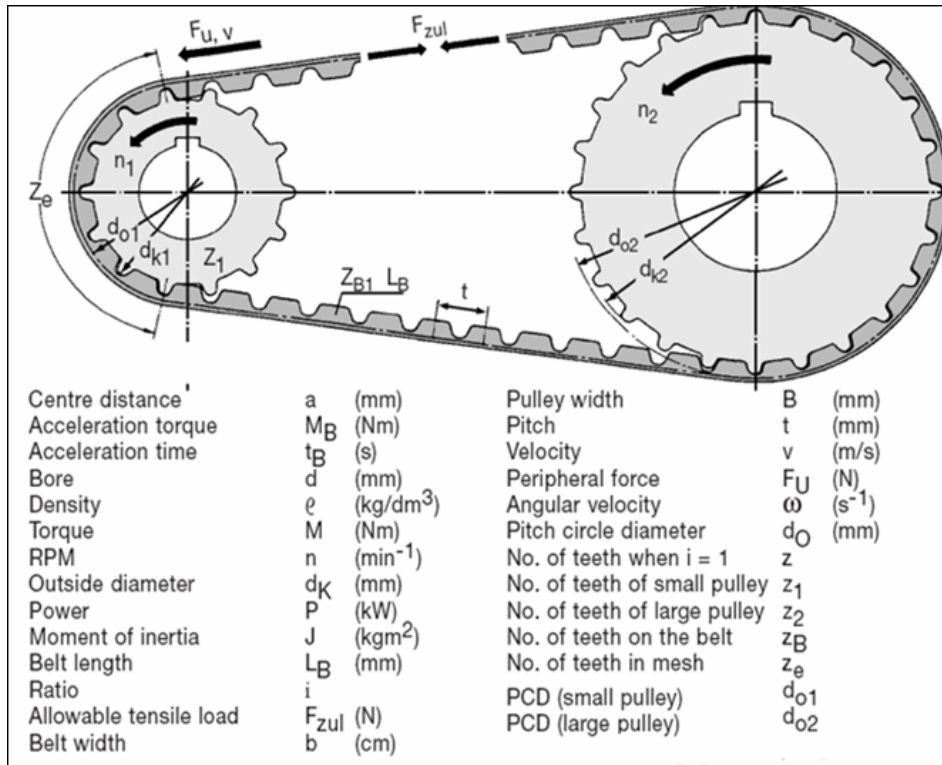


Fig. 67: Timing belts schematics (originating from [17])

The belt ratio chosen for this application equals one. Therefore the following formulas can be used:

$$Z = Z_1 = Z_2$$

$$i = \frac{Z_1}{Z_2}$$

$$a = \frac{ZB - Z_1}{2} \cdot t$$

$$L_B = 2 \cdot a + Z \cdot t$$

The belt width (in cm) required to transmit known peripheral force F_u , torque M or power P without exceeding the maximum allowable tooth shear strength, is calculated using any of the following formulas:

$$b = \frac{F_u}{Z_e \cdot F_{u_{spec}}}$$

$$b = \frac{100 \cdot M}{Z1 \cdot Ze \cdot M_{spec}}$$

$$b = \frac{1000 \cdot P}{Z1 \cdot Ze \cdot P_{spec}}$$

With:

F_{spec} = Specific peripheral force in N/cm

M_{spec} = Specific torque in Ncm/cm

P_{spec} = Specific power in W/cm

F_{spec} , M_{spec} and P_{spec} are depended of the pitch and the rotation speed (rpm).

The first step towards the design of the timing belt and pulleys is the determination of the required pitch, which depends on the rotation speed (rpm) and the design power (kW) of the small pulley and can be derived from the belt selection graph; see Appendix F.

Table 7 shows the belt selection calculations.

Table 7: Belt selection calculations

Belt selection		
HPCgears Timing belts		
Belt selection graph 3.2 => T5 (pitch 5 mm)		
P_{spez} (T.5 2000 rpm)	2,281	W/cm
M_{spez} (T.5 2000 rpm)	1,089	Ncm/cm
$F_{u_{spez}}$ (T.5 2000 rpm)	13,69	N/cm
t (pitch)	5	mm
Z1 (small pulley)	10	ul
Z2 (large pulley)	10	ul
i(ratio)	1	ul
a (centre distance)	33,7	mm
Ze (no. of teeth in mesh)	5,00	ul
belt width required	9,83	mm
belt width chosen	10	mm

3.2.3. Final Driving System

In the final driving system (Fig. 68) the following components are used:

- Maxon DC-motor (RE40, 150 watt, see Appendix C)
- Maxon Planetary Gearhead (GP42C, see Appendix D)
- Belt transmission
- Ball screw
- Crank rod mechanism

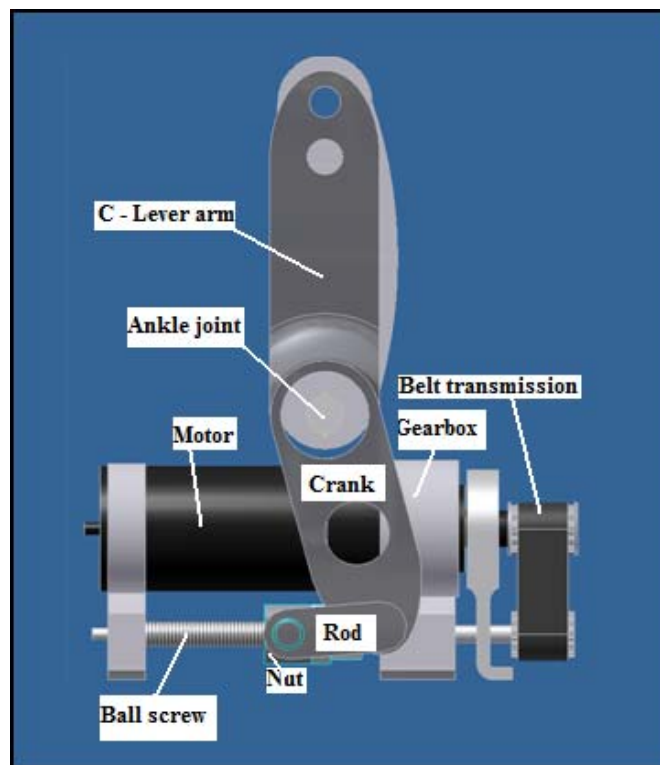


Fig. 68: Final driving system

Table 8 shows the final driving system calculations for normal, fast and slow cadence. The motor requirements are calculated for each cadence, based on the simulation results, crank-rod, ball screw, belt and gear head specifications. It is seen that the chosen motor (Maxon RE-40) can provide the required power to the PBP, by comparing the motor requirements, see Table 8 , with the selected motor data, see Table 2.

Remark that the efficiency achieved by this final driving system is 77%, which is much better than the maximum efficiency of 50% achieved by applying a gear transmission.

Table 8: Calculations of the final driving system

		CADENCE		
		NORMAL	FAST	SLOW
Requirements based on the simulation results	Required torque , RMS stride (Nm)	49,484	46,362	48,841
	Required torque peak (Nm)	126,4	127,6	118,7
	Required C-Lever arm speed (rpm)	8,469	11,165	5,466
	Crank (mm)	70,00	70,00	70,00
	C-Lever arm (mm)	100	100	100
Ball screw specifications	Ball screw lead (mm)	2,5	2,5	2,5
	Ball screw efficiency	0,9	0,9	0,9
	F_Nut RMS (N)	707	662	698
	F_Nut peak (N)	1922	1940	1805
	Required torque on the screw , RMS Stride (Nm)	0,313	0,293	0,308
	Required torque peak on the screw(Nm)	0,85	0,86	0,80
	Required nut translation speed (mm/s)	60,980	80,620	39,055
	Required ball screw speed (rpm)	1464	1935	937
Belt spesifications	Belt efficiency	0,95	0,95	0,95
	Reduction of belt transmission	1,00	1,00	1,00
Gearhead specifications	Gearhead efficiency	0,90	0,90	0,90
	Reduction of gearbox	3,50	3,50	3,50
System specifications	Total reduction	604,8	604,8	604,8
	Total efficiency	0,770	0,770	0,770
Motor requirements	Required motor torque, RMS (Nm)	0,104	0,098	0,103
	Required motor torque, peak (Nm)	0,284	0,287	0,267
	Required motor speed (Nm)	5122	6772	3281

3.2.4. Driving System for Compliance Adjustability (MACCEPA)

It is seen in *Simulations* that by regulating the pre-tension of the springs during walking, the patient is able to walk with normal, slow or fast cadence. Another benefit of regulating these pre-tensions is that one can experimentally determine the prosthesis stiffness required for each patient separately so that the patient could walk with the least required metabolic energy cost. It is shown that this regulation can be achieved by using the following components. See calculation in Appendix G.

- Ball screw (Bosh FEM-E-B, see Appendix E)
 - diameter 6 mm
- Harmonic drive (CSF Series Mini 5, see Appendix H) as shown in Fig. 69.
 - Reduction: 100
 - Weight: 25 g
 - Total length: 17 mm



Fig. 69: Harmonic drive (CSF Series Mini Gearheads [18])

- DC-motor (Maxon RE13, see Appendix I)
 - Diameter: 13 mm
 - Electrical power: 0.75 Watt
 - Voltage: 4,8 V
 - Weight: 15 g

The CAD assembly of the motor and the harmonic drive is shown in Fig. 70.

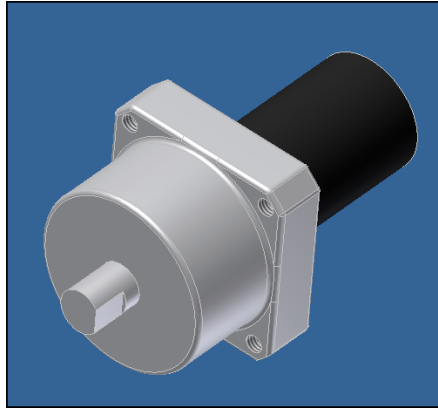


Fig. 70: CAD assembly of the motor (Maxon RE-40) and the harmonic drive (CSF Series Mini 5)

Remark that a space should be foreseen on the leg in order to situate this compliance adjusting driving system. In order to design a first PBP prototype, it is assumed that the pre-tension of the springs are regulated manually. Therefore, the CAD design of the PBP does not contain the compliance adjusting driving system.

3.2.5. Unlocking Mechanism for Ratchet and Pawl

It is seen that when a ratchet and pawl set is applied, the need to unlock them in the swing phase is inevitable since the Lever arms should return to their home position.

Unlocking a ratchet is rather straightforward in theory by using e.g. electromagnetism or a mechanical system designed for this application. Practically however, applying such mechanisms is more complex due to control issues. An elegant manner to achieve this unlocking behaviour at a favourable time is using already existing translation movements of other components.

In this chapter the motion of the motor-driven ball screw nut, is applied to control the locking behaviour of the ratchet and pawl set. The pawl is normally pushed against the ratchet and locked by a torsion spring positioned on the pawl joint. Fig. 71 shows the case that the mechanism is locked.

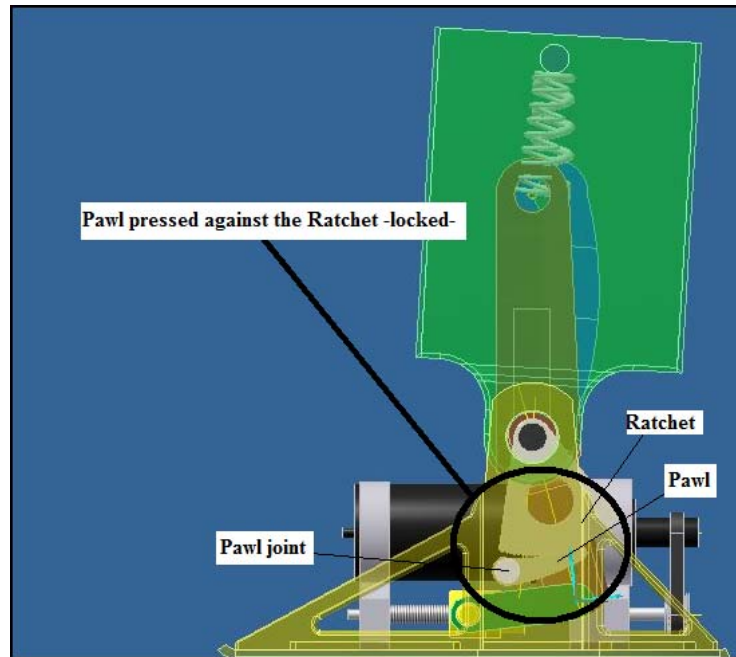


Fig. 71: Ratchet and pawl when locked

As discussed in *modelisation*, the S-Lever arm (blue component in Fig. 71) is attached to the ratchet through the ankle shaft. Therefore, the S-Lever arm is the only part that gets *DF-locked* by this mechanism, by *DF-locked* it is meant that the ratchet allows the effective motion of the Lever arm only in PF. In a best-case scenario, the ratchet should be locked in the stance phase and then released in the swing phase. In this particular design, however, this requirement can be redefined. A pin is placed on the C-Lever arm, which will operate the S-Lever arm with the occurrence of a contact (Pin-Contact). When a Pin-Contact occurs all the loads are carried by the pin so that the ratchet can be released at that point. Remark that this Pin-Contact is achieved shortly after the motor starts working. This short time delay is required to cope with the angle difference between the Lever arms.

A feasible mechanism can be achieved as follows:

The ball screw nut should be connected with the pawl through a component that meets the above-mentioned time delay. In this concept, see Fig. 72, a linear spring is used with an internal wire to limit the maximum spring extension. This mechanism works as follows:

- As the motor starts working the linear spring will begin to extend by the nut while the pawl is pushed against the ratchet by the torsion spring
- After Pin-Contact occurrence, the linear spring reaches the maximum extension limit, predefined by the length of the internal wire, and the pawl will be pulled down, unlocking the mechanism.

- Notice that during swing the ball screw nut translates in the opposite direction so that the ratchet will be locked again at the end of the swing phase.

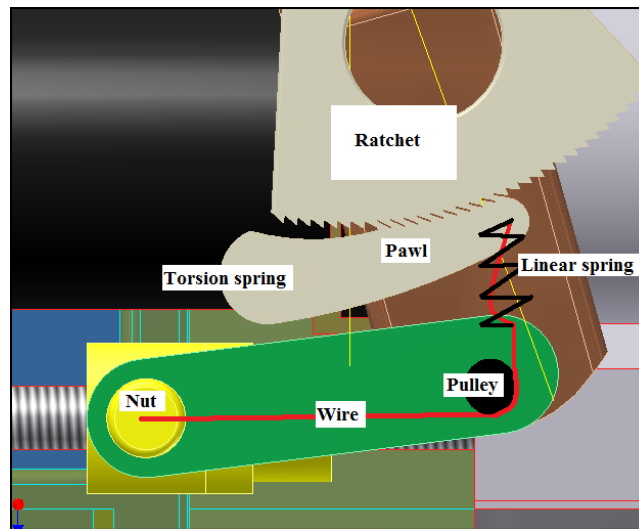


Fig. 72: Schematics of the un-locking mechanism: The pulley is placed on the side plates of the foot

3.2.6. Power Supply

The autonomy of PBP is a major design criterion. This paragraph targets this issue. As the prosthesis is a mobile device, the use of batteries as a power supply is the obvious choice. In a first stage, an estimation of the energy consumption of the motor has to be made. This will be done for slow, normal and fast cadence. Table 9 indicates the different stride characteristics such as walking times, cadences, etc for slow, normal, and fast cadence.

Table 9: The Stride characteristics

STRIDE CHARACTERISTICS	slow cadence	normal cadence	fast cadence
cadence (steps/min)	86,80	105,3	123,1
stride length (m)	1,38	1,51	1,64
speed (m/s)	1,00	1,33	1,68
speed (km/h)	3,59	4,77	6,06
stride time (s)	1,38	1,14	0,97
stance time (s)	0,83	0,68	0,58
swing time(s)	0,55	0,46	0,39
number of steps during 1,5 h walking per day	7812	9477	11079

The cadences and stride lengths were mentioned in the chapter *Biomechanics*. The other parameters were calculated assuming that stance period remains about 60% of stride for all

cadences. It is seen that the energy consumption during swing time will be quite small as only the energy for lifting up the foot is required.

Table 10 shows the system characteristics during stance period.

Table 10: System Characteristics during Stance period

SYSTEM CHARACTERISTICS during STANCE	<i>slow cadence</i>	<i>normal cadence</i>	<i>fast cadence</i>
Motor-On (% of Stride)	24	23	31
Motor-On (s)	0,332	0,262	0,302
motor speed (rpm)	4652	5124	6773
Voltage (V)	14,67	16,16	21,36

During stance, the motor should only work for about 20-30% of the total stride time. This ‘Motor-On’ period varies depending on the cadence. The stance time for fast cadence is smaller than for normal cadence, the Motor-On time however, is higher. The motor speed is calculated using the required angular velocity of the Lever arm for each cadence and converting that velocity to the required rotational speed of the ball screw. By multiplying the rotational speed of the ball screw with the proper reduction of the transmission, the motor speed is acquired. The necessary voltage is calculated by multiplying the motor speed with the rpm constant of the motor [Appendix C]. The same characteristics can be shown for the swing period, which is shown in Table 11.

Table 11: System Characteristics for Swing period

SYSTEM CHARACTERISTICS DURING SWING	<i>slow cadence</i>	<i>normal cadence</i>	<i>fast cadence</i>
Motor On (% of Stride)	24	20	17
Motor On (s)	0,28	0,23	0,19
motor speed (rpm)	5833	7076	9823
Voltage (V)	18,40	22,32	30,99

Finally, there are two methods used to calculate the energy consumption during a stride cycle. Table 12 and Table 13 show the two different methods for stance and swing period respectively.

Table 12: STANCE PERIOD: Two methods to calculate energy consumption during stance period. Method 1 uses the required torque and the corresponding current to calculate the capacity, method 2 uses the mechanical power to calculate the capacity.

Method 1	<i>slow cadence</i>	<i>normal cadence</i>	<i>fast cadence</i>
RMS Torque Motor side (Nm)	0,103	0,104	0,0978
I_motor (A)	3,75	3,80	3,56
starting capacity (Ah/stance period)	0,00009	0,00009	0,00009
Capacity per step (Ah/stance period)	0,00044	0,00037	0,00039
RMS Electrical Power (W/stance period)	38,79	61,38	76,01
energy per stance period (Wh/stance period)	0,00452	0,00595	0,00833
energy per stance period (J/stance period)	16,28	21,41	30,00
Method 2	<i>slow cadence</i>	<i>normal cadence</i>	<i>fast cadence</i>
RMS Mechanical Power (W)	35,39	56,00	69,34
RMS Electrical Power (W)	38,89	61,54	76,20
energy per stance period (Wh/stance period)	0,0045	0,0060	0,0084
energy per stance period (J/stance period)	16,31	21,45	30,06

Table 13: SWING PERIOD: Two methods to calculate energy consumption during swing period. Method 1 uses the required torque and the corresponding current to calculate the capacity, method 2 uses the mechanical power to calculate the capacity.

Method 1	<i>slow cadence</i>	<i>normal cadence</i>	<i>fast cadence</i>
RMS Torque Motor side (Nm)	0,00400	0,00396	0,00393
I_motor (A)	0,1450	0,1434	0,1427
Capacity per step (Ah/swing period)	0,00001	0,00001	0,00001
RMS Electrical Power per step (W/swing period)	2,67	3,20	4,42
energy per swing period (Wh/swing period)	0,000205	0,00020	0,00024
energy per swing period (J/swing period)	0,74	0,73	0,86
Method 2	<i>slow cadence</i>	<i>normal cadence</i>	<i>fast cadence</i>
RMS Mechanical Power (W/swing period)	2,44	2,93	4,05
RMS Electrical Power (W/swing period)	2,68	3,22	4,45
energy swing period (Wh/swing period)	0,00021	0,0002	0,0002
energy swing period (J/swing period)	0,74	0,73	0,87

Method 1 starts with the RMS value of the torque on the motor side. Using the torque constant (Nm/A) and considering the motor efficiency, the required current is computed. The starting capacity is calculated with the starting current of the motor and the starting time. The capacity per step is obtained by multiplying the current with the total Motor-On time and by

adding the starting capacity. In order to calculate the energy, the capacity must be multiplied with the voltage. In other words, Method 1 uses the electrical power to calculate the energy. Method 2 however, starts with the RMS value of the mechanical power and multiplies this power with the motor efficiency in order to acquire the electrical power. The energy is then calculated by multiplying this electrical power with the Motor-On time.

To conclude, the most important values from Table 12 and Table 13 are the consumed energy per stance and swing period, because, as mentioned before, it is very hard to estimate an energy per day consumption as this variation is quite volatile depending on the amputee's daily activities.

Notice, the very small difference in values resulting from both methods shown in Table 14.

Table 14: Difference in energy consumption calculations (Method 1 and Method 2) for both Stance and Swing phase.

	slow cadence	normal cadence	fast cadence
Stance ΔE (%)	0,20	0,19	0,19
Swing ΔE (%)	0,6	0,6	0,6

The difference between both calculation methods is due to the use of rpm and torque constants in method 1 in order to calculate the current and voltage. Nonetheless, Table 14 indicates that these differences are negligible.

The energy per stance period, swing period and stride - values are shown again for all three cadences and for both methods in Table 15.

Table 15: energy per stance period, swing period and stride - values for both methods and for all three cadences

Method 1	<i>slow cadence</i>	<i>normal cadence</i>	<i>fast cadence</i>
energy per stance period (J/stance period)	16,28	21,41	30,00
energy per swing period (J/swing period)	0,74	0,73	0,86
total energy per step (J/step)	17,02	22,14	30,87
Method 2	<i>slow cadence</i>	<i>normal cadence</i>	<i>fast cadence</i>
energy per stance period (J/stance period)	16,31	21,45	30,06
energy per swing period (J/swing period)	0,74	0,73	0,87
total energy per step (J/step)	17,05	22,19	30,93

Notice that the necessary energy during swing is very small in comparison with the necessary energy during stance. In comparison with another developed below-knee active prosthesis

[11], which consumes 22 J/step (80kg subject walking at 0,8Hz), our PBP consumes 22,19 J /step (for a 75kg subject walking at 0,88 Hz or normal cadence).

In order to have an idea, about the potential autonomy of our PBP, two cases will be elaborated, both calculated with method 1.

In the first case, the amount of batteries necessary to provide 1,5h walking per day for all three cadences is calculated. Notice that the walking time (h/day) is chosen arbitrarily and is very much a function of the individual's occupation and lifestyle. We believe that for a working individual with a typical office desk job, 1,5h a day walking or approximately 10.000 steps a day is a fair assumption.

In the second case, a commercially available 1,5 kg battery pack is used and the battery run time is calculated. This study is performed in order to have an idea of our PBP's autonomy with a standard available battery pack.

Lithium-ion polymer batteries will be used in this study. Lithium-ion polymer batteries are rechargeable batteries, which have technologically evolved from lithium-ion batteries. They possess higher energy density up to 200 Wh/kg [21]. Consider a Li-poly battery with an energy density of 200Wh/kg. Table 16 indicate the required battery weight for case 1 and the battery run time for case 2.

Table 16: energy density of a Li-Poly battery, required battery weight for 1,5h/day walking and battery run time for a 1,5kg battery pack

BATTERY CHARACTERISTICS	<i>slow cadence</i>	<i>normal cadence</i>	<i>fast cadence</i>
energy density (Wh/kg)	200,00	200,00	200,00
required battery weight for 1,5h/day walking (kg)	0,177	0,282	0,463
Approximate battery run time with 1,5kg battery pack (h)	13	8	5

The required battery weight for 1,5h walking per day can very easily be stored in this PBP, regarding the weight and available space in the PBP. Therefore, one possibility is to put a standard internal battery package of approximately 300 g in the prosthesis for 1,5 h walking per day at normal cadence and to provide an additional external battery pack of 1,2 kg (e.g. in a fanny pack), for 8h walking per day at normal cadence. In this case, the patient can choose between both options, depending on his daily activities.

3.3. Control Aspects

3.3.1. Finite State Machine

A Finite State Machine (FSM) is a model of behaviour composed of a finite number of states, transitions between these phases and actions. A FSM can be represented by a state diagram. In Fig. 27 a FSM for the control system imitating natural human ankle behaviour during walking is represented. Fig. 73 shows the different states of the FSM mimic the natural ankle gait with the PBP developed during this thesis.

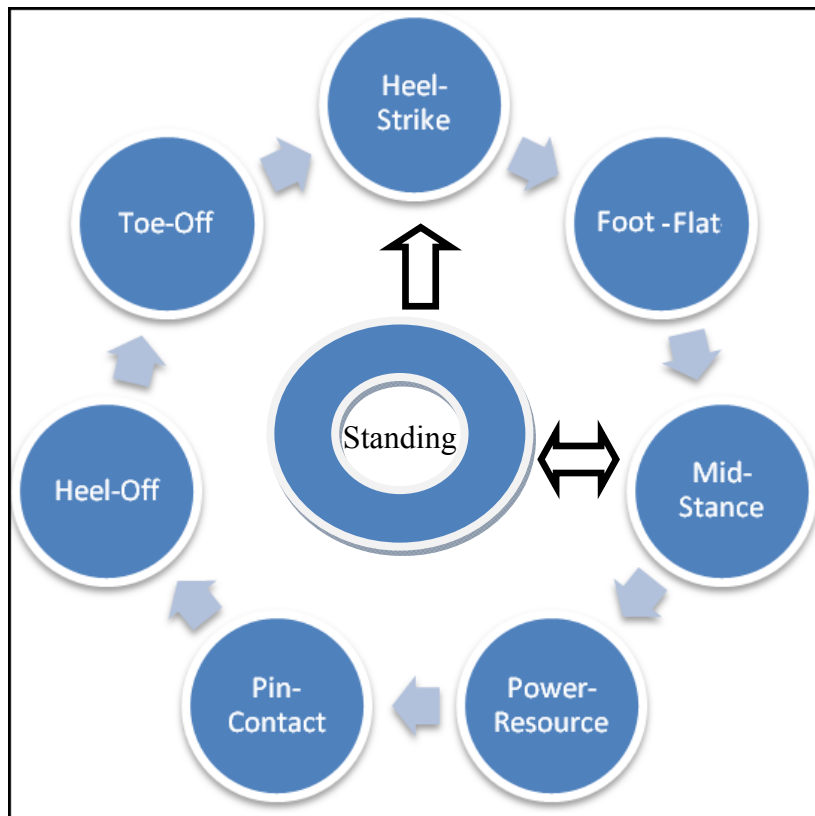


Fig. 73 : Different states to imitate natural human ankle behaviour with the PBP developed in this thesis

Notice that Standing refers to the home -equilibrium- position of the PBP. The next step is the determination of the various actions during each phase. Table 17 shows the different states and the corresponding actions.

Table 17: Different states and corresponding actions in order to imitate natural human ankle behaviour during stride. With MCP: Maximum CP ankle angle, MPP: Maximum PP ankle angle, AM: Angle added by the Motor, +: Motor on with a positive direction (Positive direction is defined as Lever arms plantar flex).

State	Heel-switch	Toe-switch	Ankle Angle (°)	Angle S-Lever arm (°)	Angle C-Lever arm(°)	Ratchet and Pawl (Controlling S-Lever arm)	Motor (Operating C-Lever arm)
Heel-Strike	On	Off	0	0	0	locked	Off
Foot-Flat	On	On	-4.4 (MCP)	MCP	0	locked	Off
Mid-Stance	On	On	0	MCP	0	locked	Off
Power-Source	On	On	7.77	MCP	0	locked	On(+)
Pin- Contact	On	On	9.37	MCP	MCP	locked	On(+)
Heel-Off	Off	On	9.62	MCP + AM	MCP + AM	locked	On(+)
Toe-Off	Off	Off	-17 (MPP)	MPP	MPP	Unlocked	On(-)
Heel-Strike	On	Off	0	0	0	locked	Off

In order to extend this analysis the inputs, outputs and intern variables of the system are determined. The inputs of the system are the Heel-Switch (0/1), Toe-Switch (0/1) and the ankle angle (°). The motor actions are considered as the output of the system. Notice that the C-Lever arm and the ratchet are directly operated by the motor and the S-Lever arm is operated by the C-Lever arm. Therefore, the state (angle) of the C-Lever arm and the S-Lever arm and the state (locked/unlocked) of the ratchet can be interpreted as the internal variables and are completely defined by the motor actions.

The developed PBP acts as a Mealy Machine, regarding the fact that the output of this FSM depends on the inputs and the internal variables [19].

For a Mealy Machine one can use the next expression assuming Output(s) = Z_n , Input(s) = X_n and Internal variable(s) = Y_n .

$$Z_n = G(X_n, Y_n)$$

In order to apply the Boolean algebra, it is assumed that the ankle angle is characterized by Table 18. The Boolean conversion of ankle angles is based on the following assumption:

If the Power-Source state is reached or in other words, if the motor should start working, the ankle angle Boolean becomes True for a short period of time. Remark that the ankle angle is known continuously (measured). The ankle angle corresponding with the Motor-On is known as well.

Table 18: Ankle Angle behaviour using Boolean algebra

State	Ankle Angle
Heel-Strike	0
Foot-Flat	0
Mid-Stance	0
Power-Source	1
Pin-Contact	0
Heel-Off	0
Toe-Off	0
Heel-Strike	0

The Boolean conversion of Heel- and Toe-Switch behaviour, shown in Table 19, is based on the following assumption:

On=1, Off=0

Table 19: Heel-Switch and Toe-Switch behaviour using Boolean algebra

State	Heel-switch	Toe-switch
Heel-Strike	1	0
Foot-Flat	1	1
Mid-Stance	1	1
Power-Source	1	1
Pin-Contact	1	1
Heel-Off	0	1
Toe-Off	0	0
Heel-Strike	1	0

The Boolean conversion of motor behaviour shown in Table 20 is based on the following assumption:

On=1X, Off= 0X, Positive Direction =X0, Negative Direction= X1.

Table 20: Motor behaviour using Boolean algebra

State	Motor (Operating C-Lever arm)
Heel-Strike	00
Foot-Flat	00
Mid-Stance	00
Power-Source	10
Pin-Contact	10
Heel-Off	10
Toe-Off	11
Heel-Strike	00

Table 21 shows a conjunction of the above mentioned results. Notice that the behaviour of ratchet, S- and C-Lever arm is not mentioned in Table 21, considering the fact that their behaviour is completely determined by the motor behaviour and the geometrical design of the prosthesis.

Table 21: Different states and actions in order to imitate natural human ankle behaviour using Boolean algebra

State	Heel-Switch (H)	Toe-Switch (T)	Ankle Angle (A)	Motor (Operating C-Lever arm) (M1-M2)
Heel-Strike	1	0	0	00
Foot-Flat	1	1	0	00
Mid-Stance	1	1	0	00
Power- Source	1	1	1	10
Pin-Contact	1	1	0	10
Heel-Off	0	1	0	10
Toe-Off	0	0	0	11
Heel-Strike	1	0	0	00

Table 21 can be used in order to implement a basic control system for the PBP.

The next step in of this study consists in the establishment of the Boolean expressions corresponding with this FSM.

3.3.2. Huffman's Method

Huffman's method can be applied in this matter [19]. With this method one could design a sequential system like ours. An important stage in this method is the determination of the various phases in the system by establishing a Phase Diagram. Fig. 74 shows the Phase Diagram of this FSM. Six different Phases are distinguished.

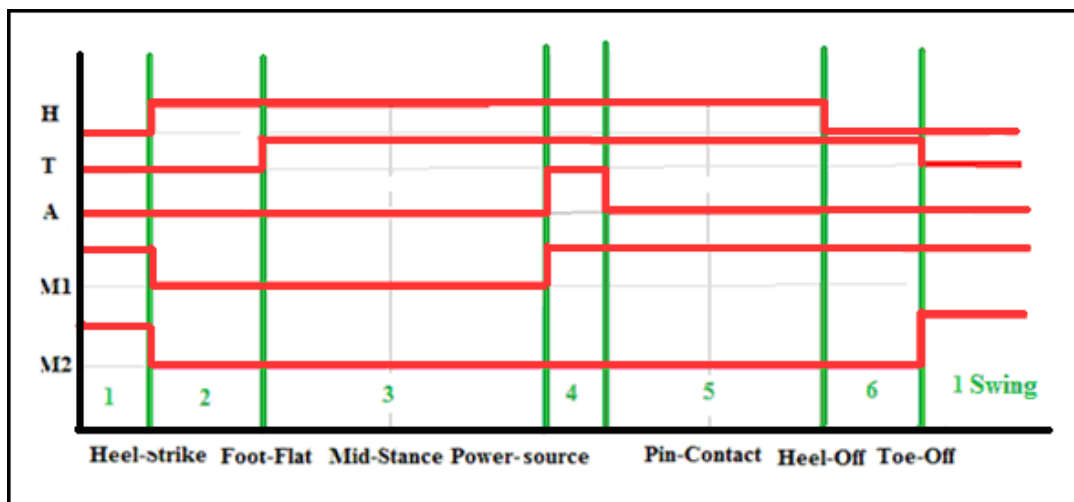


Fig. 74: Phase Diagram of the FSM in order to mimic the natural human ankle behaviour

A Phase Table could be made using the Phase Diagram shown in Fig. 74.

Table 22: Phase table of the FSM in order to mimic the natural human ankle behaviour

Phase	H	0	1	1	1	1	0	0
	T	0	0	1	1	0	1	0
	A	0	0	0	1	1	0	1
	M1							
	M2							
1		1/11	2					
2			2/00	3				
3				3/00	4			
4				5	4/10			
5				5/10			6	
6		1					6/10	

On Table 22 the stable states are indicated by bold numbers. Notice that the output combinations (M1 M2) are indicated as (Phase number /M1 M2).

Table 23 shows the reduced version of Table 22 . The phases 1, 2 and 3 are compatible and are replaced with phase 1. The phases 4, 5 and 6 are compatible as well and are replaced with phase 2. Notice that other manners are possible in order to reduce this table.

Table 23: Phase table (reduced) of the FSM in order to mimic the natural human ankle behaviour

Phase	H	0	1	1	0	1
	T	0	0	1	1	1
	A	0	0	0	0	1
1=1+2+3		1/11	1/00	1/00		2/00
2=4+5+6		1/00		2/10	2/10	2/10

Remark that different output combinations occur in each phase which is typical for a Mealy Machine.

The next step is associating intern variables Y with each Phase. 0=Phase 1 and 1=Phase 2 as illustrated in Table 24.

Table 24 : Phase table (reduced) of the FSM in order to mimic the natural human ankle behaviour associated by intern variables Y

Y	H	0	1	1	0	1
	T	0	0	1	1	1
	A	0	0	0	0	1
0		0/11	0/00	0/00		1/00
1		0/00		1/10	1/10	1/10

In order to find the Boole expressions, Table 24 is split up in 3 tables. An excitation table, which is shown in Table 25.

Table 25: Excitation table of the FSM in order to mimic the natural human ankle behaviour

Y_{N+1}	H	0	1	1	0	1
	T	0	0	1	1	1
	A	0	0	0	0	1
$Y_n=0$		0	0	0		1
$Y_n=1$		0		1	1	1

The next expression can be found based in Table 25.

$$Y_{N+1} = A + Y_n \cdot T$$

Table 26 represents output M1 and Table 27 output M2.

Table 26: Output (M1) table of the FSM in order to mimic the natural human ankle behaviour

M1	H	0	1	1	0	1
	T	0	0	1	1	1
	A	0	0	0	0	1
	Y=0	1	0	0		0
Y=1	0			1	1	1

The next expression is found based in Table 26.

$$M1 = T \cdot Y + \bar{T} \cdot \bar{H} \cdot \bar{Y}$$

Table 27: Output (M2) table of the FSM in order to mimic the natural human ankle behaviour

M2	H	0	1	1	0	1
	T	0	0	1	1	1
	A	0	0	0	0	1
	Y=0	1	0	0		0
Y=1	0			0	0	0

The next expression is found based in Table 27.

$$M2 = \bar{T} \cdot \bar{H} \cdot \bar{Y}$$

3.3.3. Conclusion

The expressions above are rewritten as follows:

$$M2 = \bar{T} \cdot \bar{H} \cdot \bar{Y}$$

$$M1 = T \cdot Y + M2$$

$$Y_{N+1} = A + Y_n \cdot T$$

The expressions above determine when the motor should work and in which direction. The first expression illustrates that the motor should work in a negative direction in swing phase, in other words, if Heel- and Toe-Switch are off. The second expression determines that the

motor should be on in the swing phase or in stance phase if the Power-Source state is started and Toe-Off not yet reached. The last expression is in fact a set reset latch. It can be characterized by the fact that it has a memory. Notice that the set action is done by Boolean A and the reset action is applied by Boolean T.

The expressions above can be useful in order to understand the system, although we believe that further refinement of these control aspects are necessary to develop a real time control system. Imagine a situation in which the amputee using the prosthesis is standing still, the Toe-Switch is on, and the ankle angle passes the value corresponding with the Power-Source state, $Y=1$. Based on expressions above the motor starts working in order to generate Heel-Off. Looking at the fact that the ankle angles do not vary immensely, it may be possible to meet the requirements above which will lead to starting the motor without really having the intension of walking. One could introduce an extra Boolean ($S=Stop$) in order to prohibit such situation.

Boolean S should equal 1 in case of continuous walking and equal 0 in case of standing or stopping. The Boolean expressions get replaced by the next ones if the Boolean S is taken into the account.

$$M1_{NEW} = M1 \cdot S$$

This results in the fact that the motor will not start working while $S=0$. Regarding the fact that ankle angle is measured at all times it is easy to work out this Boolean. Notice that Boolean S can be controlled in different ways. As an example S should equal 0 if the next expression is true.

$$\frac{\Delta(AnkleAngle)}{\Delta(Time)} = 0$$

Another way of regulating Boolean S is manually, with an extra switch operated by the patient.

By associating the PBP with a Finite State Machine (Mealy machine) and determining the Boolean expressions, one could comprehend the requirements in order to realize a robust control system.

The study above proves that this system can be controlled theoretically by using the following inputs:

- Heel-Switch to verify Heel-Contact (e.g. Pressure or micro switch)
- Toe-Switch to verify Toe-Contact (e.g. Pressure or micro switch)

- Encoder on the ankle joint to determine the ankle angle ($^{\circ}$) as a function of time.

However, this can get refined in practice by adding the next inputs to the system:

- A linear potentiometer placed on the ball screw nut, in order to determine the nut position as a function of time (to verify the motor actions)
- Load cells connected to the springs in order to clarify the spring forces as a function of time (e.g. to verify pre-tension).
- Encoder on the motor

Notice that the *variable design parameters* (pre-tensions, Power-Source timing and the duration of Power-Source) depend on the cadence speed. However, the cadence speed could be easily determined from the time interval between Heel-Contact and Toe-Off using the Heel and Toe-Switch.

The values of the *variable design parameters* are well-known for each cadence speed as well from the simulations executed based on the natural human ankle behaviour during walking (Winter [2]) as the reference. Hence, we believe that the control system should offer the possibility of adjusting these *variable parameters* manually depending on the patient choice to approach their individual ankle requirements on the most natural and energy efficient way.

3.4. Design and Assembly of the parts [20]

3.4.1. Procedure

Following the kinetics simulation of each part of the system, the actual parts have to be designed. In the design procedure, several steps are undertaken in order to avoid failing and to ensure proper working of the parts. Fig. 75 shows the procedure that has been followed throughout the design phase. The design and stress analysis are performed in Autodesk[®] Inventor 2008.

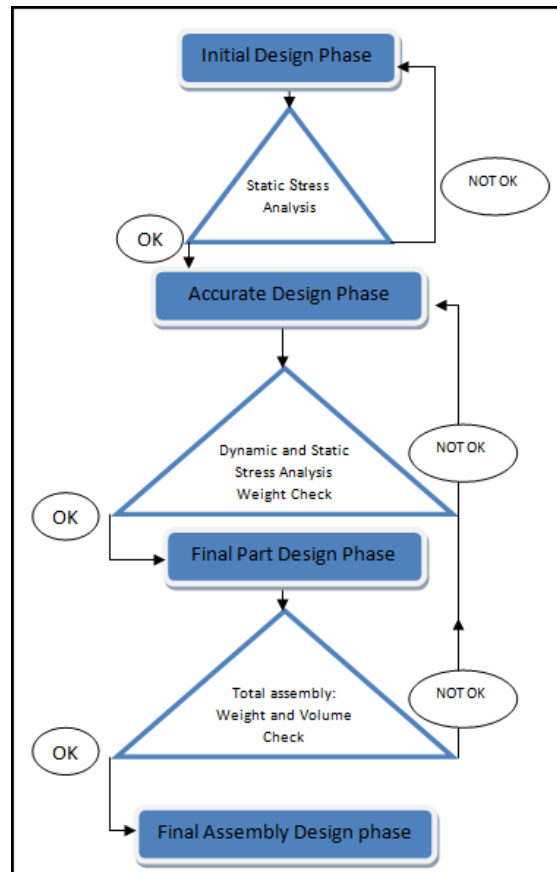


Fig. 75: Design procedure of the different parts of the prosthesis

The main challenge of designing a PBP is to respect the physical properties of a natural below-knee limb without encountering failure of the designed parts. Consequently, the related specifications are as follows:

- The maximum weight of the prosthesis may not exceed 3 kg.
- The maximum volume of the foot (up to the ankle) may not exceed the following dimensions: 300mm x 100mm x 80mm (length x width x height). For the lower leg, the minimum required volume allowing the Lever arms to rotate is considered.

In order to meet the above-mentioned requirements the designed parts should be as light and compact as possible. On the other hand, the parts should be able to carry various dynamic loads. In the following section, the design procedure shown in Fig. 75 is described.

Initial Design Phase

A simple part is drawn, considering the function, weight, and volume, followed by a material choice.

After having determined the loads acting on the different parts, a manual basic static stress analysis is carried out to have an idea of the magnitude order of the occurring stresses and safety factors. Furthermore, a stress analysis based on a Finite Element Method is carried out

in Inventor 2008. Both results are compared as a validation for the FEM results. If the results are acceptable, the *Accurate Design* phase is initiated.

Accurate Design Phase

In this phase, the part is further modified in order to achieve lower weight or lower stresses. This can be achieved by removing excessive material at low stress places or adding material to high stress places.

In the *Accurate Design Phase*, the stress analysis is more thorough as the previous one as both static and dynamic stresses are examined. If the final occurring stresses are acceptable, the part is finished and can be considered as a *Final Part Design*. If that is not the case, the part is sent back to the *Accurate Design* phase. Notice that a minimum total safety factor of 1,5 is required for final approval. The total safety factor is the static safety factor multiplied with a fatigue factor. This will be elaborated further on during the first dynamic stress analysis.

Final Part Design Phase

In this phase, all final parts are weighed and assembled. If the total weight and volume meet the desired values, the assembly continues to the next and final phase: *Final Assembly Design* phase. If the total weight or volume is exceeded, the parts return to the *Accurate Design* phase.

Final Assembly Design Phase

This is the last phase of the design process. In this phase, the assembly meets all the desired requirements.

3.4.2. Part Design

First, an identification of all the major parts is made:

- S-Lever arm
- C-Lever arm
- Nut support
- Rod
- Ankle Support
- Foot-Sole
- Leg Box
- Ankle Shaft

The bearings and bolts were designed in Inventor's Design Accelerator. The calculation of these components are carried out in Inventor *Design Accelerator* is. The formulas used in this calculation are displayed in Appendix J.

In order to perform a stress analysis, all the acting loads have to be determined. The default material choice of the Initial design phase is AlMgSi1. Table 28 states the material data of AlMgSi1.

Table 28: Material data of AlMgSi1 [http://www.dejond.com/]

E-modulus	70 000 Mpa
G	26 000 Mpa
Density	2,71e-006 kg/mm ³
Yield Strength	260 Mpa
Ultimate Strength	310 Mpa

In the following paragraph, the design process and stress analysis of the different parts are discussed. A complete elaboration of the stress analysis will be performed for the S-Lever Arm, the C-Lever arm and the Ankle Shaft. The complete elaboration of the other parts can be found in Appendix J.

The S-Lever arm

Initial Design

The S-Lever arm is attached to the S-Spring and to the Ankle Shaft (fixed constraint, not beared). The S-Lever arm is driven by the C-Lever arm through a pin. A basic initial design has been made in order to perform a manual stress analysis. This is shown in Fig. 76.

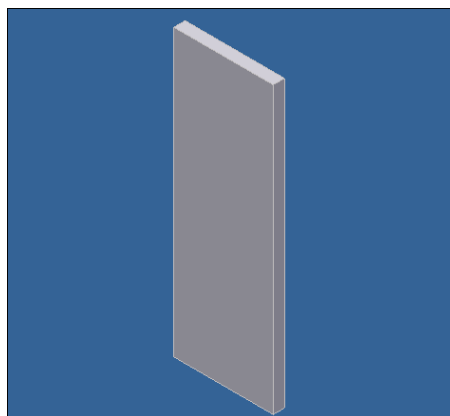


Fig. 76: The Initial Design of the S-Lever arm

The depth and width of the beam are chosen arbitrary, 4mm and 35mm respectively, the height was set at 100 mm, which is determined in the model simulations.

Acting Loads

There are 2 loads acting on the S-Lever arm:

1. $F_{S-Spring}$: The load on the upper part of the S-Lever arm caused by the spring (which will be divided in 2 loads, a horizontal and a vertical component)
2. F_{pin} : The load caused by the pin of the C-Lever arm on the upper middle part of the S-Lever arm

Notice that before Pin-Contact, which occurs at approximately 45% of stride, only $F_{S-Spring}$ is carried by the S-Lever arm. Therefore, two loading situations will be simulated. In the first situation, both $F_{S-Spring}$ and F_{pin} will be carried by the S-Lever arm (after Pin-Contact) and in the second situation, only $F_{S-Spring}$ is carried by the S-Lever arm (before Pin-Contact).

F_{pin} is acting in the opposite direction of $F_{S-Spring}$ and causes a zero resulting moment at the base of the S-Lever arm (fixed to the Ankle Shaft). The pin of the C-Lever arm is set on 65mm of the constraint.

Throughout stance, the occurring loads vary in direction and magnitude. In order to avoid material failure, the maximal loads have to be simulated in the static stress analysis. The spring load acting on the S-Lever arm is shown in Fig. 77. The load is projected on the length axis of the S-Lever arm and perpendicular to that axis. The variation of these values is dependent on the ankle angle (θ) and the C-Lever arm angle (α) and evidently to the spring characteristics (stiffness and pre-tension).

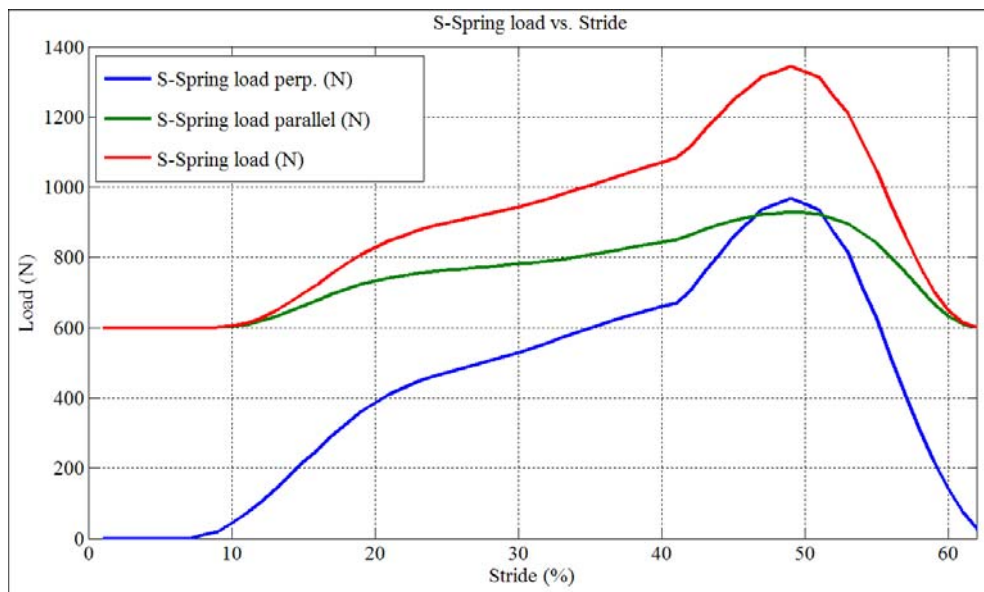


Fig. 77: The spring load acting on the S-Lever arm during stance. The force is projected on the length axis of the Lever arm (S-Spring force parallel; green) and perpendicular to that axis (S-Spring force perp.;blue).

Notice that the maximum load of both projections, $F_{S-Spring\ parallel}$ and $F_{S-Spring\ perp.}$, occurs at Heel-Off (50-60% of stride) and has a value of approximately 1000N. The second load, F_{pin} , can be found with a momentum equilibrium equation.

$$F_{pin} = 1000\text{ N} * 100\text{mm}/65\text{mm} = 1538,46\text{ N} \tag{Eqn. 16}$$

Also notice that both $F_{S-Spring\ parallel}$ and $F_{S-Spring\ perp.}$ equals approximately 900N at 45% of stride.

Loading situation 1 (after Pin-Contact)

Manual Static Stress Analysis

The basic static stress analysis has first been performed *manually* with the basic formulas of materials science, then in ISSD. ISSD is a software program that is developed at VUB MeMC and is not based on a Finite Element Method, but performs calculations on basic structure such as beams, using the ‘thin beam theory’. Regarding the fact that the *manual* results were the same as the ISSD results, ISSD will be used to perform further manual stress analysis. Fig. 78 illustrates the stresses and deformation due to the acting loads.

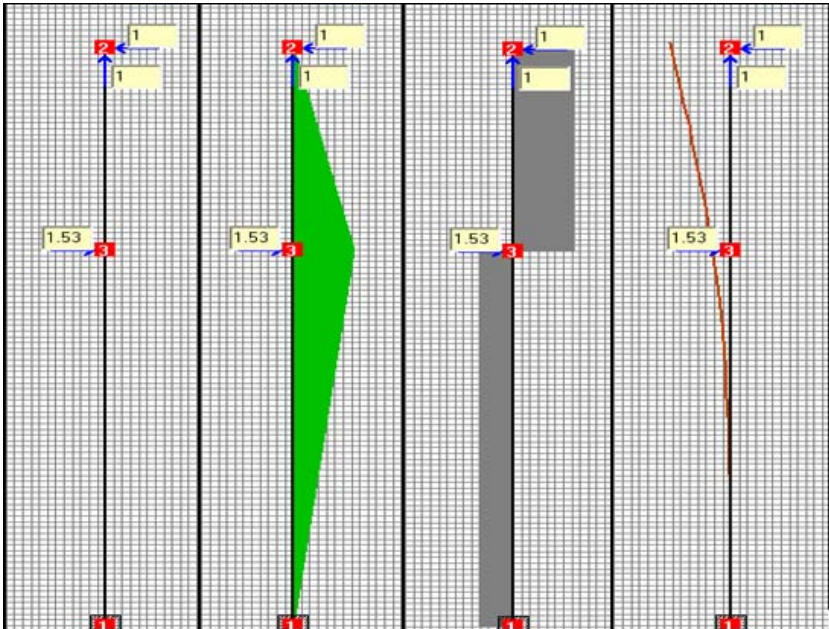


Fig. 78: Static stress analysis on S-Lever arm for loading situation 1: the acting loads on the beam in kN (left), the stress due to bending (midleft), the shear stress (midright) and the deflection shape (right).

Table 29 indicates the maximum values of the various stresses, deformation performed in ISSD and the geometry of the beam.

Table 29: S-Lever arm characteristics, maximum stresses and deformation for loading situation 1

S-Lever arm characteristics	
dimensions (mm) (h x w x d)	100 x 35 x 4
inertia (mm ⁴)	14292
E- modulus (Mpa)	70 000
STRESS <i>Mpa</i>	
normal stress on node 3 (σ_n)	
<i>due to bending</i>	42,86
<i>due to normal force</i>	7,14
shear stress (τ)	
<i>node 2 - node 3</i>	7,14
<i>node 3 - node 1</i>	3,85
DEFORMATION <i>mm</i>	
<i>node 2</i>	0,08

The Von-Mises or equivalent stress can be calculated with following equation:

$$\sigma_{\text{equiv}} = \sqrt{(\sigma_n^2 + 3 \cdot \tau^2)} \quad \text{Eqtn. 17}$$

resulting in a value of 51,5 Mpa. As the yield strength (σ_{yield}) of AlMgSi1 is 260 Mpa, the static safety factor k can be calculated with the Von Mises criterium : $\sigma_{\text{equiv}} \cdot k < \sigma_{\text{yield}}$.

The minimum static safety factor is 5. These results will be compared to a FEM stress Analysis.

FEM Static Stress Analysis

Prior to running the analysis, the part has to be meshed. Inventor 2008 offers the user a mesh relevance starting from -100 to +100. As a reference, a setting of -100 produces a coarse mesh, fast solutions and results that may include significant uncertainty. The system automatically selects an appropriate mesh type depending on the model subtype.

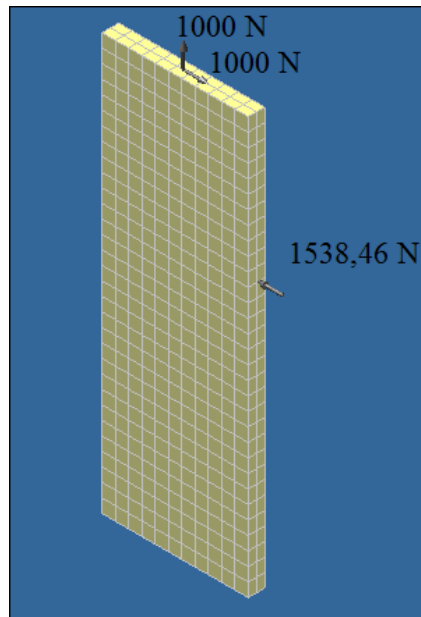


Fig. 79 : applied loads on the meshed S-Lever arm for loading situation 1

A setting of +100 generates a fine mesh, longer solution times, and the least uncertainty in the results. The default relevance setting is zero. In order to obtain the most accurate results, the finest mesh was always applied for all analysis. Fig. 79 shows the forces applied on the meshed part. The constraint is set at the base of the Lever arm.

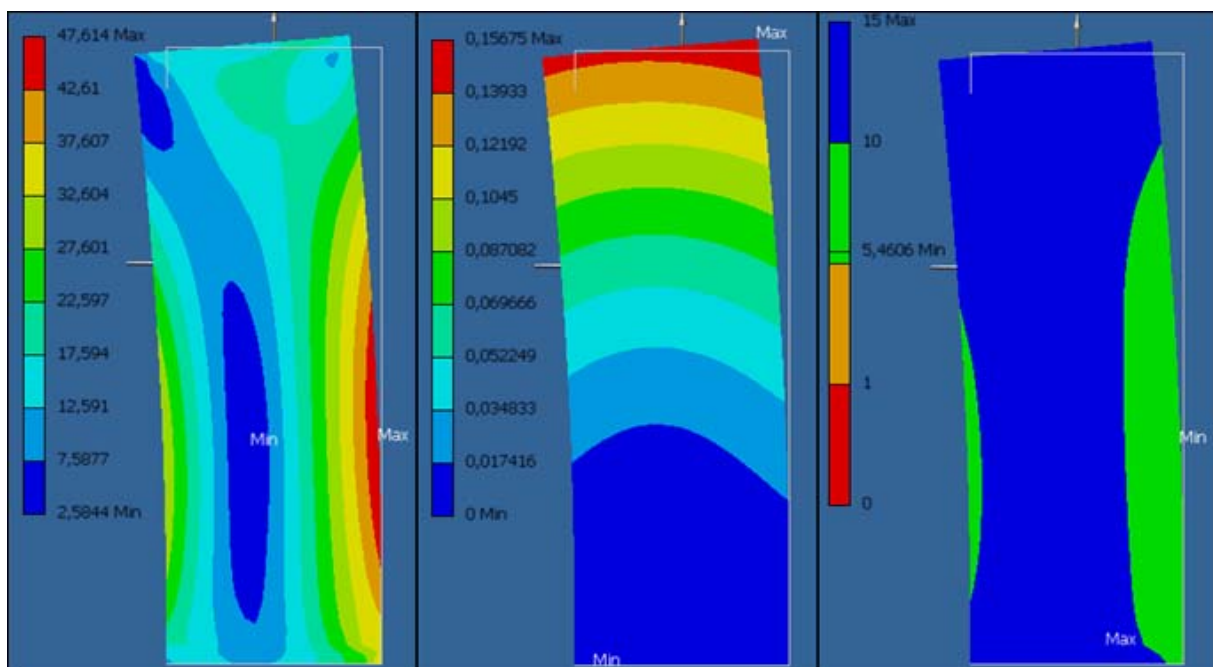


Fig. 80: FEM Static Stress Analysis for loading situation 1: the equivalent (Von Mises) stress (left) in Mpa, the deformation (middle) in mm and the safety factor (right)

Fig. 80 shows the static stress analysis performed in Inventor 2008. The equivalent or Von Mises stress is shown in the left figure (in Mpa), the deformation is shown in the middle figure (in mm), and the safety factor is shown in the right figure. The *Equivalent Stress theory*

states that failure occurs when the energy of distortion reaches the same energy for yield/failure in uni-axial tension. Equivalent stress can be used to obtain a reasonable estimation of fatigue failure, especially in cases of repeated tensile and tensile-shear loading. The equivalent stress results use colour contours to displays the stresses calculated during the solution for the model. The deformed model is displayed. The colour contours correspond with the values defined by the colour bar.

The deformation results show the deformed shape of the model after running the simulation. The safety factor is the ratio of the yield stress to the maximum equivalent stress (Von Mises criterion). The safety factor shows the areas of the model that are more likely to fail under load. Table 30 points out the results of the analysis.

Table 30: Results of the FEM Static Stress analysis for loading situation 1

max equivalent stress (Mpa)	47,61
max deformation (mm)	0,156
minimum safety factor	5,46

These results show that there is a 7,5 % difference with the stress calculated with ISSD and a 48% difference with the deformation calculated with ISSD. Also notice the difference between the course of stress along the length axis of the S-Lever arm and the one calculated using ISSD. However, the reason of this difference is rather normal. In ISSD, the ‘thin beam theory’ is used. This theory relies on *Saint-Venant's principle*, which states that the stresses remote from the point of application of the load (comparing to the part’s dimensions) are not affected by the local stresses due to the fixed constraint. This explains why no stresses due to bending occur at the constraint in ISSD. In Inventor, the thin beam theory is not applied, but a Finite Element Method is used. Local stresses at the constraint will affect the course of stress along the length axis of the S-Lever arm, resulting in a maximum stress occurring closer to the constraint as expected.

The Inventor results can be used for more complex parts, as this stress difference is acceptable.

Loading situation 2 (before Pin-Contact)

Manual Static Stress Analysis

Fig. 81 and Table 31 show the results of the analysis.

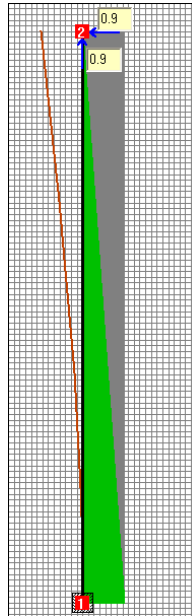


Fig. 81: Static stress analysis on S-Lever arm for loading situation 2: the acting loads on the beam in kN, the stress due to bending (green), the shear stress (grey) and the deflection shape (red).

Table 31: maximum stresses and deformation on the S-Lever arm for loading situation 2

STRESS		Mpa
normal stress @ node 1		
<i>due to bending</i>		110,2
<i>due to normal force</i>		6,43
shear stress		
<i>node 1 - node 2</i>		6,43
equivalent stress		117,1
DEFORMATION		mm
<i>node 2</i>		0,3

Notice that the stress occurring in loading situation 2 is approximately twice as high. These results are compared to a FEM static stress analysis.

FEM Static Stress Analysis

Fig. 82 and Table 30 illustrate the FEM static stress analysis by showing the equivalent stress, the deformation, and the safety factor.

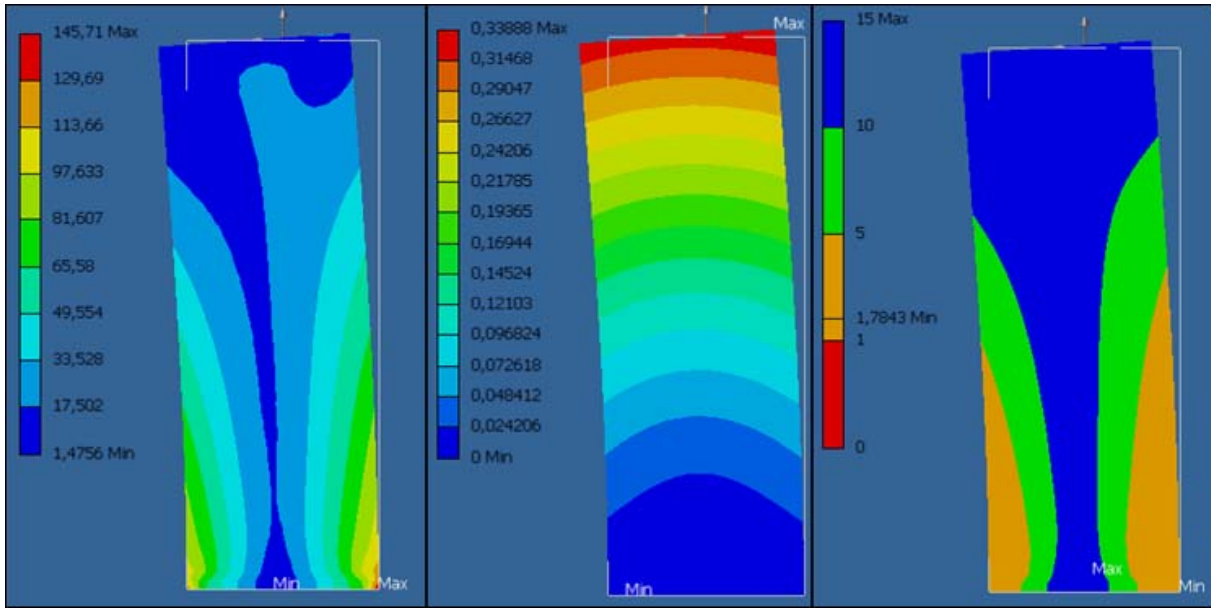


Fig. 82: FEM Static Stress Analysis for loading situation 2: the equivalent (Von Mises) stress (left) in Mpa, the deformation (middle) in mm and the safety factor (right)

Table 32: Results of the FEM static stress analysis for loading situation 2

max equivalent stress (Mpa)	145,71
max deformation (mm)	0,34
minimum safety factor	1,78

The difference in the stress and the deformation results for both calculation methods equals 19 % and 11 %, respectively, which is still acceptable.

The part can move on to the *Accurate Design Phase*, where both loading situations will be simulated.

Accurate Design

FEM Static Stress Analysis

Loading situation 1

Fig. 83 shows the accurate design of the S-Lever arm. Material has been removed at the bottom of the Lever arm and the area of pin contact and the constraint is reinforced with extra material.

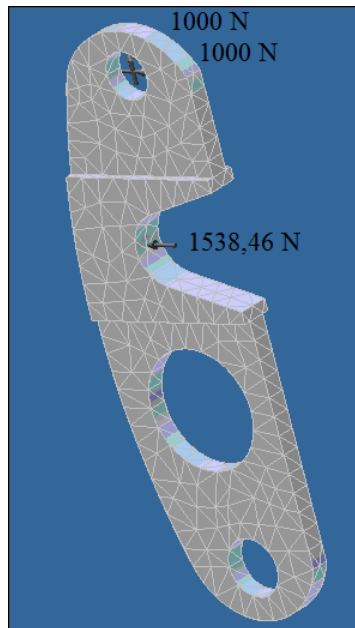


Fig. 83: applied loads (loading situation 1) on the accurate design of the S-Lever arm (meshed)

The same stress analysis is performed on the accurate part.

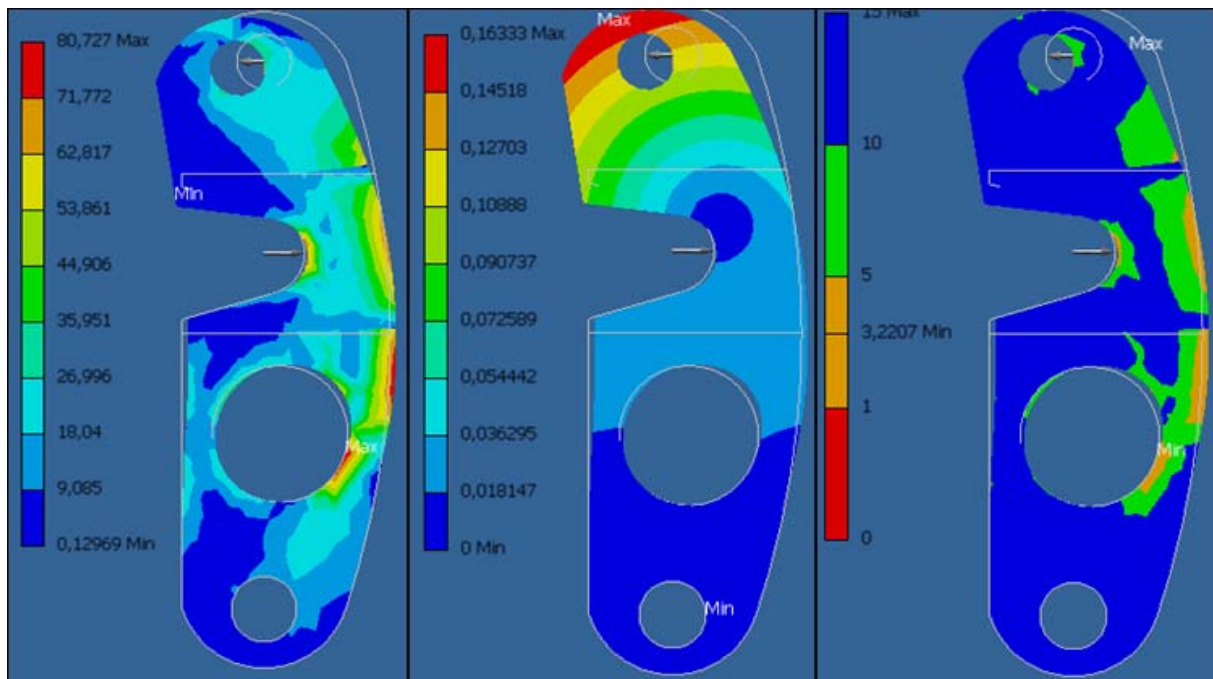


Fig. 84: Static stress analysis of the accurate design of the S-Lever arm for loading situation 1. The equivalent stress in Mpa (left), the deformation in mm (middle) and the static safety factor (right)

Loading situation 2

The accurate design had to be modified to carry the load of the second loading situation. The part has been reinforced at certain areas. Fig. 85 shows the FEM analysis of the modified accurate design for the second loading situation.

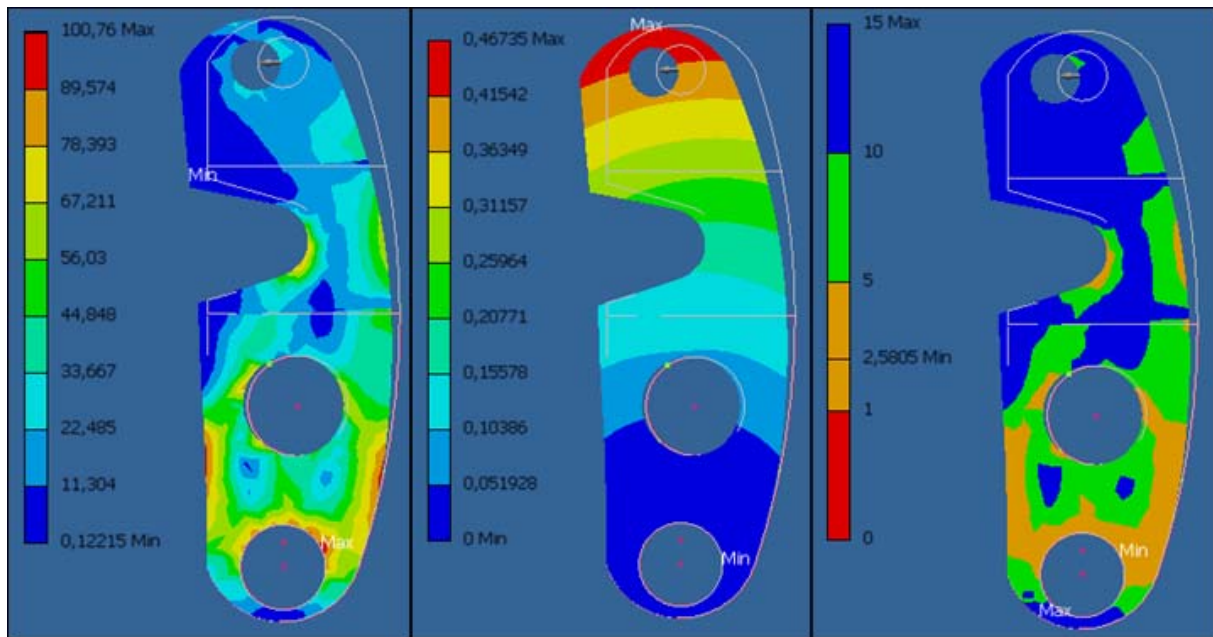


Fig. 85: Static stress analysis of the accurate design of the S-Lever arm for loading situation 2. The equivalent stress in Mpa (left), the deformation in mm (middle) and the static safety factor (right)

The FEM results for both loading situations are summarised in Table 33.

Table 33: Results of FEM static stress analysis for both loading situations

	loading situation 1	loading situation 2
max equivalent stress (Mpa)	80,73	100,76
max deformation (mm)	0,163	0,47
minimum safety factor	3,22	2,58

Notice that the second loading situation has a smaller static safety factor. The modified accurate design will be used for further analysis. The part weighs 46g.

Dynamic stress analysis

All the loads applied on all the parts of the prosthesis are purely swelling. Using the yield strength to calculate the safety factor is therefore insufficient. For dynamic loads, the *Endurance Limit* stress or $\sigma_{r\infty}$ has to be used. This endurance limit stress is the stress that can be applied to the part for an indefinite number of cycles without causing material failure. The Wöhler-curve in Fig. 86 illustrates this.

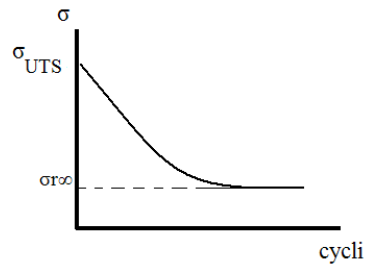


Fig. 86: Wöhler-curve: stress vs. load cycli: The Endurance Limit stress or is the stress that can be applied for an infinite number of cycles without causing material failure.[20]

This endurance limit is dependent on the ultimate strength and the loading condition (bending $\sigma_{b\infty}$, axial $\sigma_{a\infty}$ or torsion $\sigma_{t\infty}$). Table 34 illustrates the endurance limit for all the used materials and for different loading conditions.

Table 34: Endurance limit for different materials and different loading conditions [20]

	AlMgSi1	Steel HSLA	S Steel C 440	Steel 30CrNiMo8
Yield Strength (Mpa)	260	275,8	689	1050
Ultimate strength (Mpa)	310	448	861	1250
Endurance Limit (Mpa)				
Bending	232,5	336	645,75	935
bending fatigue factor	0,89	-	0,94	0,89
Axial	216	312	601	800
axial fatigue factor	0,83	-	0,87	0,76
Torsion	154	222	427	635
torsion fatigue factor	0,59	0,81	0,62	0,60

The bending, axial and torsion fatigue factor is obtained by dividing the endurance limit with the respective yield strength. This factor has to be multiplied with the static safety factor, resulting in a total safety factor for each part. Notice that if this endurance limit is higher than the yield strength, the total safety factor equals the static safety factor.

The loading condition for the S-Lever arm (AlMgSi1) is *bending*, *axial* and *torsion*. As the FEM stress analysis only generates an equivalent stress, the smallest fatigue factor will be used to ensure acceptable safety.

$$S_{\text{total}} = S_{\text{static}} \times \text{axial fatigue factor} = 2,58 \times 0,59 = 1,52$$

The part can move on to the *Final Part Design Phase*, as the total safety factor, the deformation, the weight and design are acceptable.

The C-Lever arm

Initial Design

An initial design has been made and is illustrated in Fig. 87.

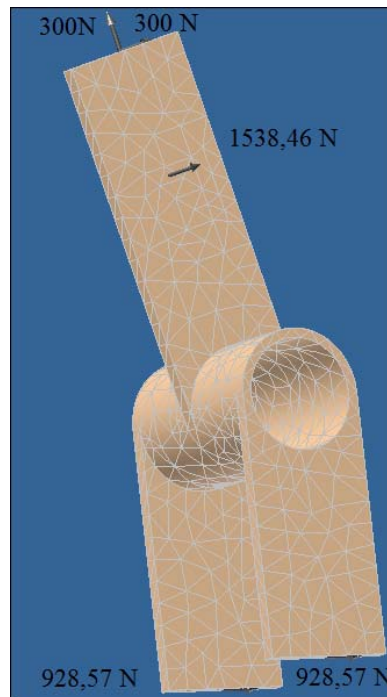


Fig. 87: applied loads on the Initial design of the meshed C-Lever arm

Only the length of the Lever arms (upper and lower side) is set in the model simulations (100mm and 70mm respectively). The other dimensions are set arbitrary. The upper part is connected to the spring. The cylinder of the Lever arm is beared on the Ankle Shaft and both lower parts are connected via rods to the nut of the ball screw. As discussed earlier, the C-Lever arm drives the S-Lever arm through a pin that is not shown in the initial design.

Acting Loads

There are four maximum loads acting on the C-Lever arm

1. F1: The load on the upper part of the C-Lever arm caused by the C-Spring (which will be divided in 2 forces, a horizontal and a vertical component)
2. F2: the load caused by the S-Lever arm on the pin of the C-Lever arm
3. F3: the load caused by the pin of the nut on the left lower part of the Lever arm
4. F4: the load caused by the pin of the nut screw on the right lower part of the Lever arm

The variation of the force acting on the upper part of C-Lever arm is shown in Fig. 88. The force is projected on the length axis of the Lever arm and perpendicular to that axis. The variation of these values is dependent of the Leg Box angle (θ) and the C-Lever arm angle (α).

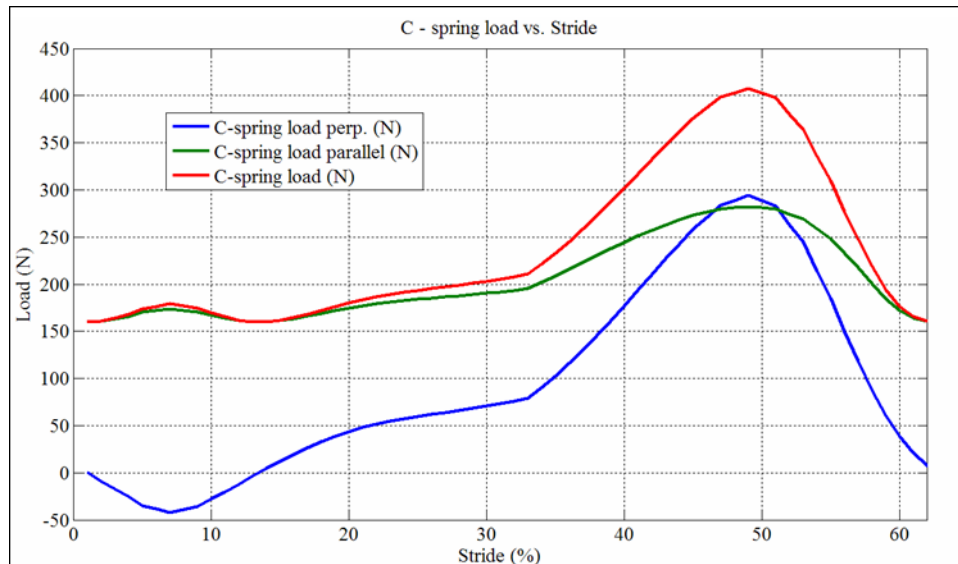


Fig. 88: the spring force acting on the upper part of the C-Lever arm. The force is projected on the length axis of the Lever arm and perpendicular to that axis.

F1, both perpendicular and parallel, has a maximum value of approximately 300N, which occurs at Heel-Off.

F2 is already calculated during the analysis of the S-Lever arm, which is 1538,46 N.

F3 and F4 are calculated in the same way F2 was calculated, by imposing a zero resulting moment at the bearing.

$$F1 * 100\text{mm} + F2 * 65\text{mm} = (F3 + F4) * 70 \text{ mm} \quad \text{Eqtn. 18}$$

Thus, $(F3 + F4) = 1857 \text{ N}$ and due to the symmetry in the geometry, $F3 = F4 = 928,57 \text{ N}$.

Now that the loads have been identified, a stress analysis can be performed.

Manual Static Stress Analysis

The same calculations for the manual stress analysis of the S-Lever arm in ISSD have been performed for the C-Lever arm. The model can be simplified into three beams and one hollow cylinder.

Beam 1 represents the upper part of the C-Lever arm. Beam 2 and 3 represent the lower parts of the C-Lever arm.

Table 35: The characteristics of the beams 1 (upper Lever arm), 2 and 3 (lower Lever arms) and the hollow cylinder

BEAMS	dimensions (h x w x d) (mm)	Inertia I (mm ⁴)
Beam 1	100 x 40 x 4	14291,66
Beam 2	70 x 35 x 3,5	12565,21
Beam 3	70 x 35 x 3,5	12565,21
CYLINDERS	dimensions (d _i , d _o) (mm)	polar inertia J _p (mm ⁴)
cylinder1	30,35	33900,9

Fig. 89 and Fig. 90 show the static stress analysis results of beam 1, 2 (3) of ISSD.

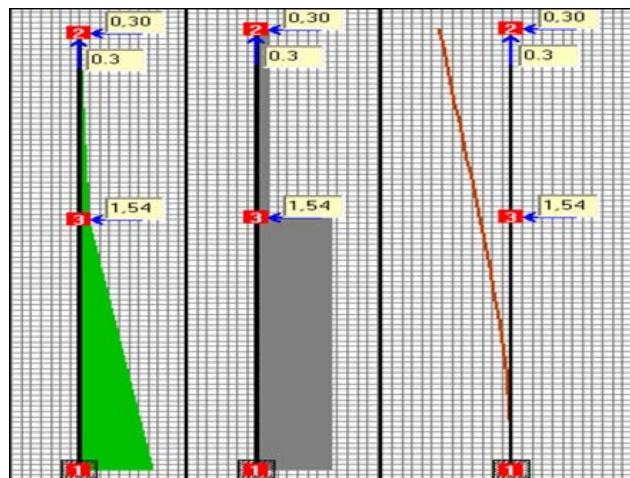


Fig. 89: Static stress analysis on beam 1: the Acting Loads on the beam in kN causing the stress due to bending (left), the shear stress (middle) and the deflection shape (right).

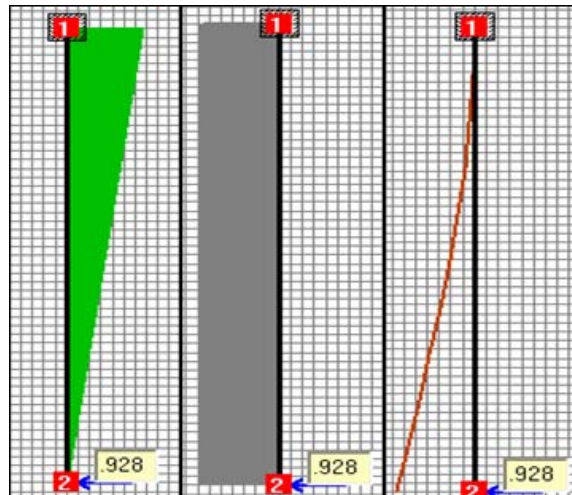


Fig. 90: Static stress analysis on beam 2 (and 3): the Acting Loads on the beam in kN causing the stress due to bending (left), the shear stress (middle) and the deflection shape (right).

Table 37 shows the results of stresses and deformation for the different parts of the C-Lever arm in ISSD. Due to high stresses and complex manufacturing, a Steel Alloy (High Strength Low Alloy) is used.

Table 36 states the material data of Steel HSLA.

Table 36: Material data of Steel HSLA

E-modulus	210 000 Mpa
G	81 000 Mpa
Density	7,84 e-006 kg/mm ³
Yield Strength	275,8 Mpa
Ultimate Strength	448 Mpa

These are the results from the static analysis with ISSD:

Table 37: Stress and deformation results for beam 1, 2, 3 of the initial design of the C-Lever arm

	Beam 1	Beam 2/ Beam 3
STRESS	Mpa	Mpa
max normal stress (σ_n)		
<i>due to bending</i>	159,18	90,9
<i>due to normal force</i>	7,14	0
max shear stress (τ)		
<i>node 2 - node 3</i>	2,14	
<i>node 3 - node 1</i>	13,13	7,57
max equivalent stress	167,87	91,84
DEFORMATION	mm	mm
<i>node 2</i>	0,118	0,04

The moments acting on the hollow cylinder are shown in Fig. 91.

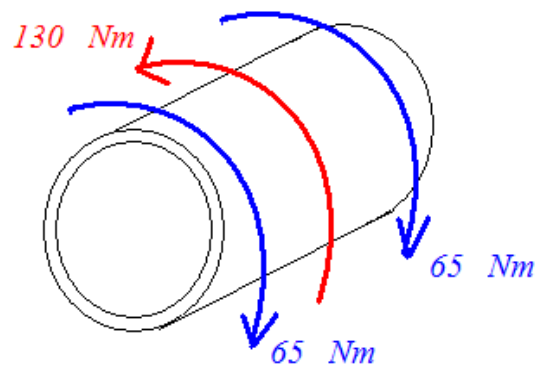


Fig. 91: Moments acting on the hollow cylinder

The stress due to torsion can be calculated with following formula:

$$\tau = G \cdot \gamma = \frac{M \cdot r}{J_p}$$

Eqtn. 19

With $M = 130 \text{ Nm}$, $r = 16,25 \text{ mm}$, $G = 26\,000 \text{ Mpa}$ and J_p is shown in Table 35.

The maximum stress due to torsion is $\tau = 62 \text{ Mpa}$. These results will be compared to the results of a FEM stress analysis.

FEM Static Stress Analysis

Fig. 92 shows the FEM static stress analysis performed on the initial design of the C-Lever arm.

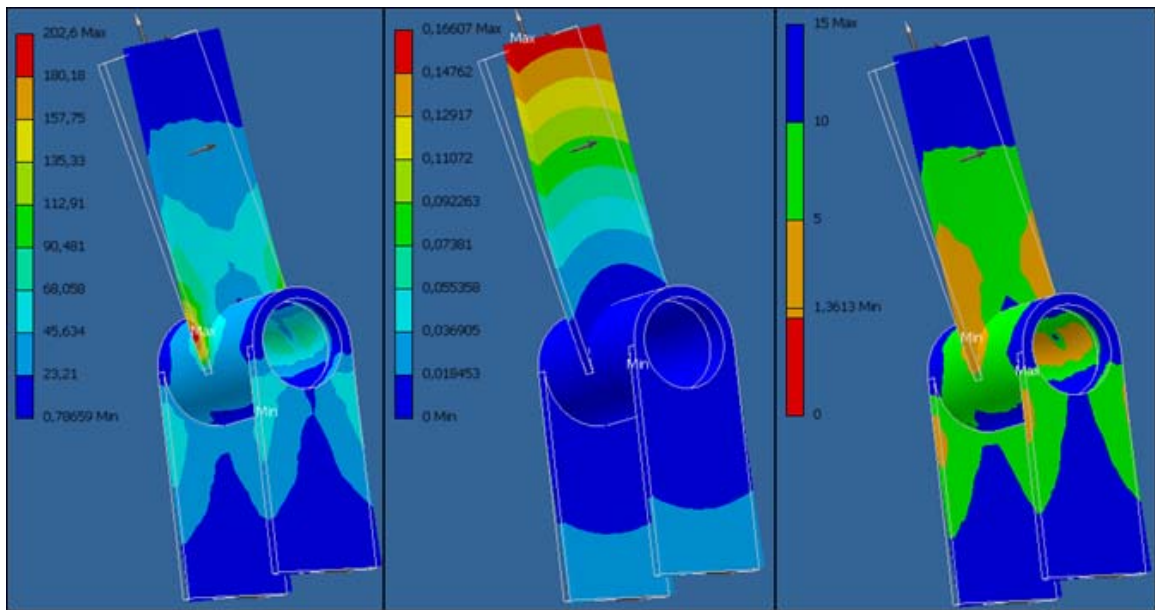


Fig. 92: Static stress analysis of the initial design of the C-Lever arm. The equivalent stress in Mpa (left), the deformation in mm (middle) and the safety factor (right)

Table 38: Results of the FEM static stress analysis of the C-Lever arm

max equivalent stress (Mpa)	202,6
max deformation (mm)	0,166
minimum safety factor	1,36
max stress in beam 1 (Mpa)	202,6
max stress in beam 2/3 (Mpa)	~ 65
mean stress in cilinder (Mpa)	~ 70
max deformation in beam 1 (mm)	0,166
max deformation in beam 2/3 (mm)	~ 0,035

Notice that the resulting stresses and deformations shown in Table 38 have a minimum difference of 17 % and 29%, respectively, in comparison with the values in Table 37.

As this stress difference is acceptable regarding the difference in calculation method, the Inventor results can be used to evaluate a more complex part. Notice that the static safety

factor is too low in comparison with the 1,5 desired value. The part will be refined and material will be added to high stress areas in order to increase the safety factor.

Accurate Design

Fig. 93 shows the accurate design of the C-Lever arm. Material removal and reinforcement has been applied on several places.

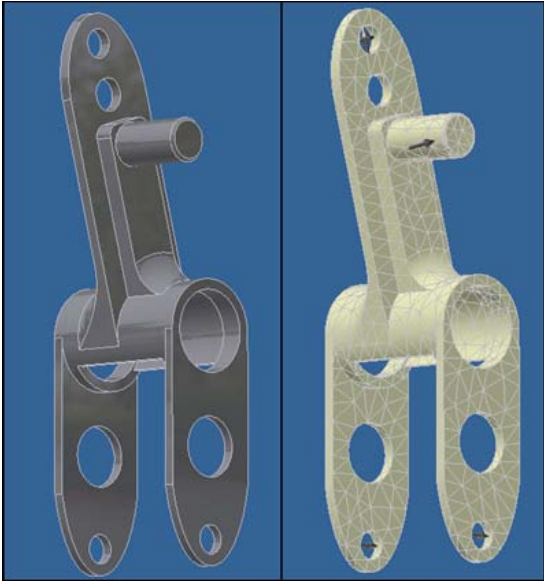


Fig. 93: An accurate design of the C-Lever arm

FEM Static Stress Analysis

The same analysis is performed on the accurate part.

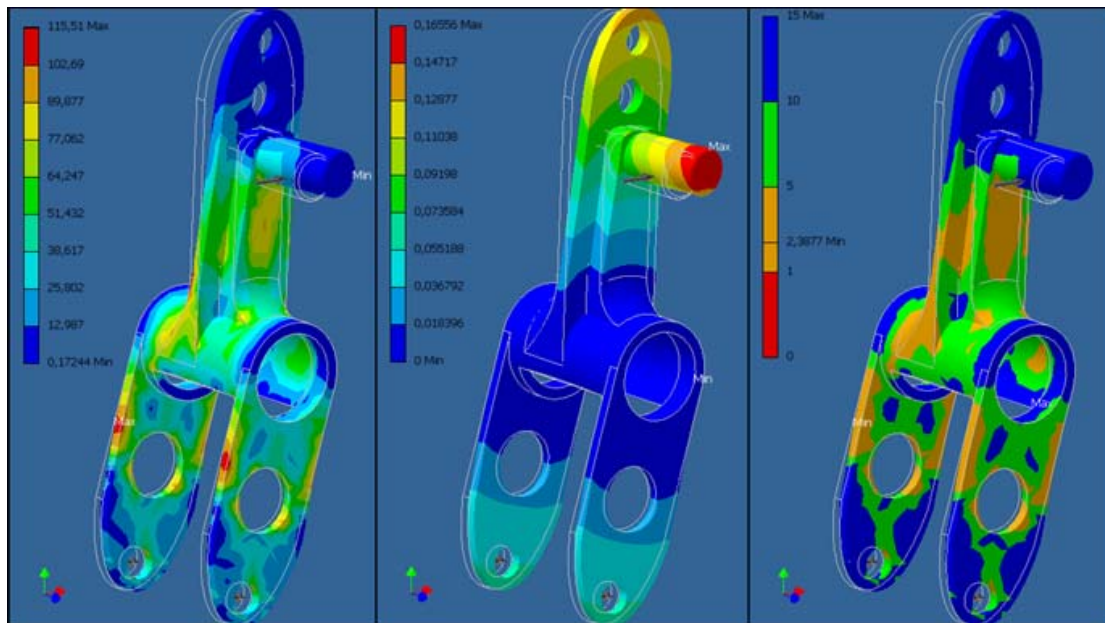


Fig. 94: Static stress analysis of the accurate design of the C-Lever arm. The equivalent stress in Mpa (left), the deformation in mm (middle) and the safety factor (right)

The same stress evolution of the basic part is recognised in the accurate part with a maximum stress of 115,51 Mpa, a maximum deformation of 0,166 mm at the pin and a minimum safety factor of 2,38. The part weighs 390g.

As the weight of this part is too high, the accurate design is modified. In this modification, stainless steel, 440 C is used as material and the Lever arms are thinner. This material has much higher yield strength. The characteristics for this material are shown in Table 39.

Table 39: Material data of Stainless Steel 440C

E-modulus	206 700 Mpa
G	80 000 Mpa
Density	7,75e-006 kg/mm ³
Yield Strength	689 Mpa
Ultimate Strength	861,250 Mpa

A FEM static stress analysis is performed on the modified part. The results are shown in Fig. 95.

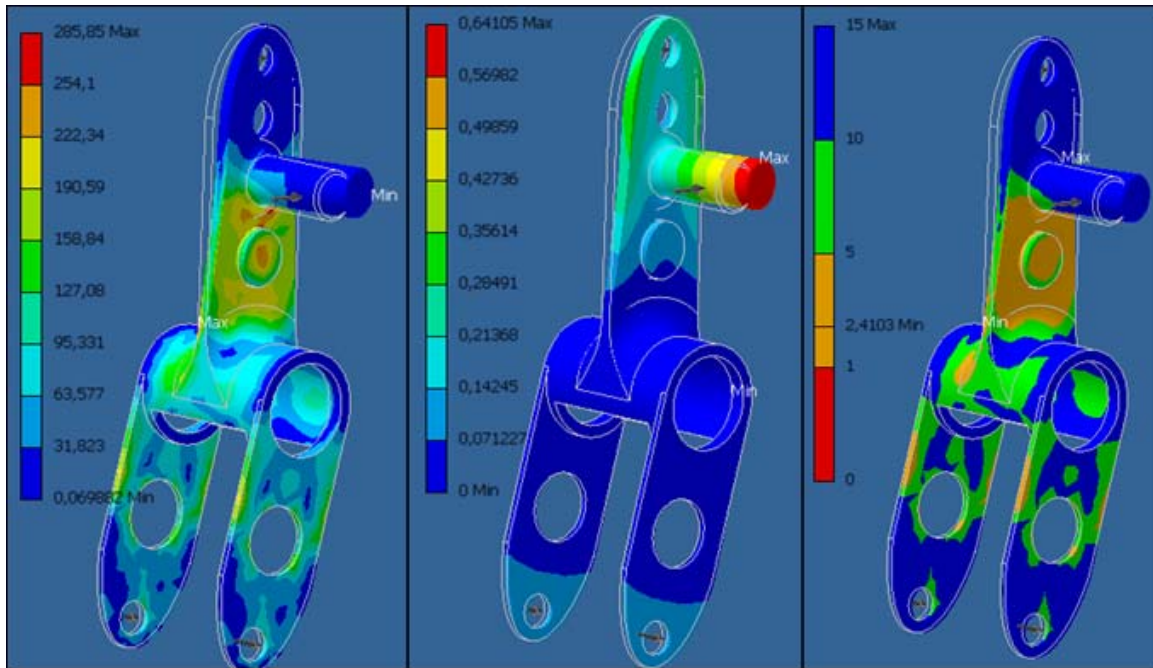


Fig. 95: Static stress analysis of the modified accurate design of the C-Lever arm. The Equivalent stress in Mpa (left), the Deformation in mm (middle) and the safety factor (right)

The same stress evolution is recognised in the modified accurate part with a maximum stress of 285,85 Mpa, a maximum deformation of 0,64 mm at the pin and a minimum static safety factor of 2,4. The part weighs 268g.

Dynamic stress analysis

The loading condition is axial, bending and torsion. According to Table 34, the torsion fatigue factor for the C-Lever arm (SS C440) is 0,62. The total safety factor is

$$S_{\text{total}} = S_{\text{static}} \times \text{torsion fatigue factor} = 2,4 \times 0,62 = 1,5$$

The part can move on to the *Final Part Design phase*, as the total safety factor, the deformation, the weight and the design are acceptable.

The nut support

The nut support is screwed on the nut and has a pin on each side. These pins are connected to the rods, which are connected to the lower part of the C-Lever arm. The accurate design is already shown in Fig. 96, as this is a simple part. The chosen material is Steel HSLA.

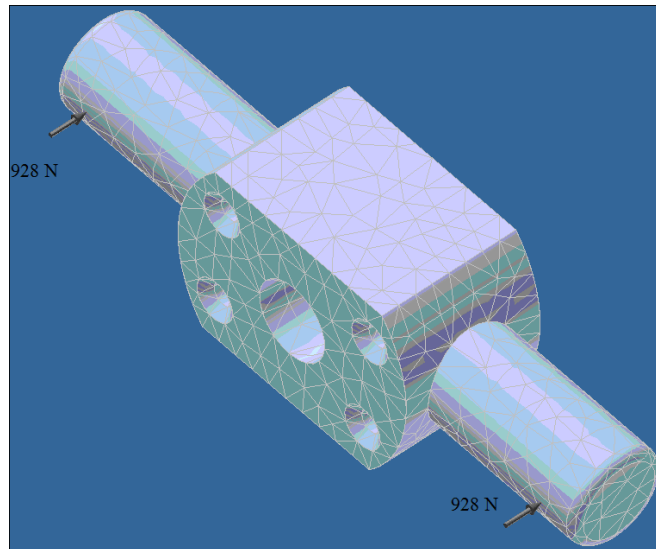


Fig. 96: Accurate design of the Nut Support and the forces acting on the meshed part

Acting Loads

The same loads acting (928N) on the lower C-Lever arm are acting on both pins of the Nut support.

Only the results of this part will be discussed. A detailed calculation of the analysis can be found in Appendix J.

Static stress analysis results

max equivalent stress (Mpa)	143
max deformation (mm)	0,01
minimum safety factor	1,93

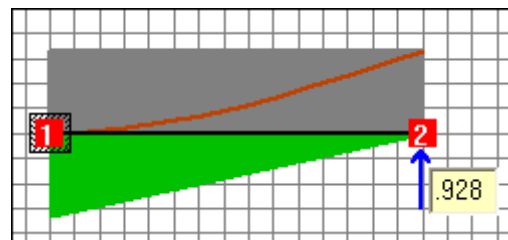


Fig. 97: Results of the ISSD static stress analysis of a loaded pin of the Nut support

max equivalent stress (Mpa)	68
max deformation (mm)	0,016
minimum safety factor	4

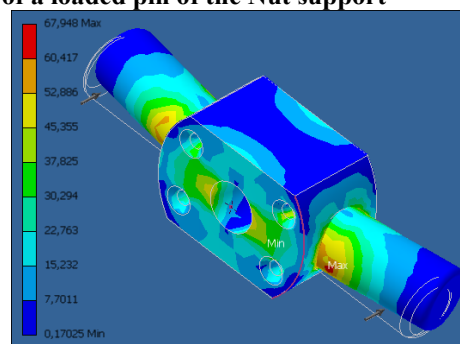


Fig. 98: FEM static stress analysis of Nut support: results

Notice that a fixed constraint at the base of the pin was used to calculate the stress with ISSD. In Inventor however, the threaded hole was constrained. This allows deformation of the

middle part, which reduces the stress at the pin constraint in the FEM analysis. The part weighs 72 g.

Dynamic stress analysis

The loading condition is *bending*. According to Table 34, the bending fatigue factor for the nut support (Steel HSLA) exceeds 1. The total safety factor is

$$S_{\text{total}} = S_{\text{static}} = 4$$

The part can move on to the *Final Part Design Phase*, as the total safety factor, the deformation, the weight and the design are acceptable.

The Rods

The rod is the connection between the C-Lever arm and the Nut support.

Fig. 99 shows a preview of a part of the assembly to give better insights in the function of the rod.

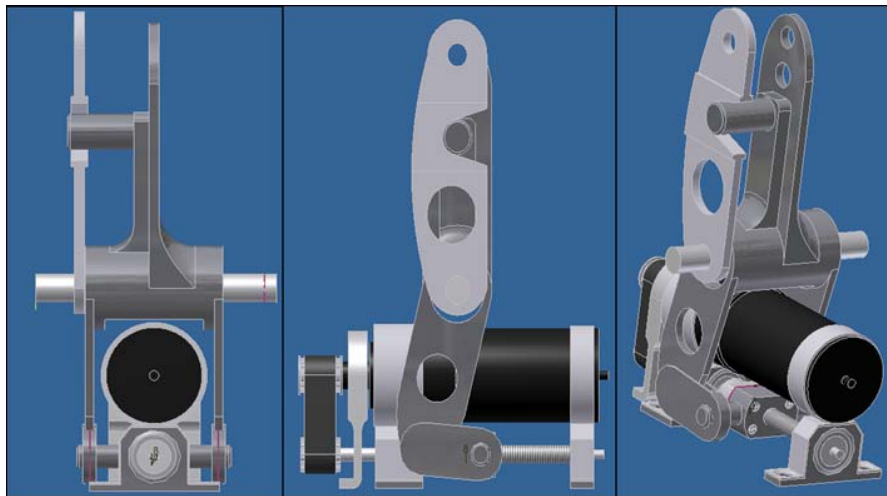


Fig. 99: Assembly of the C- Lever arm, ball screw assembly and rods (front, side and isometric view)

The Accurate design of the rod is shown in Fig. 100. The rod is made of Steel HSLA to cope with the high stresses.

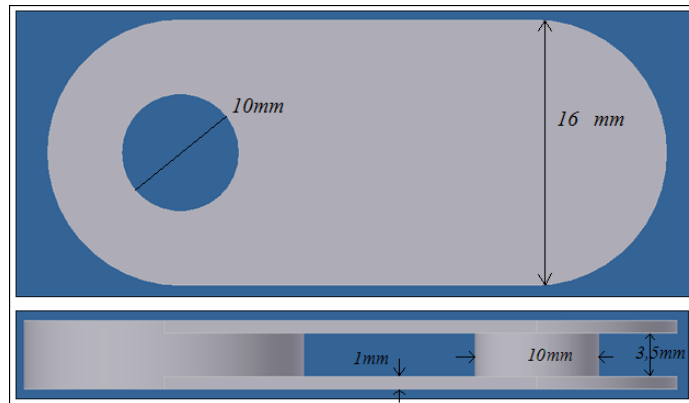


Fig. 100: Accurate design of rod (front and side)

Acting Loads

The same force that acted on the lower C-Lever arm will act on the rod (928N), as the rod is connected to the C-Lever arm (pin shown on right side of Fig. 100). Notice that this load acts on both sides of the rod. As it is difficult to achieve such loading condition in Inventor (a constraint has to be chosen, which would result in incorrect result), two situations will be simulated in Inventor. In one situation, the side plates are constraint and both pins are loaded. In the other situation, the pin is constraint and twice the load acts on the hole of the opposite side.

Static stress analysis results

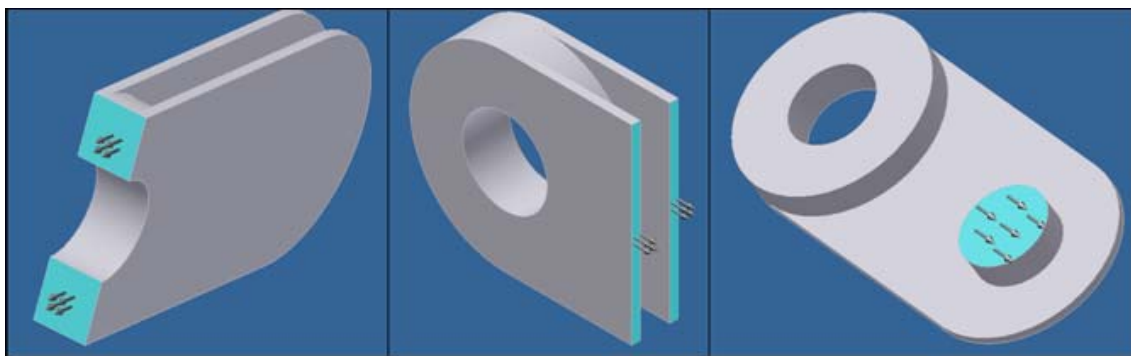


Fig. 101: Most critical zones of the rod: zones 1 (left), 2 (middle) and 3 (right)

Table 40: Results of Manual stress analysis

	zone 1	zone 2	zone 3
STRESS	Mpa	Mpa	Mpa
normal stress (Mpa)	56,24	58	-
shear stress (Mpa)	-	-	23,63

max equivalent stress (Mpa)	110,54
max deformation (mm)	0,035
minimum safety factor	2,74

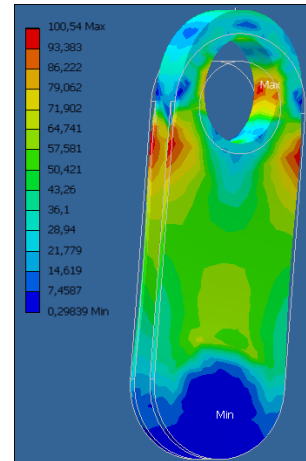


Fig. 102: FEM static stress analysis results

A more detailed analysis can be found in Appendix J.

Again, the simulated stresses are much higher than the calculated ones. That is because stress concentrations at the constraints are not incorporated in the manual stress analysis. The part weighs 15 g. Notice that the connection to the C-Lever arm is in practice achieved by an external pin. This pin is drawn as a part of the rod, as no stress analysis can be performed on an assembly.

Dynamic stress analysis

The loading condition is *axial*. According to Table 34, the axial fatigue factor for the rod (Steel HSLA) exceeds 1. The total safety factor is

$$S_{\text{total}} = S_{\text{static}} = 2,74$$

The part can move on to the *Final Part Design Phase*, as the total safety factor, the deformation, the weight and the design are acceptable.

Ankle Support

The Lever arms, ratchet, and Leg Box are connected to the Ankle Shaft, which is beared on the Ankle Supports. These supports have to carry the bodyweight load, the load of the pawl and loads due to the Lever arms.

Acting Loads

1. The half of the load due to the body weight (two Ankle Supports), which has a value of 450N. ($75 \text{ kg} * 10 * 1,2 / 2$). The factor 1,2 will be explained further on when the loads acting on the Foot Plate will be discussed.
2. The half of the load due to the Lever arms, which is 650N. $((1000 \text{ N} + 300 \text{ N}) / 2)$
3. The load due to the pawl. As already discussed, the pawl should be able to prevent the Ankle Shaft from rotating. This load is transmitted to the Ankle Support (hole in the lower part of the Ankle Support) and is 1500 N ($90 \text{ Nm} / 60\text{mm}$ radius ratchet). Notice that this load occurs until 45% of stride. During this period, the maximum loads of the Lever arms are the following:

Table 41: Maximum loads of the Lever arms before 45% of stride

	S-Lever arm	C-Lever arm
spring load (N)	1100	320
perpendicular (N)	900	275
parallel (N)	900	275

Therefore, two loading situations will be simulated. In the stress analysis, only the results of the accurate design stress analysis will be discussed, the initial design calculations can be found in Appendix J. Notice that the first loading condition, without the pawl-load, is discussed, as this situation caused higher stresses.

Accurate Design

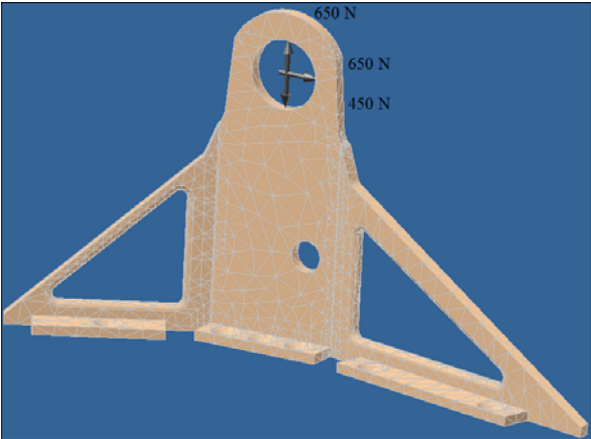


Fig. 103: Accurate design of the Ankle Support and the loads

Static Stress Analysis results

Table 42: Results of static stress analysis on the Accurate support Plate

	Beam 1/2	Beam 1/4	Beam 1/5	Beam 1/3
<i>section (mm²)</i>	29,7	14,2	160	160
STRESS	Mpa	Mpa	Mpa	Mpa
max normal stress				
<i>due to bending</i>	8,79	4,82	30,46	31,65
<i>due to normal force</i>	15,78	18,89	1,25	1,05
max shear stress	negl.	negl.	4,06	negl.
max equivalent stress	24,57	23,71	32,48	32,70
DEFORMATION	mm	mm	mm	mm
<i>node</i>			0,1	

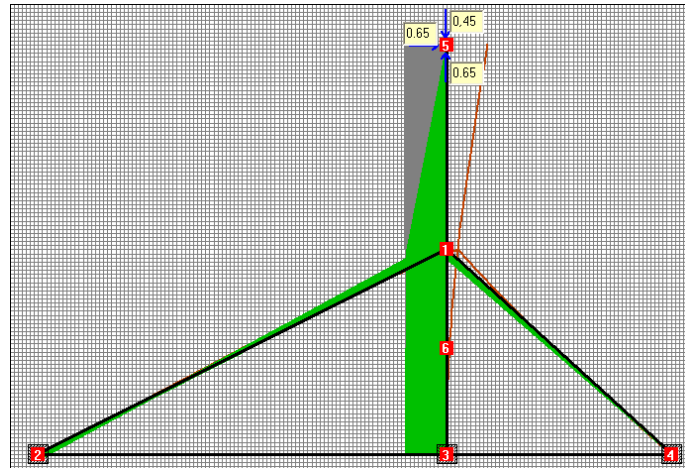


Fig. 104: Static stress analysis on the ankle support: the acting loads on the beam in kN causing the stress due to bending (green), the shear stress (grey) and the deflection shape(red)

max equiv. stress (Mpa)	52,14
max deformation (mm)	0,075
minimum safety factor	4,99

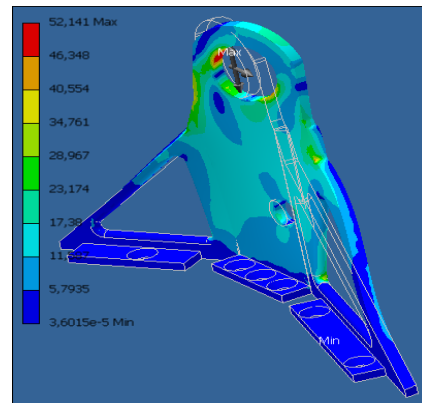


Fig. 105: left: the results of the FEM static stress analysis. right: the accurate Ankle Support with the equivalent stress in Mpa

As the safety factor is acceptable, the part can still be refined. Fig. 106 shows the final refinement of the Ankle Support resulting in a minimum static safety factor of 3,1. The Ankle Support weighs 67g.

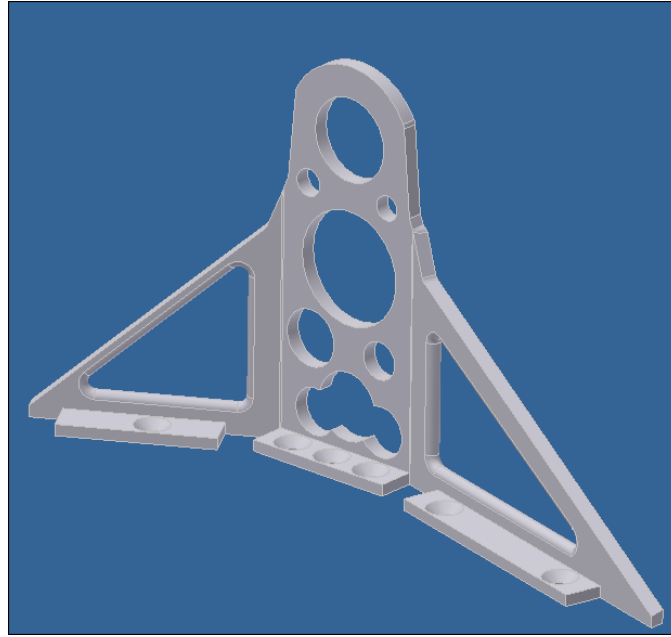


Fig. 106: Final Part Design of Ankle Support

Dynamic Stress Analysis

The loading condition is *axial*, *bending* and *torsion*. According to Table 34, the torsion fatigue factor for the Ankle Support (AlMgSi1) is 0,59. The total safety factor is

$$S_{\text{total}} = S_{\text{static}} \times \text{torsion fatigue factor} = 3,1 \times 0,59 = 1,83$$

The part can move on to the *Final Part Design Phase*, as the total safety factor, the deformation, the weight and the design are acceptable.

Foot-Sole

The Ankle Supports and the ball screw assembly are screwed into the Foot-Sole. The bolt's stress analysis is performed with the *Design accelerator*. The following stress analysis examines the stress caused by the ground reaction forces (body weight) on the Foot-Sole.

Acting Forces

Fig. 107 shows the acting ground reaction forces on the Foot-Sole and the averaged vertical amplitude of these loads during stance period.

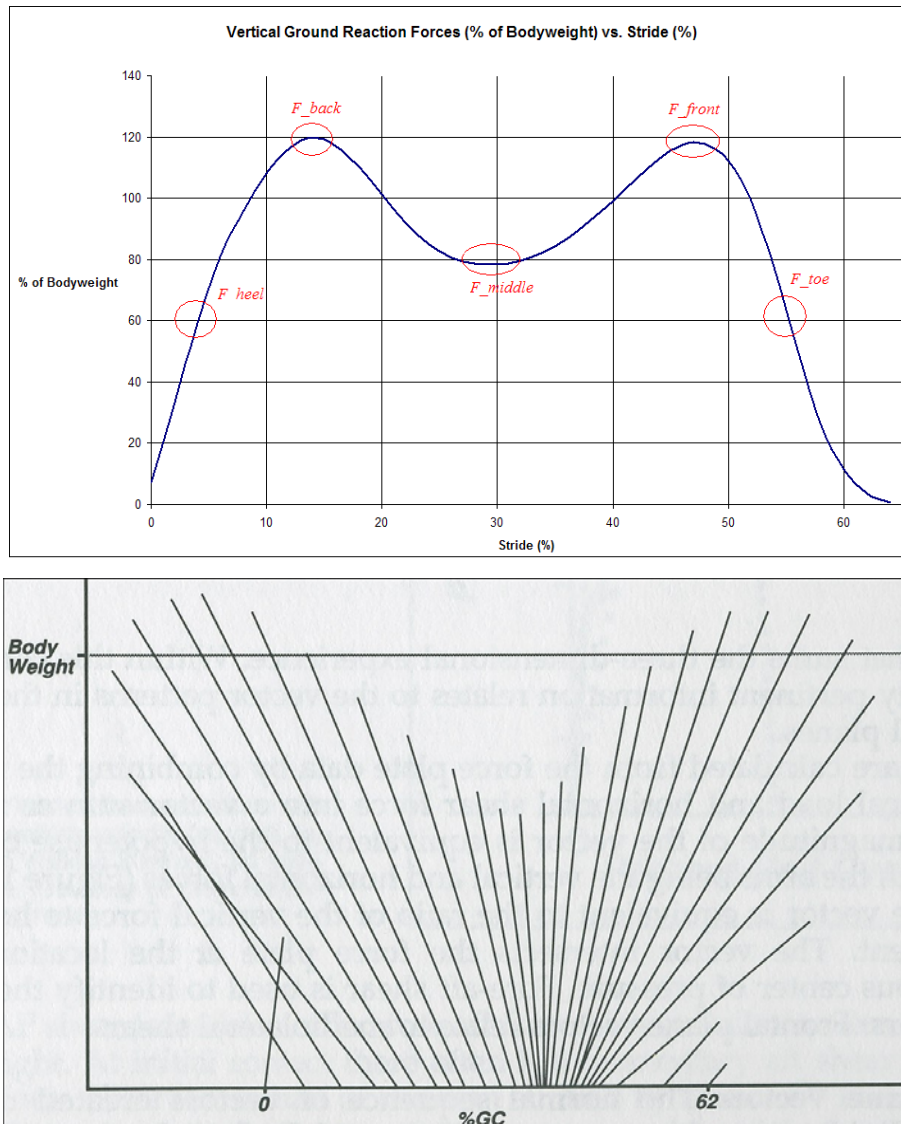


Fig. 107: the acting loads on the Foot-Sole (above) and the averaged vertical amplitude of these loads during stance period (% of Gait Cycle) (below) [1]

Notice that the peak loading is approximately 120% of the body weight, which occurs at the beginning of *Mid-Stance Phase* and at the end of *Terminal Stance Phase*.

Because it is too complex to recreate all these loads in Inventor, five loading conditions were recreated:

1. F_{heel} : 60% of body weight
2. F_{back} : 120% of body weight
3. F_{middle} : 80-100 % of body weight. This force is already simulated on the Ankle Support and will not be simulated for this part
4. F_{front} : 120% of body weight
5. F_{toe} : 60 % of body weight

The Foot-Sole should be as thin as possible to decrease the weight. For this reason, it was decided to provide the Foot-Sole with small support plates underneath. These plates are placed right under the supporting beams of the Ankle Support. This way, all the loads are transmitted to those supporting beams resulting in low stresses and deformations of the sole. Instead of applying a load, the corresponding pressure is applied to the support plates, simulating the various loads. Because of the 2D restriction of ISSD, a distributed load will be applied. This is shown in Table 43.

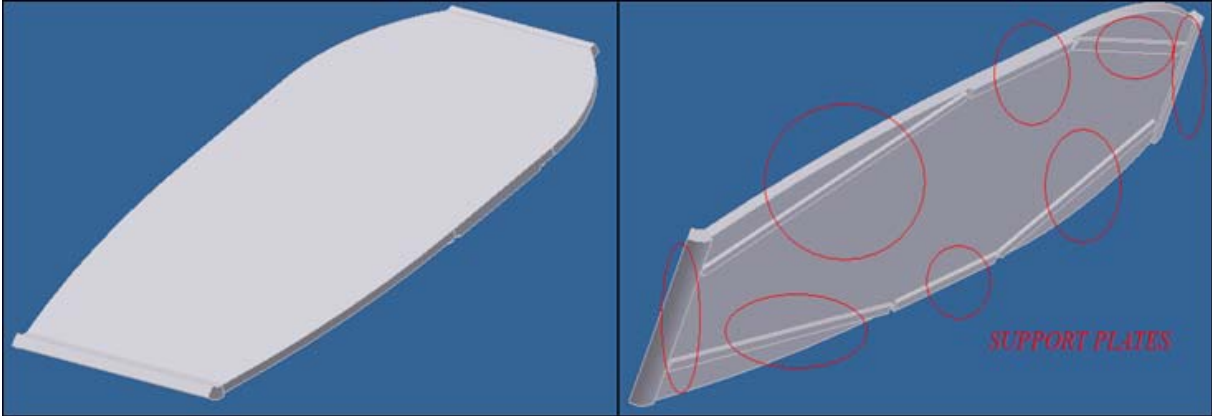


Fig. 108: The accurate design for the Foot-Sole, with the support plates underneath marked in red

Table 43: The different loads on the Foot-Sole during stance converted into pressures for Inventor and distributed loads for ISSD assuming 75 kg bodyweight

	(N)	support plate area (mm ²)	Inventor Pressure (Mpa)	ISSD loads
F_heel	450	381,704	1,18	0,225 kN
F_back	900	448,266	2,01	8,10 kN/m
F_front	900	800	1,13	4,5 kN/m
F_toe	450	523,075	0,86	0,225 kN

Only the FEM static stress analysis results will be elaborated, the ISSD and elaborate calculations can be found in Appendix J.

Static Stress Analysis: results

Performing a stress analysis on the Foot-Sole would not give realistic values, as it is intrinsically reinforced by the Ankle Supports and the bearings of the Ball screw assembly. Because it is impossible in Inventor to perform a static stress analysis on assemblies, the foot has to be recreated in one part. This is shown in Fig. 109. Notice that the ball screw and motor are not placed, because these parts should not carry any loads. All the loads should be carried

by the supporting beams and the Foot-Sole. The maximum allowed misalignment of the motor axis is 0.06 mm.

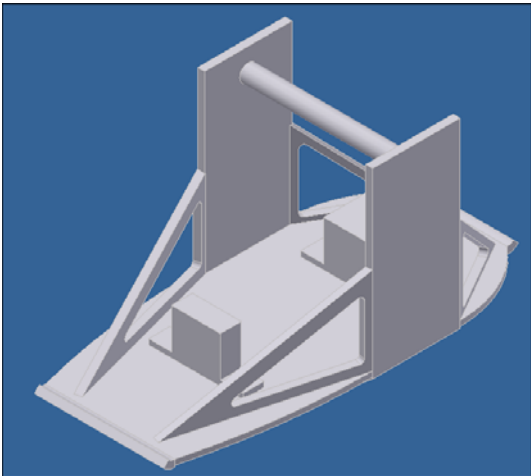


Fig. 109: design of the foot with bearings of the Ball screw assembly and Ankle Supports

Fig. 110 and Table 44 show the results of the FEM static stress analysis.

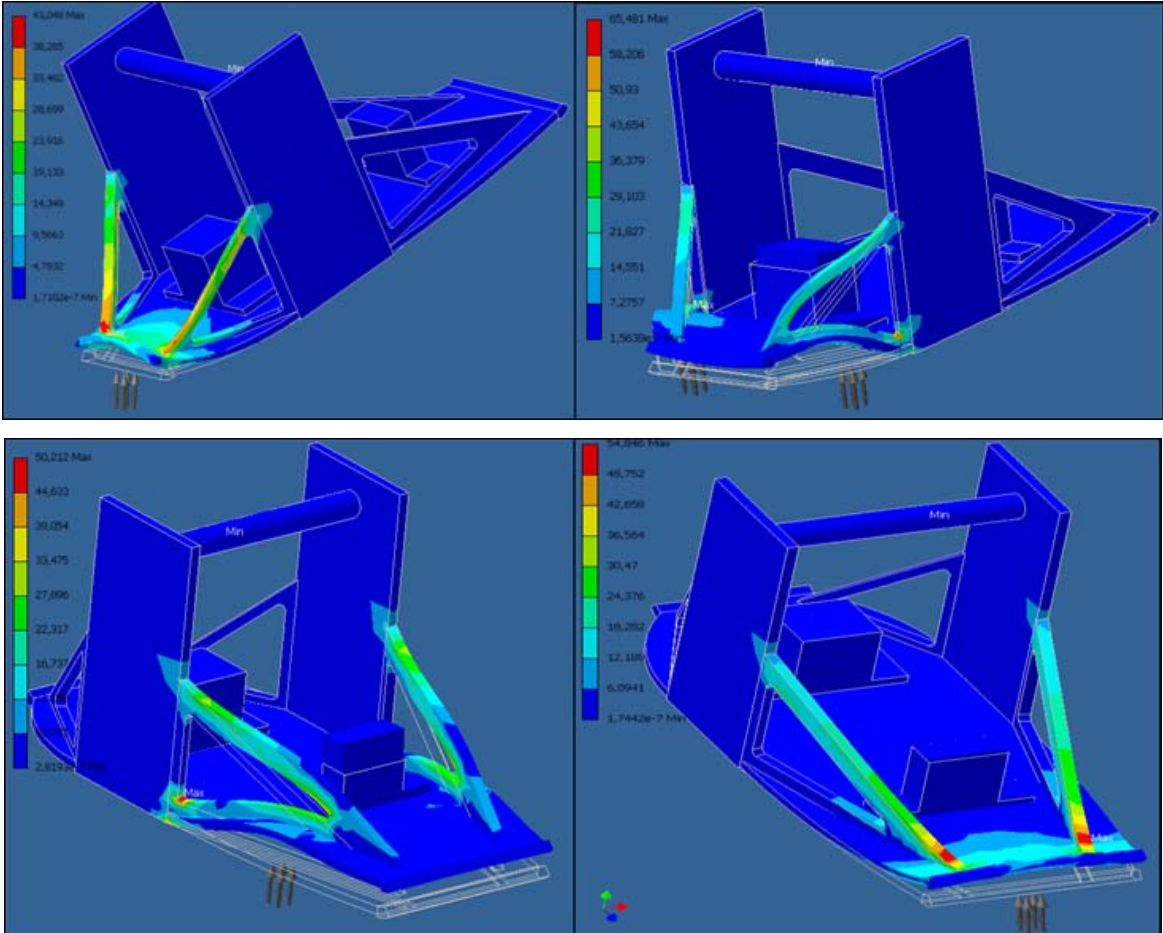


Fig. 110: FEM static stress analysis of Foot-Sole: F_heel and F_back (above) and F_front and F_toe (below): Equivalent stress in Mpa

Table 44: Results of FEM stress analysis

Inventor analysis	<i>F_heel</i>	<i>F_back</i>	<i>F_front</i>	<i>F_toe</i>
STRESS	Mpa	Mpa	Mpa	Mpa
max equivalent stress	43	65,48	50,2	54,8
DEFORMATION	<i>Mm</i>	<i>mm</i>	<i>mm</i>	<i>mm</i>
<i>maximum deformation</i>	0,1	0,046	0,065	0,166
SAFETY FACTOR				
<i>minimum safety factor</i>	6,3	4,2	5,5	5

Even though the model was simplified, the ISSD results are of the same order of magnitude than the Inventor results. Due to local stress concentrations, the FEM results are rather higher than the ISSD results. Notice that even though the safety factors are high, the deformation of the front ball screw bearing is close to the 0,06 mm limit. The Foot-Sole weighs 161g.

Dynamic Stress Analysis

The loading condition is *bending* and *axial*. According to Table 34, the axial fatigue factor for the Foot-Sole (AlMgSi1) is 0,83. The total safety factor is

$$S_{\text{total}} = S_{\text{static}} \times \text{bending fatigue factor} = 4,2 \times 0,83 = 3,49$$

As the total safety factor, deformation, weight and design are acceptable, the part can move on to the *Final Part Design Phase*.

The Leg Box

The Leg Box is the part that is connected to the limb. It is beared on the Ankle Shaft and both the C-and S-Spring are connected to the Leg Box. The box has to be large enough to allow the required rotation of the Lever arms and to allow the possible installation of the driving system for compliance adjustability (MACCEPA) and power supply described earlier. The design of the Leg Box is shown in Fig. 112 and is made of AlMgSi1. Only the static stress analysis of the accurate design will be discussed, the detailed calculations can be found in Appendix J.

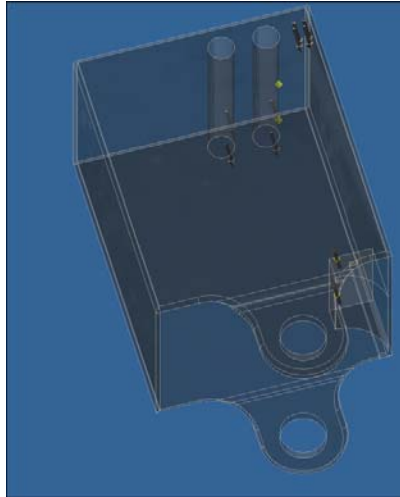


Fig. 111: Initial Design and acting forces on the Leg Box. Notice that the Leg Box is made transparent in order to have a better visualisation of the part.

Acting Loads

There are 3 loads acting on the Leg Box, when it is constrained at the bearings.

1. The body weight: $750 \text{ N} * 1,2 = 900 \text{ N}$.
2. The loads of the S-Spring and C-Spring on the pins of the Leg box: maximum 1350 N and 410 N, respectively (Fig. 77 and Fig. 88)
3. The loads of the S-Spring and C-Spring on the support plate to which the springs are attached (1350 N and 410 N)

Static Stress Analysis: Results

The results of the FEM static stress analysis can be found in Table 45.

Table 45: Results of the FEM static stress analysis of the Leg Box

max equivalent stress (Mpa)	132,97
max deformation (mm)	0,34
minimum static safety factor	1,95

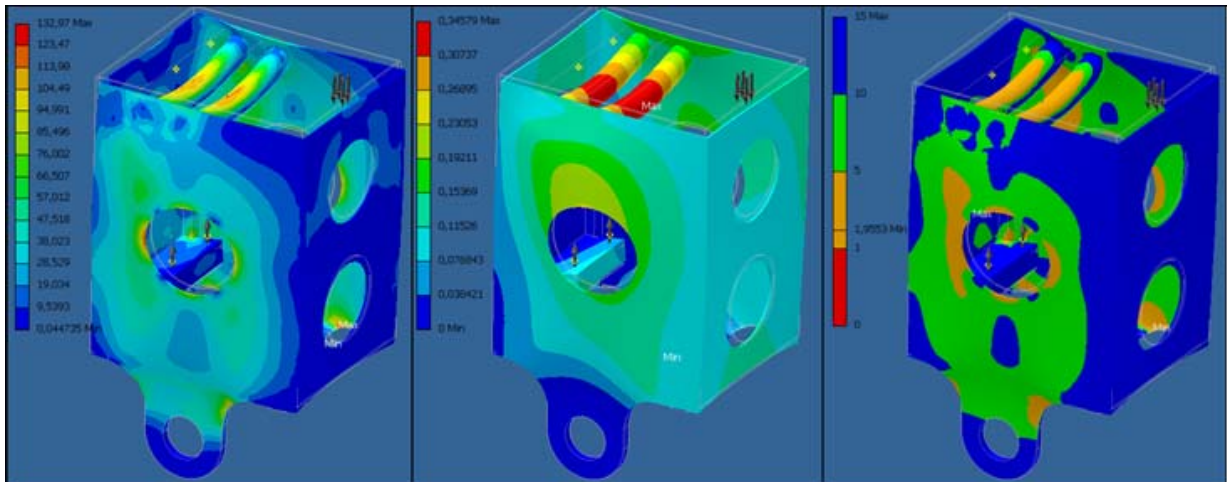


Fig. 112: FEM Static Stress Analysis of the accurate Leg Box: the equivalent (Von Mises) stress (left) in Mpa, the deformation (middle) in mm and the Safety factor (right)

Due to the fact that it is not possible to perform a stress analysis on an assembly, the 2 pins are drawn as a part of the Leg Box. In practice however, these pins are separate parts. The Leg Box, including the pins, weighs 242 g.

Dynamic Stress Analysis

The loading condition is *axial* and *bending*. According to Table 34, the axial fatigue factor for the Leg Box (AlMgSi1) is 0,83. The total safety factor is

$$S_{\text{total}} = S_{\text{static}} \times \text{axial fatigue factor} = 1,95 \times 0,83 = 1,62$$

The part can move on to the *Final Part Design Phase*, as the total safety factor, the deformation, the weight and the design are acceptable.

The Ankle Shaft

The Ankle Shaft has a complex loading condition as it has to carry all the loads of the Lever arms, the ratchet and the Leg Box.

Acting Loads

There are 7 loads and 1 torque acting on the Ankle Shaft.

1. 2 loads from the Leg Box on the Ankle Shaft. These loads are due to the body weight and the spring loads as these are attached to the Leg Box: 2660N (750N *1,2 body weight + 1760N spring load) or 1330 N on each Leg Box bearing.
2. 4 loads from the C-Lever arm: a vertical and horizontal component of the C-Spring load: 300 N and the S-Spring load. The S-Spring load is transmitted to the C-Lever arm through the pin: 3694,46 N (= 2*(300N C-Lever arm + 1538,46N S-Lever arm)) or 1838,46 N on each C-Lever arm bearing (horizontal and vertical).
3. 1 load from the S-Lever arm: a vertical component the S-Spring load: 900 N.

4. 1 torque from the ratchet and S-Lever arm: 90 Nm (maximum torque occurring at 45% of stride).

These loads do not occur simultaneously. There are 2 loading situations:

1. Before Pin-Contact (45% of stride), the S-Lever arm fixed on the Ankle Shaft is *DF-locked* by the ratchet and pawl set and the Ankle Shaft has to carry the generated torque of 90 Nm. Notice that during this period the maximum spring load for the C-Lever arm is 550 N (= 2*275N) or 275 N on each C-Lever arm bearing (horizontal and vertical). The vertical component of the S-Lever arm is 900N.
2. After Pin-Contact, the S-Lever arm is unlocked resulting in a zero torque. The maximum spring load of the C-Lever arm is 3694,46N or 1838,46 N on each C-Lever arm bearing (horizontal and vertical) as stated previously.

The accurate design of the Ankle Shaft is carried out using the above-mentioned loads. This analysis resulted in a shaft diameter of 18 mm and steel 30CrNiMo8 as the chosen material. Table 46 displays the material data.

Table 46: Material data of Steel 30CrNiMo8

E-modulus	210 000 Mpa
G	81 000 Mpa
Density	7,84 e-006 kg/mm ³
Yield Strength	1050 Mpa
Ultimate Strength	1250 Mpa

The simulations discussed below are carried out only in ISSD, due to complexity of the loading situation and the constraint restrictions in Inventor. Regarding the fact that the first loading situation is the most critical one, only this situation is discussed.

Manual Static Stress analysis

First, the stress due to the loads is analyzed in ISSD, followed by a calculation of torsion stress due to the torque. Fig. 113 and Table 47 illustrate this analysis.

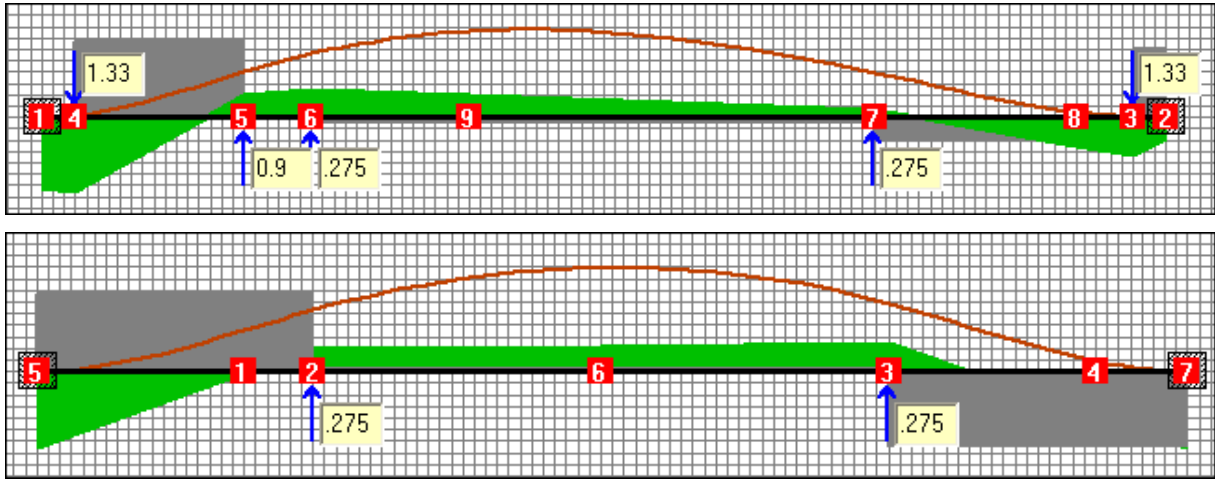


Fig. 113: ISSD static stress analysis of Ankle Shaft for loading situation 1 with the vertical loads (kN) (above) and the horizontal loads (kN) (below): the stress due to bending (green), the shear stress (grey) and the deformed shape (red)

Only the results of node 1 and 4 will be discussed as these areas encounter the highest stress.

Table 47: results of the ISSD static stress analysis for loading situation 1 of the Ankle Shaft

	vertical		horizontal	resulting
ISSD	node 1	node 4	node 1	node 1
STRESS	<i>Mpa</i>	<i>Mpa</i>	<i>Mpa</i>	<i>Mpa</i>
max normal stress (σ_n)				
<i>due to bending</i>	25	26	10,7	27,2
<i>due to normal force</i>	-	-	-	-
max shear stress (τ)	0,9	4,8	1,24	223,86
max shear (torsion) stress (τ)	157,2			
max equivalent stress	325,71	332,52	325,51	388,68
DEFORMATION	<i>mm</i>		<i>mm</i>	
<i>maximum deformation</i>	0,003		0,011	
SAFETY FACTOR				
<i>minimum static safety factor</i>				2,70

The torsion stress due to the moment can be calculated with following formula:

$$\tau = G \cdot \gamma = \frac{M \cdot r}{J_p} \quad \text{Eqtn. 20}$$

With $M = 90 \text{ Nm}$, $r = 9 \text{ mm}$ and J_p is 5153 mm^4 . The maximum stress due to torsion is $\tau = 157,2 \text{ Mpa}$. As one can see the resulting stress due to the loads is $388,68 \text{ Mpa}$.

The minimum safety factor is 2,7 and the part weighs 180g.

Dynamic Stress Analysis

The loading condition is *axial, bending* and *torsion*. According to Table 34, the torsion fatigue factor for the Ankle Shaft (Steel 30CrNiMo8) is 0,6. The total safety factor is

$$S_{\text{total}} = S_{\text{static}} \times \text{torsion fatigue factor} = 2,7 \times 0,6 = 1,62$$

The part can move on to the *Final Part Design Phase*, as the total safety factor, the deformation, the weight and the design are acceptable.

3.4.3. Total Assembly

After designing each part separately, the next stage is to study the total assembly. Table 48 shows a bill of material of the PBP.

Table 48: Bill of Material of the PBP

Item nr.	Part name	Mass	Material	QTY
MADE PARTS				
1	Foot-Sole	0,161 kg	AlMgSi1	1
2	Ankle Support	0,067 kg	AlMgSi1	2
3	Ankle Shaft	0,180 kg	Steel, 30CrNiMo8	1
4	C-Lever Arm	0,242 kg	Stainless Steel, 440C	1
5	S-Lever Arm	0,046 kg	AlMgSi1	1
6	Leg Box	0,265 kg	AlMgSi1	1
7	Rod	0,015 kg	Steel, High Strength Low Alloy	2
8	Pawl	0,030 kg	Steel, 30CrNiMo8	1
9	Ratchet	0,090 kg	Steel, 30CrNiMo8	1
10	Nut Support	0,072 kg	Steel, High Strength Low Alloy	1
PURCHASED PARTS				
11	Ball Screw	0,036 kg	Steel, High Strength Low Alloy	1
12	Locknut	0,005 kg	Steel, High Strength Low Alloy	1
13	Motor Bearing support 1	0,074 kg	Steel, High Strength Low Alloy	1
14	Motor Bearing support 2	0,035 kg	Steel, High Strength Low Alloy	1
15	Motor RE150	0,441 kg	Default	1
16	Planetary GP42C	0,301 kg	Default	1
17	Belt bearing support	0,028 kg	AlMgSi1	1
18	Synchronous Pulley	0,023 kg	Steel	2
20	Synchronous Belt	0,002 kg	Rubber	1
21	Impactrubber	0,001 kg	Rubber	1
22	Leg Connector	0,103 kg	Stainless Steel, 440C	1
23	Sole	0,120 kg	Rubber	1
BEARINGS				
24	ANSI18.1 NHM - 14 x 22 x 12	0,013 kg	Steel, Mild	3
25	ISO 104 - 0 70 12 x 22 x 5	0,007 kg	Steel, Mild	2
26	JIS B 1522 - 7001 12 x 28 x 8	0,019 kg	Steel, Mild	2
27	GB 273.3-87 - 1/18 - 12 x 21 x 5	0,006 kg	Steel, Mild	2
28	DIN 628 T1 - 7201B - 12 x 32 x 10	0,034 kg	Steel, Mild	1
BOLTS				
29	BS 4183 - M4,5 x 9	0,001 kg	Steel, Mild	12
30	BS 4183 - M5 x 11	0,002 kg	Steel, Mild	1
31	IFI 513 - M2x0,4 x 20	0,001 kg	Steel, Mild	4
32	IFI 513 - M2x0,4 x 4	0,0005 kg	Steel, Mild	6
33	IFI 513 - M5x0,8 x 13	0,002 kg	Steel, Mild	5
SPRINGS				
34	S-Spring 75x6,5x36 (6coils)	0,175 kg	spring steel	1
35	C-Spring 75x2,5x36 (6coils)	0,060 kg	spring steel	1
TOTAL		2,85 kg		65

The weight of the total assembly is 2,85 kg. Regarding the leg height of 200 mm, this is an acceptable weight value as the average weight of a below-knee limb equals 4,88 kg [3].

Fig. 114 shows the driving system assembly: The motor spindles the ball screw through a belt transmission in order to translate the nut. The C-Lever arm is driven by the nut through the

rod. The S-Lever arm is operated by the C-Lever arm and can get *DF-locked* and released through the ratchet and pawl set. Notice that the unlocking mechanism of the pawl is not shown in Fig. 114.

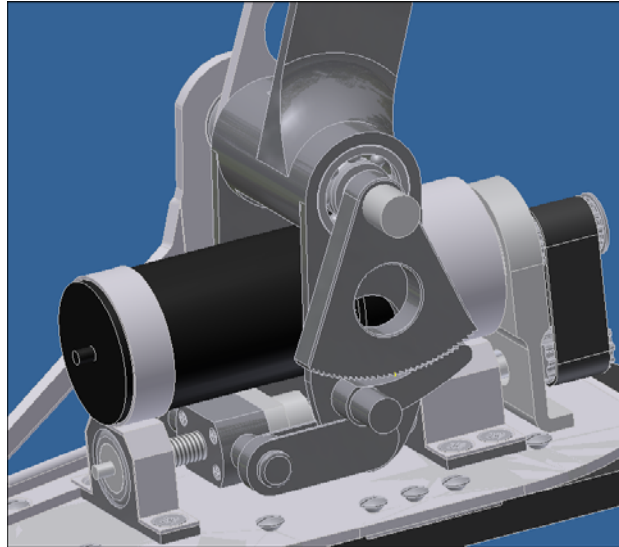


Fig. 114: Assembly of the driving system (isometric view). Notice that one of the Ankle Supports and the unlocking mechanism is not shown

Fig. 115 shows the assembly of the Leg Box. In order to illustrate the mechanism, the Leg Box is made transparent. The springs are connected to the Leg Box and the Lever arms. Regarding the fact that the pre-tension of the springs should be adjustable once the prosthesis is made, the springs are screwed into the Leg Box. In the case of implementing MACCEPA, the driving system discussed previously should be added in order to regulate the pre-tensions. Notice the available space that is foreseen for a potential driving mechanism for compliance adjustability (MACCEPA) and the batteries.

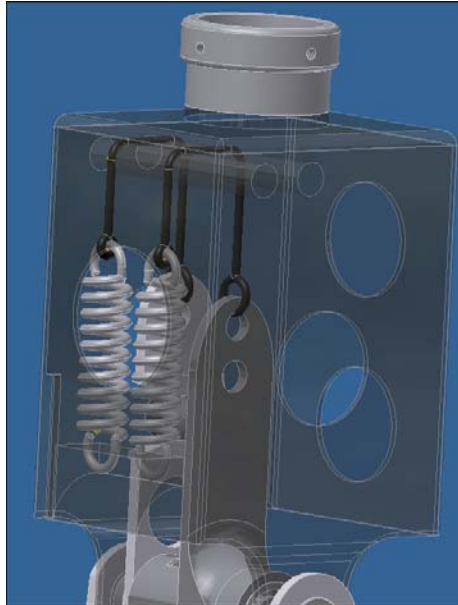


Fig. 115: Assembly of the Leg Box (isometric view)

Both assemblies together are shown in Fig. 116.

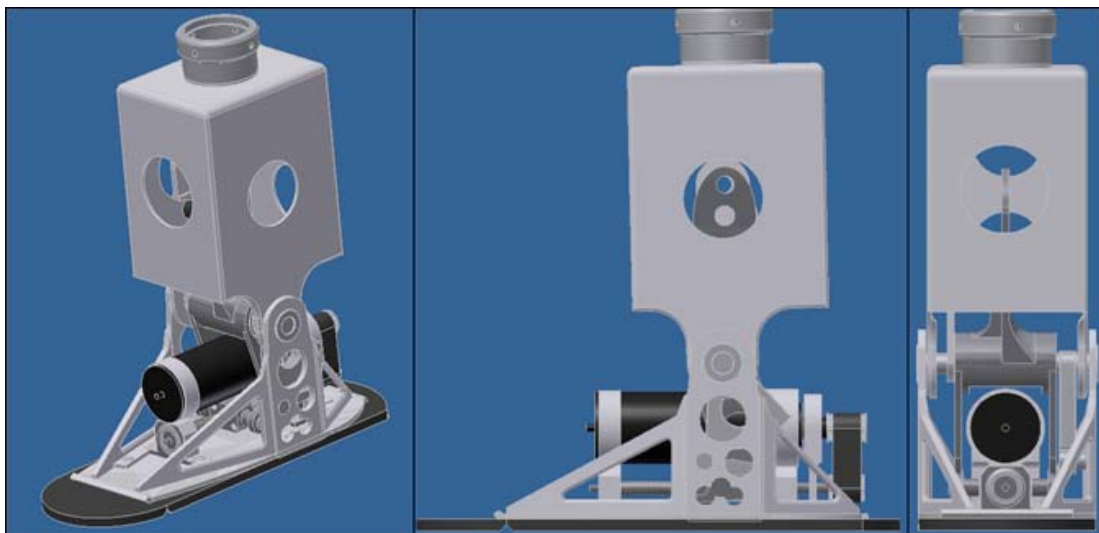


Fig. 116: Final Assembly of the Prosthesis: isometric, side and front

Table 48 shows that the approximate 3kg weight-limit is not exceeded. The volume limit for the foot was a box with dimensions (l x w x h) 300 mm x 100 mm x 80 mm, which was also respected.

3.4.4. Conclusion

This assembly is ready to go to the *Final Assembly Design Phase*, as the safety factors, the weight and the volume conditions are satisfied. Notice that in order to manufacture this

prototype, a more detailed stress analysis and a study towards the assembly of the parts should be performed.

3.5. Dynamic Simulations

3.5.1. Introduction

The dynamic simulations are carried out using the dynamic simulation environment of Inventor 2008 to confirm the PBP's behaviour resulting from the *modelisation* phase. Notice that only the *normal cadence* is simulated. The main goal of this section is to verify the achieved PBP's angles and torques in the *modelisation* phase. Therefore, two simulations were performed.

3.5.2. Dynamic Simulation Using the 'Imposed Motion'-Approach

This simulation examines the torque output of the PBP when the motion is imposed properly. The natural angle course shown in Fig. 117 is imposed on the ankle joint. The motion of both S-and C-Lever arm is imposed as well.

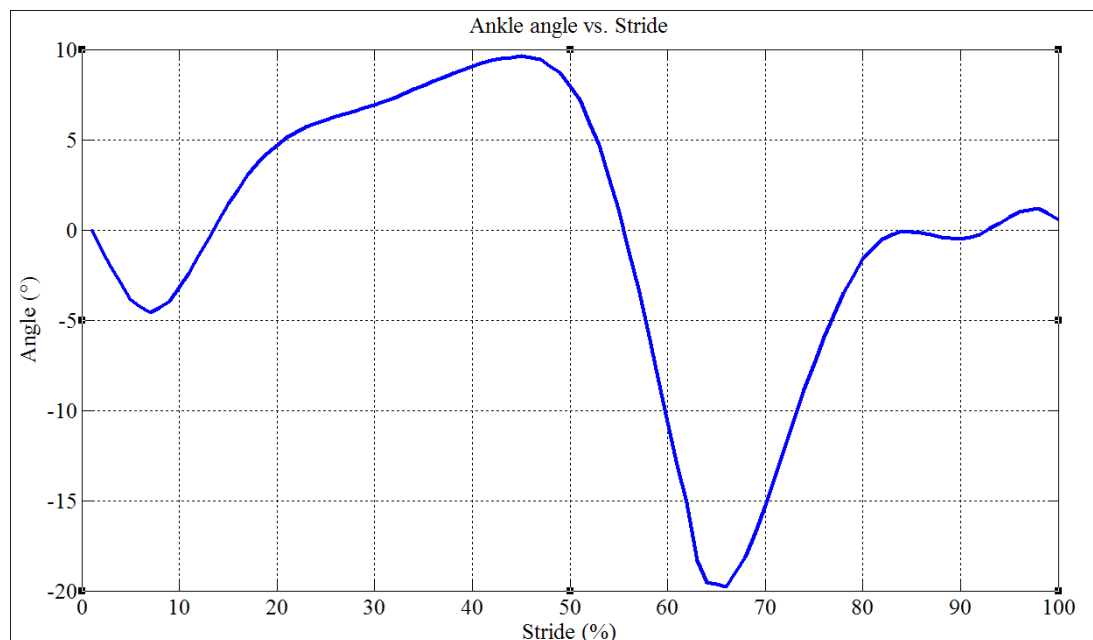


Fig. 117: Natural ankle angle course imposed on the ankle joint as a function of stride

Notice that this simulation takes into account the inertial forces and part weight, in contrast with the simulations performed in the *modelisation*.

Results

Fig. 118 shows the evolution of the PBP's motion during the different phases of the stance.

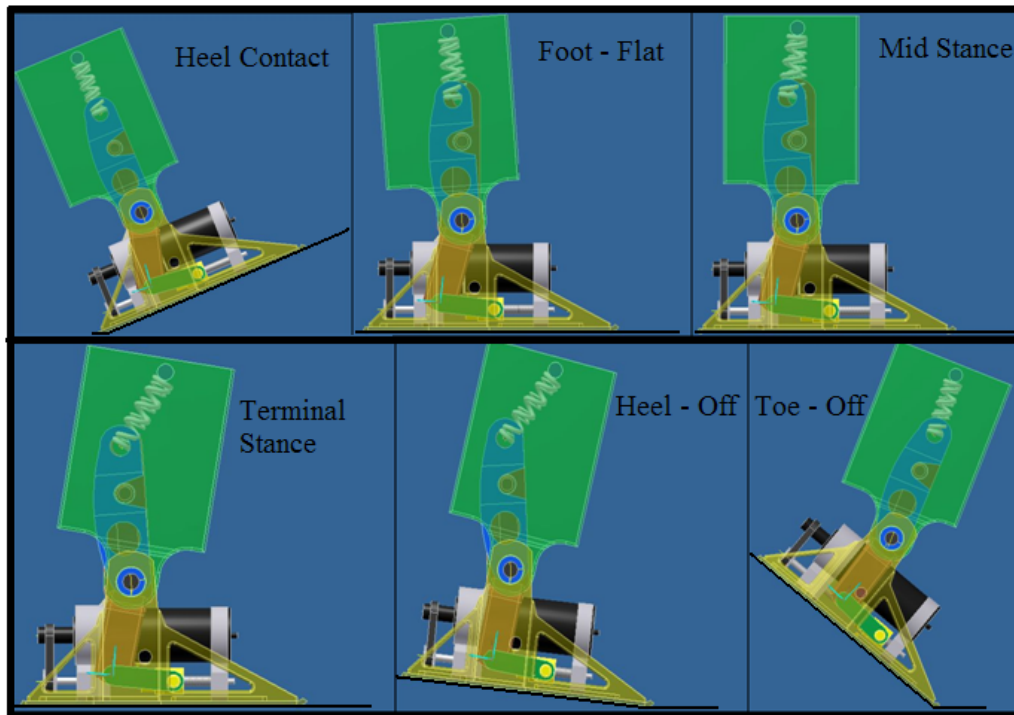


Fig. 118: the evolution of the PBP's motion during stance. The ankle and Lever arms motion is imposed. Starting from Heel-Strike, Foot-Flat, Mid-Stance, Terminal Stance, Heel-Off, until Initial swing (Toe-Off)

The ankle torque data from this simulation is compared to the torque data from the simulations performed in the *modelisation* phase and to the natural ankle torque, as shown in Fig. 119.

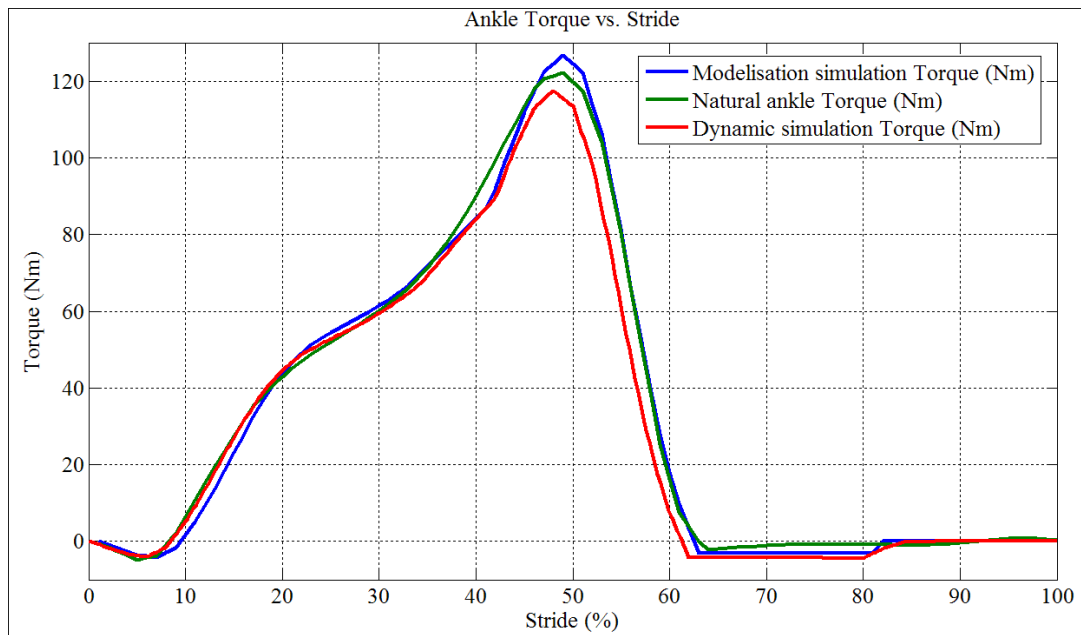


Fig. 119: Ankle torque data from dynamic and modelisation simulation and natural ankle torque vs. Stride

The spring forces from this simulation are compared to the spring forces from the simulations performed in the *modelisation* phase, as shown in Fig. 120.

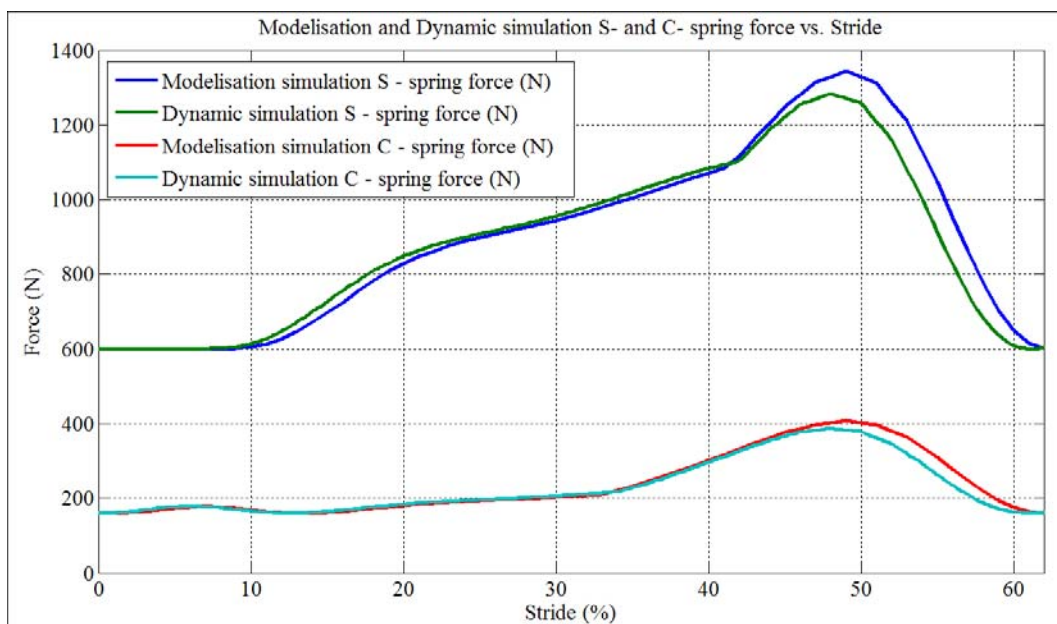


Fig. 120: S- and C-Spring forces data from dynamic and modelisation simulation vs Stride

Fig. 119 and Fig. 120 illustrate that the results of this simulation correspond with the results obtained from the *modelisation* phase.

In conclusion, when the PBP's motion is properly imposed, it is seen that the PBP will generate an acceptable torque course about the ankle joint.

3.5.3. Dynamic Simulation Using the ‘Imposed Torque’-Approach

The second simulation examines whether the required ankle motion of the PBP is achieved when the proper ankle torque and ‘Ankle Body Torque’ are applied. The ‘Ankle Body Torque’ is the torque in the ankle caused by the body weight and inertia. Thus, this simulation requires the design of a human body.

Design of the Human Body



The human body is divided into three parts (considering one leg), which are illustrated in

Fig. 121.

1. The *upper-body*, representing the entire upper body (head, arms and torso).
2. The *above-knee limb*, representing the upper leg from the pelvis to the knee.
3. The *below-knee limb*, representing the lower leg from the knee down to the foot. This part contains the designed prosthesis and a part representing the rest of the below-knee limb.

Fig. 121: Designed human body

Table 49 displays the characteristics of these parts of a human body.

Table 49: Characteristics of the upper- body, upper knee limb and lower knee limb of a human body [3]

	<i>below - knee limb</i>	<i>above - knee limb</i>	<i>upper body</i>
length (mm)	435	410	420
mass (kg)	4,88	8	54,24

Bearing in mind, these characteristics the parts are designed in Inventor.

Simulation

The most important part of ankle angle course is the Heel-Off phase, as achieving Heel-Off is one of the PBP's aims. Therefore, only the *Single Limb Support* phase (from *Mid Stance* to *Terminal Stance*) will be simulated.

In this simulation, the 'Ankle Body Torque' is applied by imposing the relative knee and hip angles originating from Winter [2]. The ankle torque originating from Winter is applied on the ankle. Notice that an extra load representing the initial inertia had to be added. Finally, the resulting ankle angle course is compared to the natural ankle angle course. The same simulation is then performed with the ankle torque obtained in the *modelisation* phase. Fig. 122 illustrates the applied natural and approached ankle torque.

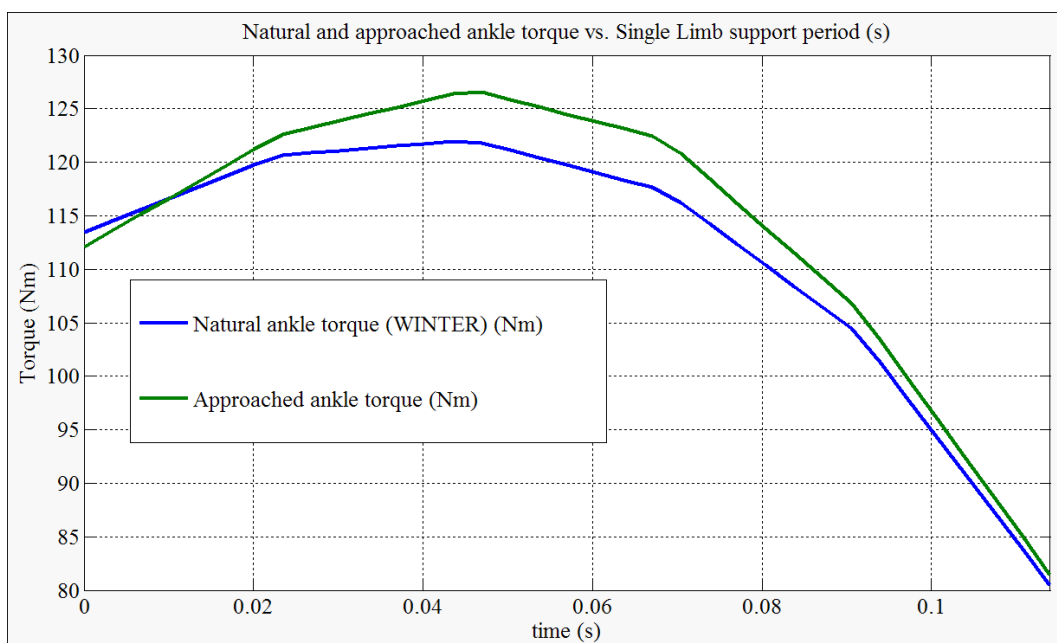


Fig. 122: natural and approached Ankle Torque applied on the Ankle during the Single Limb Support period.

Results

Fig. 123 shows the course of the ankle angle resulting from imposed natural and approached ankle torque, hip and knee angles and initial inertia.

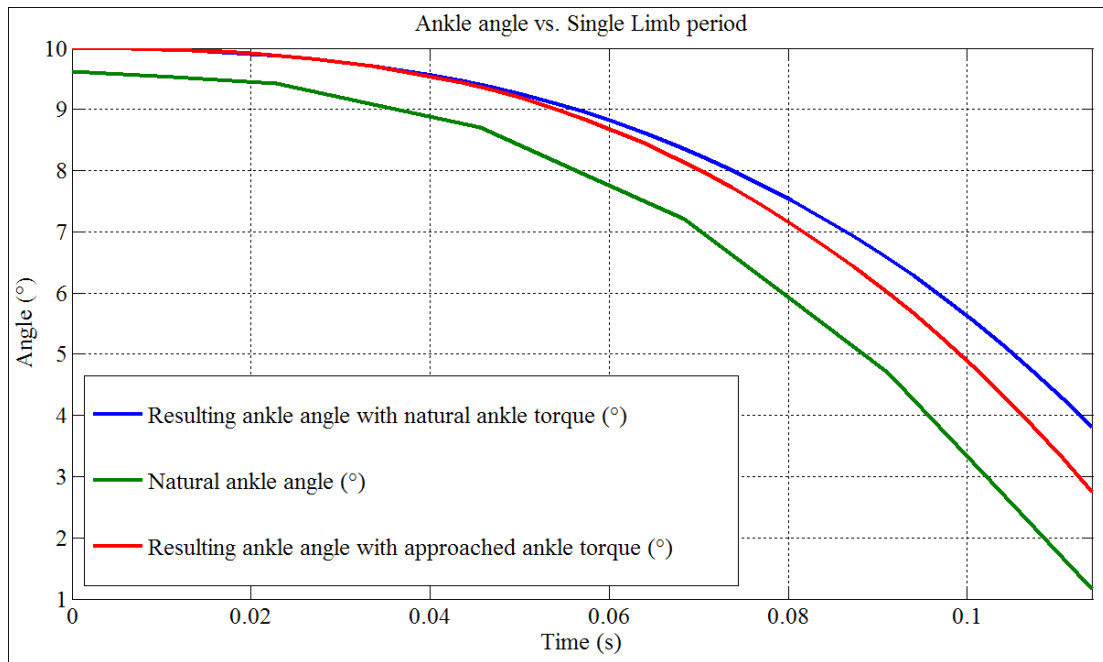


Fig. 123: The course of the ankle angle simulated with imposed natural and approached ankle torque and the natural ankle angle

As illustrated in Fig. 123, the course of both simulated ankle angle curves is similar and close to the natural angle course. The angle courses are visualised in three snapshots during Inventor Dynamic simulations and are shown in Fig. 124.

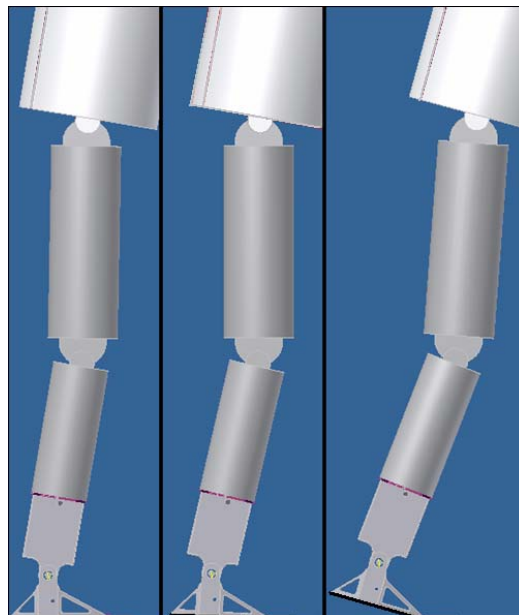


Fig. 124: Second dynamic simulation of the prosthesis performed in Inventor. The ankle torque and body position are imposed. Starting from *Mid-Stance* to *Terminal Stance* (initial contact of the opposite foot)

Notice that the angle course between the Foot-Sole and the ground surface does approximately correspond with the values published in [2].

In conclusion for this simulation, it is seen that the prosthesis will generate an acceptable ankle angle course during the *Single Limb Support* period.

More thorough dynamic simulations should be performed to examine the PBP's dynamics.

However, this exceeds this thesis' scope.

Chapter 4

General Conclusions

The objective of this thesis was the design of a compact, low-weighted and energy efficient below-knee prosthesis powered by electric drives to improve the amputee's gait. The key challenge was to design a device respecting the above mentioned requirements that mimics the natural ankle behaviour during walking.

It is shown that by incorporating a modified MACCEPA into the design, an acceptable approach of the ankle characteristic is obtained. The proposed prosthesis contains two uni-directional springs in parallel, connected to two Lever arms. It is shown that connecting one of the Lever arms to a locking mechanism controlled by a ratchet and pawl set, will improve the energy efficiency drastically. These Lever arms are driven by an ingenious driving system comprising an MAXON RE-40 motor (150W) with a MAXON C42 gearhead (3,5 reduction) connected to a ball screw mechanism through a timing belt. A satisfying total efficiency of 77% is obtained using this driving system. It is shown that the PBP's behaviour is manually adjustable depending on amputee's gait speed by regulating the pre-tension of the springs.

The model parameters were determined through an optimization procedure, which led to mimicking the *entire* required ankle torque curve during stance accurately for slow, normal and fast cadence based on the ankle data published by Winter [2].

The prosthesis is capable of providing 100% of the required Push-Off power, consuming only 22,19J per step during normal cadence (for a 75kg subject). The 300g batteries incorporated in the prosthesis will allow 1,5 h walking time per day (normal cadence) . This autonomy can be enhanced to 8h walking time per day (normal cadence) by providing the amputee with an external 1,2 kg battery pack. The prosthesis' weight, excluding the batteries, has been reduced to 2,84 kg, using a strict design procedure for each part.

Regarding the future perspectives, the driving system for adjusting the actuator compliance (MACCEPA) should be incorporated in the CAD design to obtain a mechanical regulation of the pre-tension of the springs depending on the amputee's gait speed. We believe that a revision of the designed parts is required towards the manufacturing and assembly phase. Also the study of the control aspects must be extended to obtain a robust real time controlling system.

References

- [1] J. Perry, 1992, *Gait Analysis Normal and pathological Function: Gait Analysis*, Thorofare NJ, United States of America, Slack.
- [2] D. Winter, 1991, *Biomechanics and Motor Control of Human Gait: Temporal and stride measures*, Waterloo, Ontario, Canada, second edition, University of Waterloo Press.
- [3] P. Monteyne, 2002, *Studie van de functie van de voet bij de beweging van één- en tweepotige systemen*. Master Thesis VUB Department of Mechanical Engineering.
- [4] M.L. Palmer, 2002, *Sagittal Plane Characterization of Normal Human Ankle Function Across a Range of Walking Gait Speeds*. Master thesis Massachusetts Institute of Technology Department of Mechanical Engineering.
- [5] D.H. Gates, 2004, *Characterizing Ankle Function During Stair Ascent, Descent, and Level Walking For Ankle Prosthesis and Orthosis Design*. Master thesis Boston University College of Engineering.
- [6] <http://mech.vub.ac.be/>
- [7] C.L.M. Tokuda, S. Morimoto, Y. Hashimoto, A. Nakagawa, Y. Akazawa, 2006, *Research and Development of the Intelligently-Controlled Prosthetic Ankle Joint*. Osaka University: Graduate school of Engineering, Proceedings of 2006 IEEE international conference on mechatronics and automation p.1114-1119, Luoyang, China.
- [8] <http://www.ottobock.com/>
- [9] <http://www.media.mit.edu/>
- [10] S. K. Au, J. Weber, H. Herr, 2007, *Biomechanical Design of a Powered Ankle-Foot Prosthesis*. Massachusetts Institute Technology, Proceedings of the 2007 IEEE 10th International Conference on rehabilitations Robotics p.298-303, Noordwijk, The Netherlands.
- [11] J.K.Hitt, R. Bellman, M. Holgate, T.G. Sugar, K.W. Hollander, 2007, *The SPARKY (Spring Ankle with Regenerative Kinetics Project): Design and analysis of a robotic transtibial prosthesis with regenerative kinetics*. Arizona State University: Department of Engineering, Proceedings of the ASME 2007 International Design Engineering Technical Conferences & Computers and Information in Engineering Conference p.1-10, Las Vegas Nevada.
- [12] S. K. Au, P. Dilworth, H. Herr, 2006, *An Ankle-Foot Emulation System for the Study of Human Walking Biomechanics*, Massachusetts Institute Technology, Proceedings of the 2006 IEEE International Conference on Robotics and Automation p.2939-2945, Orlando Florida.
- [13] <http://mathworks.com>
- [14] R. Van Ham, 2006, *Compliant Actuation for Biologically Inspired Bipedal Walking Robots*, PhD thesis VUB Department of Mechanical Engineering.
- [15] <http://www.bostongear.com>
- [16] <http://www.thk.com>
- [17] <http://hpcgears.com>
- [18] <http://www.harmonicdrive.net/products/gearheads/csf-mini>
- [19] P. Kool, 2006, *Mechatronica*, VUB, cursus 4 WE, België.

- [20] D. Muhs, H. Wittel, M. Becker, D. Jannasch, J. Voßiek, 2003, *Roloff/Matek Machineonderdelen*, Den Haag, 4th edition, Academic Service.
- [21] <http://en.wikipedia.org/wiki/Lithium-polymer>
- [22] R. Versluys, P. Beyl, B. Vanderborcht, M. Van Damme, A. Desomer, G. Lenaerts, L. Peeraer, G. Van der Perre and D. Lefeber, *Prosthetic Feet: State-of-the-art Review and The Importance of Mimicking Human Ankle-Foot Biomechanics*. VUB, Brussels, Belgium.

Appendices

APPENDIX A: Characterisation of the Ankle Function for slow and fast cadence [1],[2],[4],[5]

Ankle Motion

In order to compare the ankle angle of slow and fast cadence to normal cadence angle, all three curves will be presented in Fig. 125. Notice that slow cadence has a greater angle deviation during CP than normal cadence and a smaller deviation during both CD and PP. This in contrary to fast cadence, were CP has a smaller angle deviation in comparison to normal cadence and a greater one during both CD and PP.

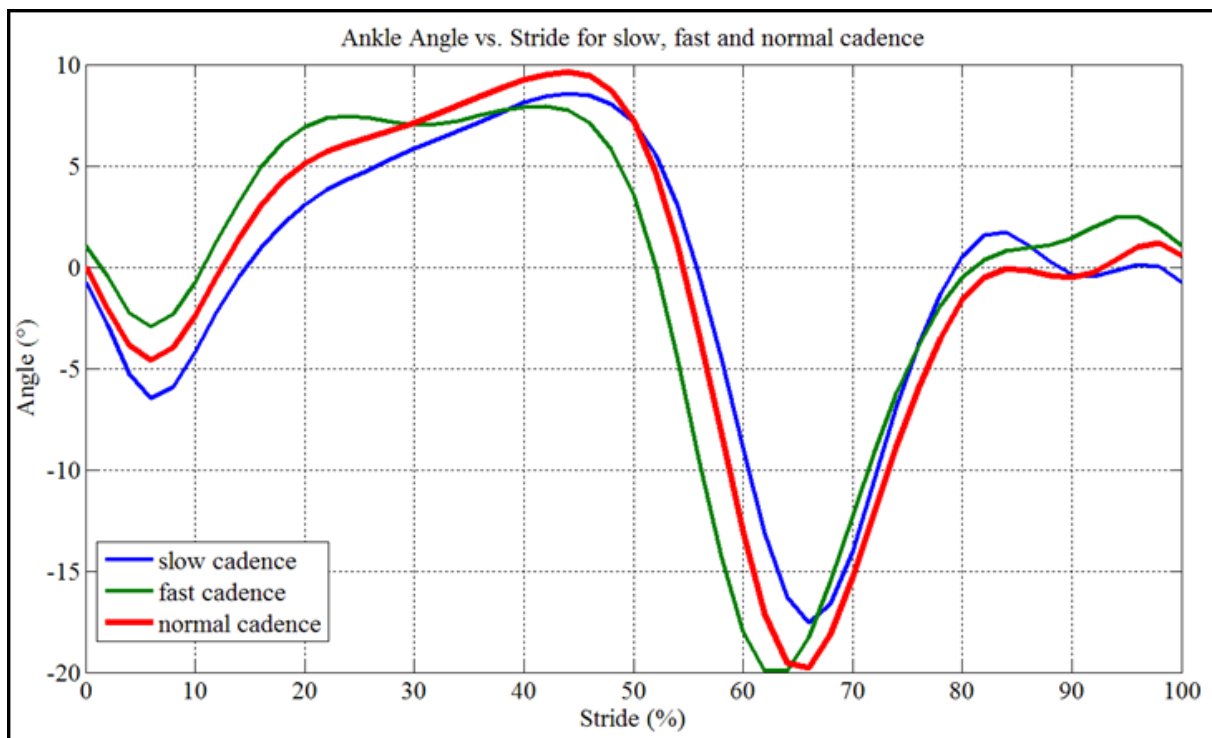


Fig. 125: Ankle Angle (°) vs. Stride (%) for slow, normal and fast cadence

The ankle angle course of fast cadence differs from the other cadences during CD and normal cadence reaches a higher maximum angle at the end of CD.

Ankle Torque

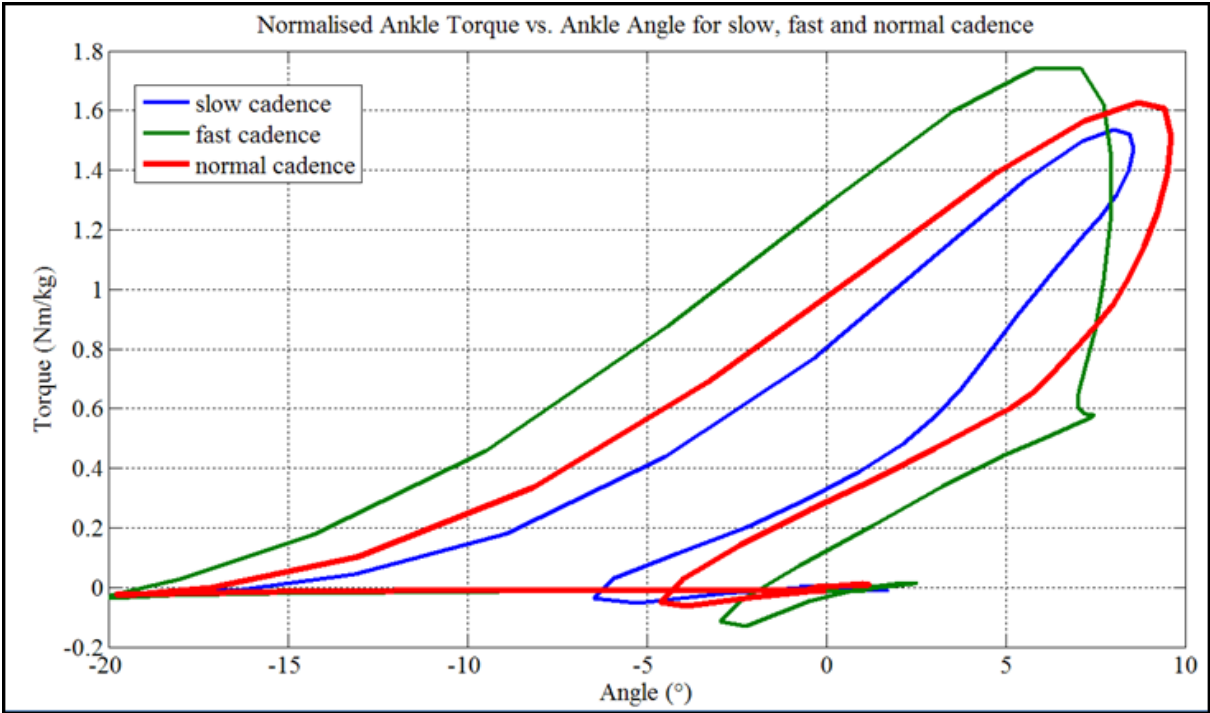


Fig. 126: Normalized Ankle Torque (Nm/kg) vs. Ankle Angle for slow, normal and fast cadence

When the ankle torques for slow, normal and fast cadences are compared, it is observed that the faster the cadence, the higher the torque during PP. The slopes of slow and normal walking are approximately the same for all phases. Fast cadence has a higher slope for CP, approximately the same slope for the first part of CD and a much higher slope for the second part CD than the other cadences. The slope of the curve during PP is again similar to all other cadences.

Ankle Angular Velocity and Ankle Power

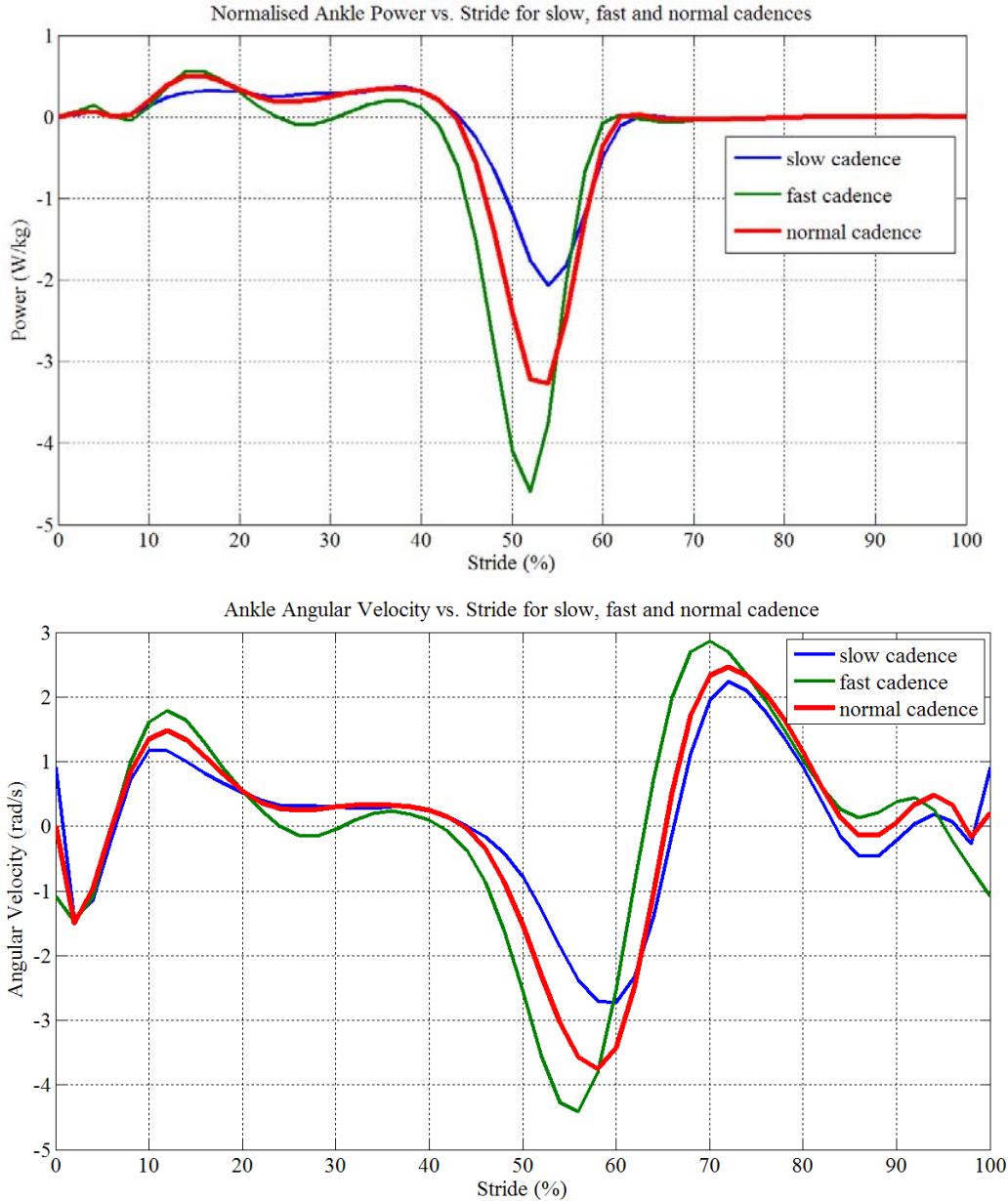


Fig. 127: Ankle Power (W/kg) vs. Stride (%) (above) and Ankle Angular Velocity (rad/s) vs. Stride (%) (below) for slow, normal and fast cadence.

In conclusion for the ankle power, it is seen that the faster the cadence the higher the required power. Notice that during mid PP the necessary torque for fast cadence is almost 50% more than the required torque for normal cadence.

As for the ankle angular velocity, it is evident that the faster the cadence, the higher the angular velocity.

APPENDIX B: *Matlab simulation programma*

```
clc
clear all
close all
figure

%-----Reference Data-----
% Natural Ankle joint angle and torque data from the data generated by
%inverse dynamics of motion capture % and force plate test data published
%by Winter for NORMAL cadence
%-----
Torque_WINTER= [
-0.009
-0.021
-0.034
-0.04864
-0.064
-0.057
-0.051
-0.011
0.028
0.085
0.143
0.20
0.26
0.312
0.368
0.419
0.469
0.507
0.545
0.572
0.601
0.626
0.65
0.671
0.692
0.714
0.736
0.757
0.78
0.803
0.825
0.853
0.881
0.915
0.951
0.995
1.037
1.091
1.144
1.20
1.26
1.32
1.388
1.452
1.513
1.571
1.608
1.618
```

```
1.628
1.597
1.565
1.474
1.388
1.229
1.073
0.883
0.69
0.5164
0.335
0.216
0.102
0.053
-0.001 ];
```

```
Theta_WINTER= [
```

```
0.02
-1.10
-2.06
-2.95
-3.88
-4.25
-4.6
-4.29
-3.98
-3.20
-2.4
-1.45
-0.45
0.52
1.45
2.21
3.04
3.68
4.27
4.69
5.13
5.42
5.71
5.91
6.1
6.27
6.43
6.60
6.76
6.94
7.12
7.33
7.54
7.77
7.99
8.21
8.44
8.65
8.86
9.05
9.23
9.37
9.51
9.56
```

```

9.62
9.52
9.43
9.05
8.7
7.95
7.2
5.91
4.69
2.90
1.15
-1.04
-3.26
-5.66
-8.17
-10.65
-13.05
-15.11
-17.13 ];

Theta_WINTER= transpose(Theta_WINTER);

%For a person weighing 75 kg
Torque_WINTER=75*Torque_WINTER;

%Final design simulations applied on Normal cadence
%-----NOTICE-----
%the procedure is identical for Slow and Fast cadence; solely the reference
%data should get adjusted
%-----
%Duration of Stance for Slow, Fast and Normal cadence
tcycle_SlowCadence=0.8294;
tcycle_NormalCadence=0.684;
tcycle_FastCadence=0.585;
%This simulation targets the NORMAL cadence
tcycle=tcycle_NormalCadence;

OmegaLeg(1)=((Theta_WINTER(1)-Theta_WINTER(length(Theta_WINTER)))*pi/180)/
(tcycle/length(Theta_WINTER));
for i=2:(length(Theta_WINTER)-1)
    OmegaLeg(i)= ((Theta_WINTER(i+1)-Theta_WINTER(i))*pi/180)/
(tcycle/length(Theta_WINTER));
end

Swing_fase=(length(Theta_WINTER)/0.63)-length(Theta_WINTER);

Boolean=1;
Cogwheel_reduction=1;
eff=1;

%-----Adjusting design parameters-----
LegLength =0.15; %the prosthesis' height up the ankle joint (m)
L0=[0.05:0.05:0.13]; %Cable length (m)
LeverArm=LegLength-L0;%Lever arm length (m)
ratio=LeverArm/L0;
% %%%%%%%%%%%

k1=[40000:5000:70000];% The stiffness of S-Spring (N/m)
k2=[5000:5000:20000]; % The stiffness of S-Spring (N/m)

```

```

p1=[0.005:0.005:0.02];%Pretension of S-Spring (m)
p2=[0.005:0.005:0.02];%Pretension of C-Spring (m)

%Equilibrium position of the prosthesis at Toe-Off (°)
Alfa_max=abs(min(Theta_WINTER));
maximum_CP=8; %i Corresponding with Foot-Flat (ul)

MotorON_PP=[30:50]; %Power Source timing (motor on)

%-----initial values-----
Min_error=Inf;
Total_error=0;
Omega_M=0;
T_M=zeros(1,length(Theta_WINTER));
P_M=zeros(1,length(Theta_WINTER));
Delta_X=zeros(1,length(Theta_WINTER));
Delta_X_K1=zeros(1,length(Theta_WINTER));

%-----weights in the case of weighed least square---
GewichtSeg1 =0.01;
GewichtSeg2 =0.01;
GewichtSeg3 =0.3;
GewichtPP =0.68;

Teller=0;
Tellen=length(L0)*length(k1)*length(p1)*length(p2)*length(MotorON_PP)..
        *length(k2)

%-----Commencing the simulations-----
for a=1:length(L0)
for b=1:length(k1)
for f=1:length(k2)
for c=1:length(p1)
for g=1:length(p2)
for d=1:length(MotorON_PP)
Teller=Teller+1

MotorON_PP_Length=[1:(length(Theta_WINTER)-
MotorON_PP(d))];
for e=1:length(MotorON_PP_Length)

Total_error=0;
Alfa(1:length(Theta_WINTER))=0;
Beta1(1:length(Theta_WINTER))=90;
Beta2(1:length(Theta_WINTER))=90;
FC_torque(1:length(Theta_WINTER))=0;
FS_torque(1:length(Theta_WINTER))=0;
FS_Radial(1:length(Theta_WINTER))=0;
FC_Radial(1:length(Theta_WINTER))=0;
Boolean=1;
contact=false;
Theta_WINTER_lim=0;

for i=1:length(Theta_WINTER)
%%%%%%%%%% MOTOR OFF
if i >= MotorON_PP(d)+MotorON_PP_Length(e)
Boolean=0;

```

```

Alfa(i)=Alfa(i-1);
T_M(i)=0;
P_M(i)=0;
end
%%%%%%%%%%%%%%%%%%%%%%%%%%%%%%%%%%%%%%%%%%%%%%%%%%%%%%%%%%%%%%%%%%%%%%%%
%%%%%%%%%%%%%%%%%%%%%%%%%%%%%%%%%%%%%%%%%%%%%%%%%%%%%%%%%%%%%%%%%%%%%%%%MOTOR ON
if i>=MotorON_PP(d)&&i<MotorON_PP(d)+MotorON_PP_Length(e) && Boolean==1
Alfa(i)=Alfa(i-1)+ (Alfa_max)/MotorON_PP_Length(e);
end
%%%%%%%%%%%%%%%%%%%%%%%%%%%%%%%%%%%%%%%%%%%%%%%%%%%%%%%%%%%%%%%%%%%%%%%%

Beta2(i)=90-(Alfa(i)+Theta_WINTER(i))-
(asin(LeverArm(a)*sin((Alfa(i)+Theta_WINTER(i))*pi/180)/(L0(a)+Delta_X(i)))
*180/pi);

Beta1(i)=90-(Theta_WINTER(i)-Theta_WINTER_lim)- (asin(LeverArm(a)
*sin((Theta_WINTER(i)-Theta_WINTER_lim)*pi/180)
/(L0(a)+Delta_X(i)))*180/pi);

Delta_X(i) = sqrt((LeverArm(a)^2) + ((L0(a)+LeverArm(a))^2) -
2*LeverArm(a)*(L0(a)+LeverArm(a))*cos((Alfa(i)+Theta_WINTER(i))*pi/180)) -
L0(a);

%-----locking mechanism-----
if i<maximum_CP

Fveer1(i)=k1(b)*(Delta_X_K1(i)+p1(c));%S-Spring force
Fveer2(i)=k2(f)*(Delta_X(i)+p2(g));%C-Spring force
Fveer(i)=Fveer2(i);
Theta_WINTER_lim=Theta_WINTER(i);

F1(i)=Fveer(i)*(LeverArm(a)*sin((Alfa(i)+Theta_WINTER(i))*pi/180)/(L0(a)+De
lta_X(i)));
else

if abs(Alfa(i)) >= abs(Theta_WINTER_lim) | (contact==true) % Als de pin
tegen de Sleverarm komt
if contact==false
icontact=i;
end

contact=true;
Delta_X_K1(i)=Delta_X(i);

Fveer1(i)=k1(b)*(Delta_X_K1(i)+p1(c));%S-Spring force
Fveer2(i)=k2(f)*(Delta_X(i)+p2(g)); %C-Spring force
Fveer(i)=Fveer1(i)+Fveer2(i);

F1(i)=Fveer(i)*(LeverArm(a)*sin((Alfa(i)+Theta_WINTER(i))*pi/180)/(L0(a)+De
lta_X(i)));
Beta1(i)=Beta2(i);

else % While Pin-Contact is realized
Delta_X_K1(i)= sqrt((LeverArm(a)^2) + ((L0(a)+LeverArm(a))^2) -
2*LeverArm(a)*(L0(a)+LeverArm(a))*cos((Theta_WINTER(i)-
Theta_WINTER_lim)*pi/180)) - L0(a);

```

```

Fveer1(i)=k1(b)*(Delta_X_K1(i)+p1(c)); %S-Spring force
Fveer2(i)=k2(f)*(Delta_X(i)+p2(g)); %C-Spring force

F1S=Fveer1(i)*(LeverArm(a)*sin(((Theta_WINTER(i)-
Theta_WINTER_lim))*pi/180)/(L0(a)+Delta_X(i)));

F1C=Fveer2(i)*(LeverArm(a)*sin((Alfa(i)+Theta_WINTER(i))*pi/180)/(L0(a)+Delta_X(i)));
F1(i)=F1C +F1S;
end
end
%-----
Ankle_torque(i)= F1(i)*(L0(a)+LeverArm(a));
%S-Spring forces
FS_torque(i)=Fveer1(i)*cos(Beta1(i)*pi/180);
FS_Radial(i)=Fveer1(i)*sin(Beta1(i)*pi/180);
%C-Spring forces
FC_torque(i)=Fveer2(i)*cos(Beta2(i)*pi/180);
FC_Radial(i)=Fveer2(i)*sin(Beta2(i)*pi/180);
if i >= MotorON_PP(d) && i < MotorON_PP(d)+MotorON_PP_Length(e) &&
Boolean==1 % MOTOR ON
Omega_M_PP=(((Alfa_max)/MotorON_PP_Length(e))*pi/180)/
(tcycle/length(Theta_WINTER));

T_CogwheelJoint=(FS_torque(i)*LeverArm(a))+(FC_torque(i)*LeverArm(a));
T_M(i)=T_CogwheelJoint/(Cogwheel_reduction);
P_M(i)=T_M(i)*Omega_M_PP ;
end
%-----Least squared error-----
LSM_error(i)= ((Ankle_torque(i)-Torque_WINTER(i))^2); %No weighs
%-----weighed method-----
LSM_error(i)= ((Ankle_torque(i)-Torque_WINTER(i))^2)*GewichtPP;
%if i <=6
% LSM_error(i)= ((Ankle_torque(i)-Torque_WINTER(i))^2)*GewichtSeg1;
% end
% if i>6 & i<=26
% LSM_error(i)= ((Ankle_torque(i)-Torque_WINTER(i))^2)*GewichtSeg2;
% end
% if i>26 & i<=77
%LSM_error(i)= ((Ankle_torque(i)-Torque_WINTER(i))^2)*GewichtSeg3;
% end

Total_error=Total_error + LSM_error(i);
% To accelerate the loop
if Total_error > Min_error
i=length(Theta_WINTER);
end
%Motor power conditioner (w)
if P_M(i)>150
i=length(Theta_WINTER);
Total_error=inf;
end
end
% Optimized design parameters
if Total_error < Min_error
Min_error=Total_error;
Alfa_=Alfa;
lengte_been=L0(a);
maccepa_K1 = k1(b);
maccepa_K2 = k2(f);

```

```

pre_tension1=p1(c);
pre_tension2=p2(g);
MotorONPP=MotorON_PP(d);
MotorONPPLength=MotorON_PP_Length(e);
Cte_Alfa=Alfa_max/MotorON_PP_Length(e);
Omega_motor_PP= Omega_M_PP;
rpm_motor_PP=(Omega_motor_PP*60/(2*pi));
T_Motor=T_M/eff;
P_Motor=P_M;
LeastSuMSquareMethode_error= LSM_error;
BEST_Torque = Ankle_torque;

FS_torque_=FS_torque;
FC_torque_=FC_torque;

FS_Radial_=FS_Radial;
FC_Radial_=FC_Radial;

FSspring=Fveer1;
FCspring=Fveer2;

i_Contact=icontact;

Beta_1=Beta1;
Beta_2=Beta2;
end
end
end
end
end
end
end

%Motor characteristics during swing phase
T_Motor_swing=-4.3;%SEE Inverse dynamics simulations
Omega_M_Swing=(Alfa_max*pi/180)/((tcycle/0.6)*0.37*0.5);
for i=length(Theta_WINTER):length(Theta_WINTER)+round(Swing_fase*0.5)
    T_Motor(i)=T_Motor_swing;
    P_Motor(i)=T_Motor(i)*Omega_M_Swing;
end
for
i=length(Theta_WINTER)+round(Swing_fase*0.5):length(Theta_WINTER)+(Swing_fa
se)
    T_Motor(i)=0;
    P_Motor(i)=0;
end
RMS_T_Motor_Swing=0;
RMS_T_Motor_Stance=0;
RMS_T_Motor_Stride=0;

%Motor characteristics during Stride
for i=1:length(Theta_WINTER)+Swing_fase
    RMS_T_Motor_Stride=RMS_T_Motor_Stride+ T_Motor(i)^2;
end
RMS_T_Motor_Stride=sqrt(RMS_T_Motor_Stride/((length(Theta_WINTER))+Swing_fa
se))
RMS_Torque_Motor_Stride(1:length(Theta_WINTER)+Swing_fase)=RMS_T_Motor_Stri
de;
%%%%%%%%%%%%%%%%%%%%%%%%%%%%%%%%%%%%%%%%%%%%%%%%%%%%%%%%%%%%%%%%%%%%%%%%

```

```

%Motor characteristics during Stance
for i=1:length(Theta_WINTER)
    RMS_T_Motor_Stance=RMS_T_Motor_Stance+ T_Motor(i)^2;
end
RMS_T_Motor_Stance=sqrt(RMS_T_Motor_Stance/((length(Theta_WINTER))+Swing_fa
se))
%%%%%%%%%%%%%%%%%%%%%%%%%%%%%%%%%%%%%%%%%%%%%%%%%%%%%%%%%%%%%%%%%%%%%%%%

%Motor characteristics during Swing
for i=length(Theta_WINTER):length(Theta_WINTER)+Swing_fase
    RMS_T_Motor_Swing=RMS_T_Motor_Swing+ T_Motor(i)^2;
end
RMS_T_Motor_Swing=sqrt(RMS_T_Motor_Swing/((length(Theta_WINTER))+Swing_fase
))
%%%%%%%%%%%%%%%%%%%%%%%%%%%%%%%%%%%%%%%%%%%%%%%%%%%%%%%%%%%%%%%%%%%%%%%%

%%plotting the simulation results%%%%%%%%%%%%%%%%%%%%%%%%%%%%%%%%%%%%%%%%%%%%%%%%%%%%%%%%%%%%%%%%%%%%%%%%
%%%%%%%%%%%%%%%%%%%%%%%%%%%%%%%%%%%%%%%%%%%%%%%%%%%%%%%%%%%%%%%%%%%%%%%%
subplot(2,2,1),
plot(1:length(Theta_WINTER),Torque_WINTER,1:length(Theta_WINTER),BEST_Torqu
e)
legend('Natural ankle torque (winter)', 'Approched ankle torque');
grid on
subplot(2,2,2),plot(Theta_WINTER,Torque_WINTER,Theta_WINTER,BEST_Torque)
legend('Natural ankle torque (winter)', 'Approched ankle torque');
grid on
subplot(2,2,3),plot(1:length(P_Motor),P_Motor,1:length(T_Motor),T_Motor,1:l
ength(T_Motor),RMS_Torque_Motor_Stride)
legend('Motor Power(watt)', 'Motor Torque(Nm)', 'RMS Torque(Nm)');
grid on
subplot(2,2,4),plot(1:length(Theta_WINTER),Alfa_)
legend('Alfa(°)');
%%%%%%%%%%%%%%%%%%%%%%%%%%%%%%%%%%%%%%%%%%%%%%%%%%%%%%%%%%%%%%%%%%%%%%%%

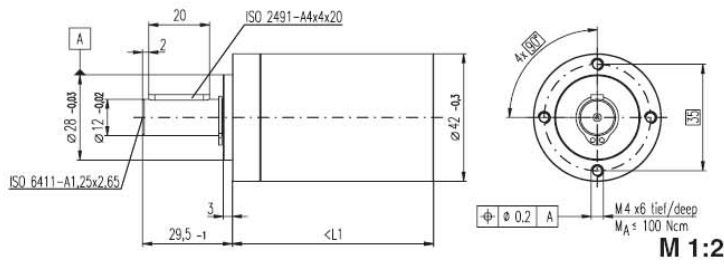
%%%%%%%%%%%%%%%%%%%%%%%%%%%%%%%%%%%%%%%%%%%%%%%%%%%%%%%%%%%%%%%%%%%%%%%%
figure
subplot(2,2,1),
plot(1:length(Theta_WINTER),FS_torque_,1:length(Theta_WINTER),FS_Radial_,1:
length(Theta_WINTER),FSspring)
legend('Torque force on S leverarm (N)', 'pull force on S leverarm
(N)', 'Force S spring (N)');
grid on
subplot(2,2,2),plot(1:length(Theta_WINTER),FC_torque_,1:length(Theta_WINTER
),FC_Radial_,1:length(Theta_WINTER),FCspring)
legend('Torque force on C leverarm (N)', 'pull force on C leverarm
(N)', 'Force C spring (N)');
grid on
subplot(2,2,3),plot(1:length(Theta_WINTER),Alfa_)
legend('Alfa(°)');
grid on
subplot(2,2,4),plot(1:length(Theta_WINTER),Theta_WINTER)
legend('Theta(°)');
grid on
%%%%%%%%%%%%%%%%%%%%%%%%%%%%%%%%%%%%%%%%%%%%%%%%%%%%%%%%%%%%%%%%%%%%%%%%
% figure
% plot(1:length(Theta_WINTER),Beta_1,1:length(Theta_WINTER),Beta_2);
% legend('Beta 1', 'Beta 2');
% grid on

```

```
figure
plot(1:length(Theta_WINTER),Theta_WINTER);
legend('Ankle Angle of a natural Ankle (Winter)' );
grid on
% figure
% plot(1:length(Theta_WINTER),LeastSuMSqureMethode_error)
% grid on
% figure
```


APPENDIX D: Gearhead GP 42C Data Sheet

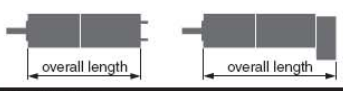
Planetary Gearhead GP 42 C $\varnothing 42$ mm, 3 - 15 Nm Ceramic Version



Technical Data	
Planetary Gearhead	straight teeth
Output shaft	stainless steel
Bearing at output	preloaded ball bearings
Radial play, 12 mm from flange	max. 0.06 mm
Axial play at axial load	< 5 N 0 mm > 5 N max. 0.3 mm
Max. permissible axial load	150 N
Max. permissible force for press fits	300 N
Sense of rotation, drive to output	=
Recommended input speed	< 8000 rpm
Recommended temperature range	-20 ... +100°C
Extended area as option	-35 ... +100°C
Number of stages	1 2 3 4
Max. radial load, 12 mm from flange	120 N 150 N 150 N 150 N

- Stock program
- Standard program
- Special program (on request)

Gearhead Data	Order Number									
	203113	203115	203119	203120	203124	203129	203128	203133	203137	203141
1 Reduction	3.5 : 1	12 : 1	26 : 1	43 : 1	81 : 1	156 : 1	150 : 1	285 : 1	441 : 1	756 : 1
2 Reduction absolute	$7/2$	$49/4$	26	$343/8$	$2197/27$	156	$2401/16$	$15379/54$	441	756
3 Mass inertia gcm ²	14	15	9.1	15	9.4	9.1	15	15	14	14
4 Max. motor shaft diameter mm	10	10	8	10	8	8	10	10	10	10
Order Number	203114	203116		203121	203125		203130	203134	203138	203142
1 Reduction	4.3 : 1	15 : 1		53 : 1	91 : 1		186 : 1	319 : 1	488 : 1	936 : 1
2 Reduction absolute	$13/3$	$91/6$		$637/12$	91		$4459/24$	$637/2$	$4394/9$	936
3 Mass inertia gcm ²	9.1	15		15	15		15	15	9.4	9.1
4 Max. motor shaft diameter mm	8	10		10	10		10	10	8	8
Order Number		203117		203122	203126		203131	203135	203139	
1 Reduction		19 : 1		66 : 1	113 : 1		230 : 1	353 : 1	546 : 1	
2 Reduction absolute		$169/9$		$1183/18$	$339/3$		$8281/36$	$28561/61$	546	
3 Mass inertia gcm ²		9.4		15	9.4		15	9.4	14	
4 Max. motor shaft diameter mm		8		10	8		10	8	10	
Order Number		203118		203123	203127		203132	203136	203140	
1 Reduction		21 : 1		74 : 1	126 : 1		257 : 1	394 : 1	676 : 1	
2 Reduction absolute		21		$147/2$	126		$1029/4$	$1183/3$	676	
3 Mass inertia gcm ²		14		15	14		15	15	9.1	
4 Max. motor shaft diameter mm		10		10	10		10	10	8	
5 Number of stages	1	2	2	3	3	3	4	4	4	4
6 Max. continuous torque Nm	3.0	7.5	7.5	15.0	15.0	15.0	15.0	15.0	15.0	15.0
7 Intermittently permissible torque at gear output Nm	4.5	11.3	11.3	22.5	22.5	22.5	22.5	22.5	22.5	22.5
8 Max. efficiency %	90	81	81	72	72	72	64	64	64	64
9 Weight g	260	360	360	460	460	460	560	560	560	560
10 Average backlash no load °	0.3	0.4	0.4	0.5	0.5	0.5	0.5	0.5	0.5	0.5
11 Gearhead length L1 mm	40.9	55.4	55.4	69.9	69.9	69.9	84.4	84.4	84.4	84.4

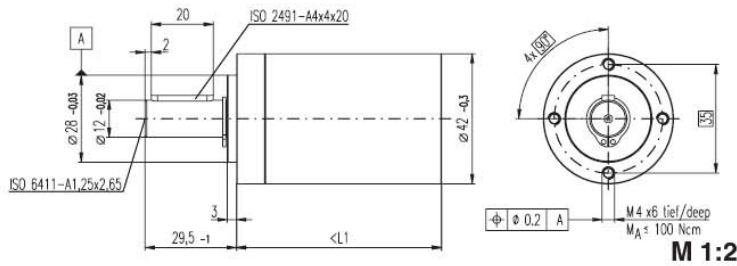


Combination													
+ Motor	Page	+ Tacho	Page	+ Brake	Page	Overall length [mm] = Motor length + gearhead length + (tacho / brake) + assembly parts							
RE 35, 90 W	81					111.9	126.4	126.4	140.9	140.9	155.4	155.4	155.4
RE 35, 90 W	81	MR	251			129.3	137.8	137.8	152.3	152.3	166.8	166.8	166.8
RE 35, 90 W	81	HED_ 5540	254/256			132.9	147.4	147.4	161.9	161.9	176.4	176.4	176.4
RE 35, 90 W	81	DCT 22	263			130.0	144.5	144.5	159.0	159.0	173.5	173.5	173.5
RE 35, 90 W	81			AB 28	300	148.0	162.5	162.5	177.0	177.0	191.5	191.5	191.5
RE 36, 70 W	82					112.2	126.7	126.7	141.2	141.2	155.7	155.7	155.7
RE 36, 70 W	82	MR	251			129.6	138.1	138.1	152.6	152.6	167.1	167.1	167.1
RE 36, 70 W	82	HED_ 5540	254/256			139.2	147.7	147.7	162.2	162.2	176.7	176.7	176.7
RE 36, 70 W	82	DCT 22	263			130.3	144.8	144.8	159.3	159.3	173.8	173.8	173.8
RE 40, 150 W	83					112.0	126.5	126.5	141.0	141.0	155.5	155.5	155.5
RE 40, 150 W	83	MR	251			123.4	137.9	137.9	152.4	152.4	166.9	166.9	166.9
RE 40, 150 W	83	HED_ 5540	254/256			132.7	147.2	147.2	161.7	161.7	176.2	176.2	176.2
RE 40, 150 W	83	HEDL 9140	259			166.1	180.6	180.6	195.1	195.1	209.6	209.6	209.6
RE 40, 150 W	83			AB 28	300	148.1	162.6	162.6	177.1	177.1	191.6	191.6	191.6
RE 40, 150 W	83			AB 28	301	156.1	170.6	170.6	185.1	185.1	199.6	199.6	199.6
RE 40, 150 W	83	HED_ 5540	254/256	AB 28	300	165.2	179.7	179.7	194.2	194.2	208.7	208.7	208.7
RE 40, 150 W	83	HEDL 9140	259	AB 28	301	176.6	191.1	191.1	205.6	205.6	220.1	220.1	220.1
EC 40, 120 W	163					111.0	125.5	125.5	140.0	140.0	154.5	154.5	154.5
EC 40, 120 W	163	HED_ 5540	255/257			129.4	143.9	143.9	158.4	158.4	172.9	172.9	172.9
EC 40, 120 W	163	Res 26	264			137.6	152.1	152.1	166.6	166.6	181.1	181.1	181.1
EC 40, 120 W	163			AB 28	300	141.8	156.3	156.3	170.8	170.8	185.3	185.3	185.3
EC 45, 150 W	164					152.2	166.7	166.7	181.2	181.2	195.7	195.7	195.7
EC 45, 150 W	164	HEDL 9140	259			167.8	182.3	182.3	196.8	196.8	211.3	211.3	211.3
EC 45, 150 W	164	Res 26	264			152.2	166.7	166.7	181.2	181.2	195.7	195.7	195.7
EC 45, 150 W	164			AB 28	301	159.6	174.1	174.1	188.6	188.6	203.1	203.1	203.1

May 2007 edition / subject to change

Planetary Gearhead GP 42 C $\varnothing 42$ mm, 3 - 15 Nm

Ceramic Version



Technical Data

Planetary Gearhead	straight teeth
Output shaft	stainless steel
Bearing at output	preloaded ball bearings
Radial play, 12 mm from flange	max. 0.06 mm
Axial play at axial load	< 5 N 0 mm > 5 N max. 0.3 mm
Max. permissible axial load	150 N
Max. permissible force for press fits	300 N
Sense of rotation, drive to output	=
Recommended input speed	< 8000 rpm
Recommended temperature range	-20 ... +100°C
Extended area as option	-35 ... +100°C
Number of stages	1 2 3 4
Max. radial load, 12 mm from flange	120 N 150 N 150 N 150 N

- Stock program
- Standard program
- Special program (on request)

Gearhead Data	Order Number									
	203113	203115	203119	203120	203124	203129	203128	203133	203137	203141
1 Reduction	3.5 : 1	12 : 1	26 : 1	43 : 1	81 : 1	156 : 1	150 : 1	285 : 1	441 : 1	756 : 1
2 Reduction absolute	$7/2$	$49/4$	26	$343/8$	$2197/27$	156	$2401/16$	$15379/54$	441	756
3 Mass inertia gcm ²	14	15	9.1	15	9.4	9.1	15	15	14	14
4 Max. motor shaft diameter mm	10	10	8	10	8	8	10	10	10	10
Order Number	203114	203116		203121	203125		203130	203134	203138	203142
1 Reduction	4.3 : 1	15 : 1		53 : 1	91 : 1		186 : 1	319 : 1	489 : 1	936 : 1
2 Reduction absolute	$13/3$	$91/6$		$637/12$	91		$4459/24$	$637/2$	$4394/9$	936
3 Mass inertia gcm ²	9.1	15		15	15		15	15	9.4	9.1
4 Max. motor shaft diameter mm	8	10		10	10		10	10	8	8
Order Number		203117		203122	203126		203131	203135	203139	
1 Reduction		19 : 1		66 : 1	113 : 1		230 : 1	353 : 1	546 : 1	
2 Reduction absolute		$169/9$		$1183/18$	$338/3$		$8281/36$	$28561/81$	546	
3 Mass inertia gcm ²		9.4		15	9.4		15	9.4	14	
4 Max. motor shaft diameter mm		8		10	8		10	8	10	
Order Number		203118		203123	203127		203132	203136	203140	
1 Reduction		21 : 1		74 : 1	126 : 1		257 : 1	394 : 1	676 : 1	
2 Reduction absolute		21		$147/2$	126		$1029/4$	$1183/3$	676	
3 Mass inertia gcm ²		14		15	14		15	15	9.1	
4 Max. motor shaft diameter mm		10		10	10		10	10	8	
5 Number of stages		1	2	2	3	3	3	4	4	4
6 Max. continuous torque Nm		3.0	7.5	7.5	15.0	15.0	15.0	15.0	15.0	15.0
7 Intermittently permissible torque at gear output Nm		4.5	11.3	11.3	22.5	22.5	22.5	22.5	22.5	22.5
8 Max. efficiency %		90	81	81	72	72	72	64	64	64
9 Weight g		260	360	360	460	460	460	560	560	560
10 Average backlash no load °		0.3	0.4	0.4	0.5	0.5	0.5	0.5	0.5	0.5
11 Gearhead length L1 mm		40.9	55.4	55.4	69.9	69.9	69.9	84.4	84.4	84.4



Combination

+ Motor	Page	+ Tacho	Page	+ Brake	Page	Overall length [mm]	= Motor length + gearhead length + (tacho / brake) + assembly parts								
EC 45, 250 W	165					185.0	199.5	199.5	214.0	214.0	228.5	228.5	228.5	228.5	
EC 45, 250 W	165	HEDL 9140	259			200.6	215.1	215.1	229.6	229.6	229.6	244.1	244.1	244.1	244.1
EC 45, 250 W	165	Res 26	264			185.0	199.5	199.5	214.0	214.0	214.0	228.5	228.5	228.5	228.5
EC 45, 250 W	165			AB 28	301	192.4	206.9	206.9	221.4	221.4	235.9	235.9	235.9	235.9	235.9
EC 45, 250 W	165	HEDL 9140	259	AB 28	301	209.4	223.9	223.9	238.4	238.4	238.4	252.9	252.9	252.9	252.9
EC-max 30, 60 W	177					105.0	119.5	119.5	134.0	134.0	134.0	148.5	148.5	148.5	148.5
EC-max 30, 60 W	177	MR	251			117.2	131.7	131.7	146.2	146.2	146.2	160.7	160.7	160.7	160.7
EC-max 30, 60 W	177	HEDL 5540	258			125.6	140.1	140.1	154.6	154.6	154.6	169.1	169.1	169.1	169.1
EC-max 30, 60 W	177			AB 20	298	137.1	151.6	151.6	166.1	166.1	166.1	180.6	180.6	180.6	180.6
EC-max 30, 60 W	177	HEDL 5540	250	AB 20	298	157.7	172.2	172.2	186.7	186.7	186.7	201.2	201.2	201.2	201.2
EC-max 40, 70 W	178					99.0	113.5	113.5	128.0	128.0	128.0	142.5	142.5	142.5	142.5
EC-max 40, 70 W	178	MR	251			114.9	129.4	129.4	143.9	143.9	143.9	158.4	158.4	158.4	158.4
EC-max 40, 70 W	178	HEDL 5540	258			122.4	136.9	136.9	151.4	151.4	151.4	165.9	165.9	165.9	165.9
EC-max 40, 70 W	178			AB 28	299	139.0	153.5	153.5	168.0	168.0	168.0	182.5	182.5	182.5	182.5
EC-max 40, 70 W	178	HEDL 5540	258	AB 28	299	162.4	176.9	176.9	191.4	191.4	191.4	205.9	205.9	205.9	205.9
EC-power 30, 100 W	185					88.0	102.5	102.5	117.0	117.0	117.0	131.5	131.5	131.5	131.5
EC-power 30, 100 W	185	MR	251			100.2	114.7	114.7	129.2	129.2	129.2	143.7	143.7	143.7	143.7
EC-power 30, 100 W	185	HEDL 5540	258			108.6	123.1	123.1	137.6	137.6	137.6	152.1	152.1	152.1	152.1
EC-power 30, 100 W	185			AB 20	298	120.1	134.6	134.6	149.1	149.1	149.1	163.6	163.6	163.6	163.6
EC-power 30, 100 W	185	HEDL 5540	258	AB 20	298	140.7	155.2	155.2	169.7	169.7	169.7	184.2	184.2	184.2	184.2
EC-power 30, 200 W	186					105.0	119.5	119.5	134.0	134.0	134.0	148.5	148.5	148.5	148.5
EC-power 30, 200 W	186	MR	251			117.2	131.7	131.7	146.2	146.2	146.2	160.7	160.7	160.7	160.7
EC-power 30, 200 W	186	HEDL 5540	258			125.6	140.1	140.1	154.6	154.6	154.6	169.1	169.1	169.1	169.1
EC-power 30, 200 W	186			AB 20	298	137.1	151.6	151.6	166.1	166.1	166.1	180.6	180.6	180.6	180.6
EC-power 30, 200 W	186	HEDL 5540	258	AB 20	298	157.7	172.2	172.2	186.7	186.7	186.7	201.2	201.2	201.2	201.2
MCD EPOS, 60 W	295					161.0	175.5	175.5	190.0	190.0	190.0	204.5	204.5	204.5	204.5
MCD EPOS P, 60 W	295					161.0	175.5	175.5	190.0	190.0	190.0	204.5	204.5	204.5	204.5

APPENDIX E: Ball screw characteristics Bosch Rexroth AG



Nuts

Miniature Single Nut with Flange FEM-E-B

Miniature series
Rexroth mounting dimensions
Flange type B

With seals
With backlash or reduced backlash
For precision-rolled screws SN-R
of tolerance grade T5, T7

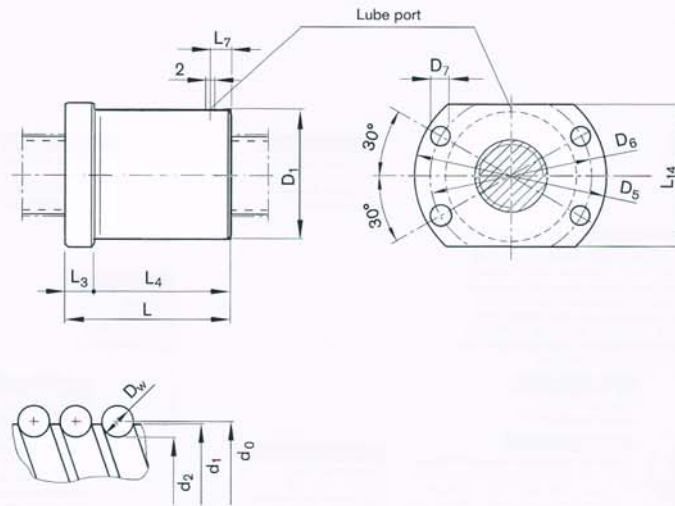


Ordering code: FEM-E-B 6 x 2R x 0.8-4 1 1 T7 R 83K060 41K050 250 0 1

d_0 = nominal diameter
P = lead
(R = right-hand, L = left-hand)
 D_w = ball diameter
i = number of ball track turns

Category	Size $d_0 \times P \times D_w - i$	Part number	Load ratings		Speed ¹⁾
			dyn. C (N)	stat. C ₀ (N)	v_{max} (m/min)
A	6 x 1R x 0.8 - 4	R1532 100 06	900	1290	3
A	6 x 2R x 0.8 - 4	R1532 120 06	890	1280	6
A	8 x 1R x 0.8 - 4	R1532 200 06	1020	1740	3
A	8 x 2R x 1.2 - 4	R1532 220 06	1870	2760	6
A	8 x 2.5R x 1.588 - 3	R1532 230 06	2200	2800	15
A	12 x 2R x 1.2 - 4	R1532 420 06	2240	4160	12
A	12 x 5R x 2 - 3	R1532 460 06	3800	5800	30
A	12 x 10R x 2 - 2	R1532 490 06	2500	3600	60

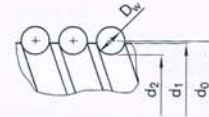
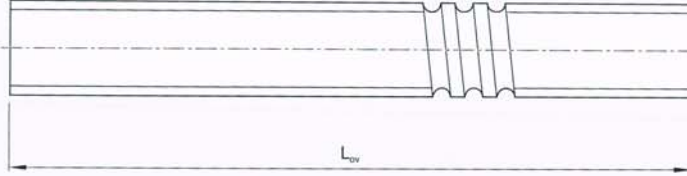
1) See Page 97 Characteristic speed $d_0 \cdot n$ and Page 118 Critical speed n_c



Size	Dimensions (mm)											Weight m (kg)	
	d ₁	d ₂	D ₁	D ₅	D ₆	D ₇	L	L ₃	L ₄	L ₇	L ₁₄		
d ₀ x P x D _w - i			g6										
6 x 1R x 0.8 - 4	6.0	5.3	12	24	18	3.4	19.5	3.5	16	3.5	16	0.020	
6 x 2R x 0.8 - 4	6.0	5.3	12	24	18	3.4	22.5	3.5	19	3.0	16	0.020	
8 x 1R x 0.8 - 4	8.0	7.3	16	28	22	3.4	22.0	6.0	16	3.5	19	0.035	
8 x 2R x 1.2 - 4	8.0	7.0	16	28	22	3.4	25.0	6.0	19	3.0	19	0.050	
8 x 2.5R x 1.588 - 3	7.5	6.3	16	28	22	3.4	16.0	6.0	10	3.0	19	0.030	
12 x 2R x 1.2 - 4	11.7	10.8	20	37	29	4.5	19.0	8.0	11	2.5	24	0.055	
12 x 5R x 2 - 3	11.4	9.9	22	37	29	4.5	28.0	8.0	20	6.0	24	0.075	
12 x 10R x 2 - 2	11.4	9.9	22	37	29	4.5	33.0	8.0	25	8.0	24	0.085	

Screws

Precision-Rolled Screw SN-R



Please state lengths in the "Inquiry/Order Form"
L_{ov} = overall length

Ordering code: SN 20 x 5R x 3 X X T7 R 00T200 00T200 1250 1 0

Size d _o x P x D _w	Part number			Dimensions (mm)		Moment of inertia J _s (kgcm ² /m)	Maximum length (mm)		Weight (kg/m)
	Tolerance grade T5	Tolerance grade T7	Tolerance grade T9	d ₁	d ₂		Standard	On request	
6x1Rx0.8	R1531 105 00	R1531 107 00	R1531 109 00	6.0	5.3	0.02	On request		0.19
6x2Rx0.8	R1531 125 00	R1531 127 00	R1531 129 00	6.0	5.3	0.02			0.19
8x1Rx0.8	R1531 205 00	R1531 207 00	R1531 209 00	8.0	7.3	0.04			0.36
8x2Rx1.2	R1531 225 00	R1531 227 00	R1531 229 00	8.0	7.0	0.04			0.36
8 x 2.5Rx1.588	R1531 235 00	R1531 237 00	R1531 239 00	7.5	6.3	0.04			0.30
12x2Rx1.2	R1531 425 00	R1531 427 00	R1531 429 00	11.7	10.8	0.13			1500
12x5Rx2	R1531 465 10	R1531 467 10	R1531 469 10	11.4	9.9	0.11			0.75
12x10Rx2	R1531 495 00	R1531 497 00	R1531 499 00	11.4	9.9	0.11			0.74
16x5Lx3	R1551 015 00	R1551 017 00	R1551 019 00	15.0	12.9	0.31			1.24
16x5Rx3	R1511 015 00	R1511 017 00	R1511 019 00	15.0	12.9	0.31			1.24
16x10Rx3	R1511 045 00	R1511 047 00	R1511 049 00	15.0	12.9	0.31			1.23
16x16Rx3	R1511 065 10	R1511 067 10	R1511 069 10	15.0	12.9	0.34			1.29
20x5Rx3	R1511 115 00	R1511 117 00	R1511 119 00	19.0	16.9	0.84			2.03
20x40Rx3.5-4	R2521 150 00	R2521 170 00	R2521 190 00	19.0	16.4	0.86			2.06
20x20Rx3.5	R1511 175 10	R1511 177 10	R1511 179 10	19.0 ¹⁾	16.7	0.81			1.99
25x5Rx3	R1511 215 00	R1511 217 00	R1511 219 00	24.0	21.9	2.22			2500
25x10Rx3	R1511 245 00	R1511 247 00	R1511 249 00	24.0	21.9	2.39			3.43
25x25Rx3.5	R1511 285 10	R1511 287 10	R1511 289 10	24.0	21.4	2.15			3.25
32x5Rx3.5	R1511 315 00	R1511 317 00	R1511 319 00	31.0	28.4	6.05			5.45
32x5Lx3.5	R1551 315 00	R1551 317 00	R1551 319 00	31.0	28.4	6.05			5.45
32x10Rx3.969	R1511 345 10	R1511 347 10	R1511 349 10	31.0	27.9	6.40			5.60
32x20Rx3.969	R1511 375 10	R1511 377 10	R1511 379 10	31.0	27.9	6.39			5.60
32x32Rx3.969	R1511 395 10	R1511 397 10	R1511 399 10	31.0	27.9	6.17			5.50
40x5Rx3.5	R1511 415 00	R1511 417 00	R1511 419 00	39.0	36.4	15.64			4500
40x5Lx3.5	R1551 415 00	R1551 417 00	R1551 419 00	39.0	36.4	15.64			8.78
40x10Rx6	R1511 445 00	R1511 447 00	R1511 449 00	38.0	33.8	13.55			4500
40x10Lx6	R1551 445 00	R1551 447 00	R1551 449 00	38.0	33.8	13.55			8.15
40x12Rx6	R1511 455 00	R1511 457 00	R1511 459 00	38.0	33.8	13.97			8.27
40x16Rx6	R1511 465 00	R1511 467 00	R1511 469 00	38.0	33.8	12.90			7.95
40x20Rx6	R1511 475 00	R1511 477 00	R1511 479 00	38.0	33.8	13.52			8.14
40x40Rx6	R1511 495 10	R1511 497 10	R1511 499 10	38.0	33.8	13.42			8.11
50x5Rx3.5	R1511 515 00	R1511 517 00	R1511 519 00	49.0	46.4	40.03			4500
50x10Rx6	R1511 545 00	R1511 547 00	R1511 549 00	48.0	43.8	35.71	4500	7500	13.25
50x12Rx6	R1511 555 00	R1511 557 00	R1511 559 00	48.0	43.8	36.58			13.41
50x16Rx6	R1511 565 00	R1511 567 00	R1511 569 00	48.0	43.8	34.37			13.00
50x20Rx6.5	R1511 575 10	R1511 577 10	R1511 579 10	48.0	43.3	34.50			13.01
50x40Rx6.5	R1511 595 10	R1511 597 10	R1511 599 10	48.0	43.3	34.34			12.98
63x10Rx6	R1511 645 00	R1511 647 00	R1511 649 00	61.0	56.8	95.82			21.72
63x20Rx6.5	R1511 675 10	R1511 677 10	R1511 679 10	61.0	56.3	93.29			21.42
63x40Rx6.5	R1511 695 10	R1511 697 10	R1511 699 10	61.0	56.3	93.08			21.40
80x10Rx6.5	R1511 745 00	R1511 747 00	R1511 749 00	78.0	73.3	256.86			35.58
80x20Rx12.7	R1501 771 00	R1501 773 00	R1501 775 00	76.0	66.9	211.51			2500

1) The outer diameter d₁ has been changed.

Friction-welded blanks made of precision-rolled screws SN-R

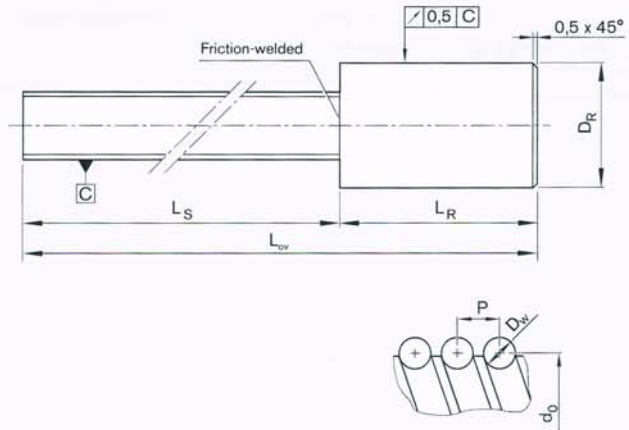
Friction-welded blanks consist of

- a precision-rolled screw part and
- an unmachined spigot.

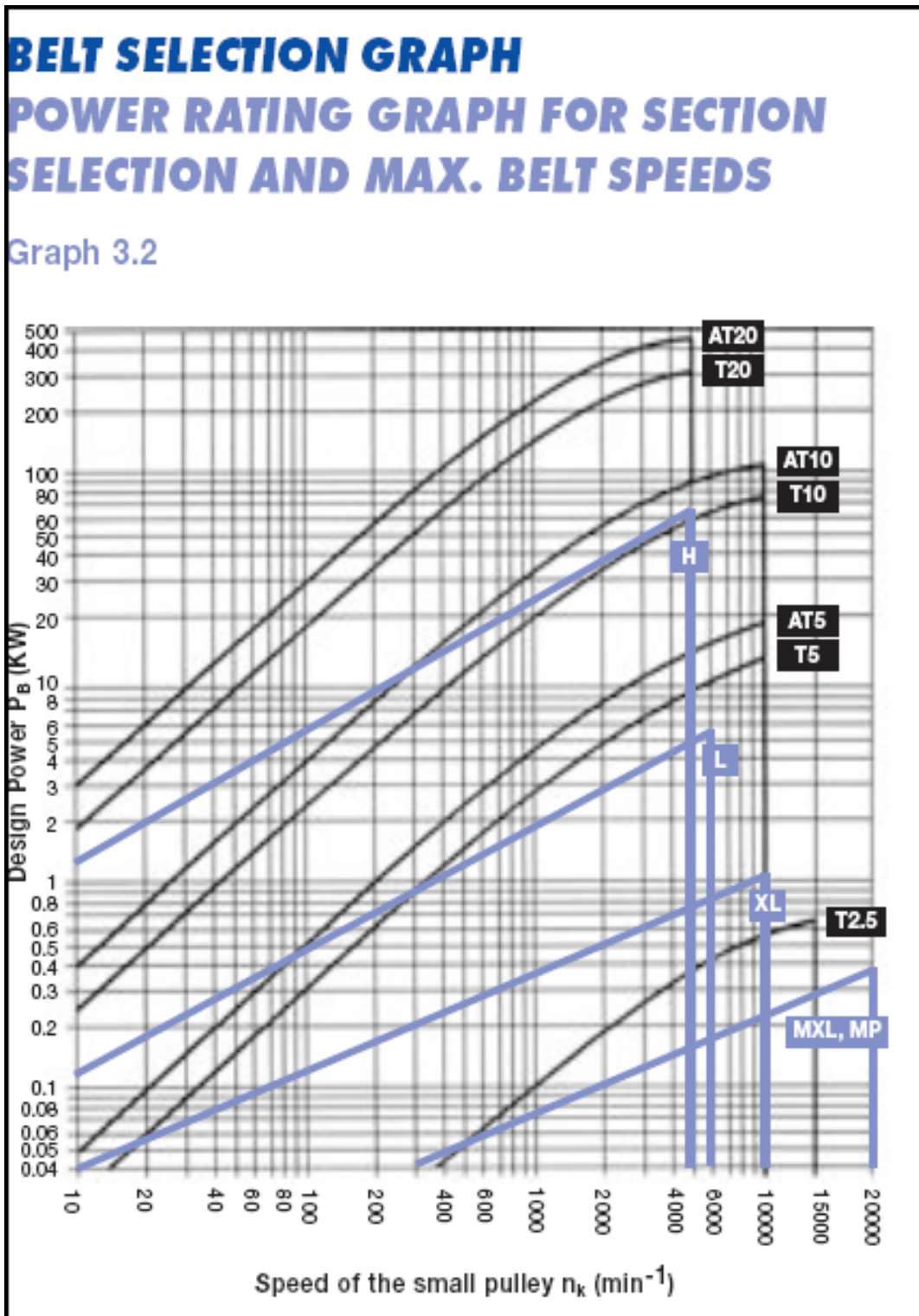
The spigot is fitted to the one end by friction welding and is available in various sizes.

We have a solution to prevent problems arising from big end bearing diameters (e.g. visible thread grooves or axial contact faces which are too small for the fixed bearing). Please ask.

Separate delivery of a screw without end machining and without nut is not planned.

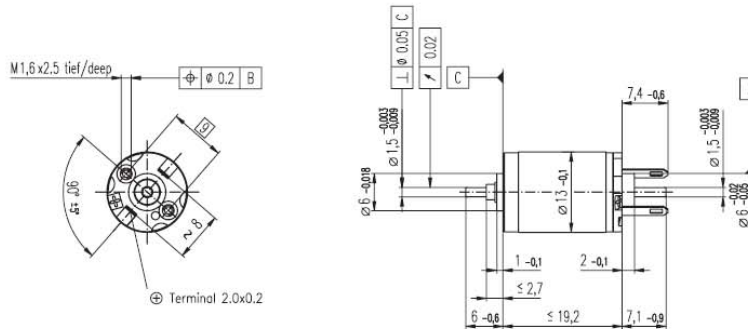


Size	Tolerance grade	Dimensions (mm)			
		D_R	L_R	L_w	L_S
$d_0 \times P \times D_w$		-1	+2		
6x1Rx0.8			On request		
6x2Rx0.8					
8x1Rx0.8					
8x2Rx1.2					
8x2.5Rx1.588	T5	14.25	100	1100	1000
12x2Rx1.2	T5	23.25	100	1100	1000
12x5Rx2	T5	23.25	150	1250	1100
12x10Rx2	T5	23.30	150	1250	1100
16x5Rx3	T5	30.35	200	1700	1500
16x10Rx3	T5	30.35	200	1700	1500
16x16Rx3	T5	30.35	200	1700	1500
20x5Rx3	T5	31.50	200	1700	1500
20x20Rx3.5	T5	30.35	160	1160	1000
25x5Rx3	T5	36.60	200	1700	1500
25x10Rx3	T5	36.60	200	1700	1500
25x25Rx3.5	T5	36.60	200	1700	1500
32x5Rx3.5	T5	46.60	250	2050	1800
32x10Rx3.969	T5	46.60	250	2050	1800
32x20Rx3.969	T5	46.60	250	2050	1800
32x32Rx3.969	T5	46.60	250	2050	1800
40x10Rx6	T5	49.30	300	2300	2000
40x20Rx6	T5	49.30	300	2300	2000
50x10Rx6	T5	61.30	300	2300	2000
50x20Rx6.5	T5	61.30	300	2300	2000



Appendix I: Motor RE13

RE 13 Ø13 mm, Precious Metal Brushes, 0.75 Watt, CE approved



M 1:1

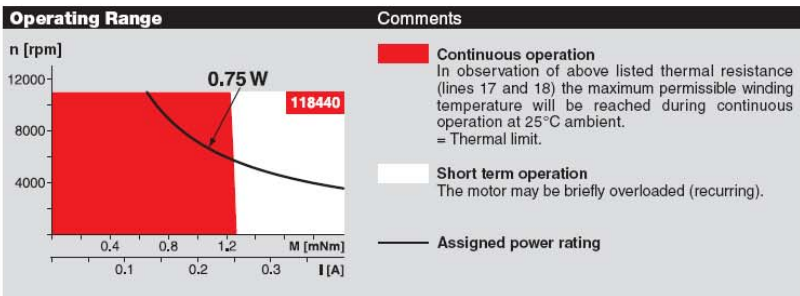
- Stock program
- Standard program
- Special program (on request)

Order Number

118431 118432 118433 118434 **118435** 118436 118437 118438 118439 **118440** 118441 118442 **118443** 118444 118445

Motor Data		118431	118432	118433	118434	118435	118436	118437	118438	118439	118440	118441	118442	118443	118444	118445
Values at nominal voltage																
1 Nominal voltage	V	0.6	0.72	0.9	1.2	1.5	1.8	1.8	2.4	3.0	3.6	4.8	6.0	6.0	7.2	10.0
2 No load speed	rpm	6860	6680	6580	7240	6990	6850	5960	6490	6700	6490	6950	7010	6540	6660	7040
3 No load current	mA	88.1	71.6	56.1	47.3	36.2	29.4	24.7	20.6	17.1	13.7	11.2	9.06	8.34	7.09	5.47
4 Nominal speed	rpm	4810	3690	2940	2690	1460	1490	2980	1560	1390	1500	1620	1620	1430	3330	1590
5 Nominal torque (max. continuous torque)	mNm	0.512	0.643	0.838	1.03	1.27	1.31	0.774	1.27	1.32	1.25	1.32	1.30	1.21	0.799	1.29
6 Nominal current (max. continuous current)	A	0.720	0.720	0.720	0.720	0.674	0.568	0.302	0.391	0.337	0.257	0.217	0.173	0.151	0.087	0.103
7 Stall torque	mNm	1.77	1.49	1.57	1.69	1.65	1.72	1.60	1.72	1.72	1.68	1.77	1.75	1.60	1.65	1.72
8 Starting current	A	2.21	1.52	1.26	1.12	0.843	0.717	0.579	0.509	0.420	0.331	0.280	0.223	0.191	0.167	0.132
9 Max. efficiency	%	64	62	63	64	63	64	63	64	64	64	64	64	63	63	64
Characteristics																
10 Terminal resistance	Ω	0.272	0.474	0.716	1.07	1.78	2.51	3.11	4.72	7.14	10.9	17.1	26.9	31.4	43.1	75.8
11 Terminal inductance	mH	0.0061	0.0091	0.0147	0.0216	0.0362	0.0545	0.0719	0.108	0.158	0.243	0.377	0.579	0.661	0.921	1.59
12 Torque constant	mNm / A	0.802	0.980	1.25	1.51	1.96	2.41	2.76	3.39	4.10	5.08	6.33	7.84	8.38	9.89	13.0
13 Speed constant	rpm / V	11900	9740	7650	6300	4870	3970	3460	2820	2330	1880	1510	1220	1140	965	734
14 Speed / torque gradient	rpm / mNm	4040	4710	4390	4470	4420	4140	3890	3930	4060	4030	4090	4180	4270	4210	4270
15 Mechanical time constant	ms	15.1	14.3	13.7	13.5	13.3	13.1	12.9	12.9	12.9	12.9	13.0	13.1	13.0	13.0	13.1
16 Rotor inertia	gcm ²	0.356	0.290	0.298	0.288	0.287	0.301	0.317	0.313	0.305	0.306	0.303	0.298	0.292	0.295	0.292

Specifications	
Thermal data	
17 Thermal resistance housing-ambient	46 K / W
18 Thermal resistance winding-housing	14 K / W
19 Thermal time constant winding	5.14 s
20 Thermal time constant motor	345 s
21 Ambient temperature	-20 ... +65°C
22 Max. permissible winding temperature	+85°C
Mechanical data (sleeve bearings)	
23 Max. permissible speed	11000 rpm
24 Axial play	0.05 - 0.15 mm
25 Radial play	0.014 mm
26 Max. axial load (dynamic)	0.8 N
27 Max. force for press fits (static) (static, shaft supported)	15 N
28 Max. radial loading, 5 mm from flange	170 N
Other specifications	
29 Number of pole pairs	1
30 Number of commutator segments	7
31 Weight of motor	15 g



maxon Modular System Overview on page 16 - 21

Encoder MR
16 CPT,
2 channels
Page 252

Encoder MR
64 - 256 CPT,
2 channels
Page 253 / 254

Encoder MEnc
Ø13 mm
16 CPT, 2 channels
Page 270

Recommended Electronics:
LSC 30/2 Page 276
Notes 18

Values listed in the table are nominal.
Explanation of the figures on page 49.

APPENDIX J : Design and Stress calculations

Parts Design

Nut Support: elaborated stress analysis calculations

Manual Stress Analysis

Both pins will be considered as beams, constraint at the middle part. The load causes bending stress and shear stress in each pin:

$$\sigma_{\text{bending}} = M * y / I = 928 \text{ N} * 15 \text{ mm} * 5 \text{ mm} / 490,9 \text{ mm}^4 = 141,7 \text{ Mpa.}$$

$$\tau = F / A = 928 \text{ N} / 78,5 \text{ mm}^2 = 11,82 \text{ Mpa.}$$

Resulting in a $\sigma_{\text{equivalent}} = 143,17 \text{ Mpa.}$

FEM Stress Analysis

A FEM stress analysis is performed and the results will be compared.

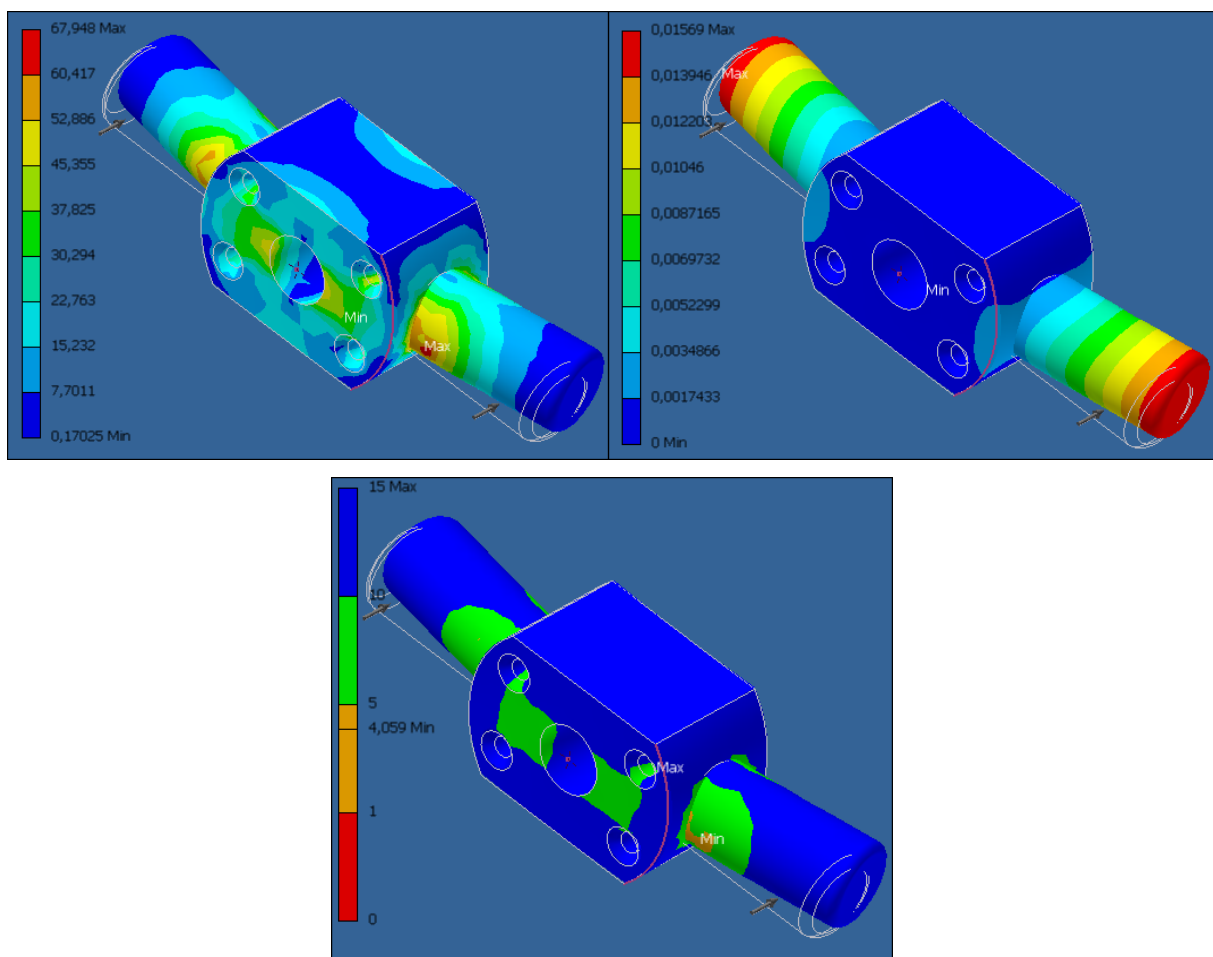


Fig. 128: FEM static stress analysis of Nut support: the equivalent stress in Mpa (left), the deformation in mm (right) and the static safety factor (under)

max equivalent stress (Mpa)	143
max deformation (mm)	0,01
minimum safety factor	1,93

Fig. 97:Results of the ISSD static stress analysis of a loaded pin of the Nut support

max equivalent stress (Mpa)	68
max deformation (mm)	0,016
minimum safety factor	4

Table 50 summarises the results of the FEM stress analysis. The part weighs 72g.

Table 50: FEM static stress results of Nut support

max equivalent stress (Mpa)	67,95
max deformation (mm)	0,016
minimum safety factor	4

Notice that the stress calculated manually is with a fixed constraint at the base of the pin. In Inventor however, the threaded hole was constraint, allowing deformation of the middle part, reducing the stress at the pin constraint.

Rod: elaborated stress analysis calculations

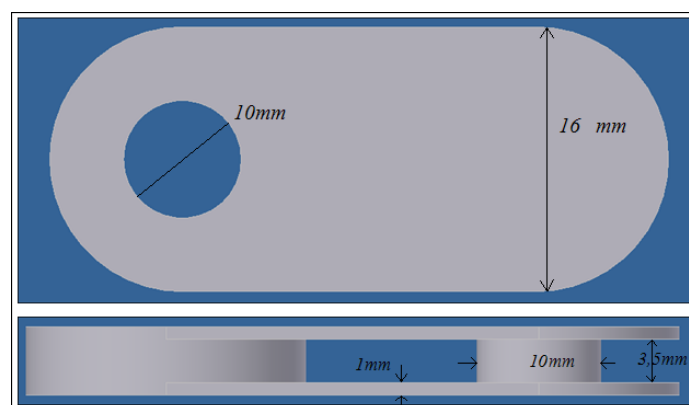


Fig. 129: Accurate design of rod (front and side)

Manual Static Stress Analysis

There are 3 zones for which a manual stress analysis will be performed, because these are the most critical zones. Fig. 101 shows the most load zones of the rod. These zones will be referred to as zone 1, 2 and 3.

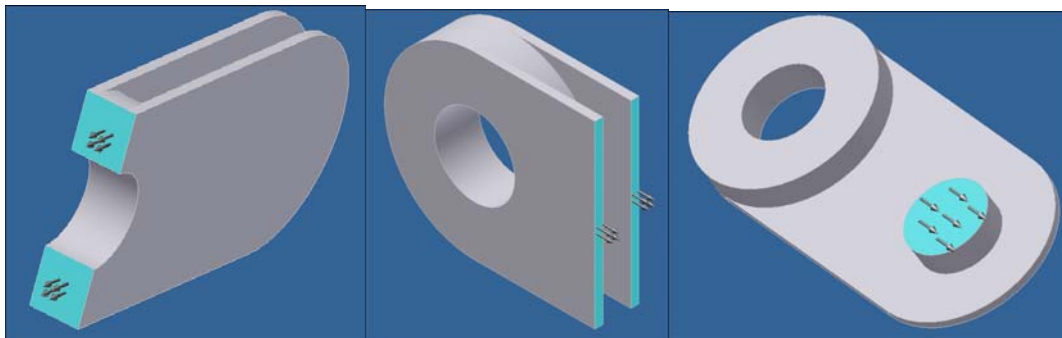


Fig. 130: Most critical zones of the rod: zones 1 (left), 2 (middle) and 3 (right)

Zone 1:

$$\sigma_{\text{normal}} = F/A = 2 \cdot 928 \text{ N} / 33 \text{ mm}^2 = 56,24 \text{ Mpa}$$

Zone 2:

$$\sigma_{\text{normal}} = F/A = 2 \cdot 928 \text{ N} / 32 \text{ mm}^2 = 58 \text{ Mpa}$$

Zone 3:

$$\tau = D / A = 2 \cdot 928 \text{ N} / 78,54 \text{ mm}^2 = 23,63 \text{ Mpa}$$

FEM Static Stress Analysis

Situation 1: load on the hole, constraint on the pin

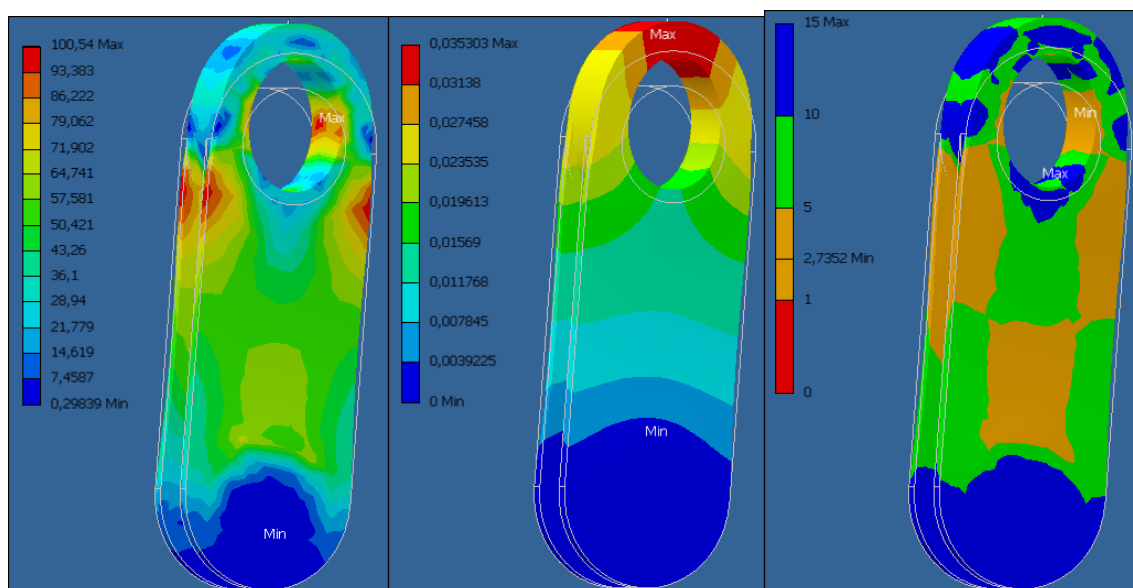


Fig. 131: FEM static stress analysis of Rod: the equivalent stress in Mpa (left), the deformation in mm (middle) and the static safety factor (right)

Table 51 summarises the results of the FEM stress analysis. The part weighs 5g.

Table 51: FEM static stress results of Rod

max equivalent stress (Mpa)	110,54
max deformation (mm)	0,035
minimum safety factor	2,74

Notice that the stress in zone 1 is much higher than calculated. This is due to stress concentrations near the corners of the part. Also Notice that these high stresses occur only at the surface of the hole and near the connection zones with the side plates. Fig. 132 illustrates this.

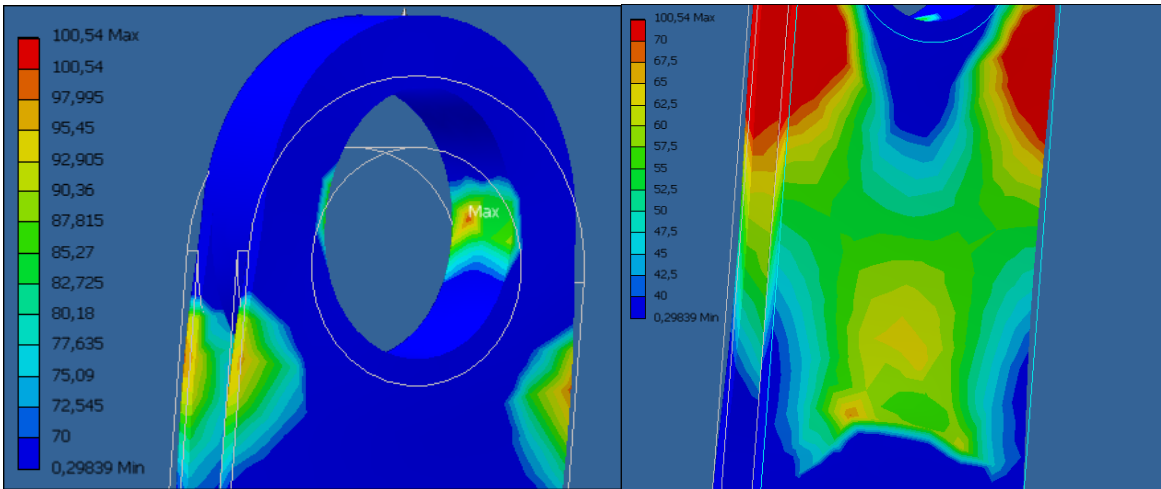


Fig. 132: high stress zones 1 and 2

The right figure shows that the stress in zone 2 (approximately 55 Mpa) corresponds with the calculated stress.

Situation 2: load on the pin, constraint on the side plates

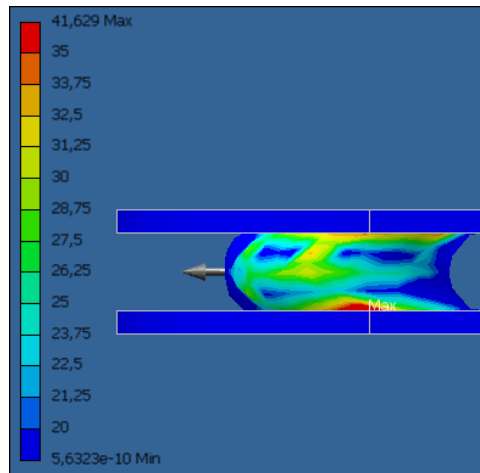


Fig. 133: high stress zone 3

Again, the simulated stresses are much higher than the calculated one. That is because stress concentrations at the constraints are not incorporated in the manual stress analysis.

Ankle Support: elaborated stress analysis calculations

Initial Design

Loading Situation 1

The Initial design for the Ankle Support is shown in Fig. 134

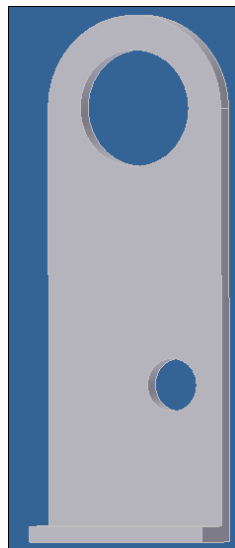


Fig. 134: Initial design for the Ankle Support

Manual Static Stress Analysis

A stress analysis has been performed in ISSD. The results are shown in Fig. 104 and Table 52.

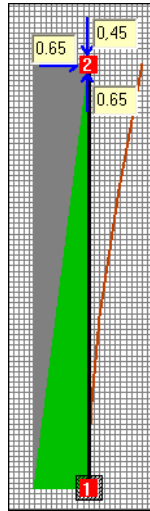


Fig. 135: Static stress analysis on Ankle Support: the Acting Loads on the beam in kN causing the stress due to bending (green), the shear stress (grey) and the deflection shape(red).

Table 52: Results of static stress analysis on Ankle Support (w x d x h = 35 x 4 x 80 mm)

STRESS	<i>Mpa</i>
max normal stress (σ_n)	
<i>due to bending</i>	63,67
<i>due to normal force</i>	1,43
max shear stress (τ)	
<i>node 2 - node 1</i>	4,64
max equivalent stress	65,59
DEFORMATION	<i>mm</i>
<i>node 2</i>	0,11

FEM static stress analysis

Analysing the part in Inventor generates following results:

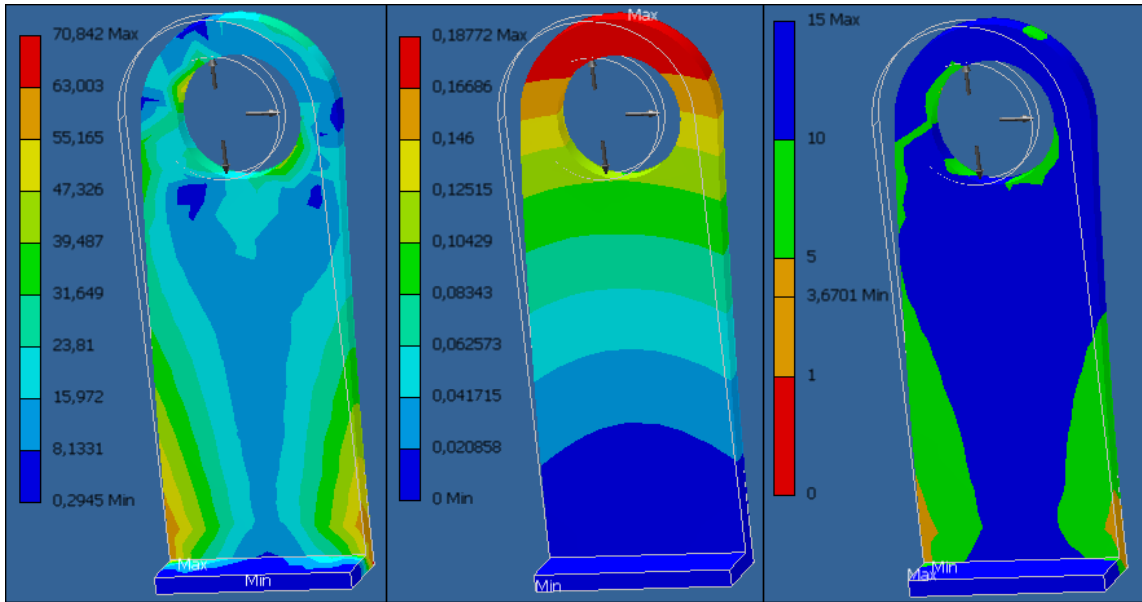


Fig. 136: FEM static stress analysis of Ankle Support with first loading situation: the equivalent stress in Mpa (left), the deformation in mm (middle) and the static safety factor (right)

Table 53: Results of the FEM static stress analysis of the Ankle Support

max equivalent stress (Mpa)	70,84
max deformation (mm)	0,188
minimum safety factor	3,67

Notice the peak stress of 70,8 obtained in Inventor is due to stress concentration at the constraint. The stress at the foot of the part is 60 Mpa (orange area in Fig. 136 left). Which differs 7,7% with the stress obtained in ISSD. Also notice that the removed circle at the top is not taken into account in the ISSD calculations.

Loading situation 2

FEM static stress analysis

Analysing the part in Inventor with the second loading situation generates following results:

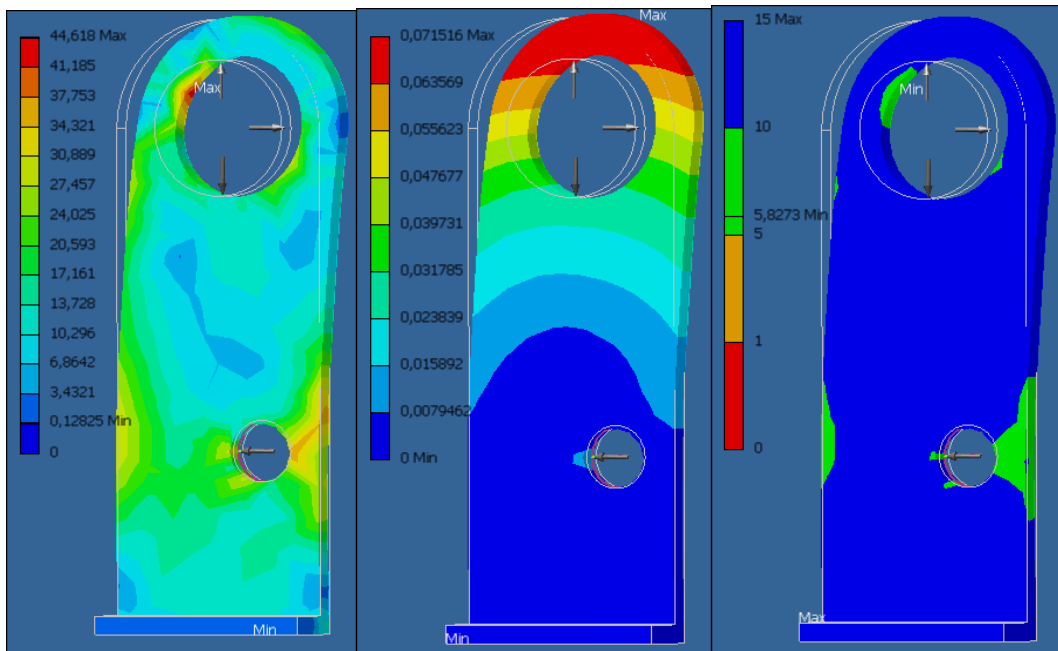


Fig. 137: FEM static stress analysis of Ankle Support with second loading situation: the equivalent stress in Mpa (left), the deformation in mm (middle) and the static safety factor (right)

Table 54: Results of the FEM static stress analysis of the Ankle Support

max equivalent stress (Mpa)	44,62
max deformation (mm)	0,071
minimum safety factor	5,82

Obviously, the first loading situation is more critical than the second loading condition.

Regarding the fact that the Foot Plate will need supporting beams to avoid failure, the Ankle Support will be redesigned with supporting beams. Only the first loading situation will be simulated for the accurate part, as this generates higher stresses than the second loading situation.

Accurate Design

Fig. 103 shows the accurate design of the meshed Ankle Support and the occurring loads.

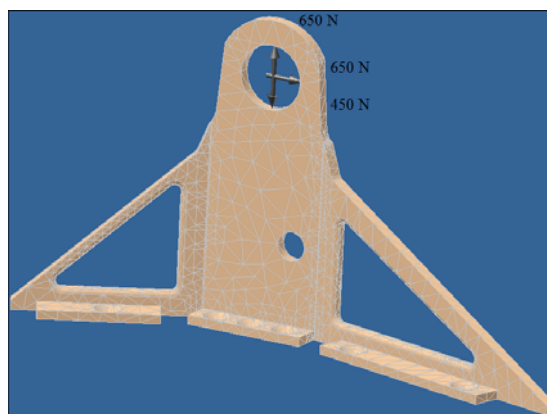


Fig. 138: Accurate design of the Ankle Support and the loads

Manual Static Stress Analysis

Fig. 139 and Table 55 shows the Static stress analysis results of a simplification of the Ankle Support in ISSD.

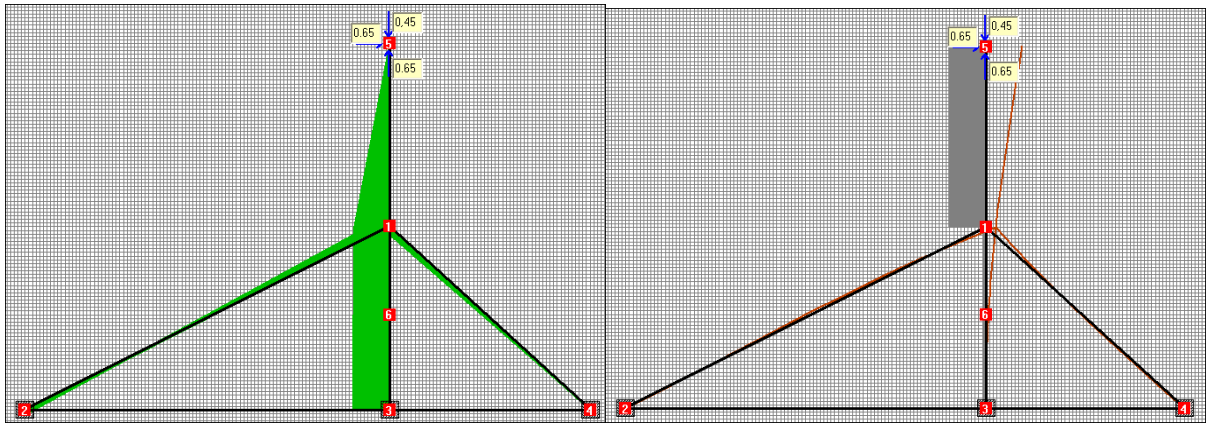


Fig. 139: Static stress analysis on accurate Ankle Support: the Acting Loads on the beam in kN causing the stress due to bending (left), the shear stress and the deflection shape(right).

Table 55: Results of static stress analysis on accurate Ankle Support

	Beam 1/2	Beam 1/4	Beam 1/5	Beam 1/3
<i>section (mm²)</i>	29,7	14,2	160	160
STRESS	Mpa	Mpa	Mpa	Mpa
max normal stress (σ_n)				
<i>due to bending</i>	8,79	4,82	30,46	31,65
<i>due to normal force</i>	15,78	18,89	1,25	1,05
max shear stress (τ)	negl.	negl.	4,06	negl
max equivalent stress	24,57	23,71	32,48	32,70
DEFORMATION	<i>mm</i>	<i>mm</i>	<i>mm</i>	<i>mm</i>
<i>node</i>			0,1	

Notice that the highest stress occurs at node 3, which has an equivalent stress of 31,65 Mpa
 These results are compared to a FEM static stress analysis shown in Fig. 139.

FEM static stress analysis

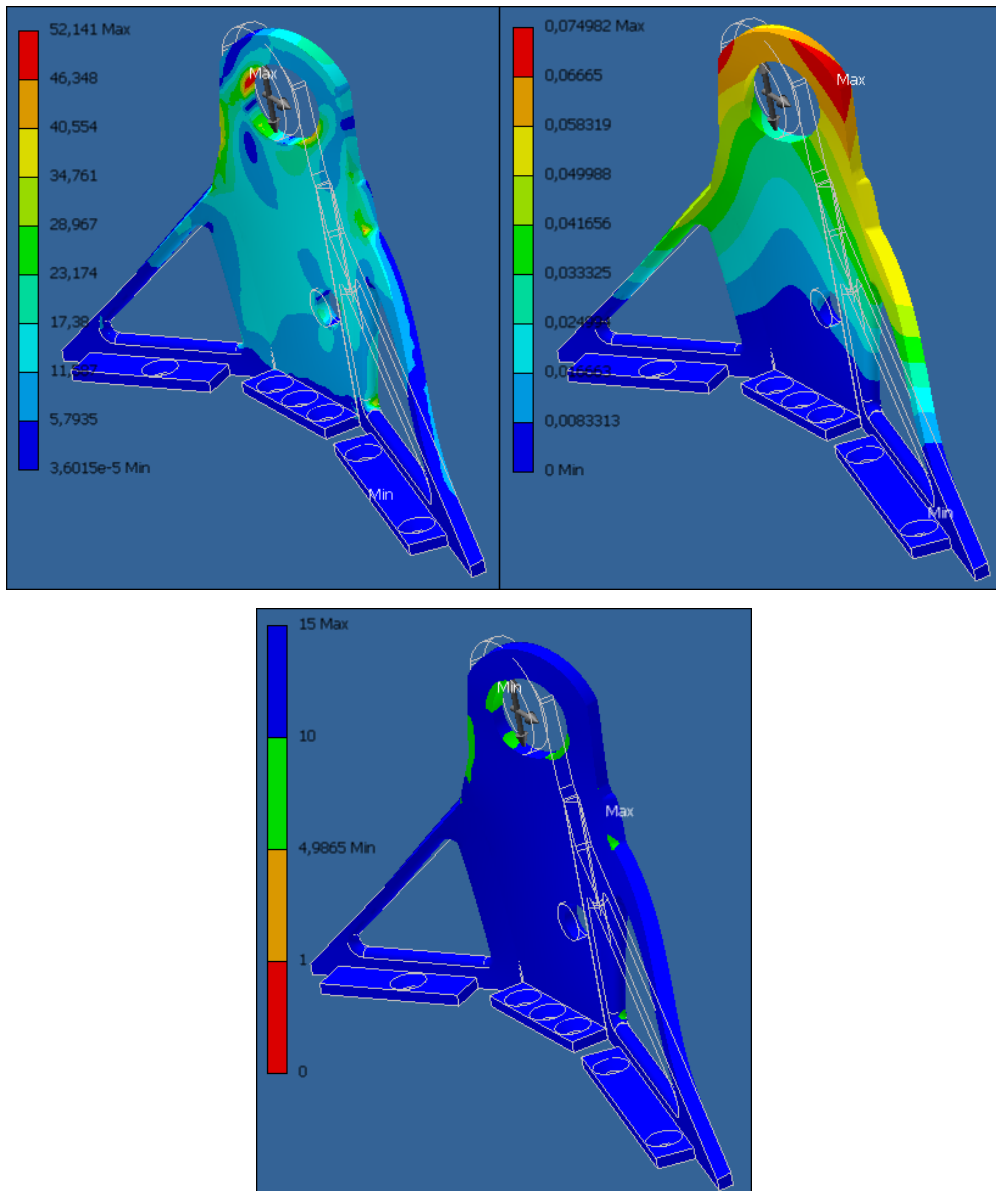


Fig. 140: FEM static stress analysis of accurate Ankle Support: the equivalent stress in Mpa (left), the deformation in mm (right) and the static safety factor (below)

Table 56: Results of the FEM static stress analysis of the accurate Ankle Support

max equivalent stress (Mpa)	52,14
max deformation (mm)	0,075
minimum safety factor	4,99

By adjusting the colour bar, the stress at node 3 and 1 become more distinct. The stress at node 3 is approximate 25 Mpa (compared to 31,65 Mpa calculated with ISSD). The maximum stress however is due to stress concentrations at the corners and at the removed circle.

Foot - Sole: elaborated stress analysis calculations

Manual Static Stress Analysis

In ISSD the model can be simplified into the following beam model, considering the fact that only the support plates and beam will bear the body loads. Notice that ISSD is a 2D program and simulating both supporting beams and the connecting Foot-sole is not possible. Due to symmetry and loading conditions, it seemed reasonable to simplify the 3D model into the following model and simply use half the load (as both supporting beams are loaded).

F_{heel} and F_{back}

Fig. 141 and Table 57 illustrate the results of the analysis.

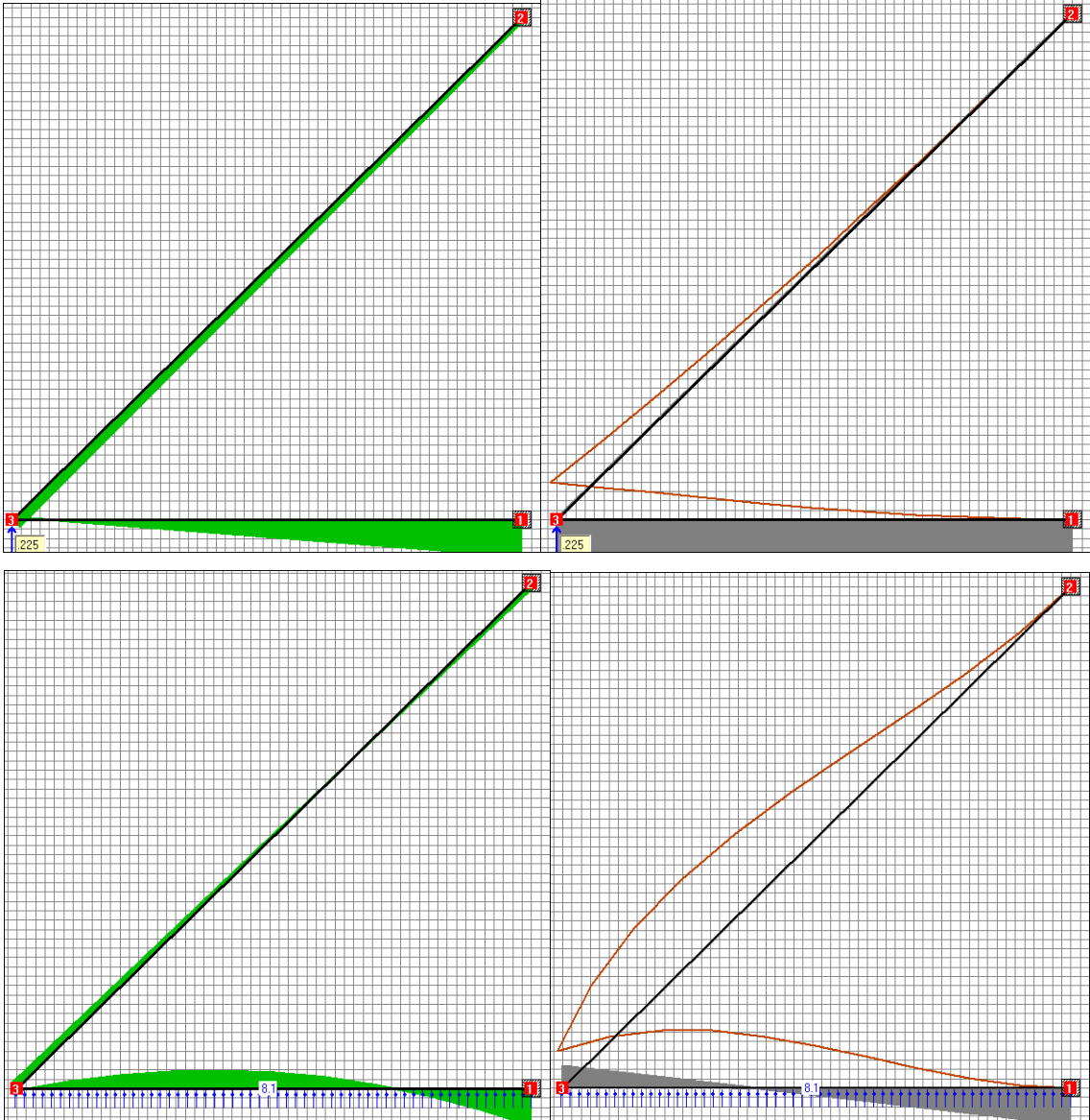


Fig. 141: Manual Static stress analysis of Foot-Sole: the Acting Load F_{heel} on the beam in kN causing the stress due to bending (above left), the shear stress and the deflection shape(above right). The Acting Load F_{back} on the beam in kN causing the stress due to bending (below left), the shear stress and the deflection shape (below right).

Table 57: Results of ISSD analysis on Foot - sole with load F_{heel} and F_{back}

ISSD analysis	F_{heel}		F_{back}	
	Beam 2/3	Beam 3/1	Beam 2/3	Beam 3/1
STRESS	Mpa	Mpa	Mpa	Mpa
max normal stress (σ_n)				
<i>due to bending</i>	2,6	9,8	22,4	109,3
<i>due to normal force</i>	21,80	8,40	16,50	6,30
max shear stress (τ)	negl.	negl.	negl.	10,45
max equivalent stress	17,25	12,87	27,51	81,74
DEFORMATION	mm	mm	mm	mm
<i>node 3</i>	0,041		0,031	

F_{toe} and F_{front}

Fig. 142 and Table 58 illustrate the results of the analysis.

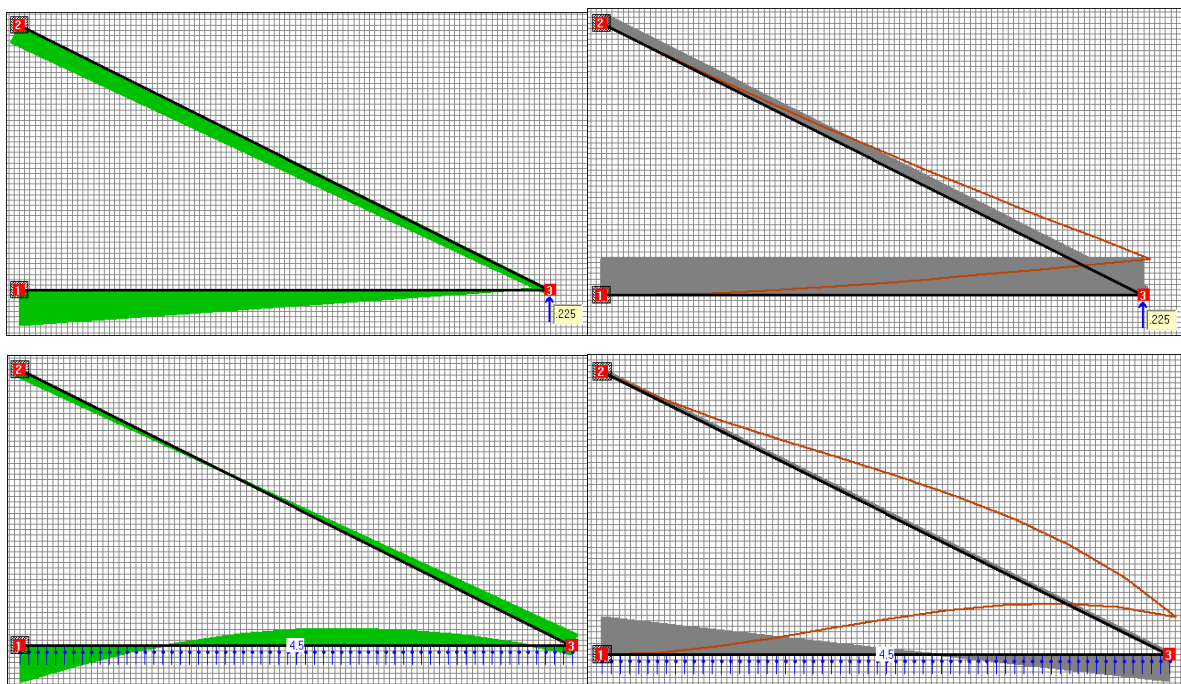


Fig. 142: Manual Static stress analysis of Foot-Sole: the Acting Load F_{toe} on the beam in kN causing the stress due to bending (above left), the shear stress and the deflection shape(above right). the Acting Load F_{front} on the beam in kN causing the stress due to bending (below left), the shear stress and the deflection shape(below right).

Table 58: Results of ISSD analysis on Foot - sole with load F_{toe} and F_{front}

ISSD analysis	<i>F_{toe}</i>		<i>F_{front}</i>	
	Beam 2/3	Beam 3/1	Beam 2/3	Beam 3/1
STRESS	Mpa	Mpa	Mpa	Mpa
max normal stress (σ_n)				
<i>due to bending</i>	5,15	9,1	33,3	99,53
<i>due to normal force</i>	16,43	12,20	12,60	9,06
max shear stress (τ)	negl.	negl.	negl.	7,38
max equivalent stress	15,26	15,06	32,46	76,78
DEFORMATION	<i>mm</i>	<i>mm</i>	<i>mm</i>	<i>mm</i>
<i>node 3</i>	0,093		0,071	

A FEM static stress analysis should now be performed in order to compare the results.

Notice that Buckling failure for the various beams is also taken into account via following formula:

$$P_k = \frac{\pi^2 \cdot E \cdot I}{l_k^2}$$

None of the loads exceeds the *Critical Buckling Loads*.

FEM Static Stress Analysis

Performing a stress analysis on the Foot–sole would not generate realistic values as it is intrinsically reinforced by the Ankle Supports and the bearings of the Ball screw assembly. As it is impossible in Inventor 2008 to perform a static stress analysis on assemblies, the foot has to be recreated in one part. This is shown in Fig. 109.

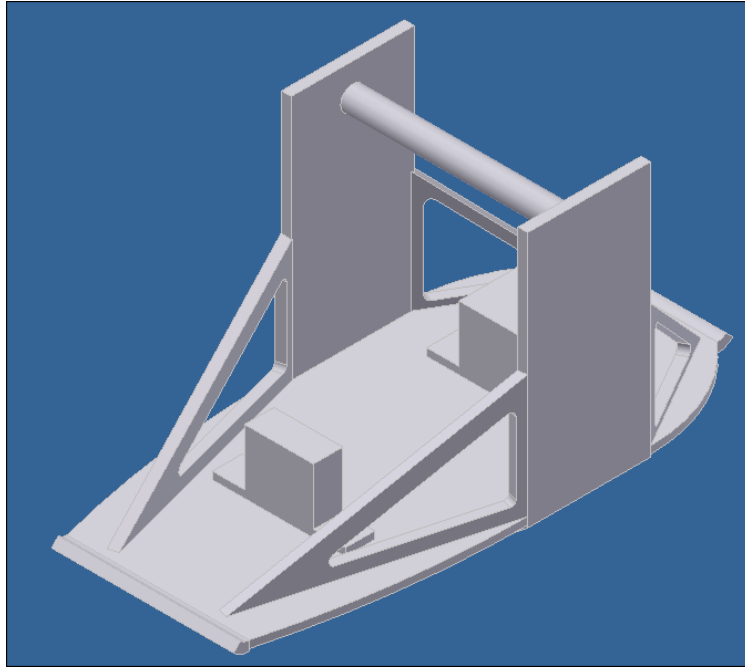
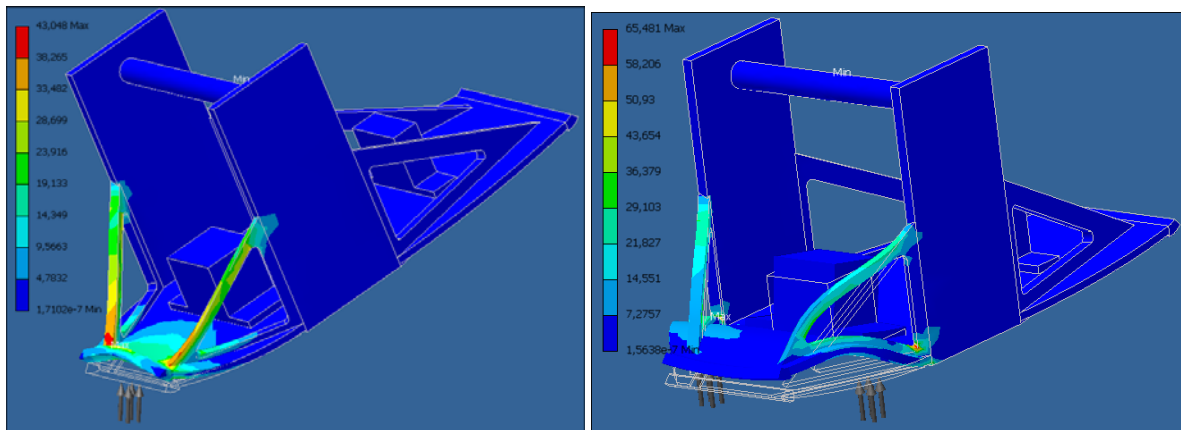


Fig. 143: Recreation of the foot with bearings of the Ball screw assembly and Ankle Supports

Notice that the ball screw and motor are not placed, because these parts should not bear any loads. All the loads should be beared by the Foot–sole. The maximum allowed misalignment of the motor axis is 0.006 mm.

Fig. 110 and Table 44 show the results of the FEM static stress analysis.



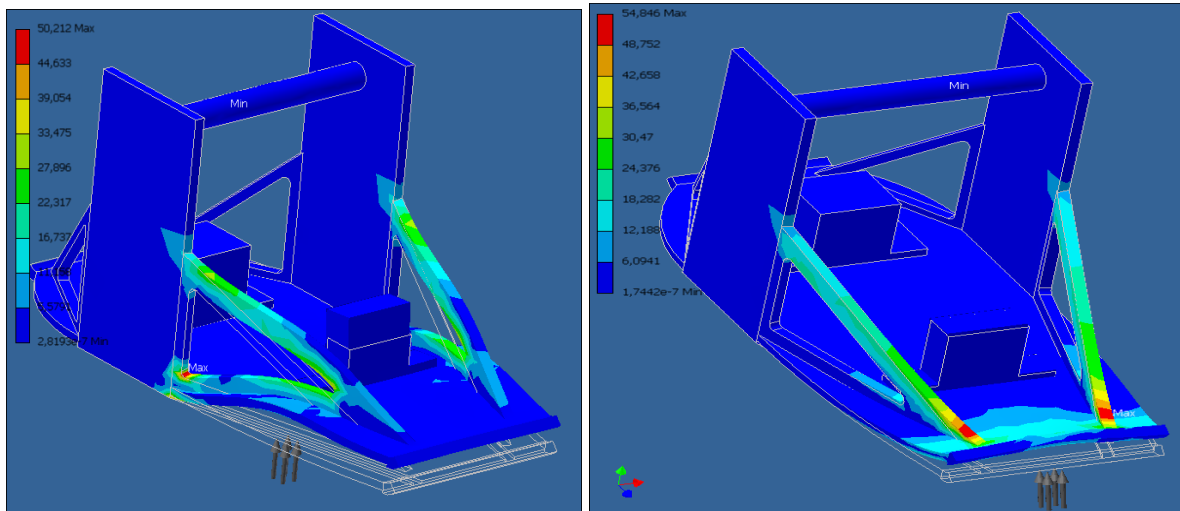


Fig. 144: FEM static stress analysis of Foot-sole: F_{heel} and F_{back} (above) and F_{front} and F_{toe} (below): Equivalent stress in Mpa

Table 59: Results of FEM stress analysis

Inventor analysis	F_{heel}	F_{back}	F_{front}	F_{toe}
STRESS	Mpa	Mpa	Mpa	Mpa
max equivalent stress	43	65,48	50,2	54,8
DEFORMATION	mm	mm	mm	mm
maximum deformation	0,1	0,046	0,065	0,166
SAFETY FACTOR				
minimum safety factor	6,3	4,2	5,5	5

Even though the model was simplified, the ISSD results are of the same order of magnitude than the Inventor results. Notice that ISSD as explained above does not take local stresses concentrations into account, which is why maximum Inventor stresses and deformations are overall rather higher than the ISSD calculated stresses.

Leg Box: elaborated stress analysis calculations

Initial DESIGN

The initial design and the acting forces on the Leg Box are shown in Fig. 145.

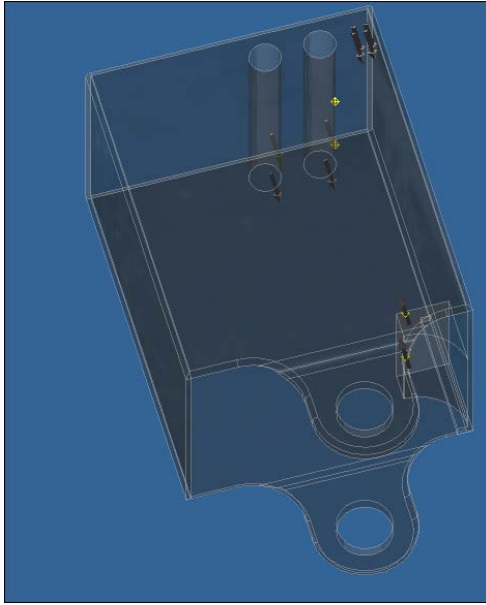


Fig. 145: Initial Design and acting forces on Leg Box

Notice that there are two pins at the top of the Leg Box. The springs will be connected to cables. These cables go round the two pins (pulleys) and are connected to the support plate. This is shown in the Final Assembly.

Manual Static Stress Analysis

Due to the complex loading condition, the different loading conditions were recreated separately:

1. a hollow beam with a load of 2660 N (900N body load and 1760 spring load)
2. a cylinder with two loads of 1350 N and 410 N, respectively
3. a plate with a load of 1760 N (1350 N and 410 N)

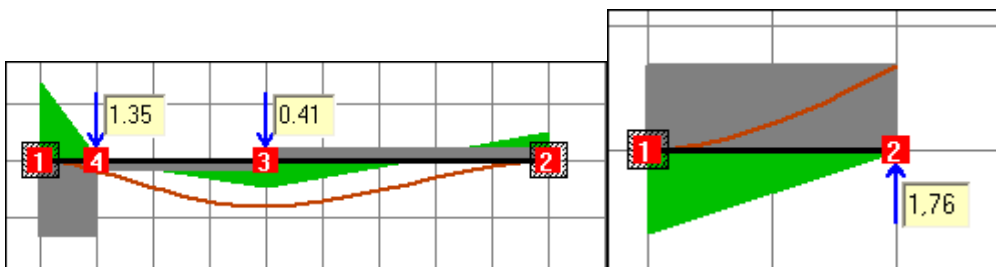


Fig. 146: ISSD static stress analysis of the pin (left) and support plate (right): the stress due to bending (green), the shear stress (grey) and the deformed shape (red)

Table 60: Results of ISSD static stress analysis of the hollow beam, pin and support plate of the Leg Box

	hollow beam	pin	plate
STRESS	Mpa	Mpa	Mpa
max normal stress (σ_n)			
<i>due to bending</i>	-	92	46,9
<i>due to normal force</i>	6,72	0,00	0,00
max shear stress (τ)	-	13,6	3,9
max equivalent stress	6,72	69,19	33,84
DEFORMATION	mm	mm	mm
node	-	0,03	0.018

These values are acceptable and can be compared to FEM analysis.

FEM Static Stress analysis

Fig. 147 and Table 61 illustrate the Fem analysis and the results.

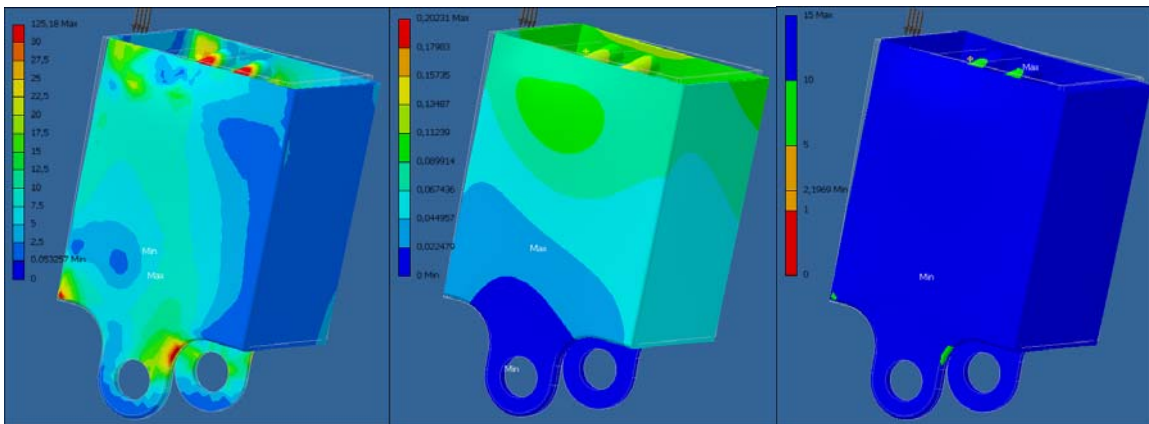


Fig. 147: FEM static stress analysis of the hollow beam of the Leg Box: Equivalent stress in Mpa (left), Deformation in mm (middle) and Safety Factor (right)

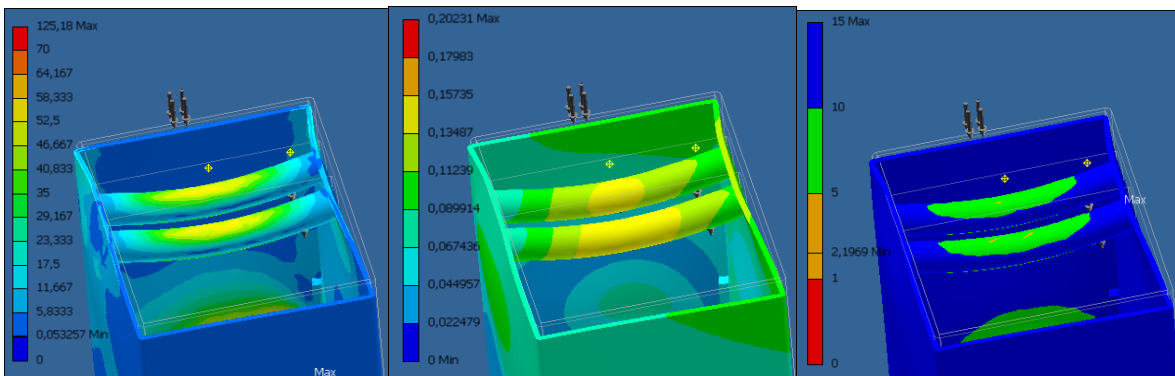


Fig. 148: FEM static stress analysis of the pin of the Leg Box: Equivalent stress in Mpa (left), Deformation in mm (middle) and Safety Factor (right)

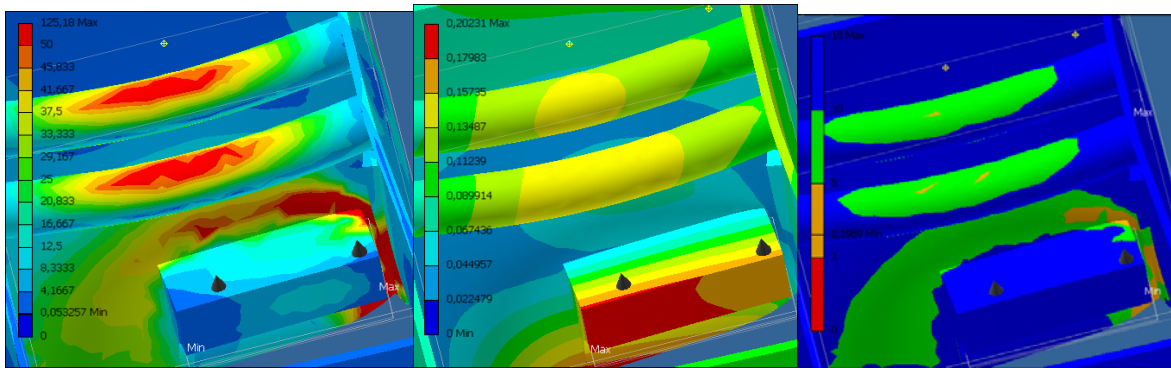


Fig. 149: FEM static stress analysis of the support plate of the Leg Box: Equivalent stress in Mpa (left), Deformation in mm (middle) and Safety Factor (right)

Table 61: Results of the FEM static stress analysis of the Hollow beam, pin and support plate

	hollow beam	pin	plate	local stresses
STRESS	Mpa	Mpa	Mpa	
max equivalent stress	5,00	58,00	30,00	125,20
DEFORMATION	mm	mm	mm	
maximum deformation	0,005	0.16	0.2	0,2
SAFETY FACTOR				
minimum static safety factor	6,3	5	5	2,2

The results of both analysis are rather similar. Again, the absence of local stresses and the model simplification in ISSD cause a difference in stress and deformation at certain areas. Notice that the deformation of the hollow beam in Inventor is of the same order of magnitude as the deformation in ISSD, the other parts however are not. This is because the calculations in ISSD for deformations were performed with a local constraint, which is not the case in Inventor. In Inventor the constraint remains at the bearings for all loads. This results in higher deformation for the Inventor results.

Design Accelerator Parts

Calculation of bearing

Dynamic Equivalent Radial Load:

The dynamic equivalent radial load for radial and angular contact ball bearings and radial roller bearings, under constant radial and axial loads, is given by

$$P = (XF_r + YF_a) \cdot f_d$$

The dynamic equivalent radial load for radial roller bearings with $\alpha = 0$, and subjected to radial load only, is given by

$$P_r = F_r$$

where:

F_r radial component of bearing load [lbforce, N].

F_a axial component of bearing load [lbforce, N].

X radial factor.

Y axial factor.

f_d coefficient of additional dynamic forces.

Dynamic Equivalent Axial Load:

The dynamic equivalent axial load for thrust ball bearings and thrust roller bearings with $\alpha \neq 0$ is given by

$$P = (XF_r + YF_a).f_d$$

Thrust ball and roller bearings with $\alpha = 0$ deg. can support axial loads only. The dynamic equivalent axial load for this type of bearings is given by

$$P_a = F_a$$

where:

F_r radial component of bearing load [lbforce, N].

F_a axial component of bearing load [lbforce, N].

X radial factor.

Y axial factor.

f_d coefficient of additional dynamic forces.

Static Equivalent Radial Load:

The static equivalent radial load for radial and angular contact ball bearing and radial roller bearing is the greater of the two values given by

$$P_{0r} = X_0 F_r + Y_0 F_{aa}$$

$$P_{0r} = F_r$$

where:

F_r radial component of bearing load [lbforce, N].

F_a axial component of bearing load [lbforce, N].

X radial factor.

Y axial factor.

Static Equivalent Axial Load:

The static equivalent axial load for thrust ball bearing and thrust roller bearing is given by

$$P_{0a} = X_0 F_r + Y_0 F_{aa}$$

where:

F_{0a} dynamic equivalent axial load, [lbforce, N]

F_r radial component of bearing load [lbforce, N].

X radial factor.

Y axial factor.

Basic Rating Life:

The basic rating life for radial ball bearing is given by

$$L_{10} = \left(\frac{C_r}{F_r} \right)^3$$

where:

C_r basic dynamic radial load rating, [lbforce, N]

P_r dynamic equivalent radial load, [lbforce, N]

The basic rating life for radial roller bearing is given by

$$L_{10} = \left(\frac{C_r}{P_r} \right)^{\frac{10}{3}}$$

where:

C_r basic dynamic radial load rating, [lbforce, N]

P_r dynamic equivalent radial load, [lbforce, N]

The basic rating life for thrust ball bearing is given by

$$L_{10} = \left(\frac{C_a}{P_a} \right)^3$$

where:

C_a basic dynamic axial load rating, [lbforce, N]

P_a dynamic equivalent axial load, [lbforce, N]

The basic rating life for thrust roller bearing is given by

$$L_{10} = \left(\frac{C_a}{P_a} \right)^3$$

where:

C_a basic dynamic axial load rating, [lbforce, N]

P_a dynamic equivalent axial load, [lbforce, N]

Adjusted Rating Life:

The basic rating life for radial ball bearing is given by

$$L_{10} = \left(\frac{C_r}{P_r} \right)^3$$

where:

C_r basic dynamic radial load rating, [lbforce, N]

P_r dynamic equivalent radial load, [lbforce, N]

Power lost by friction

$$P_z = \mu \cdot P \cdot \pi \cdot d \cdot \frac{n}{60000}$$

where:

μ Friction Factor [MPA,psi]

P Dynamic equivalent load [N]

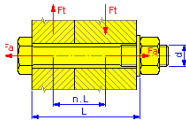
d Bearing inside diameter [mm]

n shaft rotates, [rpm]

Calculation of bolts

Basic Calculation of Bolted Connection

Calculation of a bolted connection with prestress. Loading by axial or tangential force. The calculation is carried out in metric or imperial units. With the ANSI standard set, the calculation is performed in imperial units, with corresponding bolt dimensions also included.



Input Parameters

Ψ	factor of joint tightness - If no specific joint tightness is required, the minimum value is used ($\Psi_{\min} = 0.2$). Dynamic loading (e.g. connecting rod bolts) requires higher values.
F_a	maximum operation axial force
n	force input factor
F_t	maximum operation tangential force
f	joint friction factor (between the connected materials)
z	number of bolts
d	thread diameter
p	thead pitch
d_s	mean bolt diameter
d_{\min}	minimum bolt diameter
R_e	Yield strength
k_s	safety factor (The value is selected according to the required safety level of the joint.)
p_A	allowable thread pressure (nut)
E_1	elasticity module of bolt
f_1	thread friction factor between the nut and the bolt
f_2	friction factor in the contact surface of the nut or bolt
L	width of connected material
E_2	elasticity module of connected material

Calculated Parameters

According to the following calculation formulas, the program calculates geometric dimensions of the bolt from the specified nominal bolt diameter:

Minimum diameter of the nut thread

$$D_1 = d - 1.082531 p$$

Pitch diameter of the thread

$$d_2 = d - 0.649519 p$$

Calculation of Bolted Connection:

Working force in the joint - determined by the axial force, has to secure the transfer of tangential force by friction of connected materials. Also affected by the requirement on tightness expressed by the factor of joint tightness.

$$F_{\max} = \frac{1 + \Psi}{z} \left(F_a + \frac{F_t}{f} \right)$$

Prestress force - based on the working force of the joint, takes into account the elastic yielding of bolts and flanges by using the c_n yielding constants.

$$F_0 = F_{\max} \left(\frac{c_2}{c_1 + c_2} \right) \frac{F_a}{z}$$

where:

$$c_1 = c_{10} + (1 - n) c_{20}$$

$$c_2 = n c_{20}$$

$$c_{10} = \frac{L + 0.8d}{E_1 \frac{\pi d_s^2}{4}}$$

$$c_{20} = \frac{L}{E_2 \frac{\pi}{4} \left(\left(1.5d + \frac{L}{3} \right)^2 - 1.05d^2 \right)}$$

for steel $a = 10$

for cast iron $a = 8$

for aluminum and its alloys $a = 6$

Required tightening moment - determined by the prestress force and affected by the friction factor in threads between the nut and bolt, and by the friction factor in the contact surface of the nut or bolt.

$$M_u = F_0 \left[\frac{d_2}{2} \tan \left(\frac{p}{\pi d_2} + \frac{f_1}{\cos 30^\circ} \right) + 0.7d \cdot f_2 \right]$$

Calculated tensile stress in the bolt

$$\sigma_t = \frac{4 F_0}{\pi \cdot d_{\min}^2}$$

Calculated torsion stress in the bolt

$$\tau_k = \frac{16 M_u}{\pi \cdot d_{\min}^3}$$

Reduced stress in the bolt

$$\sigma_{red} = \sqrt{\sigma_t^2 + 3 \cdot \tau_k^2}$$

Stress caused by maximum force loading the bolt

$$\sigma_{max} = \frac{4 F_{\max}}{\pi \cdot d_{\min}^2}$$

Calculated pressure in the thread

$$p_c = \frac{4 F_{\max}}{\pi (d^2 - D_1^2) \frac{0.8d}{p}}$$

Calculation check - stress in the bolt during tightening the joint and during the operation (respecting the specified joint safety), and the check of allowable pressure in threads.

$$\sigma_{red} \leq R_e / k_s \text{ and } \sigma_{max} \leq R_e / k_s \text{ and } p_c \leq p_A$$

Fatigue strength of bolted connection

Conventional check procedures at fatigue loaded bolted connection (based on the ultimate or yield strength of material) do not provide sufficient guaranty of safe joint design. That is why the fatigue strength of joint is used in check of fatigue loaded joints. The description of fatigue loaded bolted connection joints checking follows. This description follows step by step the implementation in the program:

1. Specifying an endurance limit

In the first step the calculation determines the endurance limit at constant strength σ_c for the specified type, design, loading and material of bolted connection.

2. Specifying finite-life fatigue limit

The finite-life fatigue limit σ_f is calculated for the specified joint life that is in the ($N < 10^6$ cycles) range of timed strength. Calculation continues with this finite-life fatigue limit.

3. Calculation of parameters of particular fatigue loadings

Mean values for given upper and lower cycle loadings are calculated their mean values according to the following formulas. This is done for all specified loadings.

$$F_m = \frac{F_h + F_n}{2}, F_a = \frac{F_h - F_n}{2}$$

4. Effect of strokes

If strokes affect the joint besides the fatigue loading, their influence must be included into the calculation. This is implemented by using the dynamic stroke factor in the formula for determining the maximum calculated loading:

$$F_{max} = F_m + \gamma F_a$$

5. Calculation of actuating stress in the bolted connection joint

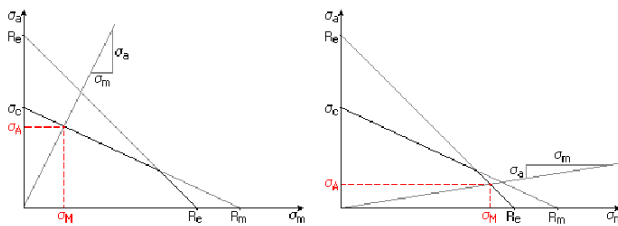
Mean cycle stress σ_m and upper cycle stress σ_h are calculated for the specified mean cycle loading F_m and maximum calculated loading F_{max} with the formulas used in static calculation. These stresses are used for calculation of cycle amplitude according to the formula:

$$\sigma_a = \sigma_h - \sigma_m$$

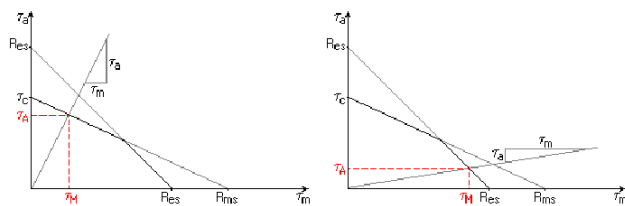
6. Specifying fatigue strength of joint

For calculated stress and known endurance limit the resulting strength of fatigue joint is easily determined according to the selected fatigue curve. The procedure of fatigue strength determination for both normal and shear stresses is obvious from the following pictures.

Haigh charts of normal stress for different σ_a / σ_m ratio (modified Goodman fatigue curve is used):



Haigh charts of normal stress for different τ_a / τ_m ratio (modified Goodman fatigue curve is used):



7. Joint check

In the last step the program calculates the joint safety factor $n_c = \sigma_A / \sigma_a$ and compares it with the required safety degree. For convenient bolted connection the condition $n_f \leq n_c$ must be satisfied.